A Predictive Potential Field Concept for Shared Vehicle Guidance

zur Erlangung des akademischen Grades eines
DOKTORS DER INGENIEURWISSENSCHAFTEN (Dr.-Ing.)
der Fakultät für Maschinenbau
der Universität Paderborn

genehmigte
DISSERTATION

von
Dipl.-Ing. Thorsten Brandt, M. S.
aus Euskirchen

Tag des Kolloquiums: 12.11.2007
Referent: Prof. Dr.-Ing. habil. Jörg Wallaschek
Korreferent: Prof. Dr. rer. nat. habil. Michael Dellnitz

Acknowledgements

This thesis owes its existence to the influence and support of many institutions and individuals. First of all, I would like to express my sincere thanks to my advisors and committee members Prof. Jörg Wallaschek, Prof. Michael Dellnitz, Prof. Ansgar Trächtler, and Prof. Rolf Mahnken.

In particular, I would like to acknowledge Prof. Wallaschek. During my time as a scholar of the International North Rhine-Westphalia Graduate School of Dynamic Intelligent Systems he was very active in continuously providing me with excellent research conditions. As a result both his research group at the Heinz Nixdorf Institute (HNI) as well as the L-LAB, a public private partnership between the University of Paderborn and the Hella KGaA Hueck & Co., were very enjoyable and stimulating places.

Therefore, I would like to say thanks to all colleagues and students within the HNI and the L-LAB. Among many, special thanks go to Silke Hanisch, diploma student of the first hour, and to Tobias Hesse, Michael Kluge, Christian Löper, and Christoph Sondermann-Wölke, whose contributions had a great impact on the synthesis of this thesis. A key role was also played by Jun.-Prof. Thomas Sattel: together we started to discover the fields of driver assistance and many ideas evolved during some intensive discussions, which I appreciate very much.

Special thanks go to the "human-machine group" at the L-LAB. The interdisciplinary ensemble of engineers and psychologists often led to vivid discussions, which made work real fun. Among these, I am particularly indebted to Michael Böhm for his help in the experimental design of the simulator study. Also, I would like to thank Dr. Frank Flemisch from the DLR in Braunschweig. With his visions, such as the h-metaphor, he had a significant influence on this thesis.

A personal highlight for me was the opportunity to spend 3 months as a visiting researcher at the group of Prof. J. Christian Gerdes at the Dynamic Design Lab at Stanford University. Therefore I thank him and his entire group - particularly Joshua Switkes. This was made possible by the financial support of the Hans-Lenze-Stiftung and the great engagement of the graduate school team headed by Dr. Eckhard Steffen as well as the administration team at the HNI and the L-LAB, who did a great job. Most notably were Kerstin Hille and Marina Kassühlke, who always kept the administrative burdens as low as possible.

My sincere thanks also go to Christoph Sondermann-Wölke, Christian Löper, Sabine Raphael, and Karina Hirsch for their great engagement in proofreading this document.

Last but not least a special mention goes to my family. Thanks - in particular to my favorite women Andrea and Emma - for all their support and their understanding, which made it possible to complete this thesis in the first place.

Abstract

Modern driver assistance systems are gradually engaging in vehicle guidance. Examples are systems for lane-keeping and for lane departure warning. For future assistance systems, e.g. for lane-change or evasion maneuvers, collision-free motion planning has to be addressed. This work combines motion planning and trajectory tracking into a unified framework of potential field methods for shared vehicle guidance between driver and assistance system. Therein, a so-called elastic band, originally introduced in robotics, acts like a virtual antenna, similar to the antennae of an insect, sensing trajectories of low hazards in the environment. Specifically for the automotive application, the motions of other traffic participants are also anticipated by extrapolation methods. The tracking algorithms consist of curvature based feedforward control in combination with a potential field based guidance controller, which is shown to be stable in the sense of Lyapunov. Besides that, a Lyapunov function provides bounds for the tracking error depending on the initial conditions and the parameters of the controller. The steering angle, proposed by the guidance system, is communicated to the driver via an assistance-torque at the steering wheel. In parallel, the driver's steering intension is incorporated to shape the planned trajectories. This interactive guidance concept is experimentally tested in a driving simulator. Therein, different configurations of the assistance torques are analyzed.

Kurzfassung

Moderne Fahrerassistenzsysteme unterstützen den Fahrer bereits heute in der Fahrzeugführung. Beispiele hierfür sind Systeme zur Spurhalteassistenz und zur Spurverlassenswarnung. Zukünftige Systeme wie Spurwechsel- oder Ausweichassistent machen Methoden zur kollisionsfreien Bewegungsplanung im Verkehrsraum erforderlich. Die vorliegende Arbeit stellt einen durchgängigen Ansatz zur Bewegungsplanung und Bahnfolgeregelung auf Basis von Potentialfeldmethoden vor. Die Umgebung des Fahrzeugs wird dabei zunächst in einer Gefahrenkarte abgebildet. Ein elastisches Band, welches ähnlich den Fühlern von Insekten vor dem Fahrzeug her geschoben wird, detektiert Bereiche des Verkehrsraums mit besonders niedrigem Gefahrenniveau. Hierbei werden, ergänzend zu Ansätzen aus der Robotik, auch die Bewegungen anderer Verkehrsteilnehmer berücksichtigt. Die Bahnfolgeregelung besteht aus einer Kombination von krümmungsbasierter Vorsteuerung und potentialfeldbasiertem Regler. Für das potentialfeldbasierte Regelkonzept wird Stabilität im Sinne Ljapunov's nachgewiesen. Über eine entsprechende Ljapunov-Funktion können abhängig von Anfangsbedingungen und Reglerparametern Schranken für Quer- und Winkelabweichung von der geplanten Trajektorie angegeben werden. Der vom Assistenzsystem vorgeschlagene Lenkwinkel wird dem Fahrer über ein entsprechendes Moment am Lenkrad kommuniziert. Der resultierende, vom Fahrer gewählte Lenkwinkel, wird wiederum in der Trajektorienplanung berücksichtigt. Diese Interaktion zwischen Fahrer und Assistenzsystem wird anhand verschiedener Ausprägungen des Assistenzmoments in einem Fahrsimulator experimentell untersucht.

Contents

Nomenclature

Reference frames

$\underrightarrow{\uparrow \mathrm{E}}$: $(E^*, {}_E\mathbf{e}_x, {}_E\mathbf{e}_y, {}_E\mathbf{e}_z)$	**E**arth-fixed frame
$\underrightarrow{\uparrow \mathrm{R}}$: $(R^*, {}_R\mathbf{e}_x, {}_R\mathbf{e}_y, {}_R\mathbf{e}_z)$	**R**oad-fixed frame
$\underrightarrow{\uparrow \mathrm{G}}$: $(G^*, {}_G\mathbf{e}_x, {}_G\mathbf{e}_y, {}_G\mathbf{e}_z)$	**G**uidance-frame (trajectory-fixed)
$\underrightarrow{\uparrow \mathrm{T}}$: $(T^*, {}_T\mathbf{e}_t, {}_T\mathbf{e}_n, {}_T\mathbf{e}_b)$	**T**rajectory-fixed (Frenet) frame
$\underrightarrow{\uparrow \mathrm{V}}$: $(V^*, {}_V\mathbf{e}_x, {}_V\mathbf{e}_y, {}_V\mathbf{e}_z)$	**V**ehicle-fixed frame
$\underrightarrow{\uparrow \mathrm{FL}}$: $(FL^*, {}_{FL}\mathbf{e}_x, {}_{FL}\mathbf{e}_y, {}_{FL}\mathbf{e}_z)$	wheel-fixed frame **F**ront **L**eft
$\underrightarrow{\uparrow \mathrm{FR}}$: $(FR^*, {}_{FR}\mathbf{e}_x, {}_{FR}\mathbf{e}_y, {}_{FR}\mathbf{e}_z)$	wheel-fixed frame **F**ront **R**ight
$\underrightarrow{\uparrow \mathrm{RL}}$: $(RL^*, {}_{RL}\mathbf{e}_x, {}_{RL}\mathbf{e}_y, {}_{RL}\mathbf{e}_z)$	wheel-fixed frame **R**ear **L**eft
$\underrightarrow{\uparrow \mathrm{RR}}$: $(RR^*, {}_{RR}\mathbf{e}_x, {}_{RR}\mathbf{e}_y, {}_{RR}\mathbf{e}_z)$	wheel-fixed frame **R**ear **R**ight

Notation of matrices and vectors

${}_E\mathbf{r}^{E^*,P}$	position vector of a point P in $\underrightarrow{\uparrow \mathrm{E}}$ (vector from the origin E^* of $\underrightarrow{\uparrow \mathrm{E}}$ to P, projected on the unit vectors ${}_E\mathbf{e}_x, {}_E\mathbf{e}_y, {}_E\mathbf{e}_z$)
${}^E_V\mathbf{v}^P$	velocity of a point P with respect to $\underrightarrow{\uparrow \mathrm{E}}$ projected on $\underrightarrow{\uparrow \mathrm{V}}$
${}^E_V v^P_x$	${}_V\mathbf{e}_x$-component of ${}^E_V\mathbf{v}^P$
${}^E_V\mathbf{a}^P$	acceleration of a point P with respect to $\underrightarrow{\uparrow \mathrm{E}}$ projected on $\underrightarrow{\uparrow \mathrm{V}}$
${}^E_V a^P_x$	${}_V\mathbf{e}_x$-component of ${}^E_V\mathbf{a}^P$
$\mathbf{C}^{E,V}$	transformation matrix from $\underrightarrow{\uparrow \mathrm{V}}$ to $\underrightarrow{\uparrow \mathrm{E}}$, e.g. ${}^E_E\mathbf{v}^P = \mathbf{C}^{E,V} \cdot {}^E_V\mathbf{v}^P$
$\frac{{}^E d}{dt}(\cdot)$	time derivative with respect to reference frame $\underrightarrow{\uparrow \mathrm{E}}$

Objects involved in motion planning

$\mathcal{R}$	center of the road
$\partial\mathcal{B}_l, \partial\mathcal{B}_r$	left and right border of the road
$\mathcal{O}_j$	obstacle
$\mathcal{V}$	host-vehicle
$\mathcal{P}$	planned path

Vehicle parameter

a, b	front and rear axle distance to the **C**enter of **G**ravity CG
d	track width
m	mass
I_z	yaw moment of inertia
C_x^q, C_α^q	longitudinal stiffness and cornering stiffness of tire q
SG	self **S**teering **G**radient

Vehicle dynamics

β	side slip angle
ψ	yaw angle
δ, δ^{SW}	steering angle at the wheels and at the steering wheel
δ_A	Ackermann steering angle
s_x^q	longitudinal slip at tire q
α^q	cornering angle at tire q
U_x, U_y	${}_V\mathbf{e}_x$- and ${}_V\mathbf{e}_y$-component of ${}^E\mathbf{v}^{CG}$, $U_x := {}^E_V v_x^{CG}$, $U_y := {}^E_V v_y^{CG}$
U_t, U_n	${}_T\mathbf{e}_t$- and ${}_T\mathbf{e}_n$-component of ${}^E\mathbf{v}^{CG}$, $U_t := {}^E_T v_t^{CG}$, $U_n := {}^E_T v_n^{CG}$
F_x^q	longitudinal force at tire q
F_y^q	lateral force at tire q
$M_{\Delta F_x}$	yaw moment caused by differential braking

Potential field motion planning and guidance

P_i	node of elastic band
$\mathbf{r}_i$	position vector of P_i with respect to $\underline{\uparrow\mathrm{R}}$
${}_R V_i^{B_l}$, ${}_R V_i^{B_r}$	hazard potential of the left and the right border of the road at P_i in $\underline{\uparrow\mathrm{R}}$
${}_R V_i^{\mathcal{O}_j}$	hazard potential of obstacle $\mathcal{O}_j$ at P_i in $\underline{\uparrow\mathrm{R}}$
${}_R V_i^{\mathrm{haz}}$	resulting hazard potential at P_i in $\underline{\uparrow\mathrm{R}}$
${}_R V_i^{\mathrm{int}}$	internal potential of elastic band at P_i in $\underline{\uparrow\mathrm{R}}$
κ, κ_G	curvature of the driven and of the proposed path
ICC	**I**nstantaneous **C**enter of **C**urvature of the driven path (instantaneous center of rotation)
ICC_G	**I**nstantaneous **C**enter of **C**urvature of the proposed path
${}_R\mathbf{q}$	generalized coordinates of the host-vehicle $\mathcal{V}$ with respect to $\underline{\uparrow\mathrm{R}}$
${}_R\Delta\mathbf{q}$	path tracking error (longitudinal, lateral, and angular deviation)
${}_R\Delta\mathbf{q}_{\mathrm{lat}}$	lateral path tracking error (lateral and angular deviation)

Chapter 1

Introduction

Driving is a complex task: wrong decisions taken by drivers contributed to approximately 86% of all accidents on German roads in 2005 (2006, [2]). About 440,000 injured and more than 5,000 killed people in the same year tragically prove that the safety on our roads needs to be increased. A very promising approach consists in *driver assistance systems* that provide support in the different subtasks of driving.

1.1 State of the Art

According to Donges (1982, [28]) driving can be divided into *navigation*, *guidance*, and *stabilization*. Therein, navigation refers to the global planning process of a route from a starting location to a desired destination. On the guidance level, trajectories are planned locally through the traffic and appropriate control inputs such as the steering angle are predefined. However, depending on the states of the vehicle and on the environmental conditions it might be necessary to adapt the control inputs in a way that the vehicle behaves stable along the planned trajectories. This task is performed on the stabilization level.

1.1.1 Driver Assistance Systems

Navigation systems basically provide comfort functionalities, whereas safety is affected by systems that act on the guidance or the stabilization level. Among these systems, Van Zanten (2002, [126]) reports the longest tradition for stabilizing systems as for example the **A**nti-lock-**B**raking **S**ystem (ABS) or the **E**lectronic **S**tability **P**rogram (ESP). Thurner (1998, [113]) expects the remaining safety potential of these accident avoiding *active safety* systems much higher than the almost exploited potential of *passive safety* systems aiming at crashworthiness, see Figure 1.1.

Today's safety systems work mostly on the stability level and therefore rely on sensors that measure the states of the vehicle such as the yaw rate. Future developments will focus on *active guidance* systems that link the vehicle to its environment. This trend mainly originates from the rapid development of environmental sensor systems such as **RA**dio **D**etection **A**nd **R**anging (RADAR), **LI**ght **D**etection **A**nd **R**anging (LIDAR), or video and effective algorithms for sensor fusion, object detection and tracking. This

development is already reflected in first systems on the market. Examples are the **A**daptive **C**ruise **C**ontrol (ACC) for longitudinal guidance (WINNER ET AL. (1996, [123])) and **L**ane **D**eparture **W**arning (LDW) for lateral guidance, see SUZUKI AND JANSSON (2003, [112]).

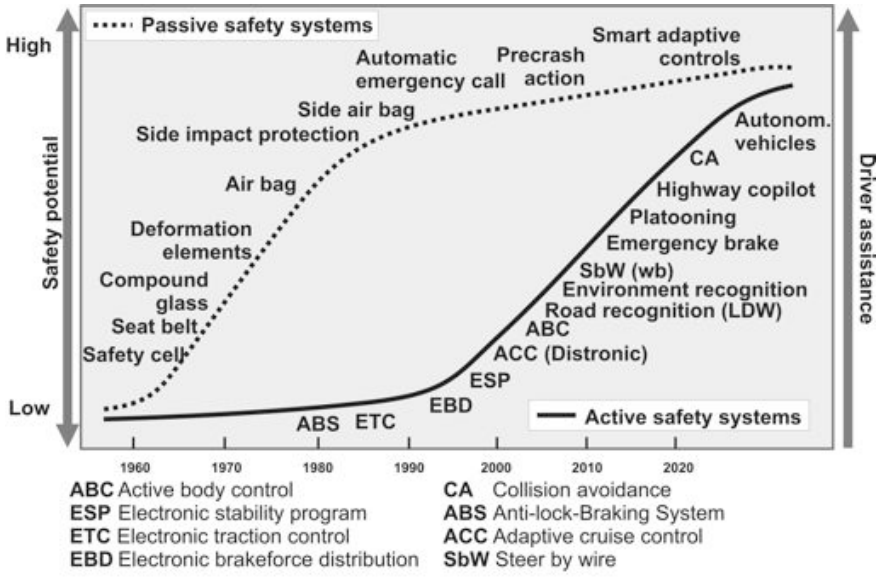

Figure 1.1: Roadmap of driver assistance and safety systems by THURNER (1998, [113])

Driver assistance for lateral vehicle guidance is also discussed by FENG, TAN AND TOMIZUKA (2000, [32]) and a general overview of research fields affected by driver assistance systems on the guidance level is given by VAHIDI AND ESKANDARIAN (2003, [117]).

1.1.2 Environmental Sensors

Arrangements of state of the art environmental sensors are already capable to achieve circumferential perceptibility as exemplary sketched in Figure 1.2.

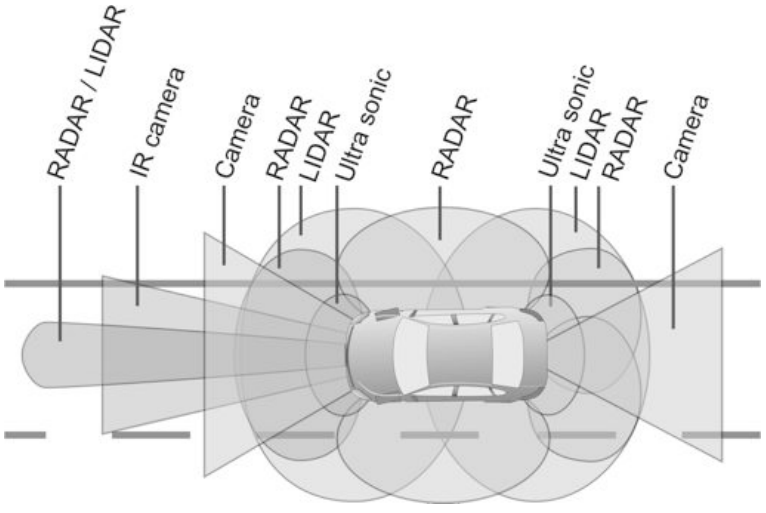

Figure 1.2: Principle sketch of environmental perception

Therein, each of the sensor systems indicated in Figure 1.2 has specific properties concerning range, precision, and robustness with respect to environmental conditions. Some representative characteristic data of state of the art environmental sensors are collected in Table 1.1.

Table 1.1: Environmental sensor specifications

Sensor type	**Range**	**Opening angle**	**Longitudinal precision**	**Velocity acquisition**	**Robustness (weather)**
LIDAR	150 m	up to 16°	< 0.5 m	derivative	good
77 GHz RADAR	150 m	8°...12°	< 1 m	direct	very good
24 GHz RADAR	50 m	70°...120°	< 0.5 m	direct	very good
Video	50 m	up to 45°	< 1 m	derivative	neutral
IR-scanner	30 m	> 120°	< 0.1 m	derivative	good

Similar data for RADAR, LIDAR, and camera systems are also compiled by REICHART (2000, [89]). Each of these single-sensor systems has already been applied in automotive applications: early algorithms for image processing at high speeds for autonomous automotive guidance were developed and experimentally tested by DICKMANNS (1990, [26]), while RADAR and LIDAR systems have primarily been used in longitudinal guidance systems such as ACC. A comprehensive review of environmental recognition, especially on vision systems, and future trends is given by DICKMANNS (2002, [24]).

Beyond the further development of single-sensor systems, as collected in Table 1.1, another innovation thrust is generated by *sensor fusion*. Sensor fusion aims at combining different sensor technologies in order to increase range, precision, and - most importantly - robustness compared to single sensor solutions. Developments in this active field of research are listed in the contributions of VUKOTICH AND KIRCHNER (2001, [121]), of KÄMPCHEN, FÜRSTENBERG AND DIETMAYER (2004, [54]), and of DARMS AND WINNER (2006, [23]).

In general, the processing of environmental sensor data can be divided into two tasks. First, static elements of the environment have to be identified. Therein, lane detection is of special interest for vehicle guidance systems. Nowadays, lane detection algorithms are sufficiently robust and already in production with systems such as LDW. A sample algorithm is given in ZHENG AND CHENG (2004, [71]). The second task involves the detection and tracking of other traffic participants. Classical tracking approaches rely on a single dynamic model to predict the motion of detected objects. Modern approaches take different parallel models into account, weighted accordingly to the previous motion of the tracked object. Therefore, the object state estimation, especially for highly dynamic driving maneuvers, is an important issue. One recent approach was tested by KÄMPCHEN, WEISS, SCHAEFER AND DIETMAYER (2004, [55]), where data, based on sensor fusion incorporating an **I**nertial **N**avigation **S**ystem (INS), a **G**lobal **P**ositioning **S**ystem (GPS) receiver, two infrared laser scanner, a 77 GHz RADAR, and a monocular vision system were processed. Alternative research deals with the prediction of trajectories of objects by means of learning algorithms as the one presented by VASQUEZ ET AL. (2004, [118]).

A further stimulus for guidance systems can be expected by using differential GPS in combination with INS and *digital maps*. Therein, modern GPS systems allow the precise

measurement of the location of the host-vehicle as well as the measurement of the dynamic states of the vehicle, see SIMON (2003, [104]) and RYU (2004, [94]). In addition, digital maps can be used to precondition driver assistance systems by predicting static elements of the environment as proposed in the work of SCHRAUT (2000, [99]).

Last but not least, the proceeding deployment of wireless network applications promises a further improvement of environmental perception by *car to car communication*, see LÜBKE (2004, [72]); and therefore a further stimulus for the development of vehicle guidance systems can be expected.

1.1.3 Human Machine Interaction

The question how to assist the driver properly in order to improve his decisions is very difficult. Up to now most systems are restricted to inform the driver, see for example BULD AND KRÜGER (2002, [13]). In the near future the other end of the spectrum might be marked by systems, such as the automatic emergency brake or evasion systems as the one proposed by STÄHLIN, SCHORN AND ISERMANN (2006, [108]), that guide the vehicle fully autonomously if an accident seems unavoidable. Though, the degree of cooperation between driver and assistance system is still very low in both variants. Furthermore, both approaches have significant drawbacks. A system, that is limited to provide information, can be quite ineffective if the driver is inattentive. On the other hand systems, that take over the driving task completely, hold the risk of failures that cannot be corrected by the driver. Beyond that, the legal situation of autonomous systems, when involved in accidents, is a precarious topic.

GOODRICH AND BOER (2000, [43]) consider the process of sharing responsibility between a human driver and a collision avoidance system as a trade off between safety enhancement and human autonomy. Therein, the predicted safety enhancement must be compelling enough to justify the cost to the drivers autonomy.

The ***h**-metaphor* of FLEMISCH ET AL. (2003, [35] and 2004, [34]) provides a guideline for shared vehicle guidance between driver and assistance system. Thereby, the **h** stands for **h**orse, comparing the interaction between driver and vehicle to the interaction between rider and horse. The main idea is to have a continuous shift of the driving task between driver and vehicle. The metaphor refers to the extremes of interaction as *loose rein* and *tight rein*. Loose rein characterizes a mode where the rider/driver might be inattentive and the horse/vehicle is in charge to move safely through its environment and for example not to collide with obstacles. When the rider indicates, by tight reins, that he is aware of the situation, he can force the horse to initiate actions, as for example to jump over a trench, that the horse would not initiate on its own. In the same way the driver can dominate over vehicle guidance and for example force the vehicle to "collide" with an beverage can lying on the road, that is wrongly identified as an obstacle by the environmental sensors.

The coordination of vehicle guidance between driver and assistance system has to be established via an appropriate *human machine interface*. Due to the gradually increasing number of systems that interact with the driver, human machine interfaces in vehicles experience a continuous change. In general, the communication with the driver is based on *visual*, *acoustic*, and *haptic* information. As the driving task is mainly based on visual information, the visual channel usually denotes the highest demand. In spite of this,

many assistance and information systems also communicate via visual information with the driver. BIELACZEK (1999, [7]) notes that this congestion may lead to a reduction of the driving performance. SCHATTENBERG (2002, [97]) approves this observation by a collection of surveys cited in his work.

One approach to resolve the conflict between a rising amount of information on the one hand and the demand on the visual channel on the other, is to distribute the communication with the driver on the visual, the acoustic and the haptic channels. In this regard the work of ZEILINGER (2005, [127]) focuses on haptic communication and gives an overview of active haptic interfaces used in automotive research projects. Figure 1.3 shows for example a vehicle equipped with active side sticks. HUANG (2004, [51]) tries to include the properties of active haptic interfaces into a description of the overall vehicle guidance control loop including driver, driver assistance system, and human machine interface.

Figure 1.3: DaimlerChrysler "SideStick" according to ZEILINGER (2005, [127])

In terms of the h-metaphor haptic interfaces are best suited to transmit bidirectional information between driver and assistance system, thereby keeping the driver continuously involved in vehicle guidance. PENKA (2001, [84]) conducted surveys, which showed that haptic interfaces such as active side sticks can lead to a higher lane-keeping precision and to a reduction of the visual demand of the driver compared to *force feedback* steering wheels. These results were supported by surveys of BULD AND KRÜGER (2002, [13]) in the scope of the project EMPHASIS (**E**ffort **M**anagement and **P**erformance **HA**ndling in **SI**cherheitskritischen **S**ituationen).

However, drivers are trained to guide their vehicles via steering wheels and will therefore hardly accept new interfaces such as active side sticks in the near future. For this reason force feedback steering wheels are favored as haptic human machine interfaces. From a technological point of view, force feedback steering wheels are further promoted by the development of active steering systems: assuming *steer-by-wire*, there is no direct mechanic link between the deflection of the steering wheel and the steering angles at the wheels. Thus, a force feedback actuator can apply a torque at the steering wheel to display information from the assistance system, while the steering angles at the wheels can be set according to the chosen guidance strategy and vehicle stability requirements. Examples of activities in the field of steer-by-wire systems are the contributions of KALTENBACH ET AL. (2000, [53]), WINNER ET AL. (2004, [122]), and BAJCINCA (2006, [5]).

State of the art steering systems are not yet based on "by-wire technology". Nevertheless, different active steering systems, keeping a mechanical link between steering wheel and wheels, have evolved. The first class of active steering systems aims at changing the

steering ratio between the deflection of the steering wheel and the steering angle at the wheels. In order to do so, a planetary gear is used to add an additional steering angle to the one commanded by the driver. This technology is for example in production at BMW (2005, [100]) to adapt the steering ratio to the driving speed.

Electro-mechanical power steering systems that apply an additional steering torque to the one actuated by the driver are another class of active steering systems. The electrical actuator, for example in production at VOLKSWAGEN (2005, [101]), can also be used to display haptic information to the driver. One of the first systems applying an assisting torque for lane-keeping was presented by NAAB AND REICHART (1994, [77]) in the scope of PROMETHEUS (**PRO**gram**M**e for an **E**uropean **T**raffic with **H**ighest **E**fficieny and **U**nprecedented **S**aftey). Other examples are listed in the contributions of POHL AND EKMARK (2003, [85]) and CONSANO AND MURDOCCO (2005, [20]).

The different steering technologies are compared by HOLLE (2004, [50]). Noteworthy is, that the combination of a planetary gear to add an additional steering angle and of an actuator to provide an additional torque at the steering wheel, yields the same functionality as a steer-by-wire system. The torque can then be used to communicate with the driver, while the additional steering angle could be used for vehicle stability enhancement.

Following the guidelines of the h-metaphor and establishing shared vehicle guidance without further increasing the visual demands of the driver, force feedback steering seems to be a promising solution. In doing so, haptic interaction can be achieved based on today's active steering systems.

1.1.4 Vehicle Guidance Control

In order to guide the vehicle cooperatively with the driver, the assistance system has to be able to generate adequate guidance strategies. Hence, maneuvers have to be planned and appropriate control inputs have to be determined. The process of planning collision-free maneuvers through the traffic is referred to as *motion planning*, while the generation of the according control inputs is denoted as *vehicle guidance control*. Noteworthy is, that vehicle guidance control provides quantities like the steering angle, which finally have to be coordinated with the driver. In general, longitudinal and lateral vehicle guidance can be distinguished. For lane-keeping and collision avoidance lateral guidance control is predominant and is therefore emphasized in the following.

The first lateral vehicle dynamics models and the analysis of the vehicle's response to steering input already date back to the 1940s and 1950s. Significant contributions are the works of RIEKERT AND SCHUNCK (1940, [91]) and SEGEL (1956, [102]). However, the question about how to set the control inputs in order to track a particular trajectory only gained interest in combination with modern sensors and controller hardware. Since the early 1990s various approaches about how to realize previously planned driving maneuvers, ranging from lane-keeping up to autonomous driving, were proposed.

One category of vehicle guidance control strategies are model based approaches. KOEPELE AND STARKEY (1990, [61]) for example compute the steering angle based on an inverse linear vehicle model. Model deficiencies due to nonlinearities are compensated by an additional feedback controller that regulates the lateral positional as well as the yaw

rate deviation. Analogously, PENG AND TOMIZUKA (1990, [83]) combine a feedback with a feedforward controller, which are both subjected to gain scheduling. A further example of model based control of the steering angle for trajectory tracking is given by CONSOLINI, PIAZZI AND TOSQUES (2001, [21]).

In parallel to model based approaches alternative control strategies evolved trying to imitate the driver's behavior. NEUSSER, NIJHUIS AND SPAANENBURG (1992, [78]) propose a neural network controller for this purpose. HATTORI, HOSAKA, TANIGUCHI AND NAKANO (1992, [47]) record human drivers behavior in following winding roads in order to create a rule base to guide vehicles along lane markings. Also KOVÁCS AND KÓCZY (1999, [64]) formulate a fuzzy logic rule base for path tracking. BULIRSCH, VÖGEL, VON STRYK, CHUCHOLOWSKI AND WOLTER (2003, [14]) formulate a driver model on two levels: the anticipation and the stabilization level. On the anticipation level optimal control problems are solved repeatedly on a moving prediction horizon to generate set points. On the stabilization level these set points are tracked by a position controller.

A control concept applicable at high lateral accelerations is given by FREUND AND MAYR (1997, [37]). The presented controller for trajectory tracking includes longitudinal as well as lateral guidance. However, the applied pole placement procedure requires knowledge of all vehicle's states, which in particular requires observation of the side slip angle. Other concepts for trajectory tracking at high curvatures are discussed by SÖNITZ (2001, [106]). In particular, the guidance control concept based on feedback linearization was recently applied in related form by STÄHLIN, SCHORN AND ISERMANN (2006, [108]) within the scope of the project PRORETA and by KÖNIG, KRETSCHMER, NEUBECK AND WIEDEMANN (2006, [63]) for maneuvers at the stability limit of lateral dynamics.

It is important to note, that especially for vehicle guidance control systems at high(way) speeds a look-ahead distance has to be incorporated in order to achieve stability, see for example PARK AND NIKRAVESH (1996, [82]) or GULDNER, TAN AND PATWARDHAN (1996, [46]), who review different control concepts in the scope of the PATH (California **P**artners for **A**dvanced **T**ransit and **H**ighways) program. The advantage of incorporating a spatial preview was also theoretically shown by PENG AND TOMIZUKA (1990, [83]).

For lane-keeping an unique approach to vehicle guidance control is given by ROSSETTER (2003, [93]): lateral and yaw deviation from the lane are combined into an error potential. This potential, in Figure 1.4 symbolized by a spring, causes a virtual guidance force applied to the vehicle. The effect of this virtual guidance force is synthesized by appropriate settings of the control inputs. Look-ahead can be realized by evaluating the potential at positions ahead of the vehicle. A more detailed discussion on *potential field methods* will be given within the scope of motion planning.

Figure 1.4: Potential field based vehicle guidance control

1.1.5 Motion Planning

Motion planning in presence of moving obstacles and therefore the need for *collision avoidance* occurs in a variety of disciplines. Examples are collision avoidance in nautics, in aviation, and in robotics. Among these, collision avoidance at sea has probably the longest tradition. Depending on the distances between the involved ships, VINCENT (1977, [120]) distinguishes between micro and macro collision avoidance and formulates the problem as differential game. Other examples are the works of DJOUANI AND HAMAM (1993, [27]), who address motion planning for ships by minimizing a multi criteria cost function with respect to time, energy, and reduction of rudder wearing. The contribution of ZWIERZEWICZ (2001, [129]) also formulates the problem of collision avoidance of two ships as nonlinear optimal control problem.

However, the proposed strategies are very specific to nautics due to the underlying kinematic and dynamic models. Furthermore, the problem at sea is less constrained than motion planning on roads considering the available space to maneuver. In general, maneuvers at sea are also less dynamic than maneuvers at highways, what relaxes the need for fast motion planning. Another difference compared to automotive problems is that communication between the involved ships is usually established. Summarizing, collision avoidance strategies working at sea are hard to transfer to automotive applications.

Collision avoidance systems in aviation are also well established. Examples can be found in TOMLIN, MITCHELL AND GHOSH (2001, [114]) and in RICHARDS AND HOW (2002, [90]). Though, also algorithms used in airborne collision avoidance seem hardly applicable to automotive problems: besides the fundamentally different dynamics of aircrafts compared to road vehicles, the third available dimension (elevation) and communication between aircrafts facilitate the problem drastically. Therefore, robotics, including manipulators, mobile robots, and car-like autonomous vehicles, is probably the field providing most suitable motion planning algorithms applicable to vehicle guidance. Hence, first an overview of various approaches to motion planning is given, before potential field methods are highlighted.

Various Approaches

MILDNER (2004, [73]) focuses on wheel based car-like robots and structures the field by classifying motion planning methods into

- model based,
- rule based,
- geometric, and
- potential field based.

Geometric methods incorporating moving objects and their velocities might more precisely be referred to as kinematic methods. Besides that, the list could be extended by probalistic methods and it should be mentioned that a variety of mixed approaches exist that cannot clearly be assigned to one of the categories above.

A unique model based method to generate emergency trajectories that avoid collisions with *one* oncoming vehicle was put forward by LACHNER (1997, [66]): the collision avoidance problem is formulated as differential game based on the *modified game of two cars*. The basic idea of the modified game of two cars is to consider the host-vehicle E (**E**vader) and an oncoming vehicle P (**P**ursuer) as parts of one dynamic system. The configuration of this system is depicted in Figure 1.5.

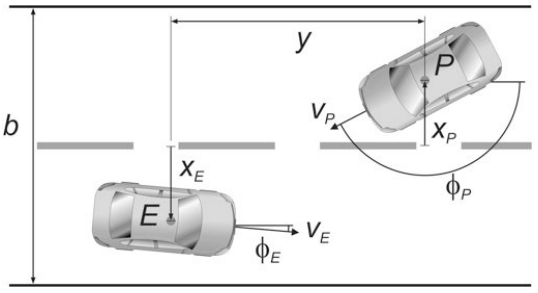

Figure 1.5: Modified game of two cars

The dynamic states of this system are the lateral distances to the road center x_E and x_P, the distance between the two vehicles along the road y, the orientations of the velocity vectors ϕ_E and ϕ_P and the speed of the host-vehicle v_E. The speed of the oncoming car v_P is assumed to be constant. The control inputs are the normalized steering-wheel deflections u_E and u_P of both vehicles as well as the normalized driving or braking force η_E. Inequality constraints result from the requirement not to leave the road of width b as well as from bounds on the control inputs. The characteristic property of this nonlinear system is that E only has control over the inputs u_E and η_E, while P can only access u_P. The objective of E is to avoid a collision with P. Thus, a minimum distance $d_{\min}$ between E and P has to be maintained. To synthesize a collision avoidance strategy for E, maximization of $d_{\min}$ is aspired. It is assumed that E and P cannot communicate. Therefore, E has no knowledge about possible strategies of P and vice versa. However, to solve the differential game a worst-case scenario is assumed: for the oncoming vehicle P an optimal strategy for hypothesized collision intension is presumed. Hence, the task is to identify the corresponding strategy of the collision avoiding vehicle E. In order to solve the problem of maximizing the minimal distance $d_{\min}$ between both vehicles, LACHNER (1997, [66]) simplifies the problem by considering the squared lateral distance $d^2_{\text{final}} = (x_P(t_f) - x_E(t_f))^2$ between both vehicles at the instant of mutual passing t_f. The applied numerical procedure needs a sufficiently accurate estimate of the start solution because convergence cannot be guaranteed in general. Furthermore, the numerical procedure is computationally very expensive and cannot be applied for online motion planning. An exclusion criterion for vehicle guidance is that the generated motion strategies are only guaranteed to be collision-free if P behaves as presumed and strives for collision!

TSOULARIS AND KAMBHAMPATI (1998, [116]) discuss another straight forward model based approach. Therein, a discrete time optimization procedure for collision avoidance is proposed. The nominal path of the robot as well as the trajectories of the obstacles are assumed to be known. In this approach the robot stays on the nominal path but changes its velocity in order not to collide with the obstacles.

Velocity obstacles are a different method to generate collision-free trajectories. Herein, maneuvers are selected in the velocity space in order to avoid collisions based on the current positions and velocities of robot and obstacles. To guarantee that the planned maneuver is dynamically feasible, FIORINI AND SHILLER (1998, [33]) intersect the set of *avoidance velocities* with the set of *admissible velocities*. A trajectory from one position to another is then generated by searching a tree of feasible avoidance maneuvers computed at discrete time intervals.

KINDEL, HSU, LATOMBE AND ROCK (2000, [60]) describe *kinodynamic* motion planning for mobile robots. The concept combines kinematic and dynamic constraints of a mobile robot with probalistic randomized motion planning.

In automotive research rule based or behavior based approaches are very popular. These algorithms rely on rules formulated for particular situations. An example could be: "if an obstacle occurs ahead and braking is not possible, initiate an evasion maneuver". An expert system for automated highway driving is discussed by NIEHAUS AND STENGEL (1990, [79]). Other examples can be found in BRÜDIGAM (1994, [12]) in combination with a linear single-track model to generate trajectories for autonomous lane change maneuvers or in REICHARDT (1996, [88]). A fuzzy controller network based on more than 300 rules that was trained by human drivers in order to drive autonomously in presence of fixed obstacles is described by LAGES (2001, [67]).

In recent research on emergency systems and autonomous vehicles different geometric or kinematic approaches for evasion maneuvers have been analyzed. LAMMEN (1993, [68]) considers two separate options for collision avoidance: changing the planned velocity or changing the parameters of the geometrically planned path. The underlying trajectories are generated by applying geometric path planning with simple functions such as sinusoids. An advanced geometric motion planning concept is proposed in STILLER, SIMON AND WEISSER (2001, [110]). Therein, discrete points satisfying geometric constraints along the corridor in front of the vehicle are chosen and interpolated by splines. By using the Bezier-method the course can be adapted locally to sudden changes in the environment. Also SIMON (2003, [104]) proposes geometric path planning based on Bezier-splines. In doing so, non-valid areas are defined that should not be penetrated by the path in order to avoid collisions. The method proposed by AMELING (2002, [4]) generates trajectories consisting of three clothoid segments approximated by third order polynomials. Therefore, discontinuities in the steering angle when following the planned trajectory are avoided. MILDNER (2004, [73]) extends the approach given by AMELING (2002, [4]) by a velocity profile along the path. The generation of this velocity profile incorporates kinematic relations between the curvature and the resulting lateral acceleration as well as the feasible deceleration of the vehicle. Therein, maneuvers are planned assuming that the driver is no part of the control loop and therefore has no influence on the driven emergency maneuver. The vehicle is finally brought to halt in order to hand over control to the driver. The path planner used by MONEMERLO, THRUN, DAHLKAMP, STAVENS AND STROHBAND (2006, [75]) in the DARPA (**D**efense **A**dvanced **R**esearch **P**rojects **A**gency) "grand challenge" generates possible paths from a smoothed version of a given baseline trajectory. Different constraints such as the number of obstacles under the path are then evaluated to select the best path. Figure 1.6 shows the autonomous vehicle "Stanley" winning the grand challenge 2006.

Figure 1.6: Autonomous vehicle Stanley, see for example Monemerlo, Thrun, Dahlkamp, Stavens and Strohband (2006, [75])

The recently proposed procedure by Stählin, Schorn and Isermann (2006, [108]) is to a large extend analog to the one proposed by Ameling (2002, [4]); the clothoid function is replaced by a sigmoid.

In addition to the motion planning approaches presented so far, artificial potential fields represent a further interesting class of motion planning methods.

Potential Field Methods

Potential field methods for motion planning and collision avoidance, originally introduced by Krogh (1984, [65]) and Khatib (1986, [57]), are well established and have been applied many times in robotics. Sample introductory texts covering potential field methods in robotics are Latombe (1991, [69]), Siegwart and Nourbakhsh (2004, [103]), and Choset et al. (2005, [18]).

The basic idea is to integrate environmental information of the robot into artificial potential fields. Therein, the potential function $V(\mathbf{r})$, with $\mathbf{r}$ denoting the position of the robot, can be composed of attractive and repulsive potentials to encode desirable areas as well as non-valid areas or obstacles. Then, the artificial potential field causes a virtual force on the robot. In absence of other forces the robot follows the virtual potential force $\mathbf{F}(\mathbf{r}) = -\nabla V(\mathbf{r})$ in direction of the negated gradient of $V(\mathbf{r})$ towards lower values of the potential. In this framework non-valid areas and obstacles act as repelling forces. The robot could be compared to a wanderer in the mountains following the steepest path downhill, avoiding intermediate peaks representing obstacles.

Therefore, potential field methods provide a straight forward way to calculate collision-free paths through the environment of the robot based on its position and environmental sensor data. Compared to rule-based approaches, potential field methods are not limited to scenarios that are a priori trained. The evolving trajectories of geometric methods are restricted to the shapes of underlying functions such as sinusoids. In contrary, the trajectories provided by potential field methods can more flexible adapt to a present scenario. A further essential advantage when compared to other methods is that there is no principal limit in the number of obstacles that can be handled by potential field methods.

However, an inherent drawback is that potential field methods act as a steepest descent optimization and the robot might get stuck at local equilibria. Critical points are positions

with vanishing gradient $\nabla V(\mathbf{r}) = \mathbf{0}$. Therein, local maxima, saddle points, and local minima can be distinguished as indicated in Figure 1.7.

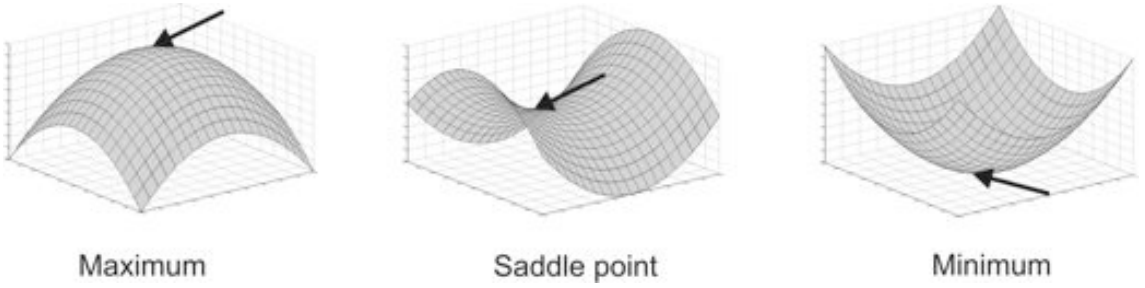

Figure 1.7: Critical points with vanishing gradient $\nabla V(\mathbf{r}) = \mathbf{0}$

Usually potential functions have isolated critical points. Hence, unless the robot starts at a local maximum or a saddle point, the potential force $\mathbf{F}$ in direction of the negated gradient guides the robot towards (local) minima, where the robot can get stuck.

Different strategies evolved to address the problem of local minima within potential field methods. One approach is to design the governing potential function $V(\mathbf{r})$ in a way that no local minima can appear. In order to do so, CONNOLLY AND GRUPEN (1993, [19]) proposed so-called *harmonic functions* to construct the potential field. Harmonic functions have zero curl and satisfy Laplace's equation $\sum_{i=1}^{n} \frac{\partial^2}{\partial x_i^2} V(\mathbf{r}) = 0$ with x_i being the components of $\mathbf{r}$. Any critical point, $\nabla V(\mathbf{r}) = \mathbf{0}$, is therefore guaranteed to be a saddle point. Also SULLIVAN, WAYDO AND CAMPBELL (2003, [111]) suggest so-called *stream functions* to construct the potential field in a way that all critical points are saddle points and therefore the robot will always reach its goal.

CHANG AND MARSDEN (2003, [16]) present another approach to the guidance problem from a start to a goal location by means of governing potential fields. Thereby, obstacles are explicitly excluded from the potential field such that a potential function free of local minima can be chosen. To avoid collisions with obstacles gyroscopic forces are applied locally. This approach was extended by CHANG, SHADDEN, MARSDEN AND OLFATI-SABER (2003, [17]) to multiple agent systems with swarming behavior.

Other subsets of potential field methods combine the potential field approach with methods from artificial intelligence. One idea is to construct the vector field depending on the present situation by means of heuristics and to apply evolutionary programming schemes, see for example KIM, KIM AND KWON (2001, [59]).

The concept of *virtual bumpers* introduced by HENNESSEY, SHANKWITZ AND DONATH (1995, [48]) is perhaps the first potential field like automotive application. The perimeter of the vehicle is surrounded by a sensor-based virtual bumper, see Figure 1.8. As the boundary of this bumper is deflected, a virtual force is generated by the compression of imaginary springs and dampers. The vehicle controller responds to this virtual force in a way that the deflection of the bumper is revoked. SCHILLER, MORELLAS AND DONATH, (1998, [98]) combine this idea with an heuristic rule base to generate motion commands for the vehicle.

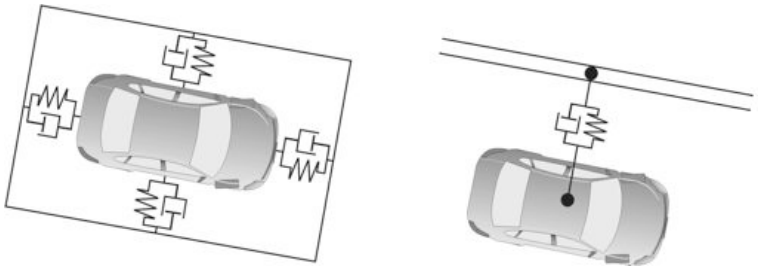

Figure 1.8: Virtual bumpers and potential field based lane-keeping

The lane-keeping approach of Rossetter (2003, [93]) differs from the concept of virtual bumpers as the vehicle is virtually coupled to the environment, see Figure 1.4 and Figure 1.8.

Kageyama and Nozaki (1995, [52]) compose a potential field of several hazard factors such as road edges and obstacles, and conclude that this approach generates control results comparable to the ones of human drivers. Gerdes, Rossetter and Saur (2001, [41]) coined the term *hazard map* to describe this way of encoding the environment in terms of potential fields.

The natural transfer of environmental sensor data, such as positions and velocities of tracked objects with respect to the host-vehicle, into a potential field hazard map is one essential advantage of potential field methods for vehicle guidance; each object is modeled by a separate repulsive potential field. If further data, for example from a video system, are available and if the objects can be classified, e.g. as pedestrians, the potentials assigned to the single objects can be scaled with respect to the hazards associated to the objects. Figure 1.9 shows a vehicle exposed to a potential field hazard map composed of the borders of the road and two obstacles.

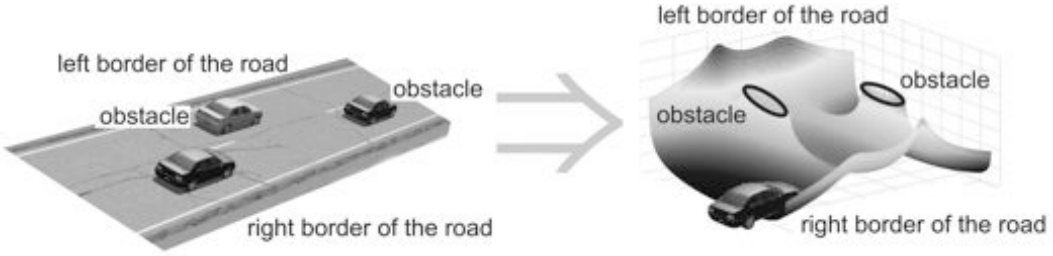

Figure 1.9: Traffic scenario encoded in potential field hazard map

The potential field methods presented so far are so-called *reactive* methods, which means that the robot or vehicle is directly affected by changes in the environment. If the potential field representing the environment is not carefully constructed as outlined above, the robot can be guided towards local minima. Furthermore, the robot, pushed by the virtual force, might react very abruptly to changes. In robotics the dynamics are often considered as a mass particle, see for example Latombe (1991, [69]), such that the robot is capable to move in arbitrary directions. The dynamics of a ground vehicle are more complex. Besides that, instantaneous reactions might lead to inconvenient driving behavior and affect the stability of the vehicle.

QUINLAN AND KHATIB (1993, [87]) proposed *elastic bands* as a *predictive* way of potential field based motion planning. Elastic bands consist of elastically coupled nodes that are exposed to the surrounding potential field. In doing so, the virtual potential forces deform the elastic band instead of directly acting on the robot. Hence, the elastic band represents collision-free trajectories for the robot. Meanwhile, elastic bands are well established, see for example KOMAINDA AND HILLER (1999, [62]). As the last node of an elastic band can be located at the goal of the robot, the problem of local minima is inherently avoided. Furthermore, the predictive way of motion planning smooths the generated trajectories as sudden reactions to environmental changes are prevented. A further essential advantage for automotive applications lies in the inherently low curvatures of the trajectories generated by elastic bands due to the internal potentials that counteract high offsets between adjacent nodes. First automotive applications were proposed by GEHRIG AND STEIN (2001, [40]) for platooning and by HILGERT, HIRSCH, BERTRAM AND HILLER (2003, [49]) for autonomous evasion maneuvers. BRANDT, SATTEL AND WALLASCHEK (2004, [8]) consider elastic bands for driver assistance. Figure 1.10 shows a vehicle guided by an elastic band through an hazard map as proposed in this thesis.

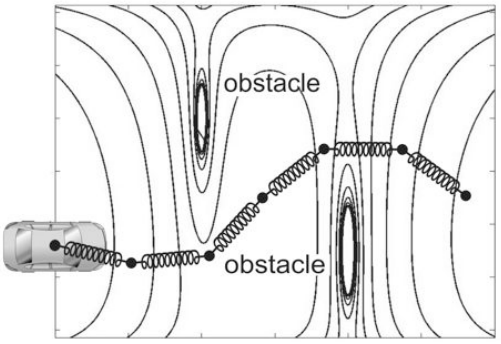

Figure 1.10: Vehicle guided by elastic band and hazard map

1.2 Thesis Contributions and Outline

This thesis provides a unified potential field framework for lateral vehicle guidance with possible applications as in lane-keeping or in collision avoidance. Thereby, motion planning as well as tracking of the planned trajectories is established by means of potential field methods. Particular emphasis is put on shared vehicle guidance and therefore on keeping the driver permanently embedded in the vehicle guidance control loop as demanded by the h-metaphor. The underlying potential field methods originating in the field of robotics are adapted and extended for driver assistance.

The motion planning concept incorporates a potential field hazard map that naturally encodes environmental sensor data such as detected lanes. In addition to hazard maps proposed so far, also moving objects and their anticipated trajectories are included. In order to do so, the dynamic states of obstacles are integrated forward in time. Therein, different behaviors as for example vehicles following their lanes are considered. Therefore, this new hazard map gives a spatial as well as a temporal representation of the traffic scenario and is not limited in the number of objects that can be handled, which is a drawback of many recently proposed geometric motion planning approaches.

Trajectories of low hazard levels are generated by elastic bands that sense the hazard map like antennae of insects, compare Figure 1.10. In this predictive approach the potential field forces act on the nodes of the elastic band instead of directly affecting the vehicle as for example in ROSSETTER (2003, [93]). The last node of an elastic band can be placed ahead of the vehicle, e.g. on the center of the right lane or on a leading vehicle.

When internal and external potential field forces, acting on the nodes of the elastic band, are in balance, the elastic band is collision-free. The equilibrium concept proposed here takes the anticipated trajectories of other traffic participants into account. Hence, the potential field forces are not only position but also time dependent. This is a substantial extension compared to previous applications of elastic bands where only snap shots of the environment were considered and changes in the environment were only incorporated by replanning. Including prediction of the motion of other traffic participants may lead to smoother trajectories and is more similar to the motion planning of human drivers, which supports shared vehicle guidance between driver and assistance system. In general, more than one collision-free solution exist. However, elastic bands belong to the so-called *local methods* and only provide one solution depending on the initial solution, see QUINLAN AND KHATIB (1993, [87]). Here, the initial solution is determined in cooperation with the driver. In doing so, the assistance system can for example propose a trajectory that passes an obstacle on the left; if the driver insists to pass it on the right, the assistance system adapts and provides corresponding trajectories passing the obstacle on the right hand side.

The gap between motion planning and guiding the vehicle along the planned trajectories is closed by combining a potential field feedback controller, which generates a steering angle by means of a virtual force depending on the tracking error, and a feedforward controller that calculates a steering angle based on the curvature of the planned trajectory.

Chapter 2 introduces the underlying lateral vehicle dynamics models for motion planning and vehicle guidance. Therein, also steering characteristics are considered and the models are compared to experimental data. The concepts of cooperative potential field motion planning including hazard map and elastic bands and the corresponding numeric procedures are outlined in Chapter 3. To accelerate the computation, one option is the reduction of the degrees of freedom of the nodes of the elastic band, which is also shown within the scope of Chapter 3. The potential field framework is completed by potential field guidance control, which is discussed in Chapter 4. The guidance controller in combination with disturbance rejection or feedforward control is shown to be stable in the sense of Lyapunov. Furthermore, a reachable set for the tracking error depending on the initial conditions and the parameters of the controller is given. This provides the basis to adapt the potential field controller to the environment in order to guarantee collision avoidance.

Subsequently, in Chapter 5 the driver assistance system is analyzed in simulator experiments with 16 test subjects. Therein, the interaction with the driver is established by means of a force feedback steering wheel. In this exploration different configurations of the assistance torques, reflecting loose rein and tight rein, are inspected. Besides that the test subjects are distracted by a secondary task in some test drives. Finally, the main results of this thesis are summarized and an outlook to future research directions is given in Chapter 6.

Chapter 2

Lateral Vehicle Dynamics

For lane-keeping and collision avoidance systems, lateral vehicle dynamics are predominant. Therefore, the aim of this chapter is to provide models that cover the dominant dynamic effects of lateral motion. Since vehicle dynamics has been a well studied field of research for many years, many very detailed models already exist. However, the models presented in this chapter are limited in their degree of complexity. One reason for this is that the generality of vehicle dynamic models tends to decrease with an increasing level of detail. Thus, results gained from the analysis of a very detailed model are often only applicable to the particular class of vehicles that is studied, see KARNOPP (2004, [56], p. 98). Besides that, complex vehicle models generally consume more computational effort, which limits their use for vehicle dynamics control systems.

The models studied in this chapter are planar and neglect effects that are associated with roll, pitch or heave motion. Therefore, also coupling effects between these degrees of freedom and the lateral motion are ignored.

First, different sets of reference frames are introduced. Subsequently, the modeling of the tires, which are the main force transmission elements between the vehicle and the road is addressed. Steering characteristics are discussed on the basis of the linear single-track model. After that, different vehicle dynamics models are compared to experimental data.

2.1 Reference Frames and Geometry

For motion planning and vehicle guidance, different inertial frames, such as a road-fixed frame, are used to describe the motion of the vehicle. Here, an earth-fixed reference frame $\underrightarrow{\text{E}}$: $(E^*, {}_E\mathbf{e}_x, {}_E\mathbf{e}_y, {}_E\mathbf{e}_z)$ is used to represent the inertial frame. Besides that, the following moving reference frames, as depicted in Figure 2.1, are used:

$\underrightarrow{\text{V}}$: $(V^*, {}_V\mathbf{e}_x, {}_V\mathbf{e}_y, {}_V\mathbf{e}_z)$ $\widehat{=}$ **V**ehicle-fixed reference frame
$\underrightarrow{\text{T}}$: $(T^*, {}_T\mathbf{e}_t, {}_T\mathbf{e}_n, {}_T\mathbf{e}_b)$ $\widehat{=}$ **T**rajectory-fixed reference frame
$\underrightarrow{\text{FL}}$: $(FL^*, {}_{FL}\mathbf{e}_x, {}_{FL}\mathbf{e}_y, {}_{FL}\mathbf{e}_z)$ $\widehat{=}$ **F**ront **L**eft wheel-fixed reference frame
$\underrightarrow{\text{FR}}$: $(FR^*, {}_{FR}\mathbf{e}_x, {}_{FR}\mathbf{e}_y, {}_{FR}\mathbf{e}_z)$ $\widehat{=}$ **F**ront **R**ight wheel-fixed reference frame
$\underrightarrow{\text{RL}}$: $(RL^*, {}_{RL}\mathbf{e}_x, {}_{RL}\mathbf{e}_y, {}_{RL}\mathbf{e}_z)$ $\widehat{=}$ **R**ear **L**eft wheel-fixed reference frame
$\underrightarrow{\text{RR}}$: $(RR^*, {}_{RR}\mathbf{e}_x, {}_{RR}\mathbf{e}_y, {}_{RR}\mathbf{e}_z)$ $\widehat{=}$ **R**ear **R**ight wheel-fixed reference frame

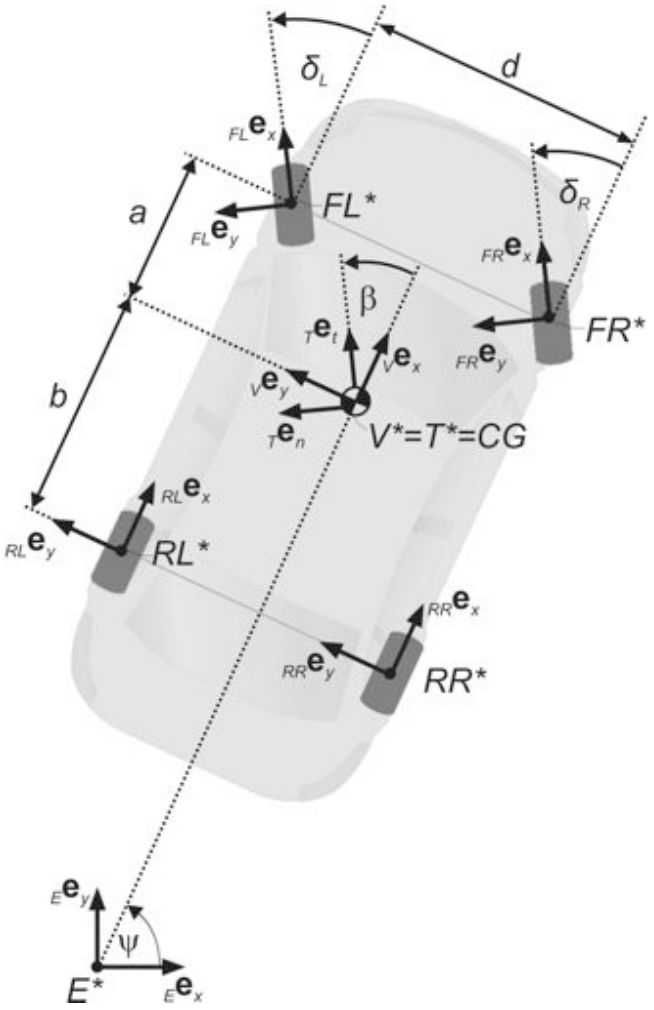

Figure 2.1: Reference frames

The vehicle-fixed reference frame $\underrightarrow{\text{V}}$: $(V^*, {}_V\mathbf{e}_x, {}_V\mathbf{e}_y, {}_V\mathbf{e}_z)$ is attached to the center of gravity CG of the vehicle. Therein, the ${}_V\mathbf{e}_x$ axis coincides with the longitudinal axis of the vehicle and points in forward direction. The ${}_V\mathbf{e}_y$ and the ${}_V\mathbf{e}_z$ axes point left and upwards, respectively. The ${}_V\mathbf{e}_x$ and ${}_E\mathbf{e}_x$ axes of the moving reference frame $\underrightarrow{\text{V}}$ and the earth fixed reference frame $\underrightarrow{\text{E}}$ contain the *yaw angle* ψ.

The trajectory-fixed reference frame $\underrightarrow{\text{T}}$: $(T^*, {}_T\mathbf{e}_t, {}_T\mathbf{e}_n, {}_T\mathbf{e}_b)$ is a so-called *Frenet* reference frame, see for example BRONSTEIN AND SEMENDJAEV (1997, [11], pp. 229). The axes of $\underrightarrow{\text{T}}$ are also attached to the center of gravity CG but can rotate relative to the vehicle. Its ${}_T\mathbf{e}_t$ axis is always tangential to the trajectory driven by the vehicle, while the ${}_T\mathbf{e}_n$ axis is normal to the driven trajectory and points towards the instantaneous center of curvature *ICC*. The ${}_T\mathbf{e}_b$ axis is called the binormal and forms a right-handed reference frame with ${}_T\mathbf{e}_t$ and ${}_T\mathbf{e}_n$. The ${}_T\mathbf{e}_t$ axis of the trajectory-fixed system $\underrightarrow{\text{T}}$ and the ${}_V\mathbf{e}_x$ axis of the vehicle-fixed reference frame $\underrightarrow{\text{V}}$ contain the *vehicle side slip angle* β.

The wheel-fixed reference frames $\underrightarrow{\text{FL}}$, $\underrightarrow{\text{FR}}$, $\underrightarrow{\text{RL}}$ and $\underrightarrow{\text{RR}}$ are attached to the center points of the respective wheels. However, they do not rotate with the wheels about the $\mathbf{e}_y$ axes! Their $\mathbf{e}_x$ axes point forward in longitudinal direction of the respective wheels. The $\mathbf{e}_y$ and $\mathbf{e}_z$ axes point to the left and upwards, respectively. The wheel-fixed reference

frames $\boxed{\text{FR}}$ and $\boxed{\text{FL}}$ attached to the front tires are rotated by the steering angles δ_L and δ_R, respectively, about the $\mathbf{e}_z$ axes with respect to the vehicle-fixed reference frame $\boxed{\text{V}}$.

The distances of the front and the rear axis to the center of gravity CG are denoted as a and b, respectively. The track width is called d, as depicted in Figure 2.1. The position of the vehicle with respect to the inertial frame $\boxed{\text{E}}$ is described by the position vector of the origin V^* of the vehicle-fixed reference frame $\boxed{\text{V}}$:

$$ {}_E\mathbf{r}^{V^*} = {}_Ex^{V^*}\ {}_E\mathbf{e}_x + {}_Ey^{V^*}\ {}_E\mathbf{e}_y \ . \tag{2.1} $$

According to Figure 2.1, the position vectors of the wheel center points in the vehicle-fixed reference frame $\boxed{\text{V}}$ become:

$$ \begin{aligned} {}_V\mathbf{r}^{V^*,FL^*} &= \ \ a\ {}_V\mathbf{e}_x + \tfrac{d}{2}\ {}_V\mathbf{e}_y \ , \\ {}_V\mathbf{r}^{V^*,FR^*} &= \ \ a\ {}_V\mathbf{e}_x - \tfrac{d}{2}\ {}_V\mathbf{e}_y \ , \\ {}_V\mathbf{r}^{V^*,RL^*} &= -b\ {}_V\mathbf{e}_x + \tfrac{d}{2}\ {}_V\mathbf{e}_y \ , \\ {}_V\mathbf{r}^{V^*,RR^*} &= -b\ {}_V\mathbf{e}_x - \tfrac{d}{2}\ {}_V\mathbf{e}_y \ . \end{aligned} \tag{2.2} $$

2.2 Tire Modeling

The tire is the main force transmission element between the vehicle and the ground. Therefore, the characteristics of the tires have significant influence on the dynamic behavior of the vehicle. In the next section, some kinematic values describing the physics of the tire are introduced. Subsequently, a tire model that provides tire forces based on the tire kinematics is given.

2.2.1 Tire Kinematics

The kinematic values for a wheel $q \in \{\text{FL}, \text{FR}, \text{RL}, \text{RR}\}$ are depicted in Figure 2.2.

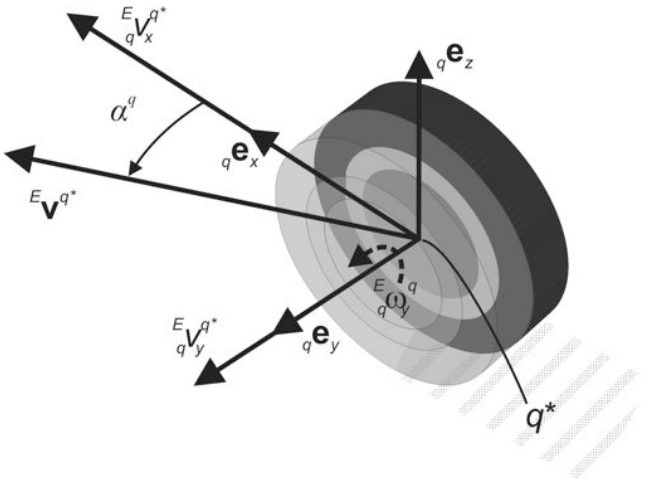

Figure 2.2: Tire kinematics

The velocity ${}^{E}\mathbf{v}^{q^*}$ of the wheel center point q^* with respect to the inertial reference frame $\underrightarrow{\text{E}}$ and the longitudinal axis ${}_{q}\mathbf{e}_x$ of the tire contain the *tire slip angle* α^q. For low velocities, e.g. for parking maneuvers, the tire slip angle α^q almost vanishes and the vehicle behaves kinematically nonholonomic with the constraint ${}^{E}\mathbf{v}^{q^*} \cdot {}_{q}\mathbf{e}_y = 0$. However, for cornering maneuvers at high speeds the cornering angle can obtain values up to 15°, see for example KIENCKE AND NIELSEN (2005, [58]), and is associated with a lateral force that guides the vehicle. The lateral slip s_α^q of the tire is usually described by means of the tire side slip angle:

$$s_\alpha^q = \tan\, \alpha^q \; . \tag{2.3}$$

In the following, degrees of freedom associated to the suspension system will not be considered. Figure 2.3 shows the free body diagram for the planar, longitudinal wheel motion.

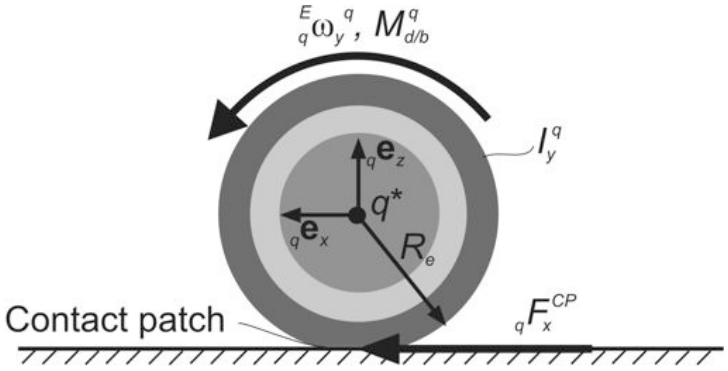

Figure 2.3: Tire forces and torques

The rotational motion of the wheel is governed by

$$I_y^q \, {}^{E}_{q}\dot{\omega}^q_y = M^q_{d/b} - {}_qF_x^{CP} R_e \; . \tag{2.4}$$

The angular acceleration of the wheel ${}^{E}_{q}\dot{\omega}^q_y$ depends on the driving or braking torque $M^q_{d/b}$ and on the longitudinal tire force ${}_qF_x^{CP}$, which acts at the contact patch *CP*. The effective running radius of the tire R_e can be estimated by the distance covered by the slip free rolling wheel $2\pi R_e$.

For rigid wheels the contact patch degenerates to a contact line. For slip free rolling wheels, $R_e \, {}^{E}_{q}\omega^q_y = {}^{E}_{q}v_x^{CP}$, as well as for combined rolling and sliding motion, the tire forces can be computed by solving the equations of motion of the wheel, see POPP AND SCHIEHLEN (1993, [86], pp. 120). In doing so, forces resulting from sliding friction can for example be obtained by assuming Coulomb friction.

However, the nonlinear elastic properties of the tire and the complex geometry of the contact patch complicate the computation of lateral and longitudinal tire forces. In general, the longitudinal tire forces are described by means of the longitudinal slip. Though, in practice different definitions for the longitudinal slip exist. MITSCHKE AND WALLENTOWITZ (2004, [74], p. 19) distinguishes between longitudinal slip for driving ($R_e \, {}^{E}_{q}\omega^q_y \geq {}^{E}_{q}v_x^{q^*}$) and for braking ($R_e \, {}^{E}_{q}\omega^q_y < {}^{E}_{q}v_x^{q^*}$) wheels:

Driving

$$s_{x,d}^{q} = \frac{R_e \, {}_{q}^{E}\omega_y^q - {}_{q}^{E}v_x^{q^*}}{R_e \, {}_{q}^{E}\omega_y^q} \tag{2.5}$$

Braking

$$s_{x,b}^{q} = -\frac{{}_{q}^{E}v_x^{q^*} - R_e \, {}_{q}^{E}\omega_y^q}{{}_{q}^{E}v_x^{q^*}} \; . \tag{2.6}$$

In the following, a combination of Equation (2.5) and Equation (2.6),

$$s_x^q = \frac{R_e \, {}_{q}^{E}\omega_y^q - {}_{q}^{E}v_x^{q^*}}{\max\left(R_e \, \left|{}_{q}^{E}\omega_y^q\right| , \left|{}_{q}^{E}v_x^{q^*}\right|\right)} \; , \tag{2.7}$$

with $s_x^q \in [-1\,, 1]$ is used, compare RILL (1994, [92], p. 55). The values of the longitudinal slip can now be interpreted as follows:

- $s_x^q = 1$: wheelspin,
- $0 < s_x^q < 1$: driving,
- $s_x^q = 0$: rolling,
- $-1 < s_x^q < 0$: braking,
- $s_x^q = -1$: locking.

2.2.2 Tire Forces: The Dugoff Model

One way to incorporate the tire characteristics in vehicle dynamics modeling is to employ experimental tire data. The drawback of this method is that data for all environmental conditions are necessary. For this reason, the use of models that describe the physics of tire road interaction is common and many different tire models for different fields of application exist and are still subject to numerous research activities. One of the most frequently used models is *Pacejka's magic tire formula*, see PACEJKA (2002, [81]). Pacejka's model is a curve fitting approach to tire test data. In doing so, many parameters need to be adapted, which makes the approach less attractive for principal investigations. Another widespread approach, with less parameters, is the tire model of Burckhardt, see KIENCKE AND NIELSEN (2005, [58]).

In the following, the *Dugoff model* introduced by DUGOFF, FANCHER AND SEGEL (1969, [30]) will be used. The Dugoff model is a physical model of the tire road interaction and has a lesser computational effort when compared with the Pacejka and the Burckhardt model. The only necessary parameters are the *longitudinal stiffness* of the tire C_x, the *cornering stiffness* C_α, and the *adhesion coefficient* μ_0 of the tire and the road surface.

The Dugoff model provides a relationship of the kinematic values and the forces acting at the tires. In doing so, the Dugoff model distinguishes explicitly between pure adhesion and combined adhesion and sliding in the contact patch. Whereas, the assumption of pure adhesion is only valid for small side slip angles α. In that region the tire deforms linearly.

Linear Deformation Model

The deformation of a tire q for small side slip angles α^q is illustrated in Figure 2.4.

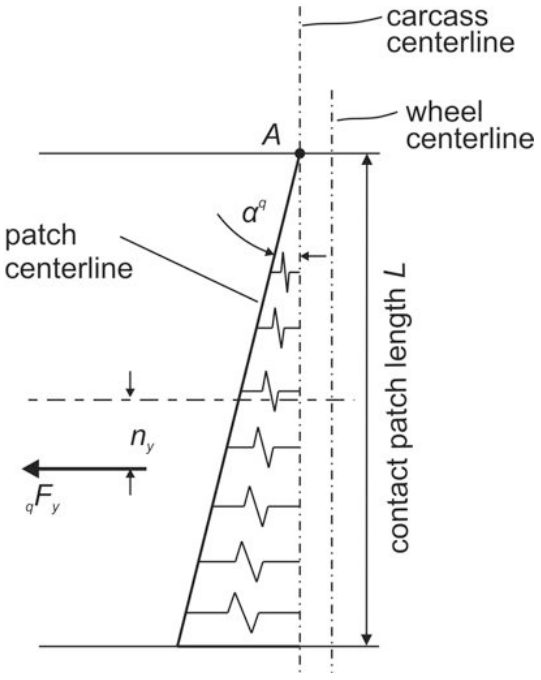

Figure 2.4: Tire deformation in the linear region according to MITSCHKE AND WALLENTOWITZ (2004, [74], p. 35)

The point A symbolizes a point on the tread of a cornering tire that enters the contact patch. With the rotation of the tire, A moves along the centerline of the contact patch and experiences a deflection with respect to the wheel. The spring elements symbolize the accompanying lateral force. As the center of the contact area lies behind the wheel center q^*, the resulting lateral force ${}_qF_y$ causes an aligning torque ${}_qM_z$. The offset n_y is called pneumatic trail and accounts in the linear region for approximately one sixth of the length of the contact patch, $n_y^{\text{lin}} \approx L/6$. The resulting equations of the linear model become:

$$ {}_qF_y = -C_\alpha^q \, \tan\alpha^q \approx -C_\alpha^q \, \alpha^q \, , \tag{2.8} $$

$$ {}_qM_z = -C_\alpha^q \, \tan\alpha^q \, n_y^{\text{lin}} \approx -C_\alpha^q \, \alpha^q \, n_y^{\text{lin}} \, . \tag{2.9} $$

The linear deformation model implies full adhesion of the contact patch. The longitudinal forces as well as the lateral forces are assumed to be well below the adhesion force, $\sqrt{{}_qF_x{}^2 + {}_q F_y^2} < \mu_0 \, {}_qF_z$, where ${}_qF_z$ denotes the normal load on the tire. In order to consider the lateral forces without taking coupling effects with the longitudinal forces into account, the longitudinal slip s_x^q as well as the cornering angle α^q need to be small.

Combined Adhesion and Sliding

For larger side slip angles α^q or longitudinal slip s_x^q the contact patch consists of areas of adhesion and of areas of sliding as indicated in Figure 2.5.

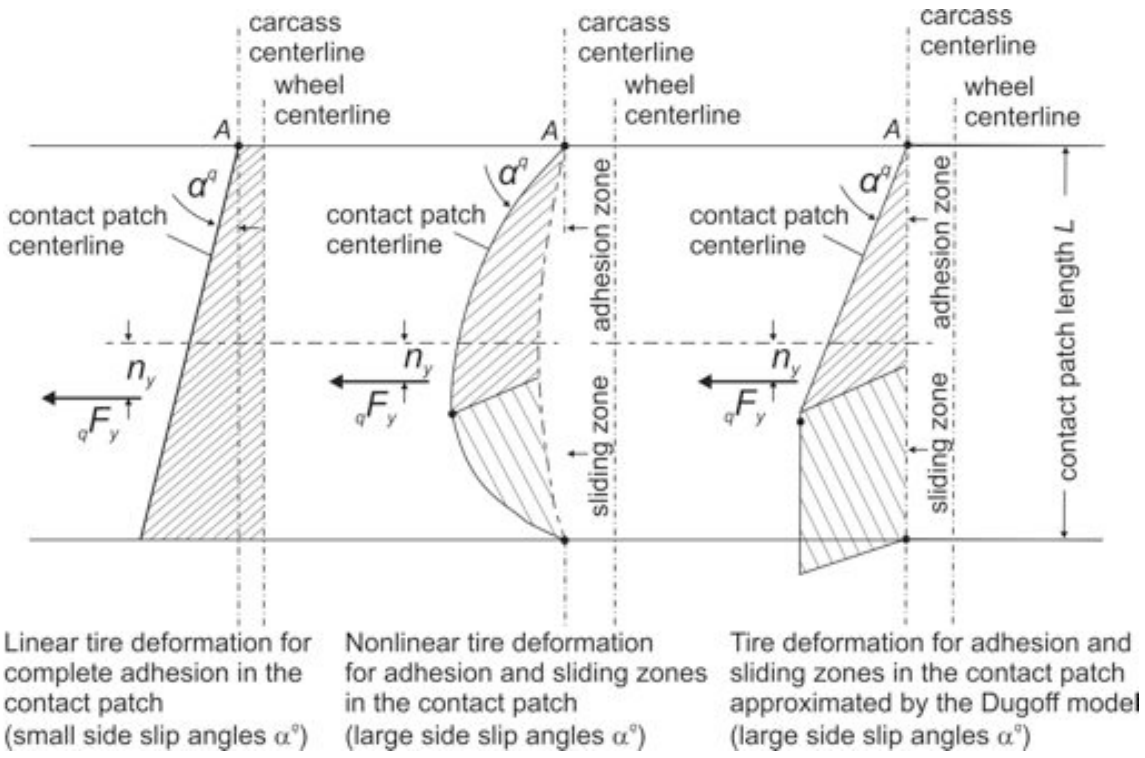

Figure 2.5: Contact patch for small and for large side slip angles α^q according to MITSCHKE AND WALLENTOWITZ (2004, [74], p. 35 and 46)

In the left part the linear tire deformation for small side slip angles α^q and complete adhesion is shown. Again point A indicates a point entering the contact patch and undergoing a linear deflection from the wheel centerline moving through the contact patch. For a large side slip angle α^q also sliding zones at the end of the contact patch form as depicted in the center part of Figure 2.5. A vivid comparison is to consider the tire as a rotating brush. Bristles that enter the contact patch stick at the ground (adhesion zones) while bristles that leave the contact patch stroke over the ground (sliding zones). The formation of adhesion and sliding zones in the contact patch is accompanied by a nonlinear deflection experienced by a point A moving through the contact patch. These effects are approximated by the Dugoff model as depicted in the right part of Figure 2.5.

The value $\bar{s}^q$ is introduced as an indicator for the transition from linear to nonlinear tire behavior

$$\bar{s}^q = \frac{\sqrt{(C_x^q\,|s_x^q|)^2 + (C_\alpha^q \tan\alpha^q)^2}}{\mu^q\;{}_qF_z(1-|s_x^q|)} \quad \text{with} \quad \bar{s}^q \le 0.5 \rightarrow \text{linear} \quad \text{and} \quad \bar{s}^q > 0.5 \rightarrow \text{nonlinear}\,. \tag{2.10}$$

The friction coefficient μ^q of tire q and the ground becomes

$$\mu^q = \mu_0 \left(1 - \epsilon \left(\left| {}^E_q v_x^{q*} \right| \sqrt{{s_x^q}^2 + \tan {\alpha^q}^2} \right) \right) \ , \tag{2.11}$$

where ϵ is the so-called adhesion reduction factor. DUGOFF, FANCHER AND SEGEL (1969, [30]) give $\epsilon = 0.011$ s/m for adhesion coefficients $\mu_0 \in [0.53\,,\ 1.05]$. The force equations of the Dugoff model read:

Longitudinal force

$${}_qF_x = \begin{cases} \dfrac{C_x^q \ s_x^q}{1 - \ s_x^q} & , \quad \bar{s}^q \leq 0.5 \\ \dfrac{C_x^q \ s_x^q}{1 - s_x^q} \ \dfrac{\bar{s}^q - 0.25}{\left(\bar{s}^q\right)^2} & , \quad \bar{s}^q > 0.5 \end{cases} \tag{2.12}$$

Lateral force

$${}_qF_y = \begin{cases} -C_\alpha^q \ \tan \alpha^q \approx -C_\alpha^q \ \alpha^q & , \quad \bar{s}^q \leq 0.5 \\ -\dfrac{C_\alpha^q \ \tan \alpha^q}{1 - s_x^q} \ \dfrac{\bar{s} - 0.25}{\left(\bar{s}^q\right)^2} & , \quad \bar{s}^q > 0.5 \end{cases} \tag{2.13}$$

Aligning torque caused by lateral tire forces

$${}_qM_z = \begin{cases} -C_\alpha^q \ \tan \alpha^q \, n_y^{\text{lin}} \approx -C_\alpha^q \ \alpha^q \, n_y^{\text{lin}} & , \quad \bar{s}^q \leq 0.5 \\ -\dfrac{C_\alpha^q \ \tan \alpha^q}{1 - s_x^q} \ \dfrac{\bar{s}^q - 0.25}{\left(\bar{s}^q\right)^2} \, n_y^{\text{nl}} & , \quad \bar{s}^q > 0.5 \end{cases} \tag{2.14}$$

The tire characteristics resulting from the force equations (2.12) and (2.13) are plotted in Figure 2.6. Figure 2.6 a) shows the longitudinal, Figure 2.6 b) the lateral tire forces against longitudinal slip s_x and the tire side slip angle α, respectively. The black line in Figure 2.6 a) indicates a none-cornering tire, $\alpha = 0$. The black line in Figure 2.6 b) highlights the lateral forces for a slip free rolling tire, $s_x = 0$. Note that positive longitudinal slip $s_x > 0$ generates positive longitudinal (driving) forces $F_x > 0$, while positive side slip angles $\alpha > 0$ produce negative lateral forces $F_y < 0$.

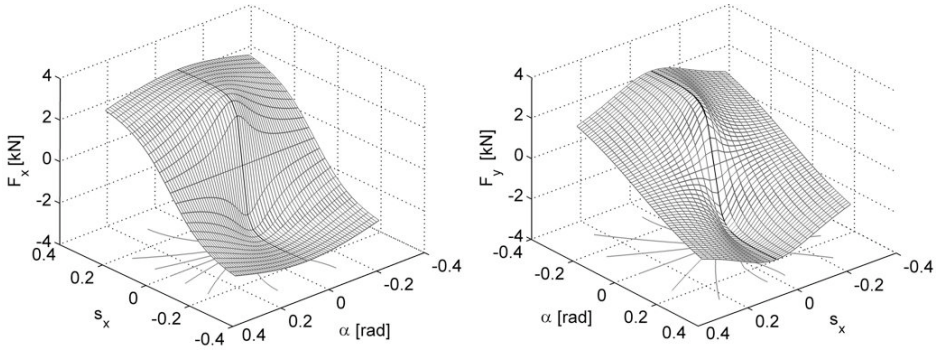

(a) Longitudinal forces (b) Lateral forces

Figure 2.6: Dugoff tire characteristics

Focusing on the black line in the left part, it can be noticed that, for small values of the longitudinal slip s_x, the longitudinal forces F_x rise linearly with the longitudinal slip. Then, the characteristic curve starts to rise on a diminishing scale and finally saturates. This behavior reflects the transition from pure adhesion to combined adhesion and sliding. On the right hand side, analogous behavior can be ascertained for the lateral forces.

Noteworthy, that the aligning torques resulting from the pneumatic trail have minor influence on vehicle dynamics and are usually neclegted, see MITSCHKE AND WALLENTOWITZ (2004, [74], p. 556). However, the aligning torque contributes to the steering torque at the steering wheel experienced by the driver. In general, the pneumatic trail depends on the distribution of the surface pressure in the contact patch. In the linear region the pneumatic trail n_y^{lin} accounts for approximately the sixth part of the length of the contact patch, $\frac{1}{6}L$, as mentioned above. In the nonlinear region the pneumatic trail depends on the pressure distribution in the range of $\frac{1}{10}L < n_y^{\text{nl}} < \frac{1}{6}L$. Approximation formula can be found in RILL (1994, [92], pp. 66).

Steering Wheel Torque

The steering wheel torque experienced by the driver due to vehicle dynamics effects is provided by a simple steering model

$$M^{\text{SW/V}} = \frac{1}{i_{\text{S}} V_{\text{PS}}} \left(M_z^{FL^*} + M_z^{FR^*} - n_c \left(F_y^{FL^*} + F_y^{FR^*} \right) \right) , \tag{2.15}$$

see for example MITSCHKE AND WALLENTOWITZ (2004, [74], p. 550). Therein, $i_{\text{S}} = \delta^{\text{SW}}/\delta$ describes the relation between steering angle at the steering wheel δ^{SW} and the steering angle at the tires δ, and is referred to as steering ratio. The effect of power steering on the torque at the steering wheel is incorporated in the steering gain V_{PS}. The term n_c is called caster and refers to the steering geometry; the caster describes the distance between the intersection points of the vertical wheel axis and the steering axis with the road. The caster due to the steering geometry is illustrated in Figure 2.7. Therefore, the driver experiences, besides the aligning torques M_z^q, a further torque at the steering wheel caused by the lateral tire forces F_y^q and the caster n_c.

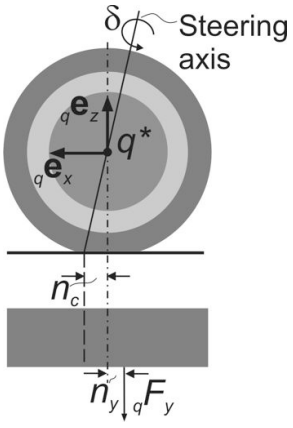

Figure 2.7: Influence of steering geometry on the steering wheel torque according to WÜRTENBERGER (1997, [125], p. 29)

2.3 Double-Track Model

The double-track model presented in this chapter is a planar model. Thus, only motions in the yaw plane (${}_E\mathbf{e}_x$, ${}_E\mathbf{e}_y$) will be considered. The geometry of the model is identical to the one given in Figure 2.1.

2.3.1 Kinematics

The motion of the vehicle with respect to the inertial frame $\underrightarrow{\mathrm{E}}$ will be expressed in the vehicle-fixed reference frame $\underrightarrow{\mathrm{V}}$, see Figure 2.1. For brevity the longitudinal and the lateral speed of the vehicle are defined as $U_x := {}^E_V v_x^{CG}$ and $U_y := {}^E_V v_y^{CG}$, respectively. Therefore, the velocity of the center of gravity CG with respect to the inertial frame $\underrightarrow{\mathrm{E}}$ reads

$$ {}^E_V\mathbf{v}^{CG} = U_x\,{}_V\mathbf{e}_x + U_y\,{}_V\mathbf{e}_y \qquad \text{and} \qquad {}^E_V\boldsymbol{\omega}^V = {}^E\omega^V\,{}_V\mathbf{e}_z = \dot{\psi}\,{}_V\mathbf{e}_z. \tag{2.16} $$

Translational and rotational speeds are combined in the vector of generalized speeds

$$ {}_V\mathbf{v} = \begin{bmatrix} U_x, & U_y, & \dot{\psi} \end{bmatrix}^{\mathrm{T}} . \tag{2.17} $$

The acceleration of the center of gravity CG becomes

$$ {}^E_V\mathbf{a}^{CG} = \frac{{}^E d}{dt}\,{}^E_V\mathbf{v}^{CG} = \frac{{}^V d}{dt}\,{}^E_V\mathbf{v}^{CG} + {}^E_V\boldsymbol{\omega}^V \times {}^E_V\mathbf{v}^{CG} = \left(\dot{U}_x - \dot{\psi}\,U_y\right){}_V\mathbf{e}_x + \left(\dot{U}_y + \dot{\psi}\,U_x\right){}_V\mathbf{e}_y \,. \tag{2.18} $$

The time derivative of the angular velocity in Equation (2.16) yields the angular acceleration

$$ {}^E_V\boldsymbol{\alpha}^{CG} = {}^E\dot{\omega}^V\,{}_V\mathbf{e}_z = \ddot{\psi}_V\mathbf{e}_z \,. \tag{2.19} $$

To track the generalized coordinates ${}_E\mathbf{q} = \left[{}_Ex^{V^*},\ {}_Ey^{V^*},\ \psi\right]^{\mathrm{T}}$ of the vehicle in the inertial frame $\underrightarrow{\mathrm{E}}$, the vector of generalized speeds ${}_V\mathbf{v}$ has to be transformed into $\underrightarrow{\mathrm{E}}$,

$$ {}_E\dot{\mathbf{q}} = \mathbf{C}^{E,V}\,{}_V\mathbf{v} \quad \text{with} \quad \mathbf{C}^{E,V} = \begin{bmatrix} \cos\psi & -\sin\psi & 0 \\ \sin\psi & \cos\psi & 0 \\ 0 & 0 & 1 \end{bmatrix} , \tag{2.20} $$

and integrated; Equation (2.20) contains the so-called kinematic differential equations.

To compute the tire forces F_x^q and F_y^q, the side slip angles α^q are also of interest. With Equation (2.16) and the position vectors of the wheel center points q^* with respect to the vehicle-fixed reference frame $\underrightarrow{\mathrm{V}}$, as given in Equation (2.2), the velocities of the wheel center points q^* can be computed according to

$$ {}^E\mathbf{v}^{q^*} = {}^E\mathbf{v}^{CG} + {}^E\boldsymbol{\omega}^V \times \mathbf{r}^{V^*,q^*} \,. \tag{2.21} $$

Now, the side slip angles α^q can be calculated by comparing the ${}_V\mathbf{e}_x$ and the ${}_V\mathbf{e}_y$ components of Equation (2.21), see also Figure 2.1 and Figure 2.2. This yields for the

side slip angles at the front tires

$$\alpha^{FL} = \arctan\left(\frac{U_y + \dot{\psi}a}{U_x - \frac{d}{2}\dot{\psi}}\right) - \delta_L \qquad \text{and} \qquad \alpha^{FR} = \arctan\left(\frac{U_y + \dot{\psi}a}{U_x + \frac{d}{2}\dot{\psi}}\right) - \delta_R\,, \tag{2.22}$$

and at the rear tires

$$\alpha^{RL} = \arctan\left(\frac{U_y - \dot{\psi}b}{U_x - \frac{d}{2}\dot{\psi}}\right) \qquad \text{and} \qquad \alpha^{RR} = \arctan\left(\frac{U_y - \dot{\psi}b}{U_x + \frac{d}{2}\dot{\psi}}\right)\,. \tag{2.23}$$

2.3.2 Dynamics

In the following, the Newton-Euler equations of the planar double-track model will be formulated. In doing so, forces due to inclinations, driving resistances and side wind will be ignored. Henceforth, the remaining forces acting on the body of the vehicle are the tire forces. However, since pitch and roll motion are not within the scope of this model, the tire forces will directly be applied at the wheel center points. Figure 2.8 shows the free body diagram of the double-track model.

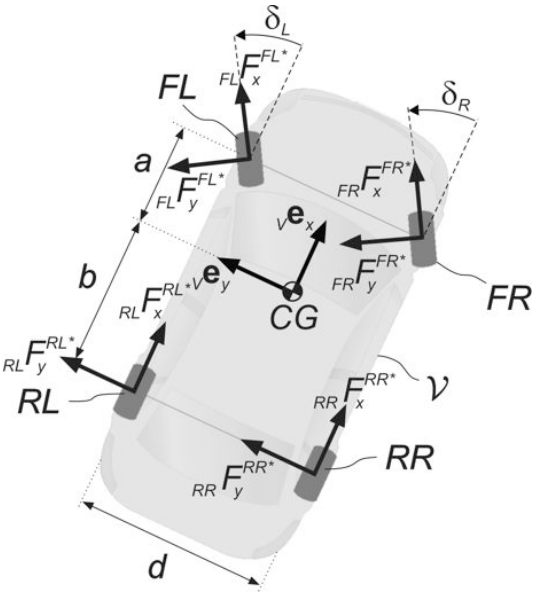

Figure 2.8: Tire forces acting upon the double-track model

The forces ${}_qF_x^{q*}$ and ${}_qF_y^{q*}$ with $q \in \{\mathrm{FL}, \mathrm{FR}, \mathrm{RR}, \mathrm{RL}\}$ can be interpreted as the resulting suspension forces.

The forces at the front tires, given in the wheel-fixed reference frames $\underrightarrow{\mathrm{FL}}$ and $\underrightarrow{\mathrm{FR}}$, have to be transformed into the vehicle-fixed reference frame $\underrightarrow{\mathrm{V}}$: ${}_V\mathbf{F}^{FL^*} = \mathbf{C}^{V,FL}{}_{FL}\mathbf{F}^{FL^*}$ and ${}_V\mathbf{F}^{FR^*} = \mathbf{C}^{V,FR}{}_{FR}\mathbf{F}^{FR^*}$ with

$$\mathbf{C}^{V,FL} = \begin{bmatrix} \cos\delta_L & -\sin\delta_L & 0 \\ \sin\delta_L & \cos\delta_L & 0 \\ 0 & 0 & 1 \end{bmatrix} \qquad \text{and} \qquad \mathbf{C}^{V,FR} = \begin{bmatrix} \cos\delta_R & -\sin\delta_R & 0 \\ \sin\delta_R & \cos\delta_R & 0 \\ 0 & 0 & 1 \end{bmatrix}\,. \tag{2.24}$$

The moments of the tire forces acting on the vehicle body with respect to the center of gravity CG become

$$\begin{aligned}
{}_V\mathbf{M}^{FL,CG} &= {}_V\mathbf{r}^{V^*,FL^*} \times {}_V\mathbf{F}^{FL^*} = {}_V\mathbf{r}^{V^*,FL^*} \times \mathbf{C}^{V,FL}(\delta_L)\,{}_{FL}\mathbf{F}^{FL^*} = {}_VM_z^{FL,CG}(\delta_L)\,{}_V\mathbf{e}_z \\
{}_V\mathbf{M}^{FR,CG} &= {}_V\mathbf{r}^{V^*,FR^*} \times {}_V\mathbf{F}^{FR^*} = {}_V\mathbf{r}^{V^*,FR^*} \times \mathbf{C}^{V,FR}(\delta_R)\,{}_{FR}\mathbf{F}^{FR^*} = {}_VM_z^{FR,CG}(\delta_R)\,{}_V\mathbf{e}_z \\
{}_V\mathbf{M}^{RL,CG} &= {}_V\mathbf{r}^{V^*,RL^*} \times {}_V\mathbf{F}^{RL^*} = {}_VM_z^{RL,CG}\,{}_V\mathbf{e}_z \\
{}_V\mathbf{M}^{RR,CG} &= {}_V\mathbf{r}^{V^*,RR^*} \times {}_V\mathbf{F}^{RR^*} = {}_VM_z^{RR,CG}\,{}_V\mathbf{e}_z
\end{aligned} \tag{2.25}$$

with the position vectors ${}_V\mathbf{r}^{V^*,q^*}$ of the tires as defined in Equation (2.2). Combining the mass of the vehicle m and the moment of inertia I_z about the ${}_V\mathbf{e}_z$ axis in the mass matrix

$$\mathbf{M} = \begin{bmatrix} m & 0 & 0 \\ 0 & m & 0 \\ 0 & 0 & I_z \end{bmatrix}, \tag{2.26}$$

the Newton-Euler equations of the double-track model can be written as

$$\mathbf{M}\,{}_V\dot{\mathbf{v}} = \mathbf{Q}\left({}_V\mathbf{F}^{q^*}, {}_V\mathbf{v}\right) = \begin{bmatrix} {}_VF_x^{FL^*}(\delta_L) + {}_VF_x^{FR^*}(\delta_R) + {}_VF_x^{RL^*} + {}_VF_x^{RR^*} \\ {}_VF_y^{FL^*}(\delta_L) + {}_VF_y^{FR^*}(\delta_R) + {}_VF_y^{RL^*} + {}_VF_y^{RR^*} \\ {}_VM_z^{FL,CG}(\delta_L) + {}_VM_z^{FR,CG}(\delta_R) + {}_VM_z^{RL,CG} + {}_VM_z^{RR,CG} \end{bmatrix}. \tag{2.27}$$

The forces and moments on the right hand side of Equation (2.27) depend on the steering angles δ_L and δ_R, which are considered as input variables. Furthermore, they depend, by means of the Dugoff tire model, equations (2.12)-(2.13), on the side slip angles α^q and the longitudinal slip values s_x^q. Knowing the generalized speeds ${}_V\mathbf{v}$, the side slip angles α^q follow from equations (2.22) and (2.23).

Besides the steering angles δ_L and δ_R, the longitudinal tire forces ${}_qF_x^{q^*}$ are also considered as input variables, i.e. $\mathbf{u} = \left[\delta_L,\ \delta_R,\ {}_{FL}F_x^{FL^*},\ {}_{FR}F_x^{FR^*},\ {}_{RL}F_x^{RL^*},\ {}_{RR}F_x^{RR^*}\right]^{\mathrm{T}}$. Noteworthy is, that not only the lateral tire forces ${}_qF_y^{q*}$ can cause a yaw moment about the ${}_V\mathbf{e}_z$ axis. Different braking forces ${}_qF_x^{q*}$ at the left and at the right tire of one axle also apply a yaw moment. As the longitudinal forces ${}_qF_x^{q*}$ are control input variables this provides a controllable input to the yaw component of Equation (2.27). Figure 2.9 shows possible configurations of differential braking.

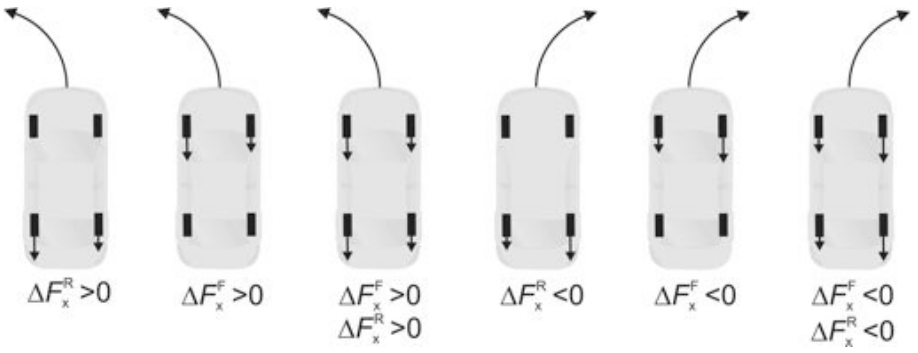

Figure 2.9: Cornering by differential braking with $\Delta F_x^F = F_x^{FR^*} - F_x^{FL^*}$ and $\Delta F_x^R = F_x^{RR^*} - F_x^{RL^*}$

By setting a driving or braking torque $M_{d/b}$, Equation (2.4) together with Equation (2.7) and equations (2.22)-(2.23) provide the corresponding longitudinal slip s_x^q and the side slip angles α^q. The longitudinal forces ${}_qF_x^{q^*}$ then follow from the Dugoff model in Equation (2.12) as illustrated in Figure 2.10.

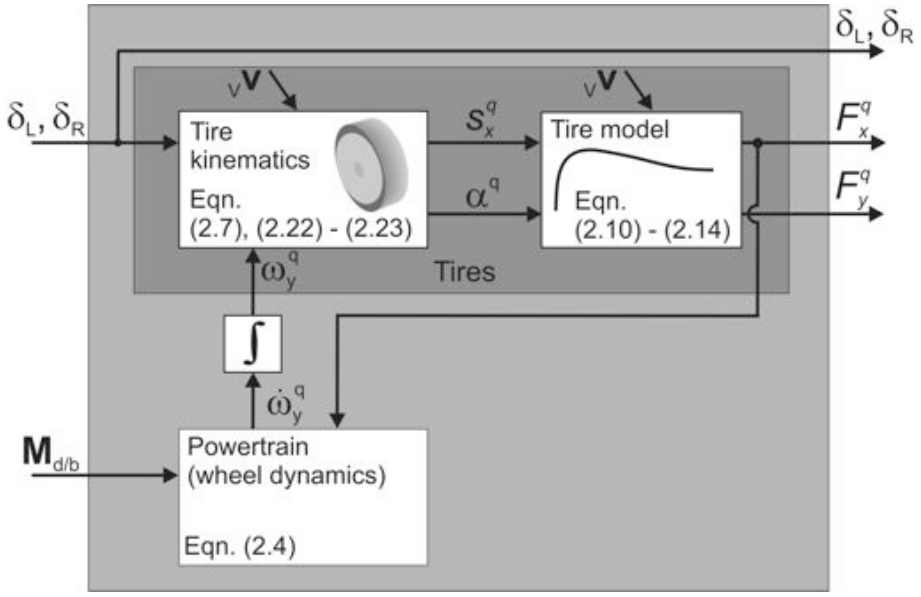

Figure 2.10: Control input variables

2.4 Single-Track Model

Starting from the double-track model, a further reduction can be achieved by assuming symmetry about the longitudinal axis, ${}_V\mathbf{e}_x$, of the vehicle. In doing so, left and right tires are lumped together resulting in a single track as illustrated in Figure 2.11.

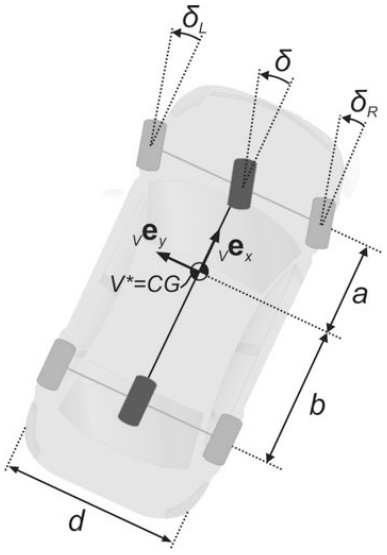

Figure 2.11: Transition from double- to single-track model

2.4.1 Kinematics

In particular, combining left and right tires implies not to distinguish between the steering angles at the left δ_L and at the right front tire δ_R, which is reasonable for sufficiently large radii of curvature, $1/\kappa >> (a+b)$, of the driven path. The steering angle of the single-track model is referred to as

$$\delta := \delta_L \stackrel{!}{=} \delta_R \,. \tag{2.28}$$

Recalling the side slip angles at the front tires according to Equation (2.22)

$$\alpha^{FL} = \arctan\left(\frac{U_y + \dot{\psi}a}{U_x - \frac{d}{2}\dot{\psi}}\right) - \delta_L \qquad \text{and} \qquad \alpha^{FR} = \arctan\left(\frac{U_y + \dot{\psi}a}{U_x + \frac{d}{2}\dot{\psi}}\right) - \delta_R \,,$$

it can be observed that α^{FL} and α^{FR} only differ in the algebraic sign of the term $\frac{d}{2}\dot{\psi}$ in the denominator. This means that a lateral tire force increasing from this component on one tire, for example on the left ${}_{FL}F_y^{FL^*}$, is accompanied by a lateral tire force decreasing from this component on the opponent, for example the right tire ${}_{FR}F_y^{FR^*}$. For the single-track model same side slip angles at the left and at the right tires are assumed. The yaw rate contribution $\frac{d}{2}\dot{\psi}$, which is small compared to the longitudinal speed, $\frac{d}{2}\dot{\psi} << U_x$, is therefore neglected in the denominator. With the steering angle δ, see Equation (2.28), the side slip angles for the single-track model become

$$\alpha^{F} = \arctan\left(\frac{U_y + \dot{\psi}a}{U_x}\right) - \delta \qquad \text{and} \qquad \alpha^{R} = \arctan\left(\frac{U_y - \dot{\psi}b}{U_x}\right) \,, \tag{2.29}$$

for the front and for the rear axis, respectively. The kinematic quantities of the single-track model are visualized in the Figure 2.12.

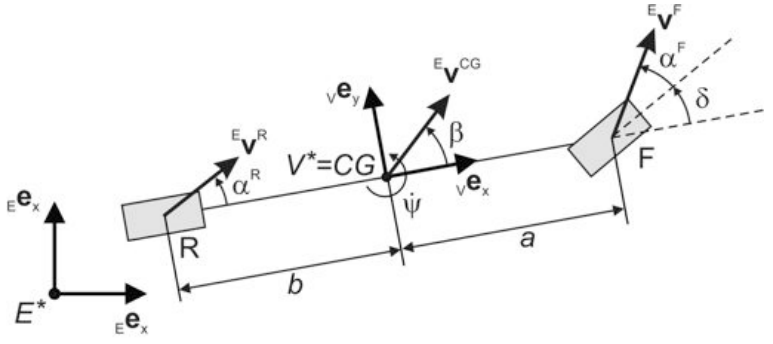

Figure 2.12: Kinematics of the single-track model

Translational velocity ${}^{E}_{V}\mathbf{v}^{CG}$ and rotational velocity ${}^{E}_{V}\boldsymbol{\omega}^{V}$, as defined in Equation (2.16), translational acceleration ${}^{E}_{V}\mathbf{a}^{CG}$ and angular acceleration ${}^{E}_{V}\boldsymbol{\alpha}^{CG}$, as given in equations (2.18) and (2.19), respectively, remain unchanged for the single-track model. Therefore, the kinematic differential Equations (2.20) also apply for single-track model.

2.4.2 Dynamics

For small values of the longitudinal slip s_x^q and equal side slip angles α^F and α^R at one axle, see Equation (2.29), the lateral forces at the tires of one axle can be combined into resulting lateral forces F_y^F and F_y^R at the front and the rear axle, respectively. Therefore, the cornering stiffness of the combined tires $C_\alpha^F = C_\alpha^{FL} + C_\alpha^{FR}$ and $C_\alpha^R = C_\alpha^{RL} + C_\alpha^{RR}$ is used in the Dugoff model, compare Section 2.2.2.

In order to maintain the possibility to apply a yaw moment on the vehicle body by means of differential braking, the longitudinal tire forces of the double-track model are combined into resulting and differential (pairs of) forces at one axle

$$\begin{aligned} F_x^F &= F_x^{FL^*} + F_x^{FR^*} , \\ F_x^R &= F_x^{RL^*} + F_x^{RR^*} , \\ \Delta F_x^F &= F_x^{FR^*} - F_x^{FL^*} , \\ \Delta F_x^R &= F_x^{RR^*} - F_x^{RL^*} . \end{aligned} \tag{2.30}$$

Figure 2.13 shows the free body diagram of the single-track model. Note that the lateral forces F_y^F and F_y^R are shown as positive in positive y-direction of the corresponding reference frames. The side slip angles α^F and α^R are also depicted as they were positive. However, when the slip angles are positive, the forces exerted on the tires would actually be in negative direction. According to KARNOPP (2004, [56], p. 102) "*This is a common problem in describing tire-roadway interactions, which leads either to negative cornering coefficients in the linearized case, or to a special way of writing the force laws to have positive coefficients*". In this case the opposing directions of side slip angles and lateral forces are captured in the lateral force equations of the Dugoff model, see Equation (2.13).

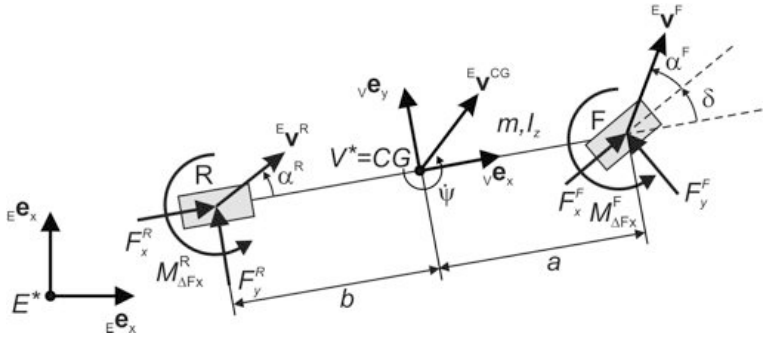

Figure 2.13: Dynamics of the single-track model

The moments about the ${}_V\mathbf{e}_z$ axis, $M_{\Delta F_x}^F = \frac{d}{2}\Delta F_x^F \cos\delta$ and $M_{\Delta F_x}^R = \frac{d}{2}\Delta F_x^R$, in Figure 2.13 indicate the influence of differential braking. With the definitions of Equation (2.30), the Newton-Euler equations of the single-track model expressed in vehicle-fixed coordinates $\uparrow_V$, see equations (2.18) and (2.19), read

$$\begin{aligned} m\,{}_V^E a_x^{CG} &= m\left(\dot{U}_x - \dot{\psi}\,U_y\right) = F_x^R + F_x^F\cos\delta - F_y^F\sin\delta \\ m\,{}_V^E a_y^{CG} &= m\left(\dot{U}_y + \dot{\psi}\,U_x\right) = F_y^R + F_x^F\sin\delta + F_y^F\cos\delta \\ I_z\,{}^E\dot{\omega}_z^V &= I_z\ddot{\psi} = a\,F_x^F\sin\delta + a\,F_y^F\cos\delta - b\,F_y^R + M_{\Delta F_x}^F + M_{\Delta F_x}^R . \end{aligned} \tag{2.31}$$

With the vector of generalized speeds ${}_V\mathbf{v}$, according to Equation (2.17), the mass matrix $\mathbf{M}$, defined in Equation (2.26), and the gyroscopic term $\mathbf{b} = [-\dot{\psi}U_y \; \dot{\psi}U_x \; 0]^{\mathrm{T}}$ the equations of motion (2.31) can be rearranged and written in matrix notation

$$\begin{aligned}\mathbf{M}\,{}_V\dot{\mathbf{v}} + \mathbf{b}\,({}_V\mathbf{v}) &= \underbrace{F_y^R \begin{bmatrix} 0 \\ 1 \\ -b \end{bmatrix}}_{\text{uncontrolled term}} + \underbrace{F_y^F \begin{bmatrix} -\sin\delta \\ \cos\delta \\ a\,\cos\delta \end{bmatrix}}_{\text{coupled term}} + \underbrace{\begin{bmatrix} F_x^R + F_x^F\cos\delta \\ F_x^F\sin\delta \\ a\,F_x^F\sin\delta + M^F_{\Delta F_x} + M^R_{\Delta F_x} \end{bmatrix}}_{\text{controlled term}} \\ &= \mathbf{Q}^{\mathrm{nc}}\left(F_y^R\,({}_V\mathbf{v})\right) + \mathbf{Q}^{\mathrm{coupl}}\left(F_y^F\,({}_V\mathbf{v}),\delta\right) + \mathbf{Q}^{\mathrm{c}}(\mathbf{u})\;, \end{aligned} \tag{2.32}$$

with $\mathbf{u} = [\delta, F_x^F, F_x^R, \Delta F_x^F, \Delta F_x^R]^{\mathrm{T}}$ being the vector of control inputs. All uncontrolled quantities such as the lateral forces are collected in the generalized force term $\mathbf{Q}^{\mathrm{nc}}$. The generalized force term $\mathbf{Q}^{\mathrm{coupl}}$ contains coupled controlled and uncontrolled quantities, while $\mathbf{Q}^{\mathrm{c}}$ only depends on the vector of control inputs $\mathbf{u}$. The simulation structure of the nonlinear single-track model is summarized in Figure 2.14.

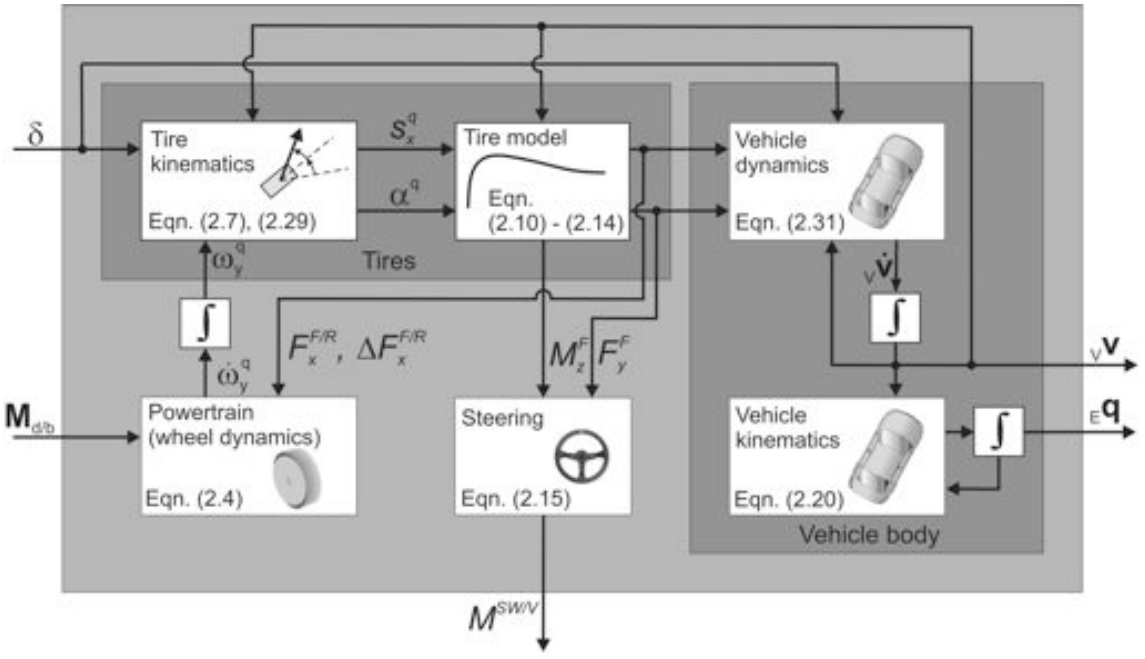

Figure 2.14: Simulation structure of the nonlinear single-track model

2.5 Linear Single-Track Model

In order to gain some insight by use of linear analysis techniques, the equations of motion of the single-track model can be linearized for a prescribed longitudinal motion. The most convenient choice is to assume the longitudinal velocity to be almost constant and the longitudinal forces to be small. In doing so, the longitudinal degree of freedom is removed from the model. In the following, two different versions of the linearized equations of motion are presented. First, the equations of motion are formulated in the vehicle-fixed reference frame $\overset{\uparrow}{\underset{\rightarrow}{\mathrm{V}}}$. The remaining two degrees of freedom of the lateral motion are

governed by the lateral velocity U_y and the yaw rate $\dot{\psi}$, respectively. Second, a formulation in the trajectory-fixed Frenet frame $\overset{\uparrow}{\underset{\rightarrow}{\mathrm{T}}}$ is given. The corresponding states of the model are the side slip angle β and the yaw rate $\dot{\psi}$.

2.5.1 Vehicle-Fixed Formulation

For a prescribed longitudinal motion $\dot{U}_x \approx 0$, the Newton-Euler equations (2.31) in ${}_V\mathbf{e}_x$-direction can be ignored; the remaining equations of lateral motion are

$$\begin{aligned} m\left(\dot{U}_y + \dot{\psi}\,U_x\right) &= F_y^R + F_x^F \sin\delta + F_y^F \cos\delta \\ I_z\ddot{\psi} &= a\,F_x^F \sin\delta + a\,F_y^F \cos\delta - b\,F_y^R + M_{\Delta F_x}^F + M_{\Delta F_x}^R\,. \end{aligned} \tag{2.33}$$

Assuming that for slowly varying or constant longitudinal speed U_x, the longitudinal forces approximately vanish, $F_x^F \approx F_x^R \approx 0$, the equations of motion (2.33) simplify further

$$\begin{aligned} m\left(\dot{U}_y + \dot{\psi}\,U_x\right) &= F_y^R + F_y^F \cos\delta \\ I_z\ddot{\psi} &= a\,F_y^F \cos\delta - b\,F_y^R + M_{\Delta F_x}^F + M_{\Delta F_x}^R\,. \end{aligned} \tag{2.34}$$

Replacing the lateral tire forces F_y^F and F_y^R by use of the linear Dugoff model, $F_y^F = -C_\alpha^F\,\alpha^F$ and $F_y^R = -C_\alpha^R\,\alpha^R$, see Equation (2.13), applying the small angle approximations

$$\begin{aligned} &\cos\delta \approx 1\,, \\ &\alpha^F = \arctan\left(\frac{U_y + \dot{\psi}a}{U_x}\right) - \delta \approx \frac{U_y + \dot{\psi}a}{U_x} - \delta\,, \\ &\alpha^R = \arctan\left(\frac{U_y - \dot{\psi}b}{U_x}\right) \approx \frac{U_y - \dot{\psi}b}{U_x}\,, \end{aligned} \tag{2.35}$$

for the steering and the side slip angles, respectively, the equations of motion (2.34) become

$$\begin{aligned} m\left(\dot{U}_y + \dot{\psi}U_x\right) &= -C_\alpha^R\left[\frac{U_y - \dot{\psi}b}{U_x}\right] - C_\alpha^F\left[\frac{U_y + \dot{\psi}a}{U_x} - \delta\right] \\ I_z\ddot{\psi} &= -aC_\alpha^F\left[\frac{U_y + \dot{\psi}a}{U_x} - \delta\right] + b\,C_\alpha^R\left[\frac{U_y - \dot{\psi}b}{U_x}\right] + M_{\Delta F_x}^F + M_{\Delta F_x}^R\,. \end{aligned} \tag{2.36}$$

In matrix notation with $\mathbf{v} = \left[U_y, \dot{\psi}\right]^{\mathrm{T}}$ and $\mathbf{u} = \left[\delta,\ M_{\Delta F_x}^F,\ M_{\Delta F_x}^R\right]^{\mathrm{T}}$, the equations of motion with respect to $\overset{\uparrow}{\underset{\rightarrow}{\mathrm{V}}}$ read

$$\mathbf{M}\,\dot{\mathbf{v}} + \left[\mathbf{G}\,(U_x) + \mathbf{D}\,(U_x)\right]\mathbf{v} = \mathbf{B}\,\mathbf{u} \tag{2.37}$$

with

$$\begin{aligned} \mathbf{M} &= \begin{bmatrix} m & 0 \\ 0 & I_z \end{bmatrix}, & \mathbf{G} &= \begin{bmatrix} 0 & mU_x \\ 0 & 0 \end{bmatrix}, \\ \mathbf{D} &= \frac{1}{U_x}\begin{bmatrix} C_\alpha^F + C_\alpha^R & C_\alpha^F a - C_\alpha^R b \\ C_\alpha^F a - C_\alpha^R b & C_\alpha^F a^2 + C_\alpha^R b^2 \end{bmatrix} \quad \text{and} & \mathbf{B} &= \begin{bmatrix} C_\alpha^F & 0 & 0 \\ C_\alpha^F a & 1 & 1 \end{bmatrix}. \end{aligned} \tag{2.38}$$

The matrix $\mathbf{G}$ is the gyroscopic matrix. Matrix $\mathbf{D}$ is positive definite and therefore a damping matrix. The according quadratic form is

$$\mathbf{v}^{\mathrm{T}}\mathbf{D}\mathbf{v} = \frac{C_\alpha^F + \left(U_y + a\dot{\psi}\right)^2 + C_\alpha^R \left(U_y - b\dot{\psi}\right)^2}{U_x} > 0 \quad \forall \|\mathbf{v}\| \neq 0 \,. \tag{2.39}$$

Rearranging Equation (2.37) yields the state space equations of the linear single-track model formulated in $\overset{\uparrow}{\underset{\rightarrow}{\mathrm{V}}}$

$${}_V\dot{\mathbf{x}} = {}_V\mathbf{A}\,{}_V\mathbf{x} + {}_V\mathbf{B}\,{}_V\mathbf{u} \tag{2.40}$$

with

$${}_V\mathbf{A} = \begin{bmatrix} -\dfrac{C_\alpha^R + C_\alpha^F}{m\,U_x} & \dfrac{C_\alpha^R\,b - C_\alpha^F\,a}{m\,U_x} - U_x \\ \dfrac{b\,C_\alpha^R - a\,C_\alpha^F}{I_z\,U_x} & -\dfrac{b^2\,C_\alpha^R + a^2\,C_\alpha^F}{I_z\,U_x} \end{bmatrix} \quad \text{and} \quad {}_V\mathbf{B} = \begin{bmatrix} \dfrac{C_\alpha^F}{m} & 0 & 0 \\ \dfrac{a\,C_\alpha^F}{I_z} & \dfrac{1}{I_z} & \dfrac{1}{I_z} \end{bmatrix} , \tag{2.41}$$

being the system and the control matrix, respectively. The state vector ${}_V\mathbf{x} = \mathbf{v}$ and the vector of control inputs ${}_V\mathbf{u} = \mathbf{u}$ are defined as above in Equation (2.37).

2.5.2 Trajectory-Fixed Formulation

Starting again from the Newton-Euler equations (2.31) considering only lateral motion and assuming that the longitudinal tire forces vanish, $F_x^F \approx F_x^R \approx 0$, leads together with the small angle approximation, $\cos\delta \approx 1$, to

$$\begin{aligned} m\,{}_V^E a_y^{CG} &= F_y^R + F_x^F \sin\delta + F_y^F \cos\delta \\ &\approx F_y^R + F_y^F \\ I_z\ddot{\psi} &= a\,F_x^F \sin\delta + a\,F_y^F \cos\delta - b\,F_y^R + M_{\Delta F_x}^F + M_{\Delta F_x}^R \\ &\approx a\,F_y^F - b\,F_y^R + M_{\Delta F_x}^F + M_{\Delta F_x}^R \,. \end{aligned} \tag{2.42}$$

Now the equations of motion are projected onto the Frenet frame $\overset{\uparrow}{\underset{\rightarrow}{\mathrm{T}}}$: $(T^*, {}_T\mathbf{e}_t, {}_T\mathbf{e}_n, {}_T\mathbf{e}_b)$ whose origin T^* is located at the center of gravity of the vehicle CG. $\overset{\uparrow}{\underset{\rightarrow}{\mathrm{T}}}$ is rotated by the side slip angle β with respect to $\overset{\uparrow}{\underset{\rightarrow}{\mathrm{V}}}$

$$\begin{bmatrix} {}_T\mathbf{e}_t \\ {}_T\mathbf{e}_n \\ {}_T\mathbf{e}_b \end{bmatrix} = \underbrace{\begin{bmatrix} \cos\beta & \sin\beta & 0 \\ -\sin\beta & \cos\beta & 0 \\ 0 & 0 & 1 \end{bmatrix}}_{\mathbf{C}^{T,V}} \begin{bmatrix} {}_V\mathbf{e}_x \\ {}_V\mathbf{e}_y \\ {}_V\mathbf{e}_z \end{bmatrix} \,. \tag{2.43}$$

Therefore, the ${}_T\mathbf{e}_t$ axis is always tangential to the path driven by the vehicle, while the ${}_T\mathbf{e}_n$ axis is normal to it. In the Frenet frame $\overset{\uparrow}{\underset{\rightarrow}{\mathrm{T}}}$, with the abbreviations $U_t := {}_T^E v_t^{CG}$ and $U_n := {}_T^E v_n^{CG}$, the only nonzero component of the velocity of the center of gravity ${}^E\mathbf{v}^{CG}$ is in ${}_T\mathbf{e}_t$-direction

$${}^E\mathbf{v}^{CG} = U_t\,{}_T\mathbf{e}_t \,. \tag{2.44}$$

With the angular velocity ${}^{E}_{T}\boldsymbol{\omega}^{T} = \left(\dot{\beta}+\dot{\psi}\right)_{T}\mathbf{e}_b$ of $\underrightarrow{\mathrm{T}}$ with respect to $\underrightarrow{\mathrm{E}}$, the acceleration of the center of gravity CG with respect to $\underrightarrow{\mathrm{E}}$ can be expressed as

$$\begin{aligned} {}^{E}_{T}\mathbf{a}^{CG} = \frac{{}^{E}d}{dt}{}^{E}_{T}\mathbf{v}^{CG} &= \frac{{}^{T}d}{dt}{}^{E}_{T}\mathbf{v}^{CG} + {}^{E}_{T}\boldsymbol{\omega}^{T} \times {}^{E}_{T}\mathbf{v}^{CG} \\ &= \dot{U}_t\,{}_{T}\mathbf{e}_t + U_t\left(\dot{\beta}+\dot{\psi}\right){}_{T}\mathbf{e}_n \ . \end{aligned} \tag{2.45}$$

Substituting the unit vectors of $\underrightarrow{\mathrm{T}}$ by the unit vectors of the reference frame $\underrightarrow{\mathrm{V}}$, according to Equation (2.43), Equation (2.45) becomes

$${}^{E}_{V}\mathbf{a}^{CG} = \underbrace{\left[\dot{U}_t\cos\beta - U_t\left(\dot{\beta}+\dot{\psi}\right)\sin\beta\right]}_{{}_{V}a_x^{CG}}{}_{V}\mathbf{e}_x + \underbrace{\left[\dot{U}_t\sin\beta + U_t\left(\dot{\beta}+\dot{\psi}\right)\cos\beta\right]}_{{}_{V}a_y^{CG}}{}_{V}\mathbf{e}_y \ . \tag{2.46}$$

Substituting the lateral acceleration in the Newton-Euler equations (2.42) with the expression from Equation (2.46) and using the linear part of the Dugoff tire model, Equation (2.13), with the small angle approximations for the tire side slip angles as given in Equation (2.35), the equations of motion become

$$\begin{aligned} m\left(\dot{U}_t\sin\beta + U_t\left(\dot{\beta}+\dot{\psi}\right)\cos\beta\right) &= -C_\alpha^F\left[\frac{U_y+\dot{\psi}a}{U_x}-\delta\right] - C_\alpha^R\left[\frac{U_y-\dot{\psi}b}{U_x}\right] \\ I_z\ddot{\psi} &= -aC_\alpha^F\left[\frac{U_y+\dot{\psi}a}{U_x}-\delta\right] + bC_\alpha^R\left[\frac{U_y-\dot{\psi}b}{U_x}\right] + M^F_{\Delta F_x} + M^R_{\Delta F_x} \ . \end{aligned} \tag{2.47}$$

As the velocity component U_n in ${}_{T}\mathbf{e}_n$-direction is zero, the velocities U_x and U_y in Equation (2.47) can be expressed by

$$\begin{aligned} U_x &= U_t\cos\beta - U_n\sin\beta = U_t\cos\beta \\ U_y &= U_t\sin\beta + U_n\cos\beta = U_t\sin\beta \ , \end{aligned} \tag{2.48}$$

therefore, the equations of motion for constant or slowly varying speed $\dot{U}_t \approx 0$ become

$$\begin{aligned} m\left[U_t\left(\dot{\beta}+\dot{\psi}\right)\cos\beta\right] &= -C_\alpha^F\left[\frac{U_t\sin\beta+\dot{\psi}a}{U_t\cos\beta}-\delta\right] - C_\alpha^R\left[\frac{U_t\sin\beta-\dot{\psi}b}{U_t\cos\beta}\right] \\ I_z\ddot{\psi} &= -aC_\alpha^F\left[\frac{U_t\sin\beta+\dot{\psi}a}{U_t\cos\beta}-\delta\right] + bC_\alpha^R\left[\frac{U_t\sin\beta-\dot{\psi}b}{U_t\cos\beta}\right] + M^F_{\Delta F_x} + M^R_{\Delta F_x} \ . \end{aligned} \tag{2.49}$$

For small side slip angles, $\cos\beta \approx 1$ and $\sin\beta \approx \beta$, the equation can be solved for $\dot{\beta}$ and $\ddot{\psi}$. The linear state space equations of the single-track model formulated in $\underrightarrow{\mathrm{T}}$ become

$${}_{T}\dot{\mathbf{x}} = {}_{T}\mathbf{A}\,{}_{T}\mathbf{x} + {}_{T}\mathbf{B}\,{}_{T}\mathbf{u} \tag{2.50}$$

with

$$ {}_T\mathbf{A} = \begin{bmatrix} -\dfrac{C_\alpha^F + C_\alpha^R}{m\,U_t} & \dfrac{C_\alpha^R\,b - C_\alpha^F\,a}{m\,U_t^2} - 1 \\ \dfrac{b\,C_\alpha^R - a\,C_\alpha^F}{I_z} & -\dfrac{a^2\,C_\alpha^F + b^2\,C_\alpha^R}{I_z\,U_t} \end{bmatrix} \quad \text{and} \quad {}_T\mathbf{B} = \begin{bmatrix} \dfrac{C_\alpha^F}{mU_t} & 0 & 0 \\ \dfrac{a\,C_\alpha^F}{I_z} & \dfrac{1}{I_z} & \dfrac{1}{I_z} \end{bmatrix}, \quad (2.51) $$

being the system and the control matrix, respectively. The state vector and the vector of control inputs read

$$ {}_T\mathbf{x} = \left[\beta,\, \dot{\psi}\right]^{\mathrm{T}} \quad \text{and} \quad {}_T\mathbf{u} = \left[\delta,\, M_{\Delta F_x}^F,\, M_{\Delta F_x}^R\right]^{\mathrm{T}} . \quad (2.52) $$

2.6 Steering Characteristics

This section provides some terms and definitions based on the analysis of the linear single-track model. First, the so-called *Ackermann* steering angle for cornering at low velocities is introduced. Subsequently, the required amount of steering for driving at higher velocities is addressed. In this context the terms *oversteering*, *understeering*, and *selfsteering gradient* are defined for steady state cornering.

2.6.1 Ackermann Steering

For low velocities ${}^E\mathbf{v}^{CG^*}$ the cornering angles at the front and at the rear tires α^F and α^R almost vanish. For circular driving on a prescribed radius of curvature $1/\kappa$ about the instantaneous center of curvature ICC with $\alpha^F = \alpha^R = 0$, the necessary steering angle can be determined from the geometry as depicted in Figure 2.15.

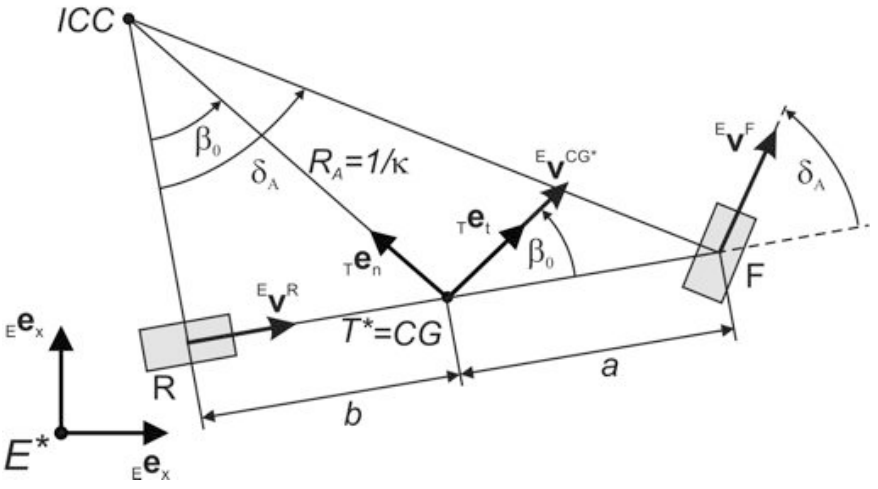

Figure 2.15: Geometry of the Ackermann model

The resulting steering angle is called Ackermann angle δ_A. Noteworthy, unlike most wheeled robots, see for example MURRAY AND SASTRY (1994, [76]) or SIEGWART AND NOURBAKHSH (2004, [103]), road vehicles are not subjected to nonholonomic constraints of the kind ${}^{E}\mathbf{v}^{F} \cdot {}_{F}\mathbf{e}_y = 0$ and ${}^{E}\mathbf{v}^{R} \cdot {}_{R}\mathbf{e}_y = 0$ that enforce the cornering angles to vanish. Road vehicles have rubber tires and the velocity constraints are therefore dissolved by elastic deformations. However, for low velocities, accompanied by low lateral forces, road vehicles behave kinematically similar to nonholonomic rigid wheeled robots. Considering both tracks of a vehicle, the Ackermann geometry would require different steering angles at the inner and at the outer front wheels. However, for the single-track model the Ackermann angle δ_A represents a mean value

$$\tan \delta_A = \frac{a+b}{\sqrt{(1/\kappa)^2 - b^2}} \, . \tag{2.53}$$

For small angles, $\tan \delta_A \approx \delta_A$, and with $b << 1/\kappa$ the Ackermann angle becomes

$$\delta_A = (a+b)\,\kappa \, . \tag{2.54}$$

The vehicle side slip angle β_0 for vanishing cornering angles can be expressed by means of the Ackermann angle, see for example ZOMOTOR (1991, [128], p. 103)

$$\beta_0 = b\,\kappa = \delta_A \, \frac{b}{a+b} \, . \tag{2.55}$$

This geometric result is consistent with the kinematic and the dynamic equations of the linear single-track model provided in sections 2.5.1 and 2.5.2. Recalling the small angle approximation for the tire side slip angles from Equation (2.35) and equating them to zero gives

$$\begin{aligned} \alpha^F &\approx \frac{U_y + \dot{\psi} a}{U_x} - \delta \stackrel{!}{=} 0 \\ \alpha^R &\approx \frac{U_y - \dot{\psi} b}{U_x} \stackrel{!}{=} 0 \, . \end{aligned} \tag{2.56}$$

Subtracting the second from the first equation in (2.56) leads to

$$\delta = \frac{\dot{\psi}\,(a+b)}{U_x} \approx (a+b)\,\kappa = \delta_A \, , \tag{2.57}$$

with $\dot{\psi} = \kappa\, U_t = \kappa\, U_x \, \cos\beta \approx \kappa\, U_x$ for steady state cornering on a circular track and small side slip angles, $\cos\beta \approx 1$.

2.6.2 Self Steering Gradient

Steady state cornering on a given radius of curvature and at fixed (low) velocity requires a particular steering angle, the Ackermann angle δ_A, as discussed in Section 2.6.1. However, if the velocity is gradually increased, the steering angle needs to be adapted. The amount

of additional steering angle to the Ackermann angle, which is necessary to remain on the same radius of curvature, depends on the steering characteristics of the vehicle.

For steady state cornering, $\dot{\beta} = 0$ and $\ddot{\psi} = 0$, on a given radius of curvature $1/\kappa$ the steering angle δ can be obtained from the steady state of the equations of motion (2.50)

$$\begin{bmatrix} -\dfrac{C_\alpha^F + C_\alpha^R}{m\,U_t} & \dfrac{C_\alpha^R\,b - C_\alpha^F\,a}{m\,U_t^2} - 1 \\ \dfrac{b\,C_\alpha^R - a\,C_\alpha^F}{I_z} & -\dfrac{a^2\,C_\alpha^F + b^2\,C_\alpha^R}{I_z\,U_t} \end{bmatrix} \begin{bmatrix} \beta \\ \dot{\psi} \end{bmatrix} + \begin{bmatrix} \dfrac{C_\alpha^F}{mU_t} & 0 & 0 \\ \dfrac{a\,C_\alpha^F}{I_z} & \dfrac{1}{I_z} & \dfrac{1}{I_z} \end{bmatrix} \begin{bmatrix} \delta \\ M^F_{\Delta F_x} \\ M^R_{\Delta F_x} \end{bmatrix} = \begin{bmatrix} 0 \\ 0 \end{bmatrix}. \tag{2.58}$$

Eliminating the side slip angle β from the set of linear equations (2.58) and substituting the yaw rate by $\dot{\psi} = \kappa\,U_t$ gives for the steering angle δ for pure steering, $M^F_{\Delta F_x} = M^R_{\Delta F_x} = 0$:

$$\delta = (a+b)\;\kappa + \frac{m\,(C_\alpha^R\,b - C_\alpha^F\,a)}{C_\alpha^F\,C_\alpha^R\;(a+b)}\,U_t^2\,\kappa\;. \tag{2.59}$$

The coefficient of the lateral acceleration ${}^E_T a_n^{CG} = U_t^2\,\kappa$ in Equation (2.59) is called *self steering gradient SG*

$$SG = \frac{m\,(C_\alpha^R\,b - C_\alpha^F\,a)}{C_\alpha^F\,C_\alpha^R\;(a+b)}\;, \tag{2.60}$$

see (2004, [1]). With the Ackermann angle, as defined in Equation (2.54), Equation (2.59) can be rewritten as

$$\delta = \delta_A + SG \cdot\; {}^E_T a_n^{CG}\;. \tag{2.61}$$

The self steering gradient, $SG = \partial\,(\delta - \delta_A)\,/\partial\,{}^E_T a_n^{CG}$, describes the change in the steering angle with respect to the lateral acceleration. In other words, the product of the self steering gradient SG and the lateral acceleration ${}^E_T a_n^{CG}$, which is proportional to the squared speed U_t^2 of the vehicle for a fixed radius of curvature $1/\kappa$, provides the amount of additional steering angle to the Ackermann angle δ_A.

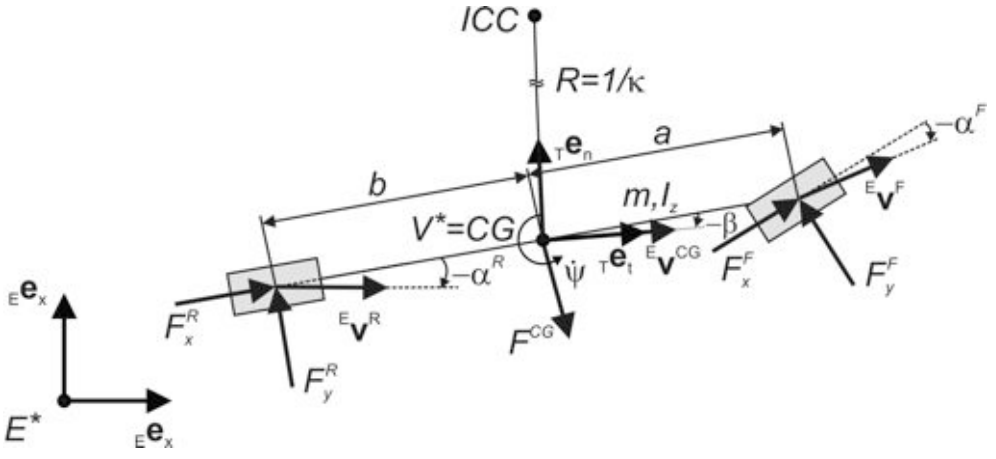

Figure 2.16: Steady state cornering on a large radius of curvature R

The steering characteristics and therefore the self steering gradient SG of a vehicle are related to the difference between the cornering angles at the front and at the rear tires, $\alpha^F - \alpha^R$. This fact is highlighted in the following. In steady state cornering the inertial force F^{CG} at the center of gravity CG is balanced by the lateral tire forces F_y^F at the front and F_y^R at the rear axle as depicted in Figure 2.16. Notice that the lateral tire forces are in positive direction but the slip angles are negative.

With the lateral acceleration, ${}^{E}_{T}a_n^{CG} = U_t^2\kappa$, the equilibrium of forces and moments yields the following approximation, which holds for large radii of curvature $1/\kappa$,

$$F_y^F \approx m\, U_t^2 \kappa \, \frac{b}{a+b} \quad \text{and} \quad F_y^R \approx m\, U_t^2 \kappa \, \frac{a}{a+b} \, . \tag{2.62}$$

Recalling the lateral tire forces in the linear region from the Dugoff model, see Equation (2.13), the lateral forces in Equation (2.62) can be substituted yielding the steady state cornering angles for a vehicle cornering about the instantaneous center of curvature (ICC) as depicted in Figure 2.16:

$$\alpha^F = \frac{m}{C_\alpha^F} \, \frac{b}{a+b} \, U_t^2 \kappa \;\text{ and }\; \alpha^R = \frac{m}{C_\alpha^R} \, \frac{a}{a+b} \, U_t^2 \kappa. \tag{2.63}$$

Therefore, the difference between the cornering angles at the front and the rear tires can be written as

$$\alpha^F - \alpha^R = \frac{m\,(C_\alpha^R\, b - C_\alpha^F\, a)}{C_\alpha^F\, C_\alpha^R\, (a+b)} \, U_t^2 \kappa \, . \tag{2.64}$$

Comparing Equation (2.64) to Equation (2.60) reveals that the product of the self steering gradient SG and the lateral acceleration ${}^{E}_{T}a_n^{CG}$ equals the difference of the cornering angles at front and rear tires

$$\alpha^F - \alpha^R = SG \cdot \, {}^{E}_{T}a_n^{CG} \, . \tag{2.65}$$

Thus, the steering angle becomes, according to Equation (2.61),

$$\delta = \delta_A + SG \cdot U_t^2 \kappa = \delta_A + \left(\alpha^F - \alpha^R\right). \tag{2.66}$$

The difference of the cornering angles at the front and at the rear axles equals the amount of additional steering angle to the Ackermann angle δ_A. Equation (2.66) is a linear equation with the slope SG. Figure 2.17 shows the steering angle δ depending on the lateral acceleration for three different configurations: $SG < 0$, $SG = 0$ and $SG > 0$. In the linear region SG is a constant, in the nonlinear region SG changes due to the tire characteristics, see Figure 2.6.

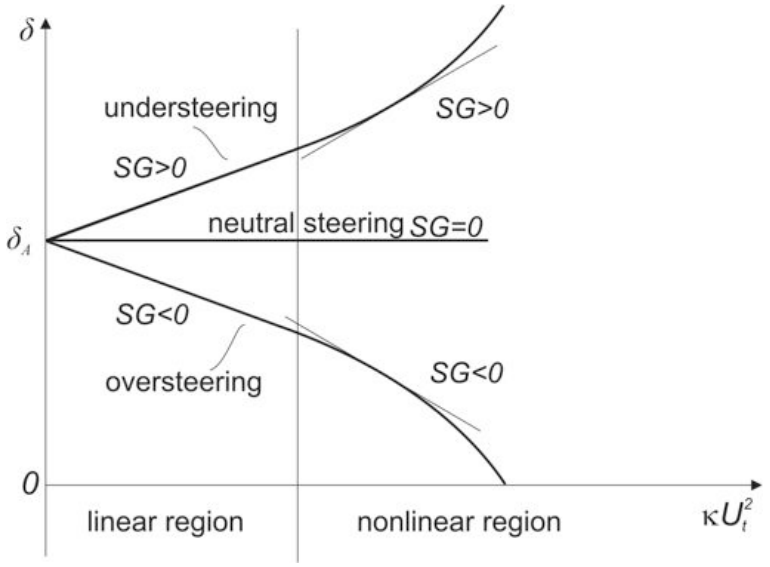

Figure 2.17: Self steering gradient according to ZOMOTOR (1991, [128], p. 109)

Concluding, the steering characteristics can be interpreted by means of the self steering gradient and categorized as *understeering*, *neutral steering* and *oversteering*:

- $SG > 0 \qquad (C_\alpha^F a - C_\alpha^R b < 0)$ **understeering**
  The steering angle needs to be increased with increasing velocity to stay on a constant radius of curvature $1/\kappa$. The vehicle tends to drift straight over the front tires. The cornering angles at the front tires are higher than at the rear tires ($\alpha^F - \alpha^R > 0$).

- $SG = 0 \qquad (C_\alpha^F a - C_\alpha^R b = 0)$ **neutral steering**
  The steering angle is independent of the velocity and identical to the Ackermann angle $\delta = \delta_A$. The cornering angles at the front and at the rear tires are equal ($\alpha^F - \alpha^R = 0$).

- $SG < 0 \qquad (C_\alpha^F a - C_\alpha^R b > 0)$ **oversteering**
  The steering angle needs to be decreased with increasing velocity to stay on a constant radius of curvature $1/\kappa$. The vehicle tends to break out at the rear wheels. The cornering angles at the rear tires are higher than at the front tires ($\alpha^F - \alpha^R < 0$).

2.7 Model Validation with Experimental Data

In this section, experimental test data[1] are used as benchmark for the nonlinear single-track model, given in Section 2.4, and for the linear single-track model as presented in Section 2.5.1. The test drives were performed with the steer-by-wire test vehicle P1 shown in Figure 2.18.

Figure 2.18: Stanford steer-by-wire test vehicle P1, Laws et al. (2005, [70])

The experimental vehicle P1 features independent left and right front wheel steering mechanisms as well as independent electric rear-wheel drive. Measurements are taken by various sensor systems as for example INS and GPS. The most important measurements that are used as reference to evaluate the vehicle dynamics models are the speed of the vehicle U_x^{ref}, the left and right steering angles δ_L^{ref} and δ_R^{ref}, the yaw rate $\dot{\psi}^{\text{ref}}$, and the lateral acceleration $\dot{U}_y^{\text{ref}}$. Table 2.1 summarizes the vehicle parameters used for the simulations.

Table 2.1: Vehicle parameters

Parameter	**Symbol**	**Value**
Mass	m	1700 kg
Yaw moment of inertia	I_z	2500 kgm^2
Front axle distance to CG	a	1.33 m
Rear axle distance to CG	b	1.17 m
Track width	d	1.62 m
Cornering stiffness front tires	C_α^F	44000 N/rad
Cornering stiffness rear tires	C_α^R	63000 N/rad
Longitudinal stiffness front tires	C_x^F	69000 N
Longitudinal stiffness rear tires	C_x^R	97000 N
Effective roll radius	R_0	0.32 m
Wheel moment of inertia	I_{wheel}	0.9 kgm^2
Adhesion coefficient	μ_0	$0.8 \ldots 0.9$

[1]The experimental test data are provided by courtesy of the Stanford Dynamics Design Laboratory headed by Professor J. Christian Gerdes.

For both models the average value

$$\bar{\delta}^{\mathrm{ref}}(t) = \frac{\delta_L^{\mathrm{ref}}(t) + \delta_R^{\mathrm{ref}}(t)}{2} \tag{2.67}$$

of the measured left and right wheel steering angles is prescribed. Besides the steering angle $\bar{\delta}^{\mathrm{ref}}(t)$ the measured speed $U_x^{\mathrm{ref}}(t)$ of the vehicle is tracked. In case of the nonlinear model the prescribed velocity profile is tracked by a PID-loop that controls the driving and braking torques

$$M_{d/b}(t) = K_P \left[U_x^{\mathrm{ref}}(t) - U_x(t)\right] + K_I \int_{t_0}^{t} U_x^{\mathrm{ref}}(\tau) - U_x(\tau)\,\mathrm{d}\tau + K_D \frac{d}{dt}\left[U_x^{\mathrm{ref}}(t) - U_x(t)\right] \ . \tag{2.68}$$

As the test vehicle P1 is rear wheel driven, the torque $M_{d/b}$ is applied solely to the rear wheels. Equation (2.68) implies that the torque is generated without time delay, which means that no powertrain is modeled. However, the focus of the model lies on lateral vehicle dynamics and the PID-loop only intends to track the velocity profiles of the test drives.

For the linear model the speed is treated as time varying parameter. Thus, the state space model, Equation (2.40), with $M_{\Delta F_x}^F = M_{\Delta F_x}^R = 0$, reads

$$\begin{bmatrix} \dot{U}_y \\ \ddot{\psi} \end{bmatrix} = \begin{bmatrix} -\dfrac{C_\alpha^F + C_\alpha^R}{m\,U_x^{\mathrm{ref}}(t)} & \dfrac{C_\alpha^R\,b - C_\alpha^F\,a}{m\,U_x^{\mathrm{ref}}(t)} - U_x^{\mathrm{ref}}(t) \\ \dfrac{b\,C_\alpha^R - a\,C_\alpha^F}{I_z\,U_x^{\mathrm{ref}}(t)} & -\dfrac{a^2\,C_\alpha^F + b^2\,C_\alpha^R}{I_z\,U_x^{\mathrm{ref}}(t)} \end{bmatrix} \begin{bmatrix} U_y \\ \dot{\psi} \end{bmatrix} + \begin{bmatrix} \dfrac{C_\alpha^F}{m} \\ \dfrac{a\,C_\alpha^F}{I_z} \end{bmatrix} \bar{\delta}^{\mathrm{ref}}(t) \ . \tag{2.69}$$

The simulation data are compared to the experimental data incorporating the following criteria proposed by FRIK (1994, [39]):

$$\epsilon_{j,r} = \frac{\max\limits_{i=1\ldots n}\left(\left|x_{ij} - x_{ij}^{\mathrm{ref}}\right|\right)}{\max\limits_{i=1\ldots n}\left|x_{ij}^{\mathrm{ref}}\right|} \tag{2.70}$$

$$\bar{\epsilon}_j = 1/n \sum_{i=1}^{n} \left|x_{ij} - x_{ij}^{\mathrm{ref}}\right| \tag{2.71}$$

$$\bar{\epsilon}_{j,r} = \frac{\sum_{i=1}^{n}\left|x_{ij} - x_{ij}^{\mathrm{ref}}\right|}{\sum_{i=1}^{n}\left|x_{ij}^{\mathrm{ref}}\right|} \ , \tag{2.72}$$

with i numbering the data in test drive j. The relative error $\epsilon_{j,r}$ describes the maximal *local* deviation of the simulation results x_{ij} from the measurements x_{ij}^{ref} with respect to the maximum of the experimental reference in the considered test drive j. The quality of the *global* solution is addressed by the mean error $\bar{\epsilon}_j$ and the mean relative error $\bar{\epsilon}_{j,r}$.

In the following, steady state and unsteady state driving maneuvers are analyzed. In doing so, the criteria in equations (2.70)-(2.72) are evaluated for different test maneuvers j, for the yaw rate as well as for the lateral acceleration, $x_{ij} \in \left\{\dot{\psi}(t_i)\ , \dot{U}_y(t_i)\right\}$.

2.7.1 Steady State Cornering Maneuver

In this section experimental data of a steady state cornering maneuver are used to validate the linear and the nonlinear single-track model. Figure 2.19 shows the steering angle $\bar{\delta}^{\text{ref}}(t)$ and the velocity profile $U_x^{\text{ref}}(t)$ of the maneuver. The vehicle accelerates from rest to a constant velocity of approximately $15m/s$. The test drive includes two periods of constant steering angle inputs of $5°$ and $-5°$, respectively. The steady state phases are highlighted by gray boxes.

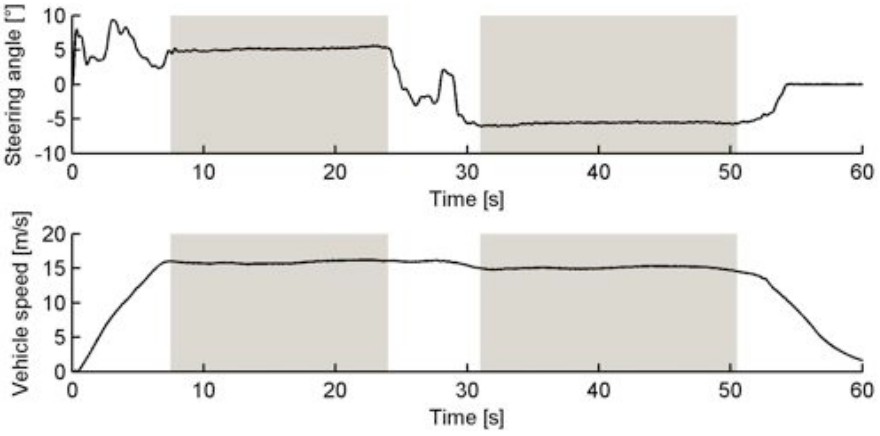

Figure 2.19: Steady state cornering maneuver

Therein, the phases of steady state cornering correspond to circles driven to the left in case of the positive steering angle and driven to the right for the negative steering angle. The radii of the circles vary between 30 m and 35 m.

The data of the steady state cornering maneuver were used to identify the tire parameters of the models given in Table 2.1. In order to do so, the ratio of the measured yaw rate $\dot{\psi}^{\text{ref}}$ and the steering angle $\bar{\delta}^{\text{ref}}$ in steady state cornering was compared to the steady state yaw rate gain of the linear model, see MITSCHKE AND WALLENTOWITZ (2004, [74], p. 563),

$$\left(\frac{\dot{\psi}^{\text{ref}}}{\bar{\delta}^{\text{ref}}}\right)_{\text{ss}} \stackrel{!}{=} \frac{1}{a+b}\,\frac{U_x^{\text{ref}}}{1+\left(\dfrac{U_x^{\text{ref}}}{U_{\text{char}}}\right)^2} \quad \text{with} \quad U_{\text{char}}^2 := \frac{a+b}{SG} = \frac{C_\alpha^F C_\alpha^R (a+b)^2}{m\left(C_\alpha^R b - C_\alpha^F a\right)}\,. \tag{2.73}$$

Inspecting the self steering gradient SG, the ratio of the cornering stiffnesses C_α^F and C_α^R can be adjusted in order to satisfy Equation (2.73). Whereas, the vehicle mass m and the distances a and b to the center of gravity CG are known from direct measurements.

The simulation results as well as the measured data for the yaw rate and the lateral acceleration are given in Figure 2.20.

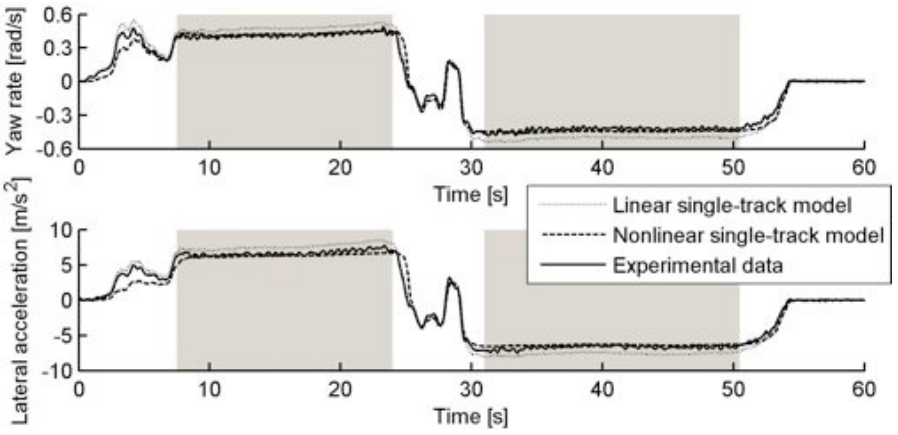

Figure 2.20: Model comparison for steady state cornering maneuver

Noteworthy, that in the acceleration phase of the test drive, at approximately $5s$, the yaw rate and the lateral acceleration simulated with the nonlinear vehicle model deviate more from the measurement results than the simulation results of the linear model. This is due to the fact that the nonlinear tire model combines longitudinal and lateral tire forces. The longitudinal tire forces are influenced by the driving torque, generated by the PID-loop, Equation (2.68). Thus, lateral vehicle dynamics are affected when the velocity of the vehicle changes. Besides that, the accuracy of the nonlinear tire model decreases at low velocities; for zero velocity the longitudinal slip is not defined.

In the steady state phases, highlighted by gray boxes, it can be observed that the linear single-track model generates slightly too high absolute values for the yaw rate as well as for the lateral acceleration. The linearization of the lateral tire forces with respect to the cornering angles is valid up to approximately one third of the maximum tire forces, which corresponds to a lateral acceleration of about $4\,\mathrm{m/s^2}$, see MITSCHKE AND WALLENTOWITZ (2004, [74], p. 36-38 and p. 560). In the steady state phases of the test drive the lateral acceleration lies between 5 and $6\,\mathrm{m/s^2}$ as presented in the lower part of Figure 2.20. Therefore, the tires leave the linear region and the linear tire model tends to generate too high lateral forces, which results in the increased values for yaw rate and lateral acceleration.

Table 2.2 shows the criteria defined in equations (2.70)-(2.72), evaluated for yaw rate and lateral acceleration as given in Figure 2.20. The lower relative errors $\epsilon_{j,r}$ of the linear single-track model compared to the relative errors of the nonlinear model document the deviations in the acceleration phase of the test drive. However, the values of the mean error $\bar{\epsilon}_j$ and of the relative mean error $\bar{\epsilon}_{j,r}$ indicate the higher quality of the global solution of the nonlinear model, which corresponds to the more accurate results in the phases of steady state cornering in Figure 2.20.

Table 2.2: Quantitative model comparison for steady state cornering

Error	Linear Single-track model	Nonlinear Single-track model
Yaw rate		
$\epsilon_{j,r}$	0.22	0.45
$\bar{\epsilon}_j$	0.04	0.03
$\bar{\epsilon}_{j,r}$	0.13	0.08
Lateral acceleration		
$\epsilon_{j,r}$	0.2	0.57
$\bar{\epsilon}_j$	0.49	0.45
$\bar{\epsilon}_{j,r}$	0.11	0.09

2.7.2 Unsteady Cornering Maneuver

While in the last section a steady state cornering maneuver was surveyed, this section deals with a maneuver where the vehicle gradually approaches the limits of adhesion and finally breaks out. Figure 2.21 shows the steering angle $\bar{\delta}^{\text{ref}}(t)$ and the velocity profile $U_x^{\text{ref}}(t)$ of the test drive. In the highlighted part of the test drive the speed of the vehicle $U_x^{\text{ref}}(t)$ is almost constant at $17m/s$ while the steering angle $\bar{\delta}^{\text{ref}}(t)$ is gradually increased from 0° to 11°.

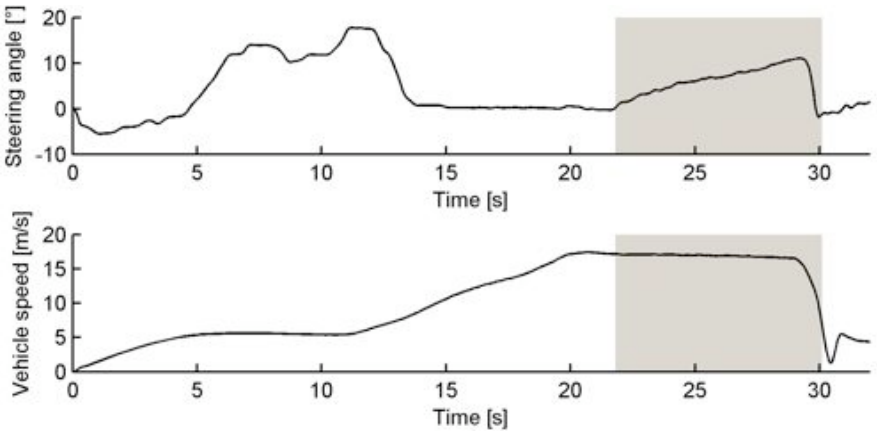

Figure 2.21: Unsteady maneuver with break out

Subsequently, Figure 2.22 provides the yaw rate and the lateral acceleration of the test drive and the corresponding simulations with the linear and the nonlinear model.

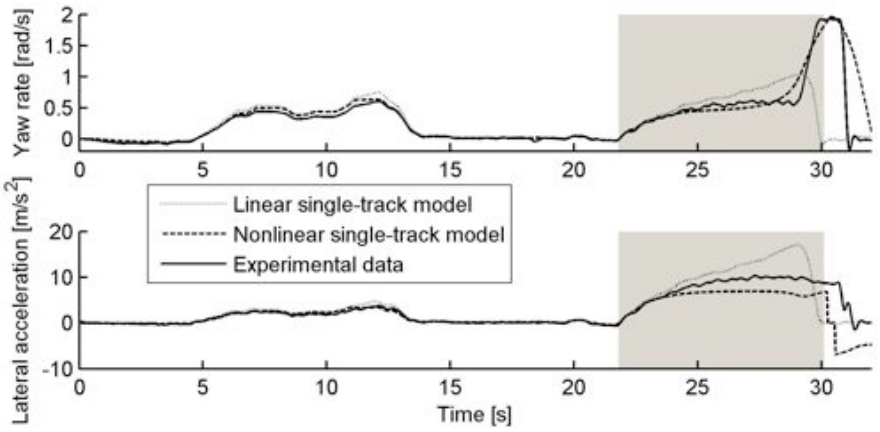

Figure 2.22: Model comparison for unsteady maneuver with break out

Focusing the observations on the highlighted phase, it can be noticed that yaw rate and lateral acceleration initially increase together with the steering angle. Then, the tires start to saturate and the force characteristic becomes highly nonlinear. Further increments of the steering angle now cause smaller increments of the yaw rate and the lateral acceleration. Subsequently, the tires exceed their limits of adhesion and the vehicle breaks out. The break out is indicated by a step in the yaw rate, which means that the vehicle starts spinning. In the end, the vehicle is decelerated to rest.

The nonlinear model nicely captures the qualitative behavior of the vehicle cornering at the limits of adhesion. The remaining differences are partly caused by the velocity profile of the test drive that is only approximated in the simulations by the PID-loop in Equation (2.68). However, with rising lateral accelerations effects such as roll and the associated shifting of weight become more evident and reduce the quality of the simulation results. These effects can only be captured by more detailed models, that on the other hand require more simulation time.

Yaw rate and lateral acceleration simulated with the linear model constantly increase with the steering angle and show no saturation effects. Thus, the break out of the vehicle is not captured by the linear model. Comparing the experimental data in Figure 2.22 with the simulation results of the linear model illustrates the effect of linearization of the tire forces in the nonlinear region.

The better solution quality of the nonlinear model becomes evident by comparing the errors given in Table 2.3. Therein, the high relative errors $\epsilon_{j,r}$ for the yaw rate and the lateral acceleration indicate the high deviations of the linear model from the experimental data at high lateral accelerations. The better global solution quality of the nonlinear model is documented by the lower mean and relative mean errors $\bar{\epsilon_j}$ and $\bar{\epsilon}_{j,r}$.

Table 2.3: Quantitative model comparison for unsteady state cornering

Error	**Linear Single-track model**	**Nonlinear Single-track model**
Yaw rate		
$\epsilon_{j,r}$	4.58	0.9
$\bar{\epsilon}_j$	0.15	0.12
$\bar{\epsilon}_{j,r}$	0.98	0.37
Lateral acceleration		
$\epsilon_{j,r}$	3.49	1.52
$\bar{\epsilon}_j$	0.99	0.67
$\bar{\epsilon}_{j,r}$	1.14	0.54

The simulations above were performed with an adhesion coefficient of $\mu_0 = 0.8$. To illustrate how sensible the simulation results are to parameter variations the simulation with the nonlinear model is repeated for $\mu_0 = 0.9$. The resulting yaw rates, presented in Figure 2.23, show that the adhesion coefficient mainly affects the part of the maneuver where the vehicle breaks out. The behavior of the vehicle cornering at high lateral accelerations but not exceeding the limits of adhesion is still captured. However, obviously the model does not break out when the adhesion coefficient is increased to $\mu_0 = 0.9$. In this case, the simulated maximal lateral force is too high.

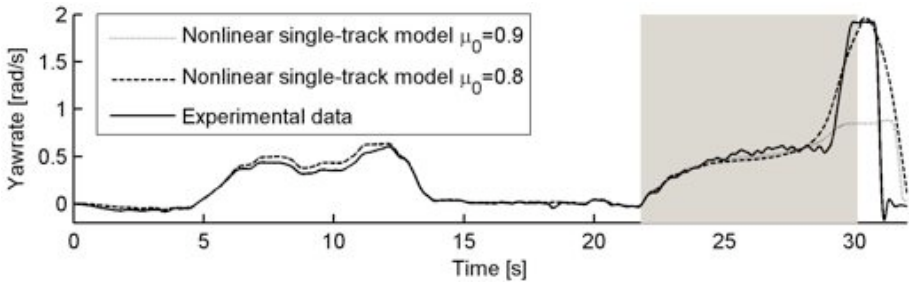

Figure 2.23: Influence of the adhesion coefficient

Summarizing, the comparison with experimental data confirms the well known statement that the linear model is only reliable up to a lateral acceleration of approximately $0.4g$, which is consistent with the literature, e.g. MITSCHKE AND WALLENTOWITZ (2004, [74]). Beyond $0.4g$ the linear model tends to generate too high lateral forces. For trajectory following this means for example that the linear model tends to follow a given trajectory at high lateral acceleration better than a real vehicle. The nonlinear vehicle model includes saturation effects at the tires and therefore generates better results at high lateral accelerations. However, as indicated by the variation of the adhesion coefficient, μ_0, the simulation results at the limits of adhesion are very sensitive to parameter variations.

Chapter 3

Potential Field based Motion Planning

A *hazard map* and a so-called *elastic band* are the main elements of the proposed potential field based motion planning. The hazard potential ${}_{R}V^{\text{haz}}$ encodes the available sensor information about the environment of the host-vehicle in terms of potential fields. Therefore, ${}_{R}V^{\text{haz}}$ is composed of information about the course of the road, represented by its centerline $\mathcal{R}$ and its borders $\partial\mathcal{B}_l$ and $\partial\mathcal{B}_r$, information about the *obstacles* $\mathcal{O}_j,\ j = 1, \ldots, M$, referring to other traffic participants as well as to static objects in the environment, and information about the host-vehicle $\mathcal{V}$. Besides that the hazard map contains information about the motion of the host-vehicle and provides a spatial as well as a temporal representation of the traffic situation. The elastic band consisting of coupled nodes $P_0, \ldots, P_N$ scans the hazard map, like a virtual antenna of an insect, for trajectories of low hazard levels. The combination of external hazard potentials and internal potentials that couple the nodes of the elastic band cause trajectories with inherent low curvatures. The composed potential field motion planning module is depicted in Figure 3.1, see also Figure 1.9.

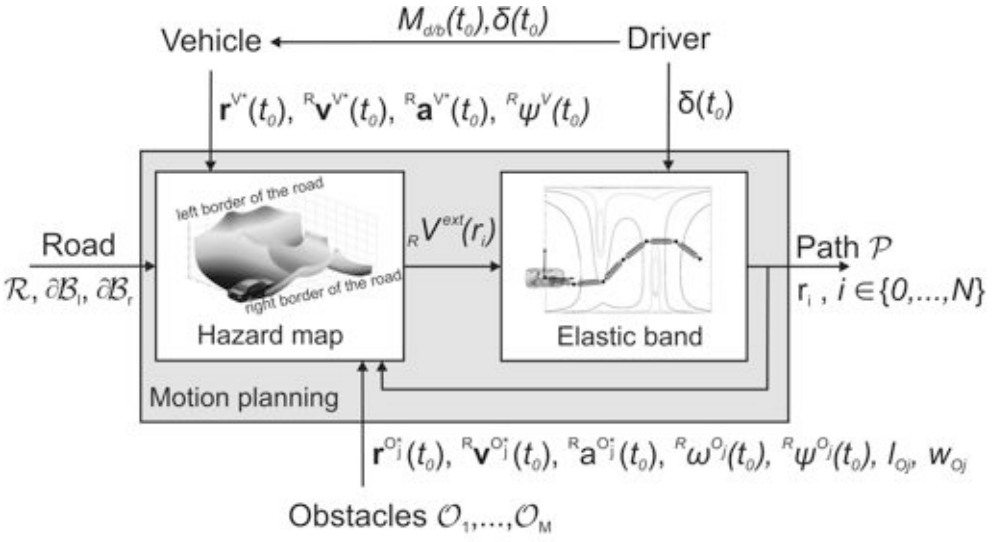

Figure 3.1: Motion planning module composed of hazard map and elastic band, based on sensor information collected at the planning instant t_0

In the sense of *shared vehicle guidance* it is mandatory that the driver has influence on the motion planning procedure: by setting the accelerometer and braking pedal, which results in driving and braking torques $M_{d/b}$, the driver prescribes the velocity profile $U_t(t)$ of the longitudinal motion of the host-vehicle. In doing so, he may be assisted by systems such as *Adaptive Cruise Control* or the *Emergency Brake*. Besides that the driver influences the motion planning directly by communicating his intended driving maneuver via the steering angle δ. The result of the motion planning process is a collision-free trajectory represented by the position vectors of the nodes of the elastic band.

Similar to driving strategies of human drivers, the motion planning concept introduced in the following is predictive and incorporates extrapolation procedures to anticipate the evolution of the traffic scenario. However, to be able to refine the extrapolation of the traffic scenario and to be able to react to unpredicted events such as new objects within the detection range, the motion planning is repeated in time intervals of ΔT, where the planning horizon ΔT depends on the update frequency of environmental sensor data. The principle procedure of handling changes in the environment is sketched in Figure 3.2. The internal coupling potentials are symbolized by springs connecting the nodes $P_0, \ldots, P_N$ of the elastic band. In the upper part of the figure the hazard map consists only of potentials due to the borders of the road, which are also symbolized by means of roundish springs; the elastic band is in an equilibrium configuration on the right lane. The obstacle on the center of the right lane is not discovered by the environmental sensors yet. Then, at time t_0, the obstacle is detected and thus contributes to the hazard map. As a consequence of the changes in the hazard potential, the elastic band is shifted into a new collision-free equilibrium configuration. The computed trajectory remains valid until new sensor data are available at time $t_0 + \Delta T$.

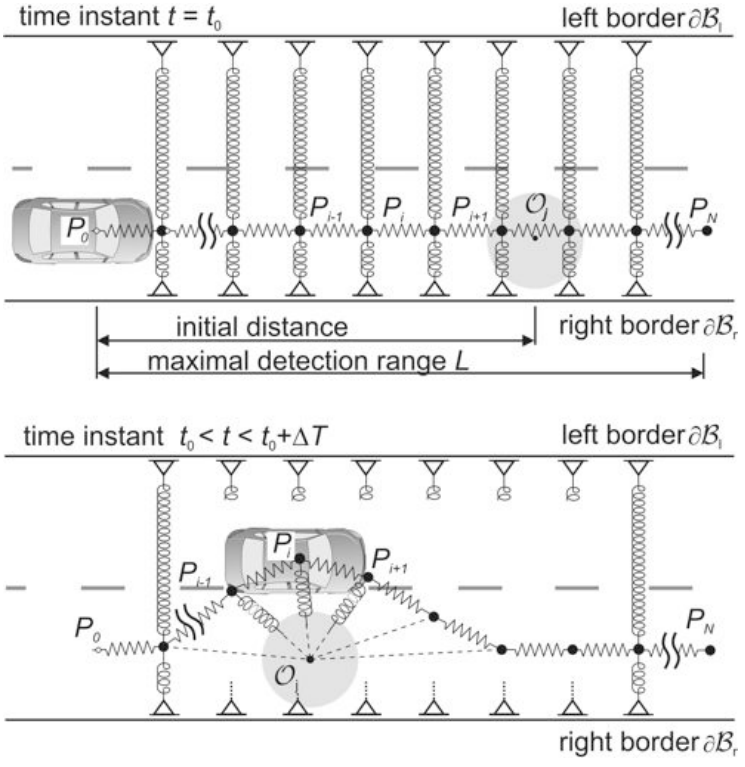

Figure 3.2: Elastic band principle

It should be mentioned that the elastic band approach originally introduced by Quinlan and Khatib (1993, [87]) for robotic path planning had to be extended significantly for automotive applications. Examples are the concept of finding an equilibrium configuration of the elastic band in a hazard map, the incorporation of obstacle motion and the interaction with the driver. However, as the approach presented here also relies on the elastic coupling of nodes of a virtual antenna exposed to potential fields, the antenna is also referred to as elastic band.

In this approach, the computation of collision-free trajectories on each planning horizon includes many different elements that are closely coupled. The hazard map for example contains extrapolated trajectories of the obstacles, which are evaluated at discrete instants in time t_i. These instants t_i in turn are prescribed by the host-vehicle passing the nodes of the elastic band. As the velocity profile driven by the host-vehicle $U_t(t)$ is determined by the driver, there is also an interplay with the driver. The shape of the elastic band also influences the instants t_i when the host-vehicle passes the nodes $P_0, \ldots, P_N$. Due to these mutual dependencies the proposed trajectory is computed by an iterative procedure, which will be outlined in this chapter.

The introduction of the different motion planning elements is structured as follows: First, the elements of the hazard map such as the road and the obstacles with the corresponding hazard potentials are presented. Then, the formulation of the elastic band with the internal coupling potentials is given. Subsequently, the interfacing elements between driver and motion planning are introduced. Next, computational aspects such as distance computations and the iterative solution of the equilibrium configuration of the elastic band are addressed. Then, sample simulation results illustrate the application of the method. Finally, the entire motion planning procedure is summarized as pseudo code.

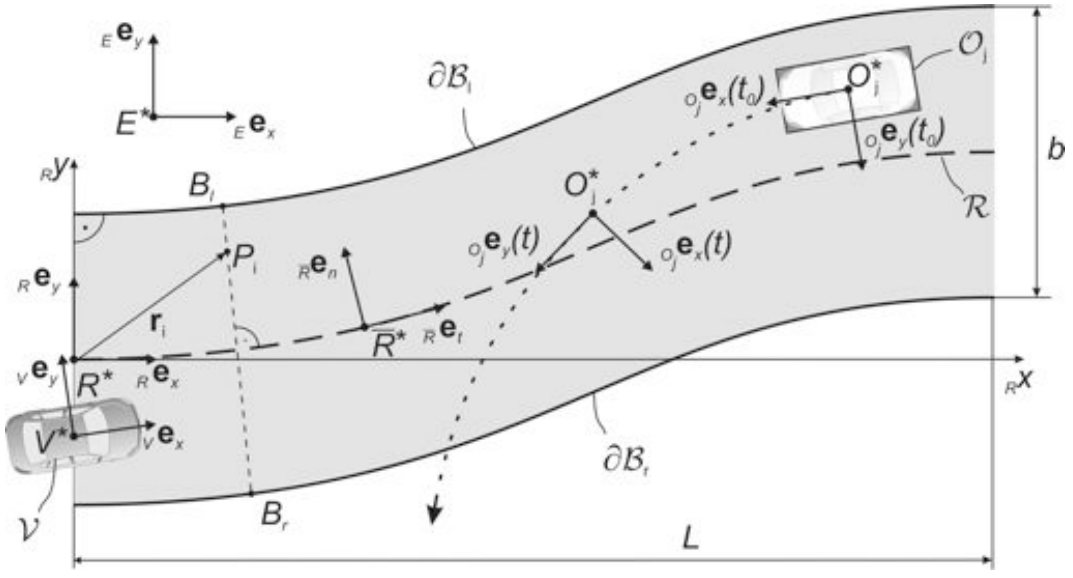

Figure 3.3: Reference frames and coordinates used in the motion planning process

The reference frames employed in the motion planning process are depicted in Figure 3.3 and are listed in the following :

$\underset{\rightarrow}{\uparrow\mathrm{E}}$: $(E^*, {}_E\mathbf{e}_x, {}_E\mathbf{e}_y, {}_E\mathbf{e}_z)$ $\widehat{=}$ **E**arth-fixed reference frame
$\underset{\rightarrow}{\uparrow\mathrm{R}}$: $(R^*, {}_R\mathbf{e}_x, {}_R\mathbf{e}_y, {}_R\mathbf{e}_z)$ $\widehat{=}$ **R**oad-fixed reference frame fixed at planning time t_0
$\underset{\rightarrow}{\uparrow\bar{R}}$: $(\bar{R}^*, {}_{\bar{R}}\mathbf{e}_t, {}_{\bar{R}}\mathbf{e}_n, {}_{\bar{R}}\mathbf{e}_z)$ $\widehat{=}$ Auxiliary reference frame shifted tangentially along the road centerline $\mathcal{R}$
$\underset{\rightarrow}{\uparrow\mathrm{V}}$: $(V^*, {}_V\mathbf{e}_x, {}_V\mathbf{e}_y, {}_V\mathbf{e}_z)$ $\widehat{=}$ **V**ehicle-fixed reference frame
$\underset{\rightarrow}{\uparrow O_j}$: $(O_j^*, {}_{O_j}\mathbf{e}_x, {}_{O_j}\mathbf{e}_y, {}_{O_j}\mathbf{e}_z)$ $\widehat{=}$ **O**bstacle-fixed reference frame

As shown in Figure 3.3 the reference frame $\underset{\rightarrow}{\uparrow\mathrm{R}}$ is oriented in tangent direction of the road centerline $\mathcal{R}$. It is fixed at the instant of planning t_0 and remains fixed for the entire planning horizon ΔT. In the next instant of planning, $t_0 + \Delta T$, $\underset{\rightarrow}{\uparrow\mathrm{R}}$ is replaced according to the new position of the host-vehicle. Meanwhile, $\underset{\rightarrow}{\uparrow\mathrm{R}}$ serves as inertial frame during each planning horizon. If not stated otherwise, position vectors are denoted with respect to R^*, e.g. $\mathbf{r}^P = \mathbf{r}^{R^*,P}$, and $\|\cdot\|$ denotes the 2-norm in distance computations. The following abbreviation is used for derivatives with respect to ${}_Rx$: $(\cdot)' = \frac{\partial}{\partial_R x}(\cdot)$ or $(\cdot)' = \frac{d}{d_R x}(\cdot)$, respectively.

3.1 Hazard Map

The environmental model represented by the hazard map is composed of potential fields capturing the course of the road and the motion of obstacles. In the following the underlying models of road geometry and obstacle motion in terms of potential fields are provided.

3.1.1 Road

In most countries roads are build according to national guidelines. In Germany for example, the construction of roads is directed by the "Richtlinien für die Anlage von Straßen (RAS-L)" (1999, [3]). The knowledge of road construction is used by intelligent environmental sensor systems to identify the course ahead of the vehicle. A broad overview of vision based automotive environmental detection is given by DICKMANNS (2002, [24]).

Road Centerline

According to (1999, [3]), German roads are designed to be continuous in curvature. In doing so, roads are composed of straight lines, circular arcs and so-called clothoids that are used as transition curves, where the curvature κ of a clothoid varies linearly with its arc length. Therefore, in each point P of a clothoid

$$A^2 = s \cdot r \tag{3.1}$$

holds with s being the arc length, r being the instantaneous radius of curvature, and A denoting the clothoid parameter; $A = 1$ characterizes an unit clothoid. From the geometry

illustrated in Figure 3.4 and with Equation (3.1) the following equation arises

$$ds = r \cdot d\tau = \frac{A^2}{s} d\tau \quad \Rightarrow \quad d\tau = \frac{s}{A^2}\, ds\ . \tag{3.2}$$

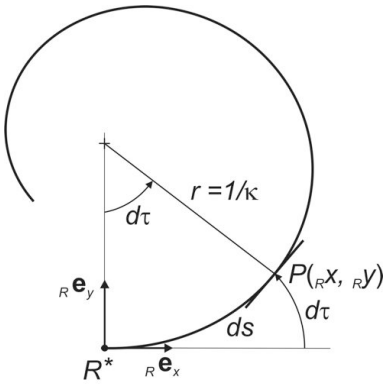

Figure 3.4: Clothoid transition element

Integration of Equation (3.2) from arc length $s_0 = 0$ to s and assuming that the clothoid starts in ${}_R\mathbf{e}_x$-direction and therefore integrating the gradient angle from $\tau_0 = 0$ to τ yields

$$\tau\,(s) = \frac{s^2}{2A^2}. \tag{3.3}$$

Therefore, differential changes in the coordinates of a point P on the clothoid projected on $\underrightarrow{\uparrow \mathrm{R}}$ read

$$d_R x = \cos\left(\tau\,(s)\right) ds = \cos\left(\frac{s^2}{2A^2}\right) ds \quad \text{and} \quad d_R y = \sin\left(\tau\,(s)\right) ds = \sin\left(\frac{s^2}{2A^2}\right) ds\ . \tag{3.4}$$

For a clothoid starting in R^* in ${}_R\mathbf{e}_x$-direction, $\tau(0) = 0$, ${}_Rx(0) = 0$, ${}_Ry(0) = 0$, see Figure 3.4, tangent orientation and position on the clothoid element in $\underrightarrow{\uparrow \mathrm{R}}$ thus become

$$\tau\,(s) = \int_0^s \kappa\,(\bar{s})\, d\bar{s}\ , \tag{3.5}$$

$${}_Rx\,(s) = \int_0^s \cos\tau\,(\bar{s})\, d\bar{s} = \int_0^s \cos\left(\frac{\bar{s}^2}{2A^2}\right) d\bar{s} \quad \text{and} \tag{3.6}$$

$${}_Ry\,(s) = \int_0^s \sin\tau\,(\bar{s})\, d\bar{s} = \int_0^s \sin\left(\frac{\bar{s}^2}{2A^2}\right) d\bar{s}\ . \tag{3.7}$$

As the curvature of a clothoid varies linearly with its arc length, $\kappa = \kappa_0 + d\kappa \cdot s$, where the rate of curvature depends on the clothoid parameter, $d\kappa = 1/A^2$, Equation (3.5) yields the tangent orientation on a clothoid with initial curvature κ_0

$$\tau\,(s) = \kappa_0 \cdot s + \frac{d\kappa}{2} s^2\,. \tag{3.8}$$

The integrals in equations (3.6) and (3.7) are known as FRESNELs integrals, see for example BRONSTEIN AND SEMENDJAEV (1997, [11], p. 647), and cannot be solved in closed form. Therefore, Taylor series expansions or numerical integration techniques have to be applied. However, in practice road curvatures especially on highways are very low. Table 3.1 gives admissible minimal radii of curvature depending on the vehicles speed according to (1999, [3]).

Table 3.1: Minimal admissible radii of curvature and arc length of clothoid transition elements depending on the speed according to (1999, [3], Tab. 5)

U_t **[km/h]**	**Minimal radius [m]**	**Minimal arc length [m]**
50	80	30
60	120	35
70	180	40
80	250	45
90	340	50
100	450	55
120	720	65

For small initial curvatures κ_0 and curvature rates $d\kappa$ small angle approximations, $\cos\tau \approx 1$ and $\sin\tau \approx \tau$, can be applied to equations (3.6) and (3.7) and yield by means of integration together with Equation (3.8)

$$ {}_R x(s) = s \,, \tag{3.9} $$

$$ {}_R y(s) = \frac{1}{2}\kappa_0 \cdot s^2 + \frac{1}{6} d\kappa \cdot s^3 \,. \tag{3.10} $$

Summarizing, the course of the road, represented by its centerline $\mathcal{R}$ in the road-fixed reference frame $\underset{\rightarrow}{\uparrow\mathrm{R}}$, can be approximated for low initial curvatures κ_0 and curvature rates $d\kappa$ by

$$ {}_R y({}_R x) = \frac{1}{2} \cdot \kappa_0 \cdot {}_R x^2 + \frac{1}{6} \cdot d\kappa \cdot {}_R x^3 \,. \tag{3.11} $$

In doing so, straight sections and circular arcs are special cases of Equation (3.11) with $\kappa_0 = 0$, $d\kappa = 0$ and $\kappa_0 \neq 0$, $d\kappa = 0$, respectively.

Considering the curvature parameters of the road to be a function of the distance along the road, they are usually estimated recursively by use of Kalman filtering techniques. One of the first applications for well-structured roads was shown by DICKMANNS AND MYSLIWETZ (1992, [25]). Meanwhile similar algorithms were also applied to less structured environments; the polynomial in Equation (3.11) provided for example the basis for the measuring system used by CREAMAN AND MURRAY (2006, [22], Eqn. (5)). Therefore, Equation (3.11) is used to model the estimated course of the road centerline $\mathcal{R}$ in the hazard map. However, the underlying low curvature assumptions apply predominantly to highways. For roads with higher curvatures, e.g. in urban environments, the model should be extended by considering higher order terms of the Taylor series expansions of equations (3.6) and (3.7).

Borders of the Road

According to the discussion above the road centerline $\mathcal{R}$, estimated by environmental sensors, is described by the third order polynomial in Equation (3.11) with respect to the road-fixed reference frame $\underline{\uparrow \mathrm{R}}_{\rightarrow}$ on each planning horizon ΔT. Thus, the position vector to an arbitrary point $\bar{R}^*$ on $\mathcal{R}$ can be described in cartesian coordinates with respect to $\underline{\uparrow \mathrm{R}}_{\rightarrow}$. With an estimation of the road width b and the auxiliary reference frame $\bar{R}$ located in $\bar{R}^*$ and with normal-tangential coordinates along the course of the road

$$ {}_{\bar{R}}\mathbf{e}_t := \frac{\mathbf{r}^{\bar{R}^*\prime}}{\left|\mathbf{r}^{\bar{R}^*\prime}\right|} = \frac{{}_R\mathbf{e}_x + {}_R y^{\bar{R}^*\prime}\, {}_R\mathbf{e}_y}{\sqrt{1+({}_R y^{\bar{R}^*\prime})^2}} , \qquad {}_{\bar{R}}\mathbf{e}_n := \frac{-{}_R y^{\bar{R}^*\prime}\, {}_R\mathbf{e}_x + {}_R\mathbf{e}_y}{\sqrt{1+({}_R y^{\bar{R}^*\prime})^2}} , \tag{3.12} $$

the corresponding points at the borders of the road are given by equations (3.11) and (3.12)

$$ \mathbf{r}^{B_q}({}_R x) = \mathbf{r}^{\bar{R}^*}({}_R x) \pm \frac{b}{2}\, {}_{\bar{R}}\mathbf{e}_n({}_R x) \quad \text{with} \quad q \in \{\mathrm{l},\ \mathrm{r}\} . \tag{3.13} $$

Road Potential Field

Potential fields are assigned separately to the left and to the right border of the road $\partial\mathcal{B}_l$ and $\partial\mathcal{B}_r$, respectively. To evaluate the potential for a node of the elastic band P_i with position vector $\mathbf{r}_i$, see Figure 3.5, the position vectors $\mathbf{r}_i^{B_q}$ to the corresponding points at the borders of the road need to be defined

$$ \mathbf{r}_i^{B_q} := \left\{ \mathbf{r}^{B_q} \in \partial\mathcal{B}_q \,|\, \left\|\mathbf{r}_i - \mathbf{r}^{B_q}\right\| = \min_{R x \in [0,L]} \left\|\mathbf{r}_i - \mathbf{r}^{B_q}({}_R x)\right\| \right\} . \tag{3.14} $$

Solving the minimum problem (3.14), see Equation (3.52), the potential of the borders of the road experienced by a node P_i can be formulated with respect to the road-fixed reference frame $\underline{\uparrow \mathrm{R}}_{\rightarrow}$,

$$ {}_R V_i^{B_q} = {}_R V^{B_q}\left(\mathbf{r}_i, \mathbf{r}_i^{B_q}\right) . \tag{3.15} $$

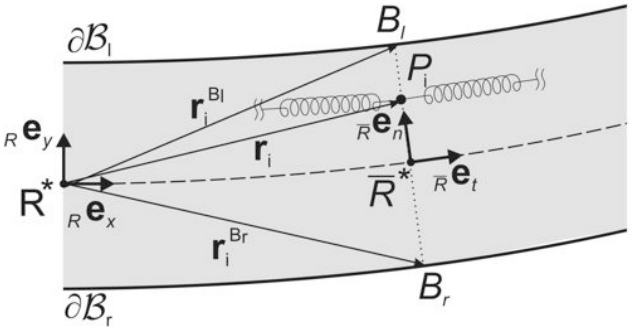

Figure 3.5: Road potential field

Adjusting the Potential Field Minimum

The minimum of the road potential field defines the course of minimal hazard along the road in absence of obstacles. By scaling the potentials of left and right border $\partial\mathcal{B}_l, \partial\mathcal{B}_r$ separately, adjusting the location of the minimum is a design choice. On a road with two lanes the minimum could for example be placed on the right lane. However, driving on the center of the road does not reflect the behavior intended by most of the drivers. In general, drivers tend to guide the vehicle closer to the road centerline than to the border of the road. On curved roads the desired lateral position depends on the curvature; MITSCHKE AND WALLENTOWITZ (2004, [74], pp. 653) summarize some empirical studies on human driving behavior and give a linear relation of the intended lateral offset to the center of the lane and the curvature κ of the road. The curvature κ of the road follows from the second derivative of the describing polynomial in Equation (3.11) with respect to ${}_R x$. One choice to design the potential field of the borders of the road is the logarithmic formulation

$$ {}_R V_i^{B_q} = -k^{B_q} \cdot \ln \left\| \mathbf{r}_i - \mathbf{r}_i^{B_q} \right\| , \qquad \frac{k^{B_\mathrm{l}}}{k^{B_\mathrm{r}}} = \frac{d_\mathrm{l}}{d_\mathrm{r}} , \tag{3.16} $$

with d_l and d_r being the distance of the minimum of the potential to the left and to the right border ∂B_l and ∂B_r, respectively. Placing the minimum on the center of the right lane on a two lane road with width b would for example lead to $\frac{k^{B_\mathrm{l}}}{k^{B_\mathrm{r}}} = \frac{0.75b}{0.25b}$. In general, k^{B_l} and k^{B_r} can be subjected to changes depending on the curvature of the road or due to strategic decisions as for example lane change maneuvers indicated by the driver.

3.1.2 Obstacles

The anticipated behavior of the obstacles $\mathcal{O}_j$, $j = 1, \ldots, M$, is modeled based on sensor information provided at the instant of planning t_0. In general, the following information are available after fusion of different environmental sensor systems, see for example MILDNER (2004, [73], p. 22-24):

- position: ${}^R\mathbf{r}^{O_j^*}(t_0)$,
- velocity: ${}^R\mathbf{v}^{O_j^*}(t_0)$,
- acceleration: ${}^R\mathbf{a}^{O_j^*}(t_0)$,
- angular velocity: ${}^R\boldsymbol{\omega}^{O_j}(t_0)$,
- orientation: ${}^R\psi^{O_j}(t_0)$ and
- geometry: length l_{O_j} and width w_{O_j} or diameter d_{O_j}.

If no information about the acceleration of an obstacle $\mathcal{O}_j$ is available, the velocity ${}^R\mathbf{v}^{O_j^*}$ is assumed to be constant on each planning horizon ΔT.

In robotics growing methods are used to virtually enlarge the dimensions of the robot or obstacles; examples are given by SPARBERT, KUMPEL AND HOFER (2001, [107]). Here, a modified growing method is applied to each obstacle yielding a *safety area* as illustrated in Figure 3.6. According to the predominant shape of an obstacle it can for example be

approximated by a circular or by a rectangular geometry. The safety area is then created in such a way that obstacle and host-vehicle do not collide if a reference point on the planned trajectory of the host-vehicle does not penetrate the safety area. In doing so, only the distances of points P_i, $i = 0, \ldots, N$, on the planned trajectory to the boundary of the safety area $\partial\mathcal{O}_j$ have to be checked in order to detect collisions. The point $\hat{\mathcal{O}}_j$ denotes the point on the border of the safety area $\partial\mathcal{O}_j$ with minimal distance to a point P_i. In contrary to this modified *growing procedure* that marks *non-valid areas* of the traffic space QUINLAN AND KHATIB (1993, [87]) used a so-called *bubble concept*, where bubbles indicated *obstacle-free areas*.

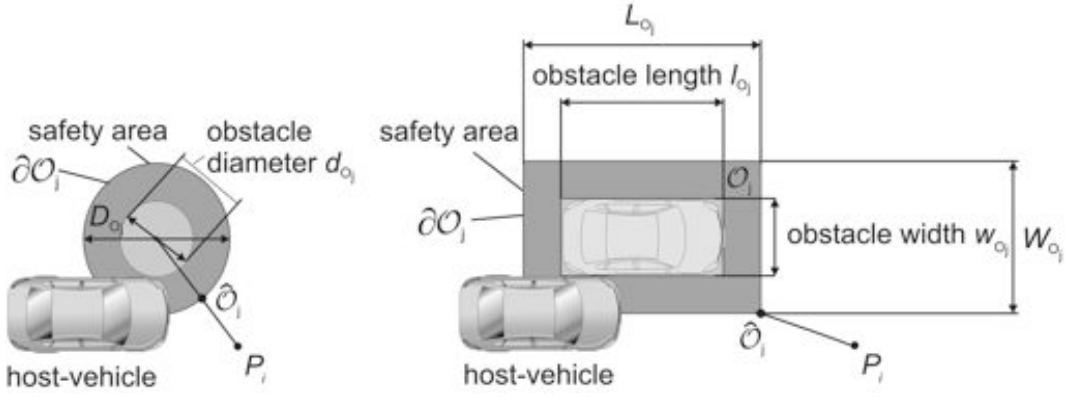

Figure 3.6: Obstacle geometry and according safety area

The orientation of the obstacle is reflected by the orientation of the obstacle-fixed reference frame $\underline{O_j}$ with respect to the road-fixed reference frame $\underline{R}$. The rotational transformation between the two reference frames is given by

$$\left[{}_{O_j}\mathbf{e}_x \, , \, {}_{O_j}\mathbf{e}_y \, , \, {}_{O_j}\mathbf{e}_z \right]^{\mathrm{T}} = \mathbf{C}^{O_j,R} \left[{}_{R}\mathbf{e}_x \, , \, {}_{R}\mathbf{e}_y \, , \, {}_{R}\mathbf{e}_z \right]^{\mathrm{T}} \tag{3.17}$$

with

$$\mathbf{C}^{O_j,R} = \begin{bmatrix} \cos {}^{R}\psi^{O_j} & \sin {}^{R}\psi^{O_j} & 0 \\ -\sin {}^{R}\psi^{O_j} & \cos {}^{R}\psi^{O_j} & 0 \\ 0 & 0 & 1 \end{bmatrix} . \tag{3.18}$$

For the motion planning, the future configuration of the obstacles $\mathbf{r}^{O_j^*}(t)\,, {}^{R}\psi^{O_j}(t)$ with $t \in \left[t_0, t_{\mathrm{f}}\right]$ and $j = 1, \ldots, M$ is extrapolated based on the initial data given in the listing above. Assuming that the side slip angle of the obstacle along its future path is small, $\beta^{O_j} \approx 0$, the orientation of the unit vectors ${}_{O_j}\mathbf{e}_x\,(t)$ and ${}_{O_j}\mathbf{e}_y\,(t)$ with respect to the predicted path is tangential and normal, respectively. In the extrapolation procedure two categories of obstacles are distinguished: either an obstacle is assumed to stay in its lane or it is assumed to depart from it. If the yaw angle ${}^{R}\psi^{O_j}(t_0)$ of an obstacle, depicted in Figure 3.7, at the instant of planning t_0 deviates only slightly from the orientation of the road tangent ${}^{R}\psi^{\bar{R}}({}_{R}x^{O_j^*})$,

$$|{}^{R}\psi^{O_j}(t_0) - k\pi - {}^{R}\psi^{\bar{R}}({}_{R}x^{O_j^*}\,(t_0))\,| < \epsilon \qquad \text{with} \qquad {}^{R}\psi^{\bar{R}} = \arctan\left(\frac{{}_{R}y^{\bar{R}^*}({}_{R}x^{O_j^*}\,(t_0))}{{}_{R}x^{O_j^*}\,(t_0)} \right) , \tag{3.19}$$

the obstacle is assumed to stay in its lane, where $k = 1$ denotes oncoming traffic and $k = 0$ indicates obstacles moving in the same direction as the host-vehicle $\mathcal{V}$.

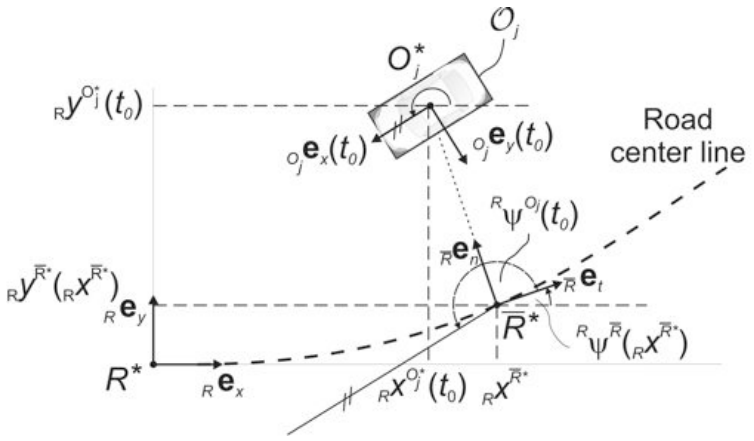

Figure 3.7: Obstacle orientation with respect to the road

In the other case, the motion of the obstacle is extrapolated based on the measured state at the planning time t_0. Both motion pattern of obstacles are principally sketched in Figure 3.8. MILDNER (2004, [73]) gives a range of $10° \ldots 20°$ for the threshold ϵ indicating lane departure intention based on empirical data. More detailed models of driver's lane change behavior are provided by EHMANNS (2003, [31]).

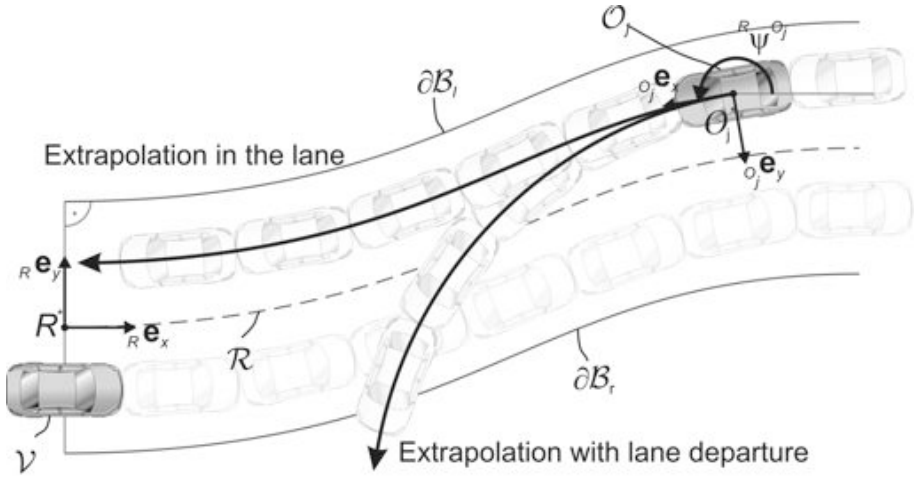

Figure 3.8: Obstacle extrapolation in lane and with lane departure

Extrapolation In Lane

The motion $\mathbf{r}^{O_j^*}(t)$ of an obstacle staying in its lane is derived now. At the instant of planning t_0 the measured obstacle position is given by

$$\mathbf{r}^{O_j^*}(t_0) = {}_R x^{O_j^*}(t_0)\, {}_R\mathbf{e}_x + {}_R y^{O_j^*}(t_0)\, {}_R\mathbf{e}_y \ . \tag{3.20}$$

Assuming small curvatures, ${}_R x^{O_j^*}(t_0) \approx {}_R x^{\bar{R}^*}$ holds, compare to Figure 3.8. With the road centerline $\mathcal{R}$ as given in Equation (3.11), this results in the position of the obstacle

along its future path

$$\mathbf{r}^{O_j^*}({}_R x^{O_j^*}) = \mathbf{r}^{\bar{R}^*}({}_R x^{O_j^*}) + \Big[{}_R y^{O_j^*}(t_0) - {}_R y^{\bar{R}^*}\big({}_R x^{O_j^*}(t_0)\big) \Big] \; {}_{\bar{R}}\mathbf{e}_n({}_R x^{O_j^*}) \; , \tag{3.21}$$

based on the initial obstacle coordinates $({}_R x^{O_j^*}(t_0),\ {}_R y^{O_j^*}(t_0))$, obtained from the sensor data. The corresponding yaw angle is given by

$${}^R\psi^{O_j}({}_R x^{O_j^*}) = {}^R\psi^{\bar{R}}({}_R x^{O_j^*}) + k\pi \; . \tag{3.22}$$

Next, the time dependent path extrapolation ${}_R x^{O_j^*}(t)$ has to be determined. The arc length $s^{O_j^*}({}_R x^{O_j^*})$ covered by an obstacle follows from integration of Equation (3.21) with respect to ${}_R x^{O_j^*}$

$$s^{O_j^*}({}_R x^{O_j^*}) = \operatorname{sgn}\Big({}^R\mathbf{v}^{O_j^*}(t_0) \cdot {}_{\bar{R}}\mathbf{e}_t({}_R x^{O_j^*})\Big) \cdot \int\limits_{{}_R x^{O_j^*}(t_0)}^{{}_R x^{O_j^*}} \| \, (\mathbf{r}^{O_j^*})'(\xi) \, \| \, \mathrm{d}\xi \; . \tag{3.23}$$

The integral in Equation (3.23) can for example be solved by truncating a Taylor series expansion. Defining the initial conditions at the planning instant,

$$v^{O_j^*}(t_0) :=^R \mathbf{v}^{O_j^*}(t_0) \cdot {}_{\bar{R}}\mathbf{e}_t({}_R x^{O_j^*}) \quad \text{and} \qquad a^{O_j^*}(t_0) :=^R \mathbf{a}^{O_j^*}(t_0) \cdot {}_{\bar{R}}\mathbf{e}_t({}_R x^{O_j^*}) \; , \tag{3.24}$$

and integrating them with respect to time yields the arc length

$$s^{O_j^*}(t) = \frac{1}{2} a^{O_j^*}(t_0)\, t^2 + v^{O_j^*}(t_0)\, t \; . \tag{3.25}$$

The values of the arc length given in equations (3.23) and (3.25) must be equal

$$s^{O_j^*}(t) - s^{O_j^*}({}_R x^{O_j^*}) = 0 \; , \tag{3.26}$$

thus, the relation ${}_R x^{O_j^*}(t)$ is found implicitly. To any time instant t, the corresponding position of the obstacle ${}_R x^{O_j^*}$ can be computed by solving the algebraic Equation (3.26). However, with the small curvature assumption, $x^{O_j^*}(t) \approx s^{O_j^*}(t) + x^{O_j^*}(t_0)$, the time depending position of an obstacle in its lane can be determined by plugging Equation (3.25) into Equation (3.21).

Extrapolation With Lane Departure

If the relative angle between the orientation of the obstacle and the road, given in Equation (3.19), exceeds the threshold ϵ, the obstacle is considered to intend lane departure. Then, the motion of the obstacle is extrapolated by integrating from the states sensed at t_0 with respect to time

$$\mathbf{r}^{O_j^*(t_0),\, O_j^*(t)} = \frac{1}{2} {}^R\mathbf{a}^{O_j^*}(t_0)\, t^2 + {}^R\mathbf{v}^{O_j^*}(t_0)\, t \; . \tag{3.27}$$

The orientation of the obstacle follows according to Figure 3.3 from

$$\cos\left({}^{R}\psi^{O_j}(t)\right) = {}_{O_j}\mathbf{e}_t\,(t)\cdot {}_{R}\mathbf{e}_x \qquad \text{with} \qquad {}_{O_j}\mathbf{e}_t = \frac{\frac{{}^{R}\mathrm{d}}{\mathrm{d}t}\mathbf{r}^{O_j^*(t_0),O_j^*(t)}(t)}{\left|\,\frac{{}^{R}\mathrm{d}}{\mathrm{d}t}\mathbf{r}^{O_j^*(t_0),O_j^*(t)}(t)\,\right|}\,. \tag{3.28}$$

Obstacle Potential Field

The contribution of the obstacles to the hazard map can, analogous to the borders of the road, be modeled as logarithmically decaying potential

$${}_{R}V_i^{O_j^*} := {}_{R}V^{O_j^*}\left(\mathbf{r}_i, \mathbf{r}_i^{\hat{O}_j}\right) = -k^{O_j}\ln\left(\left\|\mathbf{r}_i - \mathbf{r}_i^{\hat{O}_j}\right\|\right)\,. \tag{3.29}$$

Therein, P_i described by its position vector $\mathbf{r}_i$ represents a node of the elastic band being passed by the host-vehicle at t_i. As depicted in Figure 3.6 the position vector $\mathbf{r}_i^{\hat{O}_j}$ marks the point $\hat{O}_j$ on the boundary of the obstacles safety-area $\partial\mathcal{O}_j$ having the shortest distance to P_i,

$$\begin{aligned}\mathbf{r}_i^{\hat{O}_j} &:= \mathbf{r}^{\hat{O}_j}(t_i) = \left\{\mathbf{r}^{Q}(t_i)\in\partial\mathcal{O}_j \mid \|\mathbf{r}_i - \mathbf{r}^{Q}(t_i)\| = \min_{Q\in\partial\mathcal{O}_j}\|\mathbf{r}_i - \mathbf{r}^{Q}(t_i)\|\right\} \\ &\text{with}\quad \mathbf{r}^{Q}(t_i) = \mathbf{r}^{O_j^*}(t_i) + \mathbf{r}^{O_j^*,Q}(t_i) \quad \text{and} \quad t_i\in[t_0,t_\mathrm{f}]\,,\quad i=0,\ldots,N\,,\end{aligned} \tag{3.30}$$

where $\mathbf{r}^{O_j^*,Q}(t_i)$ follows from Equation (3.27). Recall that the evaluation of the potential field of the obstacle at P_i relies on enlarged dimensions of the obstacle including the dimensions of the host-vehicle, as illustrated in Figure 3.6. This growing method simplifies the necessary distance computations. For circular obstacles the point $\hat{O}_j$ lies on the connecting line of O_j^* and P_i, see Figure 3.6. For rectangular obstacles a case differentiation given in Section 3.4.1 is applied.

3.1.3 Hazard Map Composition

Finally, the hazard map is composed of the hazard potentials given by the borders $\mathcal{B}_l$ and $\mathcal{B}_r$ of the road and by the M obstacles $\mathcal{O}_j$. Hence, the hazard potential experienced at a node P_i of the elastic band with position vector $\mathbf{r}_i$ reads

$$\begin{aligned}{}_{R}V_i^{\mathrm{haz}} &:= {}_{R}V^{\mathrm{haz}}\left(\mathbf{r}_i, \mathbf{r}_i^{B_\mathrm{l}}, \mathbf{r}_i^{B_\mathrm{r}}, \mathbf{r}_i^{O_1}, \ldots, \mathbf{r}_i^{O_M}\right) \\ &= {}_{R}V^{B_\mathrm{l}}\left(\mathbf{r}_i, \mathbf{r}_i^{B_\mathrm{l}}\right) + {}_{R}V^{B_\mathrm{r}}\left(\mathbf{r}_i, \mathbf{r}_i^{B_\mathrm{r}}\right) + \sum_{j=1}^{M} {}_{R}V^{O_j}\left(\mathbf{r}_i, \mathbf{r}_i^{\hat{O}_j}\right).\end{aligned} \tag{3.31}$$

It is important to note, that in the composition of the hazard map the motion of obstacles and host-vehicle is spatially and temporally coupled by the nodes of the elastic band sensing the hazard potential. This coupling is illustrated in Figure 3.9.

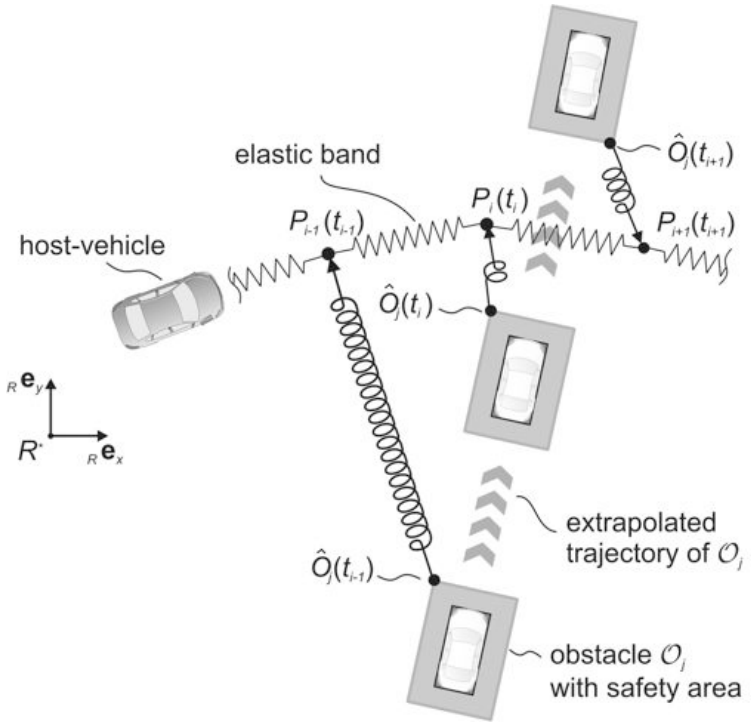

Figure 3.9: Spatial and temporal composition of the hazard map

The nodes P_{i-1}, P_i, and P_{i+1} of the elastic band are depicted in a deformed configuration. To each of these nodes the corresponding instants of time t_{i-1}, t_i, and t_{i+1} are assigned at which the host-vehicle passes the corresponding node: $P_{i-1} \leftrightarrow t_{i-1}, P_i \leftrightarrow t_i$, and $P_{i+1} \leftrightarrow t_{i+1}$. The instants of passing the nodes of the elastic band depend on the velocity profile of the host-vehicle intended by the driver. The computation of these instants is addressed in Section 3.3.2 by Equation (3.51).

At the same time, the extrapolated motion of obstacle $\mathcal{O}_j$ is discretized according to the instants when the host-vehicle passes the nodes of the elastic band: $\mathbf{r}^{\hat{O}_j}(t_{i-1}), \mathbf{r}^{\hat{O}_j}(t_i)$, and $\mathbf{r}^{\hat{O}_j}(t_{i+1})$. Then, the repulsive continuously differentiable potential field of obstacle $\mathcal{O}_j$, $j = 1, \ldots, M$, is evaluated at the position $\mathbf{r}_i$ of the node P_i and therein depends on the position of the obstacle $\mathbf{r}^{\hat{O}_j}(t)$,

$$V_i^{O_j}\left(\mathbf{r}_i, \mathbf{r}^{\hat{O}_j}(t)\right) \qquad \forall t \in [t_0, t_f] \ , \qquad i = 0, \ldots, N \ . \tag{3.32}$$

The idea of incorporating moving obstacles in the motion planning approach is now that the potential field of the obstacle $V_i^{O_j}$ should only act on those nodes of the elastic band, which correspond to the same instant of time

$$V_i^{O_j}\left(\mathbf{r}_i, \mathbf{r}^{\hat{O}_j}(t_i)\right) \ . \tag{3.33}$$

This particular coupling of obstacle motion and the trajectory of the host-vehicle by repulsive potential fields is visualized by means of springs connecting the nodes of the elastic band with the according positions of the obstacle, $P_{i-1} \leftrightarrow \hat{Q}_j(t_{i-1})$, $P_i \leftrightarrow \hat{Q}_j(t_i)$, $P_{i+1} \leftrightarrow \hat{Q}_j(t_{i+1})$, in Figure 3.9.

3.2 Elastic Band

The predictive search for trajectories of low hazard levels within the hazard map is performed by an elastic band as shown in Figure 3.10.

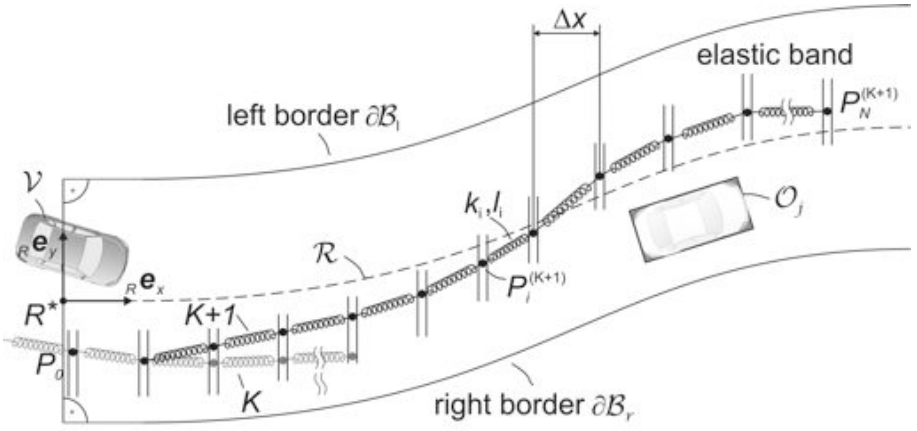

Figure 3.10: Elastic band K and consecutive elastic band *K+1*, see also Section 3.2.2

To obtain solutions of inherent low curvature the nodes P_i with $i = 0, \ldots, N$ of the elastic band are coupled by internal potentials, symbolized by springs. Assuming these springs to be linear, each node is immersed in a quadratic internal potential field,

$$\begin{aligned} &{}_R V_i^{\text{int}}(\mathbf{r}_{i-1}, \mathbf{r}_i, \mathbf{r}_{i+1}) = \tfrac{1}{2} k_{i-1} \left(\|\mathbf{r}_i - \mathbf{r}_{i-1}\| - l_{i-1} \right)^2 + \tfrac{1}{2} k_i \left(\|\mathbf{r}_{i+1} - \mathbf{r}_i\| - l_i \right)^2 \ , \\ &\text{with} \qquad i = 1, \ldots, N-1 \ . \end{aligned} \tag{3.34}$$

Therein, k_i and l_i are the stiffness parameter and the unstretched length of spring i, respectively. For simplicity, k_i and l_i are chosen to be constant for the entire elastic band. As shown in Figure 3.10 the elastic band is adapted on each planning horizon ΔT when new environmental information is available, $K \rightarrow K+1$. Furthermore, it is a suitable option in automotive applications to consider only the lateral displacement of the nodes of the elastic band, which accelerates the computation, see Section 3.4.3. In this case the distances Δx between the nodes P_i, $i = 0, \ldots, N$, along the road are prescribed, see Figure 3.10.

3.2.1 Equilibrium Configuration

To derive the potential field forces acting on each node P_i of the elastic band, the directional derivatives

$${}_R\nabla_{\mathbf{r}_i} := \left(\frac{\partial}{\partial_R x_i}, \frac{\partial}{\partial_R y_i} \right)^{\mathrm{T}} \ , \tag{3.35}$$

are defined. Then, the hazard and the internal potential field forces acting on P_i follow from

$$\mathbf{F}_i^{\text{haz}} := -{}_R\nabla_{\mathbf{r}_i} \left({}_R V_i^{\text{haz}} \right) \quad \text{and} \quad \mathbf{F}_i^{\text{int}} := -{}_R\nabla_{\mathbf{r}_i} \left({}_R V_i^{\text{int}} \right) \ , \tag{3.36}$$

with ${}_R V_i^{\text{haz}}$ and ${}_R V_i^{\text{int}}$ being the hazard and the internal potential fields defined according to Equation (3.31) and Equation (3.34), respectively. The hazard forces $\mathbf{F}_i^{\text{haz}}$ represent the environmental information contained in the hazard map and are evaluated as described in Section 3.1.3 by discretizing the estimated motion of the obstacles depending on the discretization of the elastic band. The internal forces $\mathbf{F}_i^{\text{int}}$ couple the displacements of the nodes P_i to enforce trajectories with inherently low curvatures. Additionally, also constraint forces $\mathbf{F}_i^{\text{c}}$ can be introduced, allowing only lateral displacements. In the equilibrium configuration the sum of internal, hazard, and (if applied) constraint forces on all nodes of the elastic band vanishes. The corresponding free body diagram is shown in Figure 3.11.

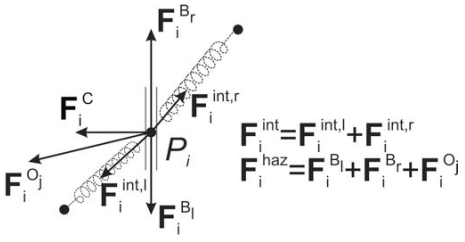

Figure 3.11: Free body diagram of node P_i

The trajectory is obtained by solving the equilibrium condition[1]

$$\begin{aligned} &\mathbf{F}_i^{\text{int}}\big(\mathbf{r}_{i-1}, \mathbf{r}_i, \mathbf{r}_{i+1}\big) + \mathbf{F}_i^{\text{haz}}\big(\mathbf{r}_i, \mathbf{r}_i^{B_l}, \mathbf{r}_i^{B_r}, \mathbf{r}_i^{\hat{O}_1}, \ldots, \mathbf{r}_i^{\hat{O}_M}\big) \\ &\quad + \quad \Big(\mathbf{F}_i^{\text{c}}\big(\mathbf{r}_i, \mathbf{r}_i^{B_l}, \mathbf{r}_i^{B_r}, \mathbf{r}_i^{\hat{O}_1}, \ldots, \mathbf{r}_i^{\hat{O}_M}\big)\Big) \quad = \quad \mathbf{0} \end{aligned} \tag{3.37}$$

for the position vectors $\mathbf{r}_i$ with $i = 0, \ldots, N$ of the elastic band as proposed by BRANDT, SATTEL AND WALLASCHEK (2004, [8] and 2006, [10]). Since Equation (3.37) is nonlinear, the position vectors are obtained numerically, which is discussed in Section 3.4. The presented elastic band approach belongs to the so-called *local methods*. Hence, if more than one solution exist, the trajectory depends on the initial solution provided to the numerical algorithm. In other words: if the initial solution passes an obstacle $\mathcal{O}_j$ to the right, the final trajectory will also pass $\mathcal{O}_j$ on the right hand side. In general, a maximum of 2^M possible local solutions exists for M obstacles. Thus, the computation of all possible solutions especially in presence of many obstacles is too time consuming. Here, the initial solution is generated in cooperation with the driver and is addressed in Section 3.4.2.

Compared to the work of QUINLAN (1993, [87]), who shifted only some nodes of the elastic band affected by an obstacle, there are different advantages of searching the equilibrium configuration in the hazard map: if the environment changes only slightly, compared to the last measurement, this will result in an equilibrium of the elastic band, which is close to the last solution. A further crucial advantage is that the equilibrium configuration very naturally provides collision-free trajectories, even for large numbers of obstacles $\mathcal{O}_j$, $j = 1, \ldots, M$; geometric methods for example are often restricted to just one obstacle,

[1] As explained later, the equilibrium condition is not evaluated for fixed nodes and only unconstraint directions of movement are considered. The constraint forces in Equation (3.37) are only introduced here for the sake of completeness.

which is not suitable for automotive applications. Formulating the hazard potentials of the borders of the road and of the obstacles according to Equation (3.16) and Equation (3.29), respectively, the following proposition holds:

Proposition 3.1. *If a collision-free trajectory locally exists and if the elastic band is in an equilibrium configuration,* $\boldsymbol{F}_i^{\text{int}} + \boldsymbol{F}_i^{\text{haz}} = \mathbf{0}$*, then no node* P_i*,* $i = 0, \ldots, N$*, of the elastic band lies within the safety area of an obstacle* $\mathcal{O}_j$*,* $j = 1, \ldots, M$*, while the node is being passed by the host-vehicle* $\mathcal{V}$ *at time* t_i*. Therefore, each equilibrium configuration of the elastic band in presence of* M *moving obstacles is collision-free.*

Proof. Taking the directional derivatives ${}_R\nabla_{\mathbf{r}_i}$, see (3.35), of the potential fields of the borders of the road ${}_RV_i^{B_q}$ and of the obstacles ${}_RV_i^{O_j^*}$, $j = 1, \ldots, M$, according to Equation (3.16) and Equation (3.29), respectively, yields potential field forces $\mathbf{F}^{B_q}$ and $\mathbf{F}^{O_j}$ being proportional to the reciprocal distance of a node P_i, $i = 0, \ldots, N$, to the closest point on the borders $\partial\mathcal{B}^q$ or on the boundaries $\partial\mathcal{O}_j$ at the instant t_i when the host-vehicle $\mathcal{V}$ passes P_i,

$$\mathbf{F}^{B_q} \sim \left\| \mathbf{r}_i - \mathbf{r}_i^{B_q} \right\|^{-1} \qquad \text{and} \qquad \mathbf{F}^{O_j} \sim \left\| \mathbf{r}_i - \mathbf{r}_i^{\hat{O}_j} \right\|^{-1} , \tag{3.38}$$

Therefore, the repulsive forces acting on a node P_i that approaches the borders of the road $\partial\mathcal{B}_q$ or the boundary of a safety area $\partial\mathcal{O}_j$ of an obstacle grow infinitely,

$$\mathbf{F}^{B_q} \xrightarrow{\left\| \mathbf{r}_i - \mathbf{r}_i^{B_q} \right\| \to 0} \infty \quad \text{and} \quad \mathbf{F}^{O_j} \xrightarrow{\left\| \mathbf{r}_i - \mathbf{r}_i^{\hat{O}_j} \right\| \to 0} \infty . \tag{3.39}$$

To be in equilibrium, $\mathbf{F}_i^{\text{int}} + \mathbf{F}_i^{\text{haz}} = \mathbf{0}$, the potential field forces due to the borders of the road $\mathbf{F}^{B_q}$ and due to obstacles $\mathbf{F}^{O_j}$ have to be balanced. As the potential field forces, acting on a node P_i, are, according to Equation (3.39), infinitly high if $\mathbf{r}_i \in \partial\mathcal{B}_q \vee \mathbf{r}_i \in \partial\mathcal{O}_j$, they can only be balanced if P_i is located on at least two boundaries $\mathbf{r}_i \in \partial\mathcal{O}_j \wedge \mathbf{r}_i \in \partial\mathcal{O}_{\bar{j}}$ with $j \neq \bar{j}$. This in turn means that locally no collision-free solution exists, see Figure 3.12. Otherwise, no node P_i of the elastic band can be located on the boundaries $\partial\mathcal{B}_q$ or $\partial\mathcal{O}_j$ if the elastic band is in an equilibrium configuration. □

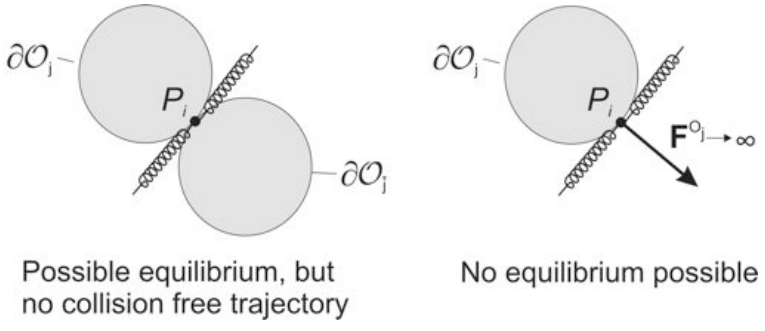

Figure 3.12: Left: P_i on the boundary of *two* obstacles $\mathcal{O}_j$ and $\mathcal{O}_{\bar{j}}$, Right: P_i on the boundary of *one* obstacle $\mathcal{O}_j$

3.2.2 Node Placement

In order to prescribe the boundary slope of an elastic band or to place a single node P_i , e.g. the first or the last, at particular positions in the traffic space, position constraints, $\mathbf{r}_i \cdot {}_R\mathbf{e}_x = const.$, $\mathbf{r}_i \cdot {}_R\mathbf{e}_y = const.$, need to be satisfied. This is guaranteed by introducing constraint forces $\mathbf{F}_i^{\mathrm{c}}$ acting on the fixed nodes P_i, see Equation (3.37). The placement of the first node P_0 of the elastic band is of particular interest. In general, the vehicle, commonly guided by a guidance controller, see Chapter 4, and the driver, will not perfectly track the planned trajectory. Therefore, at each instant of replanning t_0 the vehicle will show a lateral deviation Δy as well as an angular deviation $\Delta\psi$ to the previously planned trajectory as depicted in Figure 3.10. Based on this tracking error, the guidance controller and the driver set their control inputs such as the steering angle δ. Placing the first node of the elastic band P_0 at the current position of the vehicle would instantaneously cancel the tracking error. Thus, the vehicle guidance controller would be exposed to unintended discontinuities. To avoid this problem in the replanning process from an elastic band K at t_0 to an elastic band $K+1$ at $t_0 + \Delta T$, the first node of the new elastic band $P_0^{(\mathrm{K}+1)}$ is chosen depending on the last elastic band and on the current position of the vehicle ${}^R\mathbf{r}^{V^*}$ as illustrated in Figure 3.10,

$$\mathbf{r}_0^{(K+1)} = \mathbf{r}_i^{(K)} \quad \text{with} \quad {}_Rx_i = \min\{{}_Rx_i \in \mathcal{P} \big|\, {}_Rx_i \geq {}_Rx_i^{V*}\} \;, \quad i = 0, \ldots, N \;. \tag{3.40}$$

The first node of the previous elastic band, that lies in front of the vehicle, indicated by a higher ${}_R\mathbf{e}_x$-coordinate than the one of V^* is selected as the first node of the new elastic band.

3.2.3 Constraining Longitudinal Displacements

For lane-keeping, lane-changing, and evasion maneuvers the longitudinal displacements of the nodes are not essential. Beyond that, the efficiency of the numerical algorithm to find the equilibrium of the elastic band, see Equation (3.37), can be increased by considering only lateral displacements. The longitudinal position of a node P_i then only depends on the discretization parameter Δx of the elastic band, see Figure 3.10,

$$\mathbf{r}_i \cdot {}_R\mathbf{e}_x \;=\; const. = i \cdot \Delta x \;, \qquad i = 0, \ldots, N \;. \tag{3.41}$$

Multiplying the force equilibrium of Equation (3.37) by ${}_R\mathbf{e}_y$ and ignoring fixed nodes such as P_0, the constraint forces $\mathbf{F}_i^{\mathrm{c}}$ are eliminated, resulting in

$$F_{i,y}^{\mathrm{int}} + F_{i,y}^{\mathrm{haz}} \;=\; 0 \;, \qquad i = 1, \ldots, N \;. \tag{3.42}$$

3.3 Cooperative Motion Planning

This section describes the shaping of the elastic band in cooperation with the driver. For lateral guidance, the driver's *steering intention* defines the search direction for a collision-free trajectory in the hazard map, whereas the *maneuver strategy* influences the position of the last node of the elastic band. The longitudinal vehicle guidance remains fully

with the driver. However, the extrapolation of the vehicle's states based on the driver's longitudinal driving intent also influences the motion planning for lateral vehicle guidance.

3.3.1 Driver's Steering Intention

As aforementioned, the elastic band method is a local method. Thus, equilibrium configurations elsewhere than in the search direction, prescribed by the initial solution, are not necessarily found. In order to reflect the drivers command, the search direction is coupled on the steering angle $\delta(t_0)$ and on the orientation of the vehicle ${}^{R}\psi^{O_j}(t_0)$, as depicted in Figure 3.13. For this reason, the first n nodes, $n = 0, \ldots, N$, of the initial solution (not of the elastic band!) are fixed according to the anticipated motion of the vehicle for a fixed steering angle $\delta(t_0)$.

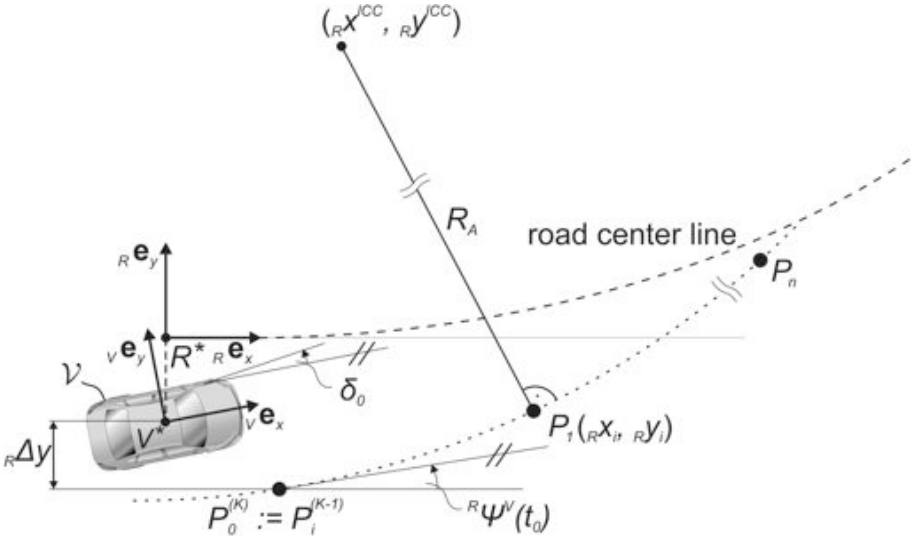

Figure 3.13: Defining the search direction by means of the Ackermann model

If for example the driver intends to pass an obstacle on the left hand side, then the motion planning should, if possible, generate a trajectory that passes the obstacle on the left. As only the rough direction of search is given by the initial solution, it is not necessary to extrapolate the motion of the vehicle very precisely. Therefore, the positions of the first n nodes of the initial solution lie on a circle determined by use of the Ackermann model, see Section 2.6.1. This is illustrated in Figure 3.13. With the steering angle δ_0 fixed at the instance of planning t_0 and the distance from front to rear axle, $a + b$, the radius of curvature according to the Ackermann model becomes

$$R_A \;=\; \frac{a+b}{\tan\delta_0}\,. \tag{3.43}$$

With the yaw angle ${}^{R}\psi^{O_j}(t_0)$ the coordinates of the instantaneous center of curvature ICC expressed in the road-fixed reference frame $\underline{R}$ read

$$\begin{pmatrix} {}_R x^{ICC} \\ {}_R y^{ICC} \end{pmatrix} \;=\; \begin{pmatrix} -R_A \sin\,{}^{R}\psi^{O_j}(t_0) \\ R_A \cos\,{}^{R}\psi^{O_j}(t_0) \end{pmatrix} + \,{}_{\cdot}\mathbf{r}^{V^*}\,. \tag{3.44}$$

Depending on the algebraic sign of $\delta(t_0)$ and ${}^{R}\psi^{O_j}(t_0)$ different cases have to be distinguished. In Figure 3.13, the situation is depicted for $\delta(t_0) > 0$ and ${}^{R}\psi^{O_j}(t_0) > 0$. For a prescribed ${}_{R}\mathbf{e}_x$-position of a node P_i, as it is illustrated in Figure 3.10, the ${}_{R}\mathbf{e}_y$-component on the circular arc follows from

$$ {}_{R}y_i \;=\; \begin{cases} \tan {}^{R}\psi^{O_j}(t_0) \cdot {}_{R}x_i, & \delta = 0 \\ {}_{R}y^{ICC} - \operatorname{sign}(\delta) \cdot \sqrt{R_A^2 - ({}_{R}x^{ICC} - {}_{R}x_i)^2}, & \delta \neq 0 \end{cases} \tag{3.45} $$

with ${}_{R}x_i = i \cdot \Delta x$. The procedure to determine the positions of the remaining nodes P_i, $i = n+1, \ldots, N$, of the initial solution is independent of the driver and is given in Section 3.4.2.

3.3.2 Vehicle State Extrapolation

The equilibrium of the elastic band, Equation (3.37) or Equation (3.42), and therefore the configuration level of the planned trajectory depends on the planned velocity profile of the host-vehicle $\mathcal{V}$. The velocity profile in turn depends on the driver who controls throttle and braking pedal. For the motion planning procedure the velocity profile is gained by extrapolation assuming constant longitudinal acceleration,

$$ {}^{R}a^{V^*} \;:=\; {}^{R}\mathbf{a}^{V^*}(t_0) \cdot {}_{V}\mathbf{e}_x \;=\; const. \tag{3.46} $$

with ${}^{R}a^{V^*}$ being positive for accelerating and being negative for braking. The extrapolation starts at $t_0 = 0$ with $s(t_0) = 0$. Therefore, the speed and the covered path length at node P_i become

$$ U_t(t_i) \approx U_x(t_i) \;:=\; {}^{R}a^{V^*}\, t_i + {}^{R}\mathbf{v}^{V^*}(t_0) \cdot {}_{V}\mathbf{e}_x \quad \text{and} \tag{3.47} $$

$$ s_i \;:=\; s(t_i) = \frac{{}^{R}a^{V^*}}{2} t_i^2 + {}^{R}\mathbf{v}^{V^*}(t_0) \cdot {}_{V}\mathbf{e}_x \; t_i \; . \tag{3.48} $$

The positions of the obstacles $\mathbf{r}_i^{O^*}$ are evaluated at time t_i when the host-vehicle passes node P_i, see Figure 3.9. The host-vehicle's speed at the instant of planning ${}^{R}\mathbf{v}^{V^*}(t_0)$ and the acceleration ${}^{R}\mathbf{a}^{V^*}(t_0)$ set by the driver are known. Since the equilibrium configuration of the elastic band is determined iteratively, see Section 3.4.3, the position vectors of the previous iteration step $\mathbf{r}_i^{(k)}$ are also known. Hence, the covered path length s_i, traveled by the host-vehicle until passing node P_i at time t_i, is prescribed and can be estimated by

$$ s_i^{(k+1)} = \sum_{j=1}^{i} \| \mathbf{r}_j^{(k)} - \mathbf{r}_{j-1}^{(k)} \| \tag{3.49} $$

with k denoting the iteration step. Solving Equation (3.47) for t_i and inserting the result into Equation (3.48) yields with Equation (3.49) the instant of passing node P_i

$$t_i = \begin{cases} \frac{s_i}{U_t(t_0)}, & {}^{R}a^{V^*} = 0 \\ -\frac{U_t(t_0)}{{}^{R}a^{V^*}} - \sqrt{\left(\frac{U_t(t_0)}{{}^{R}a^{V^*}}\right)^2 + \frac{2}{{}^{R}a^{V^*}}(s_i - s_1)}, & {}^{R}a^{V^*} < 0 \\ -\frac{U_t(t_0)}{{}^{R}a^{V^*}} + \sqrt{\left(\frac{U_t(t_0)}{{}^{R}a^{V^*}}\right)^2 + \frac{2}{{}^{R}a^{V^*}}(s_i - s_1)}, & {}^{R}a^{V^*} > 0 \end{cases} . \tag{3.50}$$

Note that, from an algorithmic point of view, the computation is accelerated by computing the instants t_i in ascending order, which results in

$$t_i = t_{i-1} + \begin{cases} \frac{s_{i,i-1}}{U_t(t_{i-1})}, & {}^{R}a^{V^*} = 0 \\ -\frac{U_t(t_{i-1})}{{}^{R}a^{V^*}} - \sqrt{\left(\frac{U_t(t_{i-1})}{{}^{R}a^{V^*}}\right)^2 + \frac{2}{{}^{R}a^{V^*}}s_{i,i-1}}, & {}^{R}a^{V^*} < 0 \\ -\frac{U_t(t_{i-1})}{{}^{R}a^{V^*}} + \sqrt{\left(\frac{U_t(t_{i-1})}{{}^{R}a^{V^*}}\right)^2 + \frac{2}{{}^{R}a^{V^*}}s_{i,i-1}}, & {}^{R}a^{V^*} > 0 \end{cases} \tag{3.51}$$

with $s_{i,i-1} = s_i - s_{i-1}$ and $U_t(t_{i-1}) = {}^{R}a^{V^*} \cdot (t_{i-1} - t_0) + U_t(t_0)$, see also SATTEL AND BRANDT (2006, [96]).

3.3.3 Driver's Maneuver Strategy

Principally, each node P_i of the elastic band can be placed in a particular position in the traffic space. Decisions on the node placement have to be taken by a higher planning instance. However, the last node P_N is of particular interest. It can for example be placed on the center of the right lane or on the center of a neighboring lane if the driver commands to change lanes by setting the indicator. Formally, assigning a position to the last node reads $\mathbf{r}_N := \mathbf{r}_{\text{des}}$, where $\mathbf{r}_N$ is then excluded from the equilibrium search, see Equation (3.37). If *vehicle following* is intended, the last node P_N of the elastic band can be placed on the leading vehicle. The path driven by the leading vehicle could serve as initial solution to the elastic band in that case.

3.4 Algorithm and Computation

In the last sections the general procedure of path planning based on elastic bands was outlined. Now, some algorithmic aspects of distance computations, finding an initial solution and zero finding in order to solve for the equilibrium configuration of the elastic band, see Equation (3.37), are addressed. Subsequently, the numerical procedure is summarized as pseudo-code.

3.4.1 Distance Computation

The external forces, Equation (3.36), are derived from the hazard map, Equation (3.31). To evaluate the external forces at node P_i, the corresponding position vectors to the borders of the road $\mathbf{r}_i^{B_r}$, $\mathbf{r}_i^{B_l}$ and to the obstacles $\mathbf{r}_i^{\hat{O}_j}$ have to be determined.

Distance to Borders of the Road

A necessary condition for the minimum distance, defined in Equation (3.14), is

$$\frac{\mathrm{d}\|\mathbf{r}_i - \mathbf{r}^{B_q}({}_R x)\|^2}{\mathrm{d}\,{}_R x} = 0 \quad \Rightarrow \quad \Big[{}_R x_i - {}_R x\Big] + \Big[{}_R y_i - {}_R y^{B_q}({}_R x)\Big]\,{}_R y^{B_q\,\prime}({}_R x) = 0 \tag{3.52}$$

with $\mathbf{r}^{B_q}$ being the position vector of points on the border $\mathcal{B}_q$ of the road, see Equation (3.13). Solving Equation (3.52) results in ${}_R x = {}_R x^{\hat{B}_q}$ with $q \in \{l, r\}$.

Distance to Obstacles

As the distance computation to circular obstacles is straight forward, the remaining problem lies in the distance computation between a point P_i of the elastic band and the boundary $\partial\mathcal{O}_j$ of a rectangular obstacle $\mathcal{O}_j$, as shown in Figure 3.6. Therefore, the position vector ${}_R\mathbf{r}_i^{\hat{O}_j}$, see Equation (3.30), of the point $\hat{O}_j$ on the border $\partial\mathcal{O}_j$, having minimal distance to P_i, has to be determined. This computation is facilitated by using the obstacle-fixed reference frame $\underline{\uparrow O_j}$. In order to do so, the position vector of P_i is transformed

$${}_{O_j}\mathbf{r}^{O_j^*,P_i} = \mathbf{C}^{O_j,R}\left({}_R\mathbf{r}_i - {}_R\mathbf{r}^{O_j^*}\right) \quad \text{with} \quad \mathbf{C}^{O_j,R} = \begin{bmatrix} \cos{}^R\psi^{O_j} & \sin{}^R\psi^{O_j} & 0 \\ -\sin{}^R\psi^{O_j} & \cos{}^R\psi^{O_j} & 0 \\ 0 & 0 & 1 \end{bmatrix}. \tag{3.53}$$

As illustrated in Figure 3.14, the surrounding space of a rectangular obstacle can be divided into the four quadrants of the obstacle-fixed reference frame $\underline{\uparrow O_j}$.

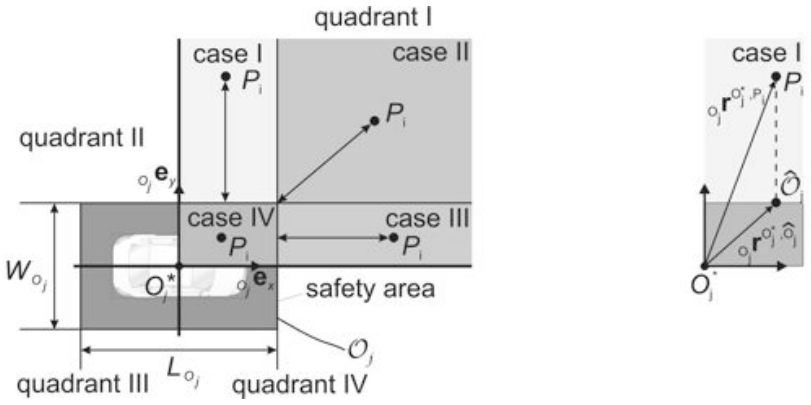

Figure 3.14: Computation of distance to obstacle $\mathcal{O}_j$

In each quadrant again four cases have to be distinguished for the distance computations. In the following, these cases are discussed for the first quadrant; the determination of $\hat{O}_j$ in the remaining quadrants works analogously only differing in the algebraic signs.

Case I:
P_i lies besides $\mathcal{O}_j$ with $\left(0 \leq {}_{O_j}\mathbf{r}^{O_j^*,P_i} \cdot {}_{O_j}\mathbf{e}_x \leq \frac{L_{O_j}}{2}\right) \wedge \left({}_{O_j}\mathbf{r}^{O_j^*,P_i} \cdot {}_{O_j}\mathbf{e}_y \geq \frac{W_{O_j}}{2}\right)$, then
${}_{O_j}\mathbf{r}^{O_j^*,\hat{O}_j}(t_i) = {}_{O_j}x_i \; {}_{O_j}\mathbf{e}_x + \frac{W_{O_j}}{2}\text{sign}({}_{O_j}y_i) \, {}_{O_j}\mathbf{e}_y$.

Case II:
P_i lies closest to a corner of $\mathcal{O}_j$ with $\left({}_{O_j}\mathbf{r}^{O_j^*,P_i} \cdot {}_{O_j}\mathbf{e}_x \geq \frac{L_{O_j}}{2}\right) \wedge \left({}_{O_j}\mathbf{r}^{O_j^*,P_i} \cdot {}_{O_j}\mathbf{e}_y \geq \frac{W_{O_j}}{2}\right)$, then
${}_{O_j}\mathbf{r}^{O_j^*,\hat{O}_j}(t_i) = \frac{L_{O_j}}{2}\text{sign}({}_{O_j}x_i) \, {}_{O_j}\mathbf{e}_x + \frac{W_{O_j}}{2}\text{sign}({}_{O_j}y_i) \, {}_{O_j}\mathbf{e}_y$.

Case III:
P_i lies in front of $\mathcal{O}_j$ with $\left({}_{O_j}\mathbf{r}^{O_j^*,P_i} \cdot {}_{O_j}\mathbf{e}_x \geq \frac{L_{O_j}}{2}\right) \wedge \left({}_{O_j}\mathbf{r}^{O_j^*,P_i} \cdot {}_{O_j}\mathbf{e}_y \leq \frac{W_{O_j}}{2}\right)$, then
${}_{O_j}\mathbf{r}^{O_j^*,\hat{O}_j}(t_i) = \frac{L_{O_j}}{2}\text{sign}({}_{R}x_i) \, {}_{O_j}\mathbf{e}_x + {}_{R}\, y_i \, {}_{O_j}\mathbf{e}_y$.

Case IV:
P_i lies inside $\mathcal{O}_j$ if $\left(0 < {}_{O_j}\mathbf{r}^{O_j^*,P_i} \cdot {}_{R}\mathbf{e}_x < \frac{L_{O_j}}{2}\right) \wedge \left({}_{O_j}\mathbf{r}^{O_j^*,P_i} \cdot {}_{R}\mathbf{e}_y < \frac{W_{O_j}}{2}\right)$, then
no distance is computed.

Finally, the position vector ${}_{O_j}\mathbf{r}^{O_j^*,\hat{O}_j}(t_i)$ is transformed into the road-fixed reference frame $\underline{R}$,

$$ {}_{R}\mathbf{r}^{\hat{O}_j}(t_i) = {}_{R}\mathbf{r}^{O_j^*}(t_i) + \mathbf{C}^{R,O_j} \, {}_{O_j}\mathbf{r}^{O_j^*,\hat{O}_j}(t_i) \quad \text{with} \quad \mathbf{C}^{R,O_j} = (\mathbf{C}^{O_j,R})^{\mathrm{T}} \; . \tag{3.54} $$

3.4.2 Initial Solution

In general more than one trajectory of low hazard levels exist. Hence, the numerically determined equilibrium depends on the initial solution, which in turn may be chosen according to the application. For vehicle following it is suitable to consider the trajectory driven by the leading vehicle as initial solution. However, for individually guiding the host-vehicle, the initial solution has to be generated automatically at each replanning instant t_0. The procedure described in the following incorporates the hazard map as well as the lateral displacements to the preceding nodes of the elastic band. To find the initial solution, the road is discretized in ${}_{R}\mathbf{e}_x$- and in ${}_{R}\mathbf{e}_y$-direction. The equidistant discretization is

$$ \Delta x := \frac{L}{N} \; , \qquad \Delta y := \frac{b}{J} \; , \tag{3.55} $$

recalling L being the length of the elastic band, N the number of nodes, b the width of the road, and J the number of possible lateral positions. The grid of possible positions for the nodes in the initial solution is visualized in Figure 3.15.

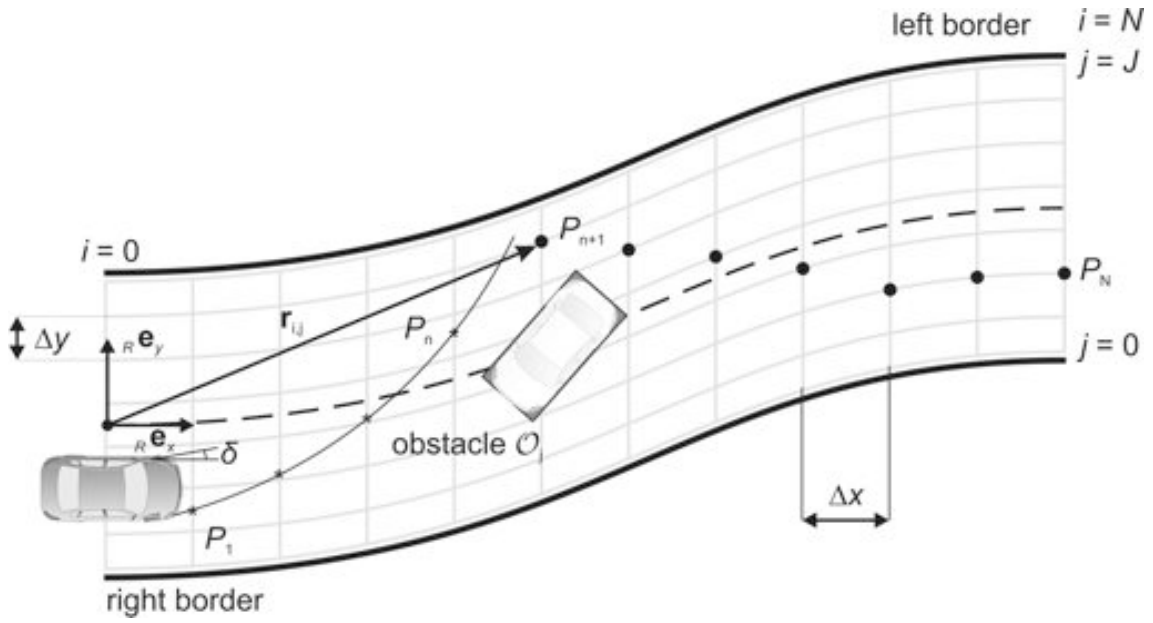

Figure 3.15: Grid structure of initial solution: * Nodes from Ackermann model, • nodes from initial solution

Be reminded that the first n nodes of the initial solution $P_0, \ldots, P_n$ are prescribed according to the Ackermann model, as explained in Section 3.3.1. The lateral positions of these nodes are not restricted to the grid points. In order to define an initial solution, the position vectors at the Kth replanning instant,

$$\tilde{\mathbf{r}}_i^{(K)} = i\,\Delta x\ {}_R\mathbf{e}_x + \left(j_i^*\,\Delta y + {}_R y^{\bar{\mathrm{R}}^*}(i\,\Delta x) - \frac{b}{2}\right) {}_R\mathbf{e}_y\ , \qquad i = n+1, \ldots, N\ , \tag{3.56}$$

for the remaining nodes $P_{n+1}, \ldots, P_N$ have to be determined using the road definition given in Equation (3.11). Therefore, the row index, $j_i^* \in \{0, \ldots, J\}$, describing the lateral position of node P_i on the grid, has to be found. In order to do so, the hazard potential V^{haz}, including the borders of the road and the obstacles, is evaluated at the grid points

$$\mathbf{V}^{\mathrm{haz}} \;=\; \begin{pmatrix} V_{0,n} & V_{0,n+1} & \cdots & V_{0,N} \\ V_{1,n} & V_{1,n+1} & & V_{1,N} \\ \vdots & & \ddots & \vdots \\ V_{J,n} & V_{J,n+1} & \cdots & V_{J,N} \end{pmatrix}. \tag{3.57}$$

Therein, the instants t_i, when the host-vehicle passes a node P_i, are estimated by Equation (3.51) with $s_{i,i-1} = \Delta x$. Each column i of the array $\mathbf{V}^{\mathrm{haz}}$ in Equation (3.57) refers to the hazard potential experienced by node P_i on all possible lateral positions on the grid. Each row of the array $\mathbf{V}^{\mathrm{haz}}$ in Equation (3.57) corresponds to one lateral position on the grid. Next, $\mathbf{V}^{\mathrm{haz}}$ is normalized according to

$$\widetilde{V}_{j,i}^{\mathrm{haz}} \;=\; \frac{V_{j,i}^{\mathrm{haz}} - \min\limits_{j\in\{0,\ldots,J\}}\left(V_{j,i}^{\mathrm{haz}}\right)}{\max\limits_{j\in\{0,\ldots,J\}}\left(V_{j,i}^{\mathrm{haz}}\right) - \min\limits_{j\in\{0,\ldots,J\}}\left(V_{j,i}^{\mathrm{haz}}\right)} \quad \text{with} \quad \widetilde{V}_{j,i}^{\mathrm{haz}} \in [0,\ 1]\ , \tag{3.58}$$

with $\mathbf{V}^{\text{haz}}_{j,i=const.}$ being an $(J+1) \times 1$ array containing the values of the hazard potential evaluated for all possible positions of node P_i.

In order to keep the curvature low and to avoid high lateral displacements between two adjacent nodes, the initial solution is not solely generated by the hazard potential. The positions of the nodes of the initial solution are determined in ascending order from node P_{n+1} to node P_N. Therein, the array of all possible lateral displacements from a node P_{i-1}, that is already fixed, to the following node P_i reads

$$ {}_R\Delta\mathbf{y}_i := {}_R\mathbf{y}_i - {}_R y_{i-1} \cdot \left[1, \ldots, 1\right]^{\mathrm{T}}. \tag{3.59} $$

Next, the array of all possible lateral displacements from a node P_{i-1} to the following node, Equation (3.59), is normalized

$$ {}_R\Delta\widetilde{y}_{j,i} = \frac{{}_R\Delta y_{j,i} - \min\limits_{j\in\{0,\ldots,J\}} \left({}_R\Delta y_{j,i}\right)}{\max\limits_{j\in\{0,\ldots,J\}} \left({}_R\Delta y_{j,i}\right) - \min\limits_{j\in\{0,\ldots,J\}} \left({}_R\Delta y_{j,i}\right)} \quad \text{with} \quad {}_R\Delta\widetilde{y}_{j,i} \in [0,\ 1]\ , \tag{3.60} $$

Finally, the initial solution is generated by minimizing the weighted sum of hazard potential $\widetilde{V}^{\text{haz}}_{j,i}$ and lateral displacement ${}_R\Delta\widetilde{y}_{j,i}$ to the preceding node for all remaining nodes of the elastic band $P_{n+1}, \ldots, P_N$. The index of the lateral position of node P_i becomes

$$ \begin{aligned} j_i^* &:= \left\{ j \in [0, \ldots, J] \,\middle|\, \left[(1-\gamma) \cdot \widetilde{V}^{\text{haz}}_{j,i} + \gamma \cdot {}_R\Delta\widetilde{y}_{j,i}\right] \right. \\ &= \left. \min_{j\in\{0,\ldots,J\}} \left[(1-\gamma) \cdot \widetilde{V}^{\text{haz}}_{j,i} + \gamma \cdot {}_R\Delta\widetilde{y}_{j,i}\right] \right\}\ . \end{aligned} \tag{3.61} $$

Together with Equation (3.56) the initial solution for the elastic band is given. The parameter γ can be used to adjust the weight of lateral displacement to the preceding node and the influence of the hazard map. Noteworthy, positions on the grid that would collide with an obstacle are not selected for the initial solution, $\mathbf{r}_i^{(0)} \notin \mathcal{O}_j$.

3.4.3 Equilibrium Solution

In order to find the equilibrium configuration of the elastic band, the equilibrium condition Equation (3.37) or Equation (3.42) has to be solved for the position vectors $\mathbf{r}_i$ of the nodes P_i with $i = 1, \ldots, N$. Due to the geometry as well as to the hazard potential this is a nonlinear algebraic problem with the $2N$ components of the position vectors $\mathbf{r}_i$ being the unknowns. For the numerical solution the problem can be stated in general form as

$$ \mathbf{F}\left(\mathbf{z}\right) = \mathbf{0} \tag{3.62} $$

with the array of position vectors $\mathbf{z} = [\mathbf{r}_1^{\mathrm{T}}, \ldots, \mathbf{r}_N^{\mathrm{T}}]^{\mathrm{T}}$ and the array of resultant forces at each node $\mathbf{F} = [\mathbf{F}_1^{\mathrm{sum}^{\mathrm{T}}}, \ldots, \mathbf{F}_N^{\mathrm{sum}^{\mathrm{T}}}]^{\mathrm{T}}$, whereas $\mathbf{F}_i^{\mathrm{sum}} = \mathbf{F}_i^{\mathrm{int}} + \mathbf{F}_i^{\mathrm{haz}} + \mathbf{F}_i^{\mathrm{c}}$ is composed of internal, hazard, and constraint forces acting on node P_i. However, if the position of a node P_i is fixed, its position vector is a priori known. Therefore, the zero finding problem in Equation (3.62) can be reduced by the number of fixed nodes. The start node P_0 for

instance is generally fixed, thus its position vector $\mathbf{r}_0$ does not appear in Equation (3.62); analogously all nodes that should remain at a fixed position $\mathbf{r}_i$ are removed.

The zero finding problem in Equation (3.62) is solved by employing a Newton-Raphson method, wherein the Newton-Raphson iteration can be interpreted as a linear approximation

$$\mathbf{F}(\mathbf{z}) \simeq \tilde{\mathbf{F}}(\mathbf{z}) := \mathbf{F}(\mathbf{z}^{(k)}) + \mathbf{J}(\mathbf{z}^{(k)})(\mathbf{z} - \mathbf{z}^{(k)}), \tag{3.63}$$

obtained by truncating the Taylor series expansion of $\mathbf{F}$ at $\mathbf{z}^{(k)}$ after the linear term and then solving the resulting linear equation $\tilde{\mathbf{F}}(\mathbf{z}) = \mathbf{0}$, calling the solution $\mathbf{z}^{(k+1)}$, see for example ORTEGA AND RHEINBOLDT (1970, [80], p. 181-185). The matrix $\mathbf{J}$ denotes the Jacobian of $\mathbf{F}$. Performing an iteration step leads to

$$\mathbf{z}^{(k+1)} = \mathbf{z}^{(k)} - \mathbf{J}^{-1}(\mathbf{z}^{(k)})\ \mathbf{F}(\mathbf{z}^{(k)}), \quad k = 0, 1, 2, \ldots\ . \tag{3.64}$$

Starting from an initial vector $\mathbf{z}^{(0)}$, sufficiently close to the solution, the iteration converges quadratically to a root $\mathbf{z}^*$. As the hazard forces of the left and of the right border of the road, $\partial\mathcal{B}_l$ and $\partial\mathcal{B}_r$, become infinite when a node P_i approaches the borders, see Equation (3.39), it is ensured that, if the road is not blocked by obstacles $\mathcal{O}_j$, equilibrium solutions only exist on the road. The iteration is terminated if a sufficient accuracy ϵ is achieved,

$$\epsilon \geq \max\left(\Delta\mathbf{z}_i^{(k)}\right) := \max\left(\left[-\mathbf{J}^{-1}(\mathbf{z}^{(k)})\ \mathbf{F}(\mathbf{z}^{(k)})\right]_i\right)\ . \tag{3.65}$$

To avoid that the Newton-Raphson algorithm shifts nodes P_i of the elastic band, $\mathbf{r}_i \notin \mathcal{O}_j \wedge \mathbf{r}_i \in]\partial\mathcal{B}_l, \partial\mathcal{B}_l[$, into *non-valid areas* such as into obstacles or outside the borders of the road, the step size of each node is controlled independently. Thus, the step size is limited by the distance to the closest object, which is either an obstacle $\mathcal{O}_j$ or one of the borders of the road $\partial\mathcal{B}_l$ or $\partial\mathcal{B}_r$. This does not take high computational effort as the necessary distance computations have already been performed in the evaluation of the external potentials at the nodes of the elastic band. Besides that, a fixed maximal step size Δ_{max} is applied to all nodes in order to avoid large displacements in one iteration step.

The internal forces and the hazard forces $\mathbf{F}_i^{\text{int}}$ and $\mathbf{F}_i^{\text{haz}}$, respectively, as given in Equation (3.36), contribute in a different manner to the Jacobian matrix $\mathbf{J}$. Splitting the hazard forces into their components due to the road and due to obstacles, the Jacobian matrix reads

$$\mathbf{J} \ = \ \mathbf{J}^{\text{int}} + \mathbf{J}^{\text{road}} + \mathbf{J}^{\text{obs}} = \frac{\partial\mathbf{F}^{\text{int}}}{\partial\mathbf{z}} + \frac{\partial\mathbf{F}^{\text{road}}}{\partial\mathbf{z}} + \frac{\partial\mathbf{F}^{\text{obs}}}{\partial\mathbf{z}}\ . \tag{3.66}$$

As the internal forces $\mathbf{F}_i^{\text{int}}$ depend on the position of a node $\mathbf{r}_i$ as well as on the positions of the preceding and the subsequent node $\mathbf{r}_{i-1}$ and $\mathbf{r}_{i+1}$, the contribution of the internal forces to the Jacobian matrix has tridiagonal form. The forces due to the potential of the borders of the road depend only on the position of the considered node $\mathbf{r}_i$. Therefore, the

borders of the road contribute only on the main diagonal to the Jacobian matrix,

$$\mathbf{J}^{\text{int}} = \begin{pmatrix} \mathbf{J}^{\text{int}}_{1,1} & \mathbf{J}^{\text{int}}_{1,2} & & \mathbf{0} & \\ \mathbf{J}^{\text{int}}_{2,1} & \mathbf{J}^{\text{int}}_{2,2} & \mathbf{J}^{\text{int}}_{2,3} & & \\ & \mathbf{J}^{\text{int}}_{3,2} & \mathbf{J}^{\text{int}}_{3,3} & \mathbf{J}^{\text{int}}_{3,4} & \\ & & \ddots & \ddots & \ddots \\ & \mathbf{0} & & \mathbf{J}^{\text{int}}_{N,N-1} & \mathbf{J}^{\text{int}}_{N,N} \end{pmatrix}, \mathbf{J}^{\text{road}} = \begin{pmatrix} \mathbf{J}^{\text{road}}_{1,1} & & \mathbf{0} & \\ & \mathbf{J}^{\text{road}}_{2,2} & & \\ \mathbf{0} & & \ddots & \\ & & & \mathbf{J}^{\text{road}}_{N,N} \end{pmatrix}. \quad (3.67)$$

The hazard forces caused by moving obstacles depend on the extrapolated trajectories of both, the obstacles and the host-vehicle, see Section 3.1.3. Therefore, the positions of all preceding nodes, already passed by the host-vehicle in the extrapolation, influence the external hazard forces due to moving obstacles on a node P_i. This coupling is due to the fact that the course of the elastic band to a node P_i influences the time t_i, when the host-vehicle passes that node. In the computation of the hazard forces, the estimated trajectories of the obstacles are evaluated at the instants t_i and therefore depend on the position vectors of the preceding nodes $\mathbf{r}_0, \ldots, \mathbf{r}_{i-1}$. Hence, the contribution of the hazard forces due to moving obstacles in the Jacobian matrix has a triangular structure,

$$\mathbf{J}^{\text{obs}} = \begin{pmatrix} \mathbf{J}^{\text{obs}}_{1,1} & & & & \\ \mathbf{J}^{\text{obs}}_{2,1} & \mathbf{J}^{\text{obs}}_{2,2} & & \mathbf{0} & \\ & \mathbf{J}^{\text{obs}}_{3,2} & \mathbf{J}^{\text{obs}}_{3,3} & & \\ \vdots & & \ddots & \ddots & \\ \mathbf{J}^{\text{obs}}_{N,1} & \cdots & & \mathbf{J}^{\text{obs}}_{N,N-1} & \mathbf{J}^{\text{obs}}_{N,N} \end{pmatrix}, \quad (3.68)$$

whereas a non-moving obstacle $\mathcal{O}_j$ results, like the borders of the road ∂B_l and ∂B_r, in a diagonal contribution to the Jacobian matrix. To demonstrate the influence of moving obstacles $\mathcal{O}_j$ on the Jacobian $\mathbf{J}$, the example of a pedestrian crossing the road at constant speed is considered.

Example: *A pedestrian PE may be modeled by a circular safety area of diameter D_j walking at constant speed $v^{PE^*}(t_0)$ measured at t_0. Extrapolating the trajectory of the pedestrian according to Equation (3.27) for constant speed and evaluating the position vectors of the pedestrian $\mathbf{r}^{PE}(t)$ at the instants t_i, when the host-vehicle $\mathcal{V}$ passes the nodes P_i of the elastic band with constant speed U_t, estimated according to Equation (3.49) and Equation (3.50) and plugging the result into equations (3.29) and (3.33), respectively, gives*

$$V_i^{PE}\ (\mathbf{r}_0, \ldots, \mathbf{r}_i) = -k^{PE} \ln \left(\left\| \mathbf{r}_i - \mathbf{r}^{PE}(t_0) - v^{PE^*}(t_0) \left(\frac{\sum_{k=1}^{i} \|\mathbf{r}_k - \mathbf{r}_{k-1}\|}{U_t} - t_0 \right) \right\| - \frac{D_j}{2} \right). \quad (3.69)$$

It can be seen that the hazard potential of the pedestrian V_i^{PE} evaluated at a node P_i of the elastic band also depends on the preceding nodes $P_0, \ldots, P_{i-1}$. Therefore, also the hazard forces due to the pedestrian $\mathbf{F}^{PE}$ show the same dependencies, so the structure of the Jacobian matrix $\mathbf{J}$ is analog to Equation (3.68). If the pedestrian does not move, $v^{PE^*} = 0$, it becomes obvious from Equation (3.69) that the dependence on the preceding nodes $\mathbf{r}_0, \ldots, \mathbf{r}_i$ vanishes and the hazard potential of the pedestrian V^{PE} would only contribute to the main diagonal of the Jacobian $\mathbf{J}$.

In order to accelerate the computation in each iteration step, the off-diagonal elements in Equation (3.68) caused by moving obstacles are neglected

$$\tilde{\mathbf{J}}^{\text{obs}} = \begin{pmatrix} \mathbf{J}_{1,1}^{\text{obs}} & & & & \\ & \mathbf{J}_{2,2}^{\text{obs}} & & \mathbf{0} & \\ & & \mathbf{J}_{3,3}^{\text{obs}} & & \\ & \mathbf{0} & & \ddots & \\ & & & & \mathbf{J}_{N,N}^{\text{obs}} \end{pmatrix} . \tag{3.70}$$

However, the motion of the obstacles is still considered in each iteration step by means of the hazard forces of the obstacles $\mathbf{F}^{\text{obs}}$ in Equation (3.64). In general, the approximation of the Jacobian, $\mathbf{J}^{\text{obs}} \approx \tilde{\mathbf{J}}^{\text{obs}}$, may result in more iteration steps, but, as the number of iterations is relatively low, this drawback is outbalanced by the reduction of computations in each iteration step.

A further substantial reduction of computational effort is achieved by restricting the node's degrees of freedom to the lateral direction ${}_R y$. Thus, only the equilibrium conditions in the direction of free displacements have to be considered. These are obtained by projecting the equilibrium equations onto the free directions, as described by Equation (3.41) and Equation (3.42). What remains is to solve these equations with the Newton-Raphson procedure (3.64) at each node for ${}_R y_i$, as ${}_R x_i = i\Delta x$ is prescribed by the discretization of the elastic band. In finding the equilibrium for each node in ${}_R x$- and in ${}_R y$-direction, the submatrices of the Jacobians, (3.67) and (3.68), have the structure

$$\mathbf{J}_{i,j} = \begin{pmatrix} \frac{\partial F_x}{\partial x_j} & \frac{\partial F_x}{\partial y_j} \\ \frac{\partial F_y}{\partial x_j} & \frac{\partial F_y}{\partial y_j} \end{pmatrix} \quad \text{and thus:} \quad \dim\left(\mathbf{J}_{i,j}^{\text{int}}\right) = \dim\left(\mathbf{J}_{i,j}^{\text{road}}\right) = \dim\left(\mathbf{J}_{i,j}^{\text{obs}}\right) = 2 \times 2 \, . \tag{3.71}$$

For N nodes P_i, the Jacobian $\mathbf{J}$, Equation (3.66), therefore has dimension $2N \times 2N$. If only the lateral positions of the nodes P_i are considered, the submatrices in equations (3.67) and (3.68) are reduced to scalars of the type $\frac{\partial F_{y_i}}{\partial y_j}$. Thus, considering only lateral displacements reduces the number of components in the Jacobian $\mathbf{J}$ by factor 4.

Note that for the transition from one planning update K to the next motion planning step $K+1$ the configuration of the elastic band has to be stored in the assistance system with respect to the earth-fixed reference frame $\overset{\uparrow}{\underset{\rightarrow}{\text{E}}}$ or with respect to the last road-fixed reference frame $\overset{\uparrow}{\underset{\rightarrow}{\text{R}^{(K)}}}$.

3.5 Simulations

The potential field motion planning procedure introduced in this chapter is now demonstrated for some traffic scenarios.

3.5.1 Scenario I: Entering Traffic

In this simulation example the functioning of the proposed motion planning method is highlighted. One of the main advantages of the presented approach is, that it works in a predictive rather than in a reactive manner. In order to illustrate the effect of the extrapolation of obstacle motion, as proposed, the same scenario is simulated twice: in the first simulation run the extrapolation is turned off and the obstacle is treated as a static obstacle in each update of the elastic band; in the second simulation run the motion of the obstacle is extrapolated based on its previous behavior. However, to have a "fair" comparison, the obstacle changes its behavior during the simulation and therefore does not travel in a way that can perfectly be predicted. The scenario set up is depicted in Figure 3.16. The scenario description is completed by the data given in Table 3.2, while the parametrization of the hazard map and the elastic band motion planning is summarized in Table 3.3.

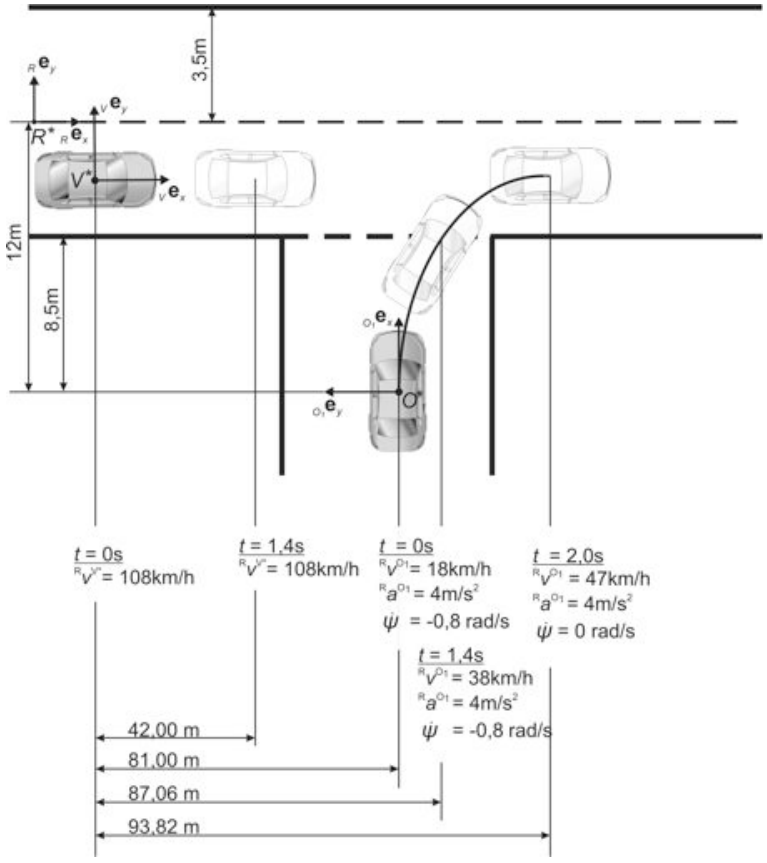

Figure 3.16: Scenario I: A vehicle entering the highway

In this scenario two vehicles are involved: the host-vehicle traveling along a highway at a speed of 108 km/h and a second vehicle, considered to be the obstacle, that turns into the

highway from a side road. Entering the highway the obstacle has a speed of 18 km/h. Due to the difference in speed, the obstacle is fast approached by the host-vehicle. However, the obstacle accelerates at a rate of $4\,\mathrm{m/s^2}$. The host-vehicle detects the obstacle after 1.4 s. The position of the obstacle at $t = 1.4\,\mathrm{s}$ is sketched in Figure 3.16. At $t = 2\,\mathrm{s}$ the obstacle has completed the entering maneuver and travels down the highway.

Table 3.2: Scenario data

Symbol	Value	Description
b	7 m	road width
b_{lanes}	3.5 m	lane width
κ_0	$0\ \mathrm{m^{-1}}$	initial road curvature
$\dot{\kappa}$	$0\ \mathrm{m^{-1}s^{-1}}$	road curvature rate
l_{O_1}	4 m	obstacle length
w_{O_1}	2 m	obstacle width

For the entire scenario the speed of the host-vehicle remains constant at 108 km/h. For this reason the motion planning procedure initiates a passing maneuver. However, due to the high acceleration of the obstacle, the obstacle reaches the speed of the host-vehicle before the passing maneuver is completed. The host-vehicle returns to the right lane and follows the obstacle. The driven paths are depicted in Figure 3.17 with and without extrapolation of the obstacle motion. It becomes evident that the driven trajectory without extrapolation is more wavy than the one with. This is due to the fact that in each replanning the new trajectory differs significantly from the previously planned, because the environment has changed (the obstacle occurs in a different position). Using the extrapolation, the motion of the obstacle was anticipated and therefore the difference between two consecutively planned trajectories is smaller.

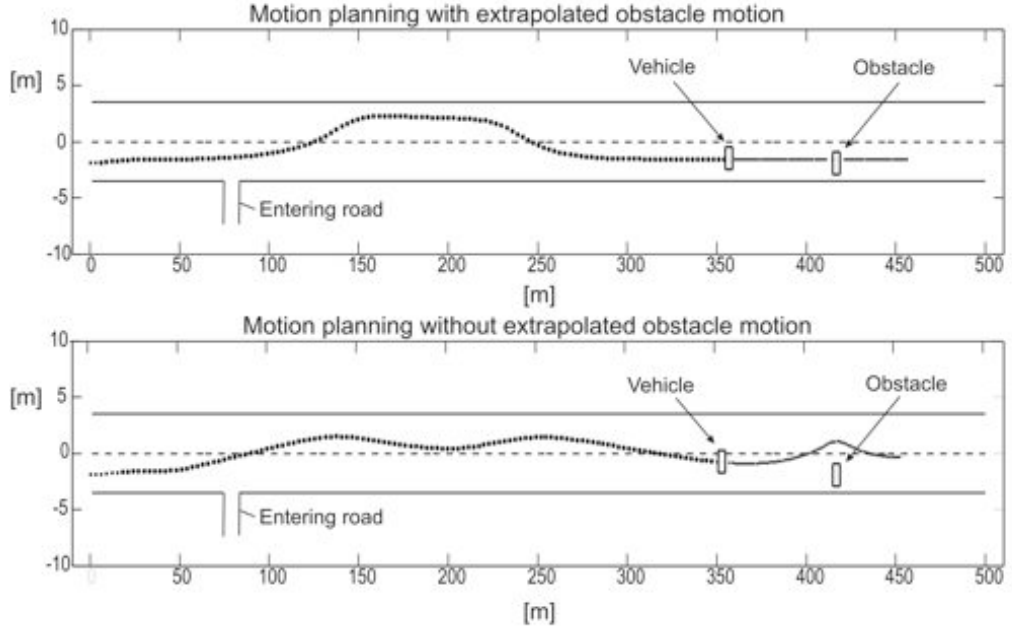

Figure 3.17: Motion planning with and without extrapolation of obstacle motion

Table 3.3: Hazard map and elastic band motion planning parameter

Symbol	Value	Description
l	1.5 m	node distance
l_0	1.35 m	unstreched spring length
k^{int}	30000 N/m	spring constant
k^{B_l}, k^{B_r}	750, 250	scaling factor of the potentials of the borders of the road
k^O	1000	scaling factor of obstacle potential
l_P	100 m	planning distance
ΔT	0.1 s	planning update interval
Δ_{max}	1.5 m	maximal displacement in each iteration step
ϵ	0.05 m	tolerance

3.5.2 Scenario II: Crossing Animal

In the last scenario it was seen, that it can be beneficial to incorporate extrapolation into the predictive motion planning in order to keep variations between two consecutively planned trajectories as small as possible. In the second scenario an even more dramatic example is given: the host-vehicle without extrapolation collides with an animal crossing the road, while the host-vehicle with extrapolation avoids the collision. The scenario is depicted in Figure 3.18.

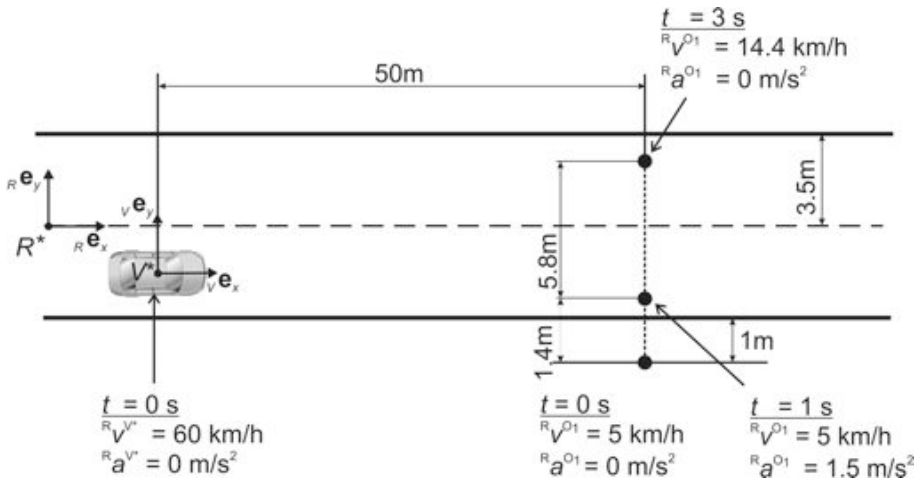

Figure 3.18: Scenario II: An animal crossing the road

The host-vehicle drives at a constant speed of 60 km/h on a road modeled according to Table 3.2. At a distance of 50 m ahead of the host-vehicle an animal, approaching the road at a speed of 5 km/h from the right shoulder, is detected. After 1.4 s the animal becomes aware of the host-vehicle and accelerates. After 3 s the animal suddenly stops in panic and remains at the left lane of the road. The parameters of the motion planning algorithm are chosen identical to the last scenario, according to Table 3.3. The safety area of the animal is modeled by a circle with a diameter of 0.5 m.

In Figure 3.19 the simulated paths with and without extrapolation are shown. In the left column the scenario with extrapolation is given: at t=0 s the host-vehicle has not yet detected the animal and intends to follow the right lane. In the next depicted instant at t=1.5 s the animal was incorporated in the motion planning. It can be observed, that the motion of the animal towards the left lane was already anticipated by the motion planning procedure, as the host-vehicle turns to the right. Finally, the host-vehicle passes the animal on the right lane.

In the right column the simulation is repeated without extrapolation. Initially the animal is considered to be a static obstacle on the right lane. Therefore, the motion planning algorithm intends to pass it on the left. However, as the animal moves towards the left border of the road, also the planned trajectory of the host-vehicle is shifted to the left with each adaptation of the trajectory. Finally, the host-vehicle collides with the animal at approximately t=3.1 s.

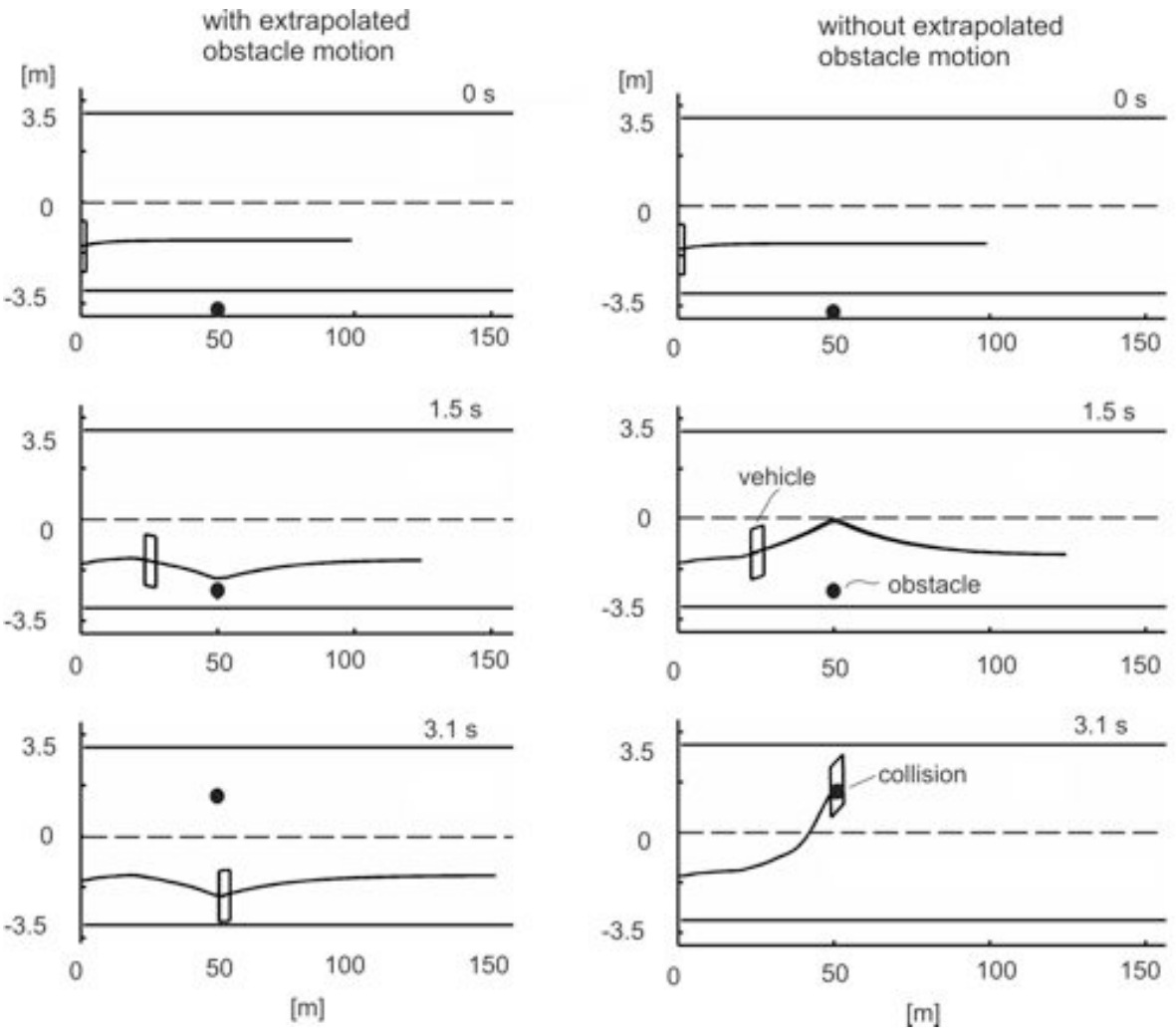

Figure 3.19: Comparison of algorithm with and without extrapolation

3.5.3 Scenario III: Passing Maneuver with Oncoming Traffic

The two preceding scenarios included traffic traveling in the same direction as the host-vehicle and an animal crossing the road. Now, a passing scenario is given including a static obstacle as well as oncoming traffic. The scenario is depicted in Figure 3.20. The vehicle in front of the host-vehicle suddenly brakes and stops 40 m ahead of the host-vehicle. At this instant the host-vehicle has a speed of 108 km/h; thus, braking is hardly feasible. The host-vehicle evades the static vehicle and remains at constant speed for the rest of the scenario. It has to return to the right lane before it collides with the oncoming vehicle.

Figure 3.21 shows the trajectories simulated with and without extrapolation. In contrary to the last scenarios no significant difference in the result of the two motion planning algorithms can be noted. Both algorithms intend to pass the resting vehicle and return to the right lane, to the minimum of the hazard potentials of the borders of the road. Curvature and curvature rate of the road are $\kappa = 0.003\,1/\mathrm{m}$ and $\dot{\kappa} = 10^{-6}\,1/\mathrm{ms}$, respectively. For static obstacles there is no difference between the algorithm with and without extrapolation.

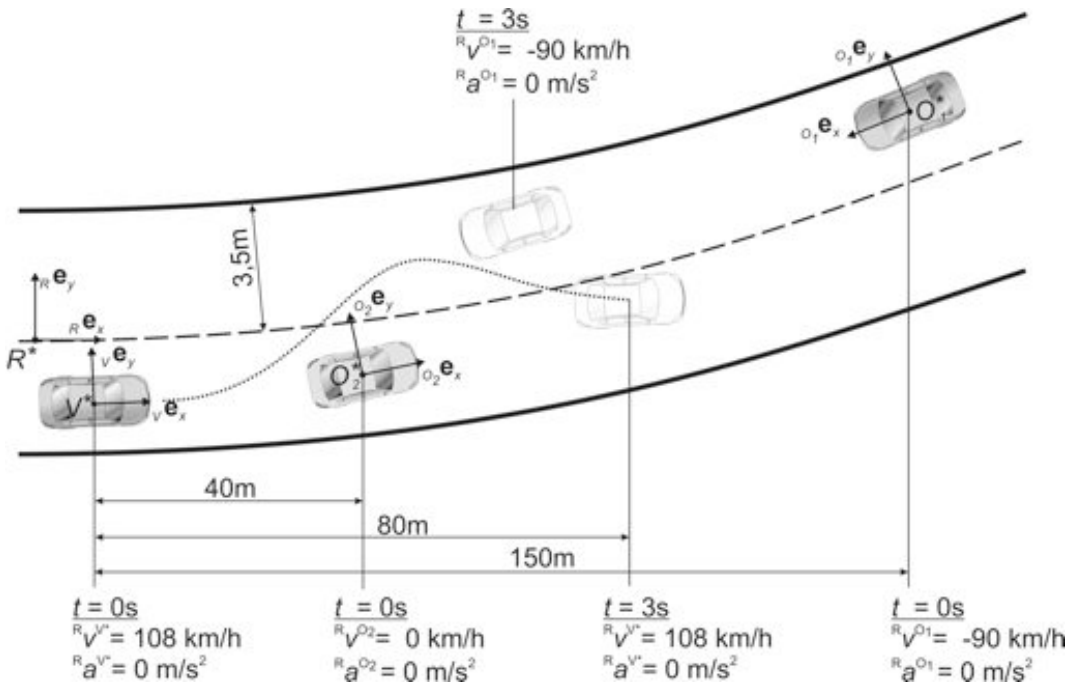

Figure 3.20: Scenario III: Passing maneuver with oncoming traffic

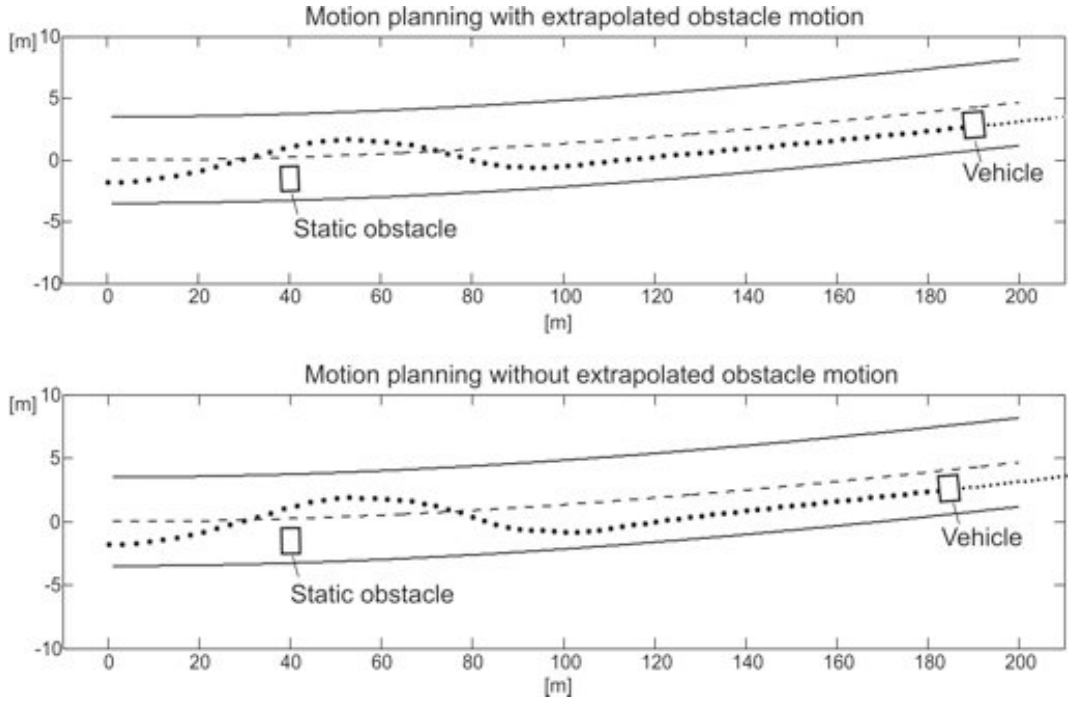

Figure 3.21: Passing maneuver simulated with and without extrapolation

3.5.4 Pseudo Code of Motion Planning Algorithm

Finally, the potential field motion planning algorithm is summarized as pseudo-code.

Initialize: $K = 0$

planning instant: t_0

1. **Get sensor data**:

   (a) road: $\left(b, ({}_V x_i, {}_V y_i) \in \mathcal{R}\right) \quad \Rightarrow \quad \mathbf{r}^{\bar{R}^*}$, Eqn. (3.11)

   (b) obstacles: $\left(\mathbf{r}^{O_j^*}(t_0), {}^R\mathbf{v}^{O_j^*}(t_0), {}^R\mathbf{a}^{O_j^*}(t_0), {}^R\boldsymbol{\omega}^{O_j}(t_0), l_{O_j}, w_{O_j}\right)$, see Fig. 3.1

   (c) driver/vehicle: $\left(\delta(t_0), {}^R\mathbf{v}^{V^*}(t_0), {}^R\mathbf{a}^{V^*}(t_0)\right)$, see Fig. 3.1

2. **Get previous path**: $\mathbf{r}_0^{(K-1)}, \ldots, \mathbf{r}_N^{(K-1)}$

3. **Generate hazard map**: ${}_R V^{\text{haz}}$ Eqn. (3.31)

   3.1 Generate potential of the road: ${}_R V^{B_q}$ Eqn. (3.16) with Eqn. (3.11)-(3.15) and (a)

   3.2 Generate potential of the obstacles: $\sum_{j=1}^{M} {}_R V^{O_j}$ in Eqn. (3.29)

      3.2.1 Identify type of obstacle motion by Eqn. (3.19): IN LANE / LANE DEPARTURE

      3.2.2 Extrapolate obstacle motion: $\mathbf{r}^{O_j^*}(t) \quad \text{with} \quad t \in [t_0, t_f]$

         If IN LANE: $\mathbf{r}^{O_j}(t)$, ${}^R\psi^{O_j}(t)$ Eqn. (3.20)-(3.26) with (b)

         If LANE DEPARTURE: $\mathbf{r}^{O_j}(t)$, ${}^R\psi^{O_j}(t)$ Eqn. (3.27)-(3.30) with (b)

4. **Generate initial solution**:

   4.1 Set: $\tilde{\mathbf{r}}_0^{(K)}$ Eqn. (3.40), $\tilde{\mathbf{r}}_1^{(K)}, \ldots, \tilde{\mathbf{r}}_n^{(K)}$ Eqn. (3.43)-(3.45) and (c), see Fig. 3.13, 3.15

   4.2 Compute distances: $(\mathbf{r}_{j,i}^{B_l}, \mathbf{r}_{j,i}^{B_r})$ Eqn. (3.52), and $\left(\mathbf{r}_{j,i}^{\hat{O}_1}, \ldots, \mathbf{r}_{j,i}^{\hat{O}_M}\right)$ Eqn. (3.54)
   for $i = n+1, \ldots, N$ and $j = 0, \ldots, J$, see Fig. 3.15

   4.3 Evaluate hazard potential: ${}_R V_{j,i}^{\text{haz}} = {}_R V^{\text{haz}}\left(\mathbf{r}_{j,i}, \mathbf{r}_{j,i}^{B_l}, \mathbf{r}_{j,i}^{B_r}, \mathbf{r}_{j,i}^{O_1}, \ldots, \mathbf{r}_{j,i}^{O_M}\right)$ Eqn. (3.57)

   4.4 Set: $\tilde{\mathbf{r}}_{n+1}^{(K)}, \ldots, \tilde{\mathbf{r}}_N^{(K)}$ Eqn. (3.56) and Eqn. (3.58)-(3.61)

5. **Compute equilibrium solution**:

   Set k=0 and $\max\left(\Delta\mathbf{z}_i^{(0)}\right) > \epsilon$, set $\mathbf{z}^{(0)} = \left[\left(\tilde{\mathbf{r}}_1^{(K)}\right)^{\mathrm{T}}, \ldots, \left(\tilde{\mathbf{r}}_N^{(K)}\right)^{\mathrm{T}}\right]^{\mathrm{T}}$ according to 4.

   while: $\max\left(\Delta\mathbf{z}_i^{(k)}\right) > \epsilon$

      compute distances:

      borders of the road: $\mathbf{z}^{B(k)} := \left[\left(\mathbf{r}_1^{B_l}\right)^{\mathrm{T}}, \left(\mathbf{r}_1^{B_r}\right)^{\mathrm{T}}, \left(\mathbf{r}_2^{B_l}\right)^{\mathrm{T}}, \ldots, \left(\mathbf{r}_N^{B_r}\right)^{\mathrm{T}}\right]^{\mathrm{T}}$ Eqn. (3.52)

      obstacles: t_i Eqn. (3.51) $\Rightarrow \mathbf{r}_i^{\hat{O}_1}, \ldots, \mathbf{r}_i^{\hat{O}_M}$ for $i = 1, \ldots, N$ Eqn. (3.53), (3.54)

      $\mathbf{z}^{O(k)} := \left[\left(\mathbf{r}_1^{\hat{O}_1}\right)^{\mathrm{T}}, \ldots, \left(\mathbf{r}_N^{\hat{O}_1}\right)^{\mathrm{T}}, \left(\mathbf{r}_1^{\hat{O}_2}\right)^{\mathrm{T}}, \ldots, \left(\mathbf{r}_N^{\hat{O}_M}\right)^{\mathrm{T}}\right]^{\mathrm{T}}$

      compute $\mathbf{J}^{(k)} = \mathbf{J}^{\text{int}}\left(\mathbf{z}^{(k)}\right) + \mathbf{J}^{\text{road}}\left(\mathbf{z}^{(k)}; \mathbf{z}^{B(k)}\right) + \tilde{\mathbf{J}}^{\text{obs}}\left(\mathbf{z}^{(k)}; \mathbf{z}^{O(k)}\right)$ Eqn. (3.67), (3.68)

      compute $\mathbf{F}^{(k)} = \mathbf{F}\left(\mathbf{z}^{(k)}; \mathbf{z}^{B(k)}, \mathbf{z}^{O(k)}\right)$ Eqn. (3.36)

      solve: $\mathbf{J}^{(k)}\,\Delta\mathbf{z}^{(k+1)} = -\mathbf{F}^{(k)} \quad \Rightarrow \quad \Delta\mathbf{z}^{(k+1)}$

      set maximal step size: $\Delta z_{i,\max}^{(k+1)} = \min\left(\Delta z_{i,\max}, \| \mathbf{r}_i - \mathbf{r}_1^{B_l} \|, \ldots, \| \mathbf{r}_i - \mathbf{r}_1^{\hat{O}_M} \|\right)$

      check step size: if $\Delta z_i^{(k+1)} \geq \Delta z_{i,\max}^{(k+1)} \quad \Rightarrow \quad \Delta z_i^{(k+1)} = \Delta z_{i,\max}^{(k+1)}$

      $\mathbf{z}^{(k+1)} = \mathbf{z}^{(k)} + \Delta\mathbf{z}^{(k+1)}$

      $k = k + 1$

   end

next replanning: at $t_0 = t_0 + \Delta T$, $K = K + 1$

Chapter 4

Potential Field based Vehicle Guidance Control

In the last chapters, vehicle dynamics models and potential field based motion planning methods were introduced. In the next steps guidance laws for trajectory tracking have to be formulated and the guidance strategy has to be coordinated with the driver. In the sense of a consistent framework for motion planning and vehicle guidance, the control problem is addressed by potential field methods. However, it has to be emphasized that the longitudinal guidance of the vehicle remains with the driver. Consequently, the velocity profile of the planned trajectory is not affected by the control laws given in this chapter; the vehicle is guided with respect to the path $\mathcal{P}$, which represents the configuration level of the elastic band. In order to do so, the guidance potential field is formulated in terms of the lateral path tracking error. Therein, the reference position is that position on the path $\mathcal{P}$ being closest to the current position of the host-vehicle. Subsequently, a generalized virtual guidance force is derived from the guidance potential. By means of the vehicle dynamics models given in Chapter 2, the generalized virtual guidance force is finally mapped onto the control inputs of the vehicle.

Principally, the curvature of the path $\mathcal{P}$ acts as a disturbance that has to be regulated by the guidance controller. However, as the planned path $\mathcal{P}$ and its curvature κ_G are known, the disturbances can be compensated by feedforward control. Therefore, the potential field controller only has to regulate initial disturbances, for example due to side wind or bank. For the potential field controller, in combination with feedforward control, stability in the sense of Lyapunov can be shown. Furthermore, a Lyapunov function is employed to provide bounds for the maximal tracking error depending on the initial disturbance. For a known initial configuration, the Lyapunov function can be used to guarantee collision avoidance by guaranteeing a deviation from $\mathcal{P}$ being smaller than the distance to the closest obstacle.

4.1 General Concept of Potential Field Guidance

The main idea of the potential field controller consists in deriving a generalized virtual guidance force from the potential of the path tracking error ${}_G\Delta\mathbf{q}_{\mathrm{lat}}(t)$. Therein, the

generalized virtual guidance force

$$ {}_V\mathbf{Q}_{\text{lat}}^{\text{guid}}(t) = \mathbf{f}\left({}_G\Delta\mathbf{q}_{\text{lat}}\left(t\right)\right) \tag{4.1} $$

is composed of a lateral force and a moment in the yaw plane, respectively. In Figure 4.1 an example of a potential field, symbolized by a spring regulating the lateral deviation from the path, is shown.

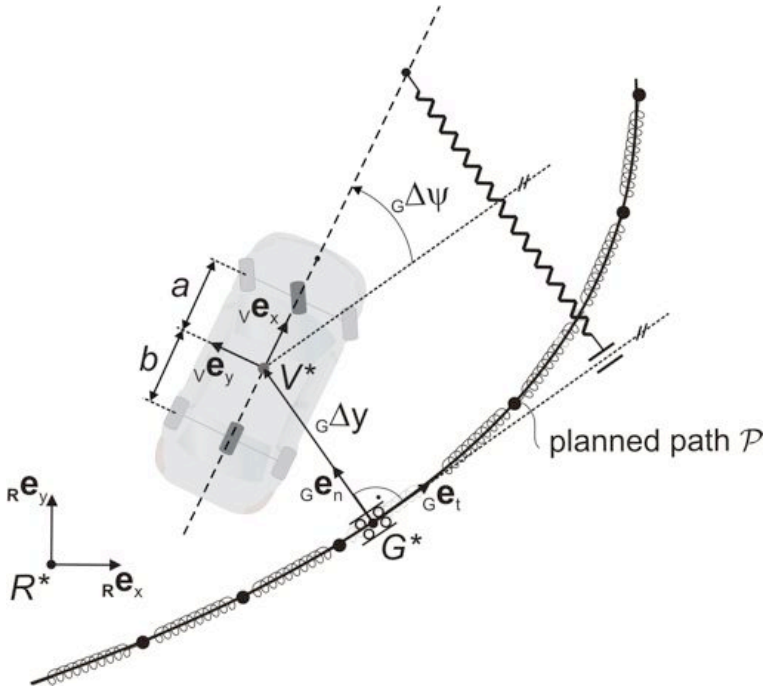

Figure 4.1: Design example of a guidance potential field, see Section 4.6.5

With the controller matrix $\mathbf{K}^{\text{guid}}$ the potential in the lateral deviation ${}_G\Delta\mathbf{q}_{\text{lat}}\left(t\right)$ is chosen to be quadratic

$$ {}_GV^{\text{guid}}({}_G\Delta\mathbf{q}_{\text{lat}}) := \frac{1}{2}\,{}_G\Delta\mathbf{q}_{\text{lat}}^{\text{T}}\,\mathbf{K}^{\text{guid}}\;{}_G\Delta\mathbf{q}_{\text{lat}}\;. \tag{4.2} $$

The generalized virtual guidance force with respect to the guidance frame $\uparrow\underline{\text{G}}_{\rightarrow}$ is then computed by the taking gradient

$$ {}_G\mathbf{Q}_{\text{lat}}^{\text{guid}} := -\,{}_G\nabla_{\Delta\mathbf{q}}\;{}_GV^{\text{guid}}({}_G\Delta\mathbf{q}_{\text{lat}}) = -\mathbf{K}^{\text{guid}}\;{}_G\Delta\mathbf{q}_{\text{lat}}\;. \tag{4.3} $$

Therein, the origin G^* of the guidance frame $\uparrow\underline{\text{G}}_{\rightarrow}$ is identical to that point on $\mathcal{P}$ having the smallest distance to the actual position of the vehicle, represented by V^*, see Section 4.3. To map the generalized guidance force on the control inputs it has to be transformed into the vehicle-fixed reference frame $\uparrow\underline{\text{V}}_{\rightarrow}$

$$ {}_V\mathbf{Q}_{\text{lat}}^{\text{guid}} = \begin{bmatrix} {}_VF_y^{\text{guid}} \\ {}_VM_z^{\text{guid}} \end{bmatrix} = \mathbf{C}^{V,G}\;{}_G\mathbf{Q}_{\text{lat}}^{\text{guid}} \quad \text{with} \quad \mathbf{C}^{V,G} = \begin{bmatrix} \cos\,{}_G\Delta\psi(t) & \sin\,{}_G\Delta\psi(t) & 0 \\ -\sin\,{}_G\Delta\psi(t) & \cos\,{}_G\Delta\psi(t) & 0 \\ 0 & 0 & 1 \end{bmatrix}. \tag{4.4} $$

4.2 Mapping a Virtual Guidance Force on Control Inputs

The aim of this section is to provide a map of the generalized virtual guidance force ${}_V\mathbf{Q}_{\text{lat}}^{\text{guid}}$ on the control inputs $\mathbf{u}$ of the vehicle. In doing so, maps on the control inputs of the nonlinear as well as on the control inputs of the linear single-track model are given.

4.2.1 Nonlinear Mapping

To determine the corresponding control inputs of the vehicle model for a given generalized virtual guidance force ${}_V\mathbf{Q}_{\text{lat}}^{\text{guid}}$, the equations of motion of the nonlinear single-track model in Equation (2.32) with differential braking are recalled

$$\mathbf{M}\,{}_V\dot{\mathbf{v}} + \mathbf{b}\left({}_V\mathbf{v}\right) \;=\; \mathbf{Q}^{\text{nc}}\left(F_y^R\left({}_V\mathbf{v}\right)\right) + \mathbf{Q}^{\text{coupl}}\left(F_y^F\left({}_V\mathbf{v}\right),\delta\right) + \mathbf{Q}^{\text{c}}\left(\mathbf{u}\right)\,. \tag{4.5}$$

The term $\mathbf{Q}^{\text{coupl}}\left(F_y^F\left({}_V\mathbf{v}\right),\delta\right)$ depends on the lateral tire forces at the front tires F_y^F as well as on the steering angle δ. The lateral tire forces are not directly accessible, while the steering angle is one of the control inputs. Therefore, the term $\mathbf{Q}^{\text{coupl}}$ is approximately separated into two parts, one depending on the lateral forces, the other depending on the steering angle. In doing so, the lateral tire forces in

$$\mathbf{Q}^{\text{coupl}}\left(F_y^F\left({}_V\mathbf{v}\right),\delta\right) = F_y^F\left[-\sin\delta,\ \cos\delta,\ a\,\cos\delta\right]^{\text{T}} \tag{4.6}$$

are substituted by the lateral tire forces, $F_y^F = -C_\alpha^F\alpha^F$, generated by the Dugoff model in the linear region, see Equation (2.13), compare also BRANDT, SATTEL AND WALLASCHEK (2005, [9]). Together with the small angle approximation, $\alpha^F \approx \left(\frac{U_y+\dot{\psi}a}{U_x}\right) - \delta$, for the front cornering angle, defined in Equation (2.29), Equation (4.6) becomes

$$\mathbf{Q}^{\text{coupl}} \approx -C_\alpha^F \underbrace{\left(\frac{U_y+\dot{\psi}a}{U_x}\right)}_{:=\bar{\alpha}^F} \begin{bmatrix} -\sin\delta \\ \cos\delta \\ a\,\cos\delta \end{bmatrix} + C_\alpha^F\delta \begin{bmatrix} -\sin\delta \\ \cos\delta \\ a\,\cos\delta \end{bmatrix}\,. \tag{4.7}$$

Applying the small angle approximations, $\sin\delta \approx \delta$, $\cos\delta \approx 1$, and $\bar{\alpha}^F\,\delta \approx 0$, to the first addend in Equation (4.7) the following separation arises,

$$\mathbf{Q}^{\text{coupl}} \approx \underbrace{-C_\alpha^F\bar{\alpha}^F \begin{bmatrix} 0 \\ 1 \\ a \end{bmatrix}}_{:=\mathbf{Q}_{\text{nc}}^{\text{coupl}}} + C_\alpha^F\delta \begin{bmatrix} -\sin\delta \\ \cos\delta \\ a\,\cos\delta \end{bmatrix}\,. \tag{4.8}$$

Now, a procedure analog to the one proposed by ROSSETTER (2003, [93], pp. 16) can be applied: the zero term, $\mathbf{Q}_{\text{nc}}^{\text{coupl}} - \mathbf{Q}_{\text{nc}}^{\text{coupl}}$, is added to the right hand side of the equations of motion (4.5),

$$\mathbf{M}\,{}_V\dot{\mathbf{v}} + \mathbf{b}\left({}_V\mathbf{v}\right) \;=\; \underbrace{\mathbf{Q}^{\text{nc}} + \mathbf{Q}_{\text{nc}}^{\text{coupl}}}_{:=\bar{\mathbf{Q}}^{\text{nc}}} - \underbrace{\mathbf{Q}_{\text{nc}}^{\text{coupl}} + \mathbf{Q}^{\text{coupl}} + \mathbf{Q}^{\text{c}}}_{:=\bar{\mathbf{Q}}^{\text{c}}}\,. \tag{4.9}$$

The right hand side of the equations of motion is now approximately decoupled; the generalized force term $\bar{\mathbf{Q}}^{\mathrm{nc}}$ only depends on the states of the vehicle, while $\bar{\mathbf{Q}}^{\mathrm{c}}$ absorbed the controllable part of the couple term $\mathbf{Q}^{\mathrm{coupl}}$ and depends on the control inputs $\mathbf{u}$.

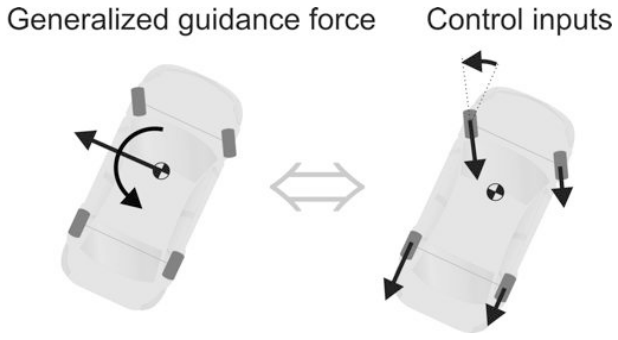

Figure 4.2: Equivalence of generalized guidance force and control inputs: steering angle and differential braking

Finally, equivalence of the generalized virtual guidance force ${}_{V}\mathbf{Q}_{\mathrm{lat}}^{\mathrm{guid}}$ and the controllable part on the right hand side of the equations of motion $\bar{\mathbf{Q}}^{\mathrm{c}}(\mathbf{u})$ is required

$$ {}_{V}\mathbf{Q}_{\mathrm{lat}}^{\mathrm{guid}} \equiv \bar{\mathbf{Q}}^{\mathrm{c}}\left(\mathbf{u}^{\mathrm{guid}}\right) \ . \tag{4.10} $$

The required equivalence of the generalized lateral guidance force ${}_{V}\mathbf{Q}_{\mathrm{lat}}^{\mathrm{guid}}$ containing the lateral force ${}_{V}F_{y}^{\mathrm{guid}}$ and the yaw moment ${}_{V}M_{z}^{\mathrm{guid}}$ and the control inputs, being the steering angle δ and the yaw moments due to differential braking at the front and at the rear axle $M_{\Delta F_x}^{F}$ and $M_{\Delta F_x}^{R}$, respectively, is visualized in Figure 4.2. Notice that longitudinal forces at the tires other than the differential braking forces are not considered as only lateral vehicle guidance is intended.

To sum up, the required equivalence in Equation (4.10) gives *two* equations while *three* control inputs for lateral vehicle dynamics are available. Hence, an additional condition is necessary to solve for the control inputs. A natural choice is to prescribe the distribution of differential braking at front and rear axle. In doing so, a static characteristic curve can be defined or the distribution can be chosen to be dependent on the dynamic handling characteristics of the vehicle.

4.2.2 Linear Mapping

Recalling the equations of motion (2.37)

$$ \mathbf{M}\,\dot{\mathbf{v}} + \left[\mathbf{G}\left(U_x\right) + \mathbf{D}\left(U_x\right)\right]\mathbf{v} = \mathbf{B}\,\mathbf{u} \tag{4.11} $$

of the linear single-track model, it is obvious that the control inputs $\mathbf{u}$ are already decoupled from the dynamic states of the vehicle. Thus, the required equivalence of the generalized virtual guidance force ${}_{V}\mathbf{Q}_{\mathrm{lat}}^{\mathrm{guid}}$ and the right hand side of Equation (4.11),

$$ {}_{V}\mathbf{Q}_{\mathrm{lat}}^{\mathrm{guid}} = \begin{bmatrix} {}_{V}F_{y}^{\mathrm{guid}} \\ {}_{V}M_{z}^{\mathrm{guid}} \end{bmatrix} \equiv \mathbf{B}\,\mathbf{u}^{\mathrm{guid}} = \begin{bmatrix} C_{\alpha}^{F}\delta \\ aC_{\alpha}^{F}\delta + M_{\Delta F_x}^{F} + M_{\Delta F_x}^{R} \end{bmatrix} \tag{4.12} $$

gives again *two* equations for the *three* control inputs δ, $M^F_{\Delta F_x}$, and $M^R_{\Delta F_x}$. Again, prescribing a distribution, $M^F_{\Delta F_x} = f\left(M^R_{\Delta F_x}\right)$, of the differential braking gives the additional condition to solve Equation (4.12) for the control inputs.

The structure of the potential field guidance control is depicted in Figure 4.3. The path $\mathcal{P}$, representing the configuration level of the trajectory planned by the driver and the potential field motion planning, see Chapter 3, is compared to the actual states of the vehicle ${}_R\mathbf{q}$ and ${}_R\dot{\mathbf{q}}$. Recall that the path $\mathcal{P}$ is only recalculated in intervals of ΔT, where K labels the version of $\mathcal{P}$; the pseudo-code of the motion planning is given in Section 3.4. The comparison of the actual vehicle states and the planned path $\mathcal{P}$, in Figure 4.3 denoted as $\ominus$, yields the path tracking error and is addressed in the next section. Based on the path tracking error ${}_G\Delta\mathbf{q}_{\text{lat}}$ the guidance potential field and therefore the virtual guidance force is computed. The virtual guidance force ${}_G\mathbf{Q}^{\text{guid}}_{\text{lat}}$ is then mapped on the control inputs $\mathbf{u}^{\text{guid}}$ of the vehicle.

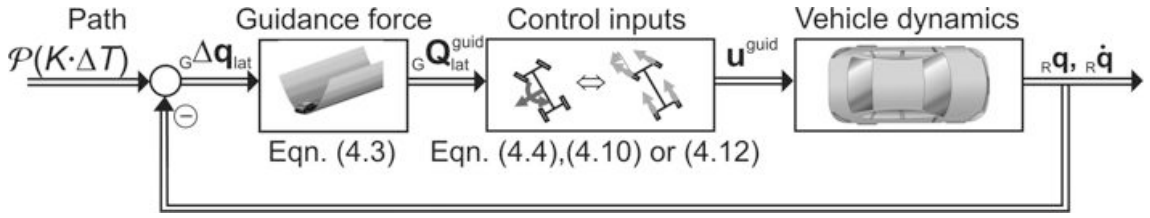

Figure 4.3: Structure of potential field guidance control

4.3 Path Tracking Error

The motion planning provides the path $\mathcal{P}$ for the next planning horizon $t \in [t_0,\ t_f]$[1] with respect to $\underline{\uparrow\mathrm{R}}$,

$$\mathbf{r}^{R^*,G^*} = {}_Rx\,{}_R\mathbf{e}_x + {}_Ry^{G^*}({}_Rx)\,{}_R\mathbf{e}_y \quad \text{with tangent orientation} \quad {}^R\psi^G = \arctan\left({}_Ry^{G\prime}\left({}_Rx\right)\right)\ . \tag{4.13}$$

Therein, the notation $(\cdot)' = \frac{\mathrm{d}}{\mathrm{d}_R x}(\cdot)$ is used. For any instant $t \in [t_0,\ t_f]$ position and orientation of the vehicle in $\underline{\uparrow\mathrm{R}}$ may be given by

$$\mathbf{r}^{R^*,V^*}(t) = {}_Rx^{V^*}(t)\,{}_R\mathbf{e}_x + {}_Ry^{V^*}(t)\,{}_R\mathbf{e}_y \quad \text{and} \quad {}^R\psi^V(t)\ . \tag{4.14}$$

The origin G^* of the guidance frame $\underline{\uparrow\mathrm{G}}$ is identical to that point on $\mathcal{P}$ having the smallest distance to the actual position of the vehicle, represented by V^*; this situation is depicted in Figure 4.4.

[1]Note that t_f denotes the point in time until that the trajectory is planned, while ΔT refers to the time after that the motion planning is updated.

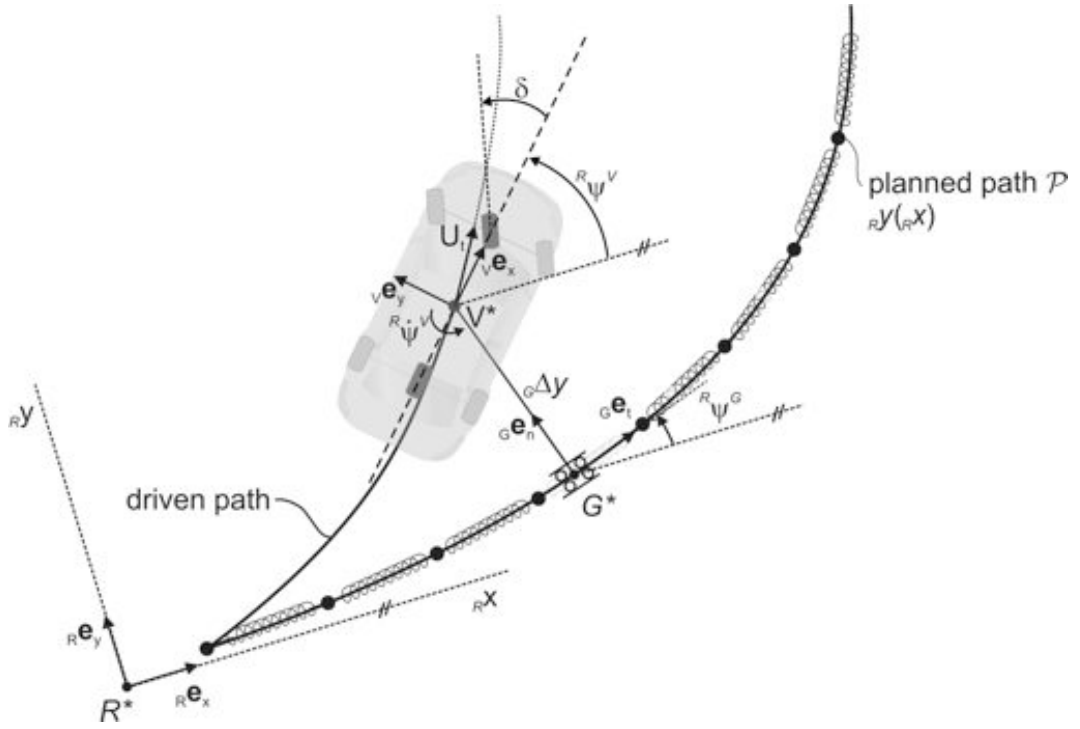

Figure 4.4: Geometry of vehicle guidance problem

Therefore, the desired position and orientation of the vehicle on $\mathcal{P}$ are given by

$$\mathbf{r}^{R^*,G^*}(t) = {}_R x^{G^*}(t)\,{}_R\mathbf{e}_x + {}_R y^{G^*}\left({}_R x^{G^*}(t)\right){}_R\mathbf{e}_y \text{ and } {}^R\psi^G(t) = \arctan\left({}_R y^{G^{*\prime}}\left({}_R x^{G^*}(t)\right)\right), \tag{4.15}$$

where the coordinate ${}_R x^{G^*}(t)$ satisfies the minimum condition

$$\mathbf{r}^{G^*,V^*} = \left\{ \mathbf{r}^{G,V^*} \mid \left\| \mathbf{r}^{R^*,V^*} - \mathbf{r}^{R^*,G} \right\| = \min_{{}_R x \in [0,\, L]} \left\| \mathbf{r}^{R^*,V^*} - \mathbf{r}^{R^*,G}\left({}_R x\right) \right\| \right\}. \tag{4.16}$$

Defining the set of mutually perpendicular unit vectors of $\underrightarrow{\mathrm{G}}$,

$${}_G\mathbf{e}_t := \frac{\mathbf{r}^{R^*,G^{*\prime}}}{|\mathbf{r}^{R^*,G^{*\prime}}|} = \frac{{}_R\mathbf{e}_x + {}_R y^{G^{*\prime}}\,{}_R\mathbf{e}_y}{\sqrt{1+({}_R y^{G^{*\prime}})^2}} \quad \text{and} \quad {}_G\mathbf{e}_n := \frac{-{}_R y^{G^{*\prime}}\,{}_R\mathbf{e}_x + {}_R\mathbf{e}_y}{\sqrt{1+({}_R y^{G^{*\prime}})^2}}, \tag{4.17}$$

being tangential and normal to $\mathcal{P}$

$$\left|\mathbf{r}^{R^*,V^*} - \mathbf{r}^{R^*,G^*}\right| \cdot {}_G\mathbf{e}_t\left({}_R x^{G^*}\right) = 0, \tag{4.18}$$

must hold and results in

$$\left[{}_R x^{V^*} - {}_R x^{G^*}\right] + \left[{}_R y^{V^*} - {}_R y^{G^*}({}_R x^{G^*})\right]_R y^{G^{*\prime}}({}_R x^{G^*}) = 0. \tag{4.19}$$

Therefore, the arrays containing the actual state and the desired state of the vehicle with respect to $\underrightarrow{\mathrm{R}}$ can be defined as

$${}_R\mathbf{q}(t) := \left[{}_R x^{V^*}(t),\ {}_R y^{V^*}(t),\ {}^R\psi^V(t)\right]^{\mathrm{T}} \quad \text{and} \quad {}_R\mathbf{q}_{\mathrm{des}}(t) := \left[{}_R x^{G^*}(t),\ {}_R y^{G^*}(t),\ {}^R\psi^G(t)\right]^{\mathrm{T}}. \tag{4.20}$$

The tracking error becomes

$$ {}_{R}\Delta\mathbf{q}\,(t) = {}_{R}\mathbf{q}\,(t) - {}_{R}\mathbf{q}_{\mathrm{des}}\,(t)\ . \tag{4.21} $$

To formulate potential field control laws in terms of the guidance frame $\underset{\rightarrow}{\uparrow\mathrm{G}}$ the tracking error has to be transformed according to

$$ {}_{G}\Delta\mathbf{q}\,(t) = \mathbf{C}^{G,R}\,{}_{R}\Delta\mathbf{q}\,(t) \quad \text{with} \quad \mathbf{C}^{G,R} = \begin{bmatrix} \cos{}^{R}\psi^{G}(t) & \sin{}^{R}\psi^{G}(t) & 0 \\ -\sin{}^{R}\psi^{G}(t) & \cos{}^{R}\psi^{G}(t) & 0 \\ 0 & 0 & 1 \end{bmatrix}\ . \tag{4.22} $$

As the longitudinal guidance of the vehicle remains with the driver, only the lateral tracking error, see Figure 4.4, is necessary for guidance control and is defined as

$$ {}_{G}\Delta\mathbf{q}_{\mathrm{lat}}\,(t) := \left[\,{}_{G}\Delta\mathbf{q}\,(t)\right]_{(y,\,\psi)} = \begin{bmatrix} {}_{G}\Delta y(t) \\ {}_{G}\Delta\psi(t) \end{bmatrix} = \begin{bmatrix} -\sin{}^{R}\psi^{G}(t)\,({}_{R}x^{V^*}(t) - {}_{R}x^{G^*}(t)) + \cos{}^{R}\psi^{G}(t)\,({}_{R}y^{V^*}(t) - {}_{R}y^{G^*}(t)) \\ {}^{R}\psi^{V}(t) - {}^{R}\psi^{G}(t) \end{bmatrix}\ . \tag{4.23} $$

Notice that the first equation

$$ {}_{G}\Delta x(t) = \cos{}^{R}\psi^{G}(t)\,({}_{R}x^{V^*}(t) - {}_{R}x^{G^*}(t)) + \sin{}^{R}\psi^{G}(t)\,({}_{R}y^{V^*}(t) - {}_{R}y^{G^*}(t)) \tag{4.24} $$

is identically fulfilled since ${}_{R}\Delta x^{G^*}(t) = 0$ is demanded and Equation (4.19) holds.

4.4 Guidance Kinematics

In the last section the path tracking error ${}_{G}\Delta\mathbf{q}_{\mathrm{lat}}$ of the vehicle with respect to the planned path $\mathcal{P}$, represented by the guidance frame $\underset{\rightarrow}{\uparrow\mathrm{G}}$, was derived. Based on ${}_{G}\Delta\mathbf{q}_{\mathrm{lat}}$ a guidance potential ${}_{G}V^{\mathrm{guid}}$ was defined in order to generate a generalized virtual guidance force ${}_{V}\mathbf{Q}^{\mathrm{guid}}_{\mathrm{lat}}$, which is mapped onto the control inputs $\mathbf{u}$ of the vehicle model. However, so far lateral guidance control was only addressed at the configuration level. In order to study stability properties of the proposed potential field control scheme, the perturbation equations of motion have to be considered. The discussion of stability properties is prepared by deriving the underlying guidance kinematics.

In order to derive the lateral guidance state variables, ${}_G\Delta\dot{y}$ and ${}_G\Delta\dot{\psi}$, describing the deviation from the desired velocitiy of G^* and from the desired yaw rate $\dot{\psi}_{\text{des}}$ of $\overset{\uparrow}{\underset{\rightarrow}{\text{G}}}$, the velocity of the vehicle, represented by V^*, with respect to $\overset{\uparrow}{\underset{\rightarrow}{\text{G}}}$

$$
\begin{aligned}
{}^{G}\mathbf{v}^{V^*} &= \frac{{}^{G}\mathrm{d}}{\mathrm{d}t}\mathbf{r}^{G^*,V^*} = \frac{{}^{G}\mathrm{d}}{\mathrm{d}t}\mathbf{r}^{R^*,V^*} - \frac{{}^{G}\mathrm{d}}{\mathrm{d}t}\mathbf{r}^{R^*,G^*} && (4.25)\\
&= \frac{{}^{R}\mathrm{d}}{\mathrm{d}t}\mathbf{r}^{R^*,V^*} + {}^{G}\boldsymbol{\omega}^{R} \times \mathbf{r}^{R^*,V^*} - \left[\frac{{}^{R}\mathrm{d}}{\mathrm{d}t}\mathbf{r}^{R^*,G^*} + {}^{G}\boldsymbol{\omega}^{R} \times \mathbf{r}^{R^*,G^*}\right] && (4.26)\\
&= \frac{{}^{R}\mathrm{d}}{\mathrm{d}t}\mathbf{r}^{R^*,V^*} - \frac{{}^{R}\mathrm{d}}{\mathrm{d}t}\mathbf{r}^{R^*,G^*} + {}^{G}\boldsymbol{\omega}^{R} \times \left(\mathbf{r}^{R^*,V^*} - \mathbf{r}^{R^*,G^*}\right) && (4.27)\\
&= {}^{R}\mathbf{v}^{V^*} - {}^{R}\mathbf{v}^{G^*} + {}^{G}\boldsymbol{\omega}^{R} \times \mathbf{r}^{G^*,V^*} && (4.28)
\end{aligned}
$$

is considered.

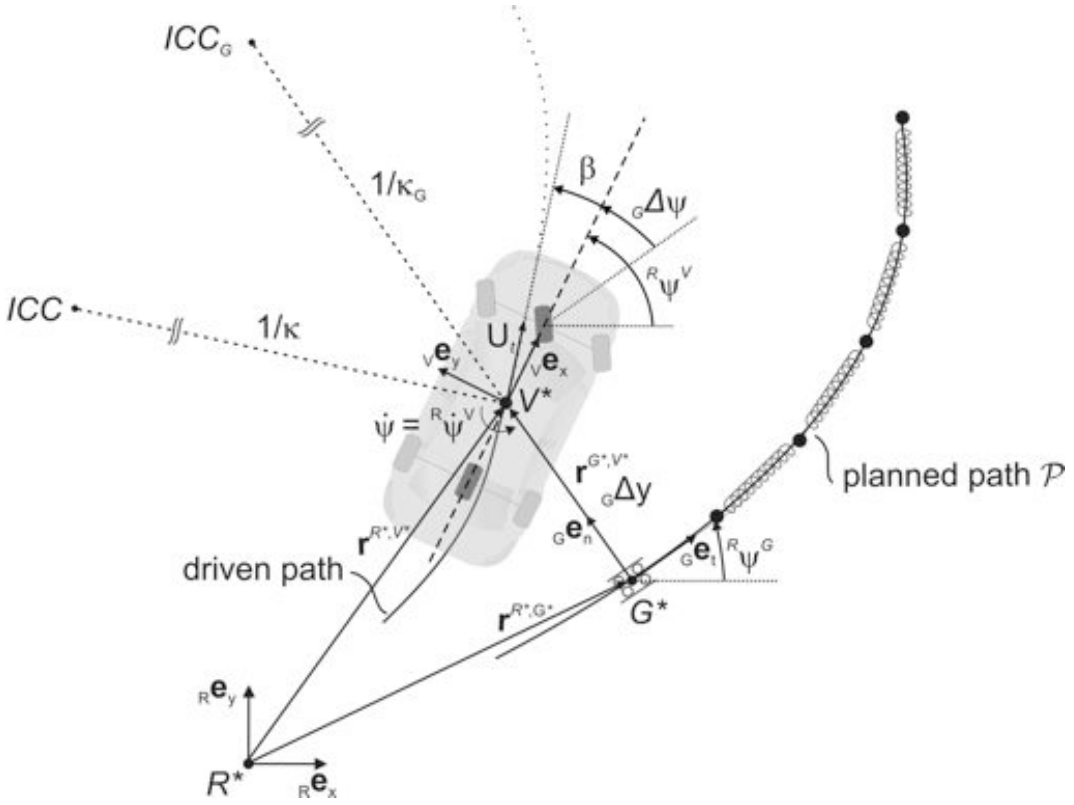

Figure 4.5: Lateral guidance kinematics: host-vehicle and guidance frame $\overset{\uparrow}{\underset{\rightarrow}{\text{G}}}$ rotating about their instantaneous centers of curvature ICC and ICC_G, respectively

The velocity of the guidance frame $\overset{\uparrow}{\underset{\rightarrow}{\text{G}}}$ can be expressed by means of its rotation about its instantaneous center of curvature ICC_G, see Figure 4.5. With

$$
{}^{R}_{G}\mathbf{v}^{G^*} = {}^{R}\boldsymbol{\omega}^{G} \times \mathbf{r}^{ICC_G,G^*} \tag{4.29}
$$

and ${}^{R}\boldsymbol{\omega}^{G} = -{}^{G}\boldsymbol{\omega}^{R}$, Equation (4.28) becomes

$$
{}^{G}\mathbf{v}^{V^*} = {}^{R}\mathbf{v}^{V^*} - {}^{R}\boldsymbol{\omega}^{G} \times \left(\mathbf{r}^{ICC_G,G^*} - \mathbf{r}^{G^*,V^*}\right) . \tag{4.30}
$$

Next, Equation (4.30) is projected on the unit vectors of $\overset{\uparrow}{\underset{\rightarrow}{\mathrm{G}}}$. With the transformation given in Equation (4.4), ${}^{R}\mathbf{v}^{V^*}$ becomes

$$ {}^{R}_{G}\mathbf{v}^{V^*} = (U_x \cos {}_{G}\Delta\psi - U_y \sin {}_{G}\Delta\psi)\ {}_{G}\mathbf{e}_t + (U_x \sin {}_{G}\Delta\psi + U_y \cos {}_{G}\Delta\psi)\ {}_{G}\mathbf{e}_n \ . \tag{4.31} $$

Substituting the position vectors in Equation (4.30) by $\mathbf{r}^{ICC_G,G^*} = -\frac{1}{\kappa_G}\,{}_{G}\mathbf{e}_n$ and by $\mathbf{r}^{G^*,V^*} = {}_{G}\ \Delta y\ {}_{G}\mathbf{e}_n$, see Figure 4.5, and the angular velocity by ${}^{R}\boldsymbol{\omega}^{G} = \dot{\psi}_{\mathrm{des}}\,{}_{G}\mathbf{e}_z$, yields

$$ \begin{aligned} {}^{G}_{G}\mathbf{v}^{V^*} = & \underbrace{\left[U_x \cos {}_{G}\Delta\psi - U_y \sin {}_{G}\Delta\psi - \dot{\psi}_{\mathrm{des}}\left(\frac{1}{\kappa_G} - {}_{G}\Delta y\right)\right]}_{:= {}_{G}\Delta\dot{x}}\ {}_{G}\mathbf{e}_t \\ & + \underbrace{\left[U_x \sin {}_{G}\Delta\psi + U_y \cos {}_{G}\Delta\psi\right]}_{:= {}_{G}\Delta\dot{y}}\ {}_{G}\mathbf{e}_n \ . \end{aligned} \tag{4.32} $$

With the constraint ${}_{G}\Delta\dot{x} = 0$, the desired yaw rate $\dot{\psi}_{\mathrm{des}}$ follows from the ${}_{G}\mathbf{e}_t$-component in Equation (4.32)

$$ \dot{\psi}_{\mathrm{des}} = \frac{U_x \cos {}_{G}\Delta\psi - U_y \sin {}_{G}\Delta\psi}{1/\kappa_G - {}_{G}\Delta y} = \frac{\kappa_G U_x \cos {}_{G}\Delta\psi - \kappa_G U_y \sin {}_{G}\Delta\psi}{1 - \kappa_G\, {}_{G}\Delta y} \ . \tag{4.33} $$

Assuming only small angular deviations, $\cos {}_{G}\Delta\psi \approx 1$ and $\sin {}_{G}\Delta\psi \approx {}_{G}\Delta\psi$, from the planned path $\mathcal{P}$, and ignoring the higher order terms, $\kappa_G \cdot {}_{G}\Delta y \approx 0$ and $\kappa_G \cdot {}_{G}\Delta\psi \approx 0$, the guidance state variables can be written in matrix form

$$ \begin{bmatrix} {}_{G}\Delta\dot{y} \\ {}_{G}\Delta\dot{\psi} \end{bmatrix} = \begin{bmatrix} U_y \\ \dot{\psi} \end{bmatrix} + \begin{bmatrix} {}_{G}\Delta\psi \\ -\kappa_G \end{bmatrix} U_x \tag{4.34} $$

with ${}_{G}\Delta\dot{\psi} = \dot{\psi} - \dot{\psi}_{\mathrm{des}}$. By taking the time derivative of Equation (4.34), the deviation from the planned path $\mathcal{P}$ on the acceleration level becomes

$$ \begin{bmatrix} {}_{G}\Delta\ddot{y} \\ {}_{G}\Delta\ddot{\psi} \end{bmatrix} = \begin{bmatrix} \dot{U}_y \\ \ddot{\psi} \end{bmatrix} + \begin{bmatrix} \dot{\psi}U_x - \kappa_G U_x^2 + {}_{G}\Delta\psi\dot{U}_x \\ -\dot{\kappa}_G U_x - \kappa_G \dot{U}_x \end{bmatrix} \ . \tag{4.35} $$

Notice that in the first equation of (4.35), ${}_{G}\Delta\dot{\psi}$ was replaced by the second equation of (4.34), ${}_{G}\Delta\dot{\psi} = {}_{G}\dot{\psi} - \kappa_G U_x$, and that the term $U_x\dot{\psi}$, see for example Equation (2.18), was taken into account in the derivative. With ${}_{G}\Delta\dot{\mathbf{q}}_{\mathrm{lat}} = \left[{}_{G}\Delta\dot{y},\ {}_{G}\Delta\dot{\psi}\right]^{\mathrm{T}}$, ${}_{G}\Delta\ddot{\mathbf{q}}_{\mathrm{lat}} = \left[{}_{G}\Delta\ddot{y},\ {}_{G}\Delta\ddot{\psi}\right]^{\mathrm{T}}$, $\mathbf{v} = \left[U_y,\ \dot{\psi}\right]^{\mathrm{T}}$, and $\dot{\mathbf{v}} = \left[\dot{U}_y,\ \ddot{\psi}\right]^{\mathrm{T}}$, the guidance states in Equation (4.34) and the time derivatives of the guidance states in Equation (4.35) read

$$ {}_{G}\Delta\dot{\mathbf{q}}_{\mathrm{lat}} = \mathbf{v} + \begin{bmatrix} {}_{G}\Delta\psi \\ -\kappa_G \end{bmatrix} U_x \ , \tag{4.36} $$

$$ {}_{G}\Delta\ddot{\mathbf{q}}_{\mathrm{lat}} = \dot{\mathbf{v}} + \begin{bmatrix} \dot{\psi}U_x - \kappa_G U_x^2 + {}_{G}\Delta\psi\dot{U}_x \\ -\dot{\kappa}_G U_x - \kappa_G \dot{U}_x \end{bmatrix} \ . \tag{4.37} $$

4.5 Guidance Dynamics

Guidance dynamics describe the motion of the vehicle with respect to the planned path $\mathcal{P}$. In order to do so, the deviation from the path on the acceleration level, Equation (4.37), is multiplied by the mass matrix $\mathbf{M}$

$$\mathbf{M}_{G}\Delta\ddot{\mathbf{q}}_{\text{lat}} = \mathbf{M}\dot{\mathbf{v}} + \mathbf{M}\begin{bmatrix} \dot{\psi}U_x - \kappa_G U_x^2 + {}_{G}\Delta\psi\dot{U}_x \\ -\dot{\kappa}_G U_x - \kappa_G \dot{U}_x \end{bmatrix} . \tag{4.38}$$

Recalling the equations of motion of the linear single-track model from Equation (2.37)

$$\mathbf{M}\,\dot{\mathbf{v}} = -\big[\mathbf{G}\,(U_x) + \mathbf{D}\,(U_x)\,\big]\,\mathbf{v} + \mathbf{B}\,\mathbf{u}\,, \tag{4.39}$$

$\mathbf{M}\dot{\mathbf{v}}$ in Equation (4.38) can be replaced by Equation (4.39), leading to

$$\mathbf{M}_{G}\Delta\ddot{\mathbf{q}}_{\text{lat}} = -\big[\mathbf{G}\,(U_x) + \mathbf{D}\,(U_x)\,\big]\,\mathbf{v} + \mathbf{B}\,\mathbf{u} + \mathbf{M}\begin{bmatrix} \dot{\psi}U_x - \kappa_G U_x^2 + {}_{G}\Delta\psi\dot{U}_x \\ -\dot{\kappa}_G U_x - \kappa_G \dot{U}_x \end{bmatrix} . \tag{4.40}$$

Next, inserting $\mathbf{v} = {}_{G}\Delta\dot{\mathbf{q}}_{\text{lat}} - \begin{bmatrix} {}_{G}\Delta\psi,\ -\kappa_G \end{bmatrix}^{\mathrm{T}} U_x$ from Equation (4.36) yields

$$\begin{aligned} \mathbf{M}_{G}\Delta\ddot{\mathbf{q}}_{\text{lat}} \;=\; & -\big[\mathbf{G}\,(U_x) + \mathbf{D}\,(U_x)\,\big]\,{}_{G}\Delta\dot{\mathbf{q}}_{\text{lat}} - \begin{bmatrix} {}_{G}\Delta\psi,\ -\kappa_G \end{bmatrix}^{\mathrm{T}} U_x + \mathbf{B}\,\mathbf{u} \\ & + \mathbf{M}\begin{bmatrix} \dot{\psi}U_x - \kappa_G U_x^2 + {}_{G}\Delta\psi\dot{U}_x \\ -\dot{\kappa}_G U_x - \kappa_G \dot{U}_x \end{bmatrix} . \end{aligned} \tag{4.41}$$

Rearranging Equation (4.41) in terms of ${}_{G}\Delta\ddot{\mathbf{q}}_{\text{lat}}$, ${}_{G}\Delta\dot{\mathbf{q}}_{\text{lat}}$, ${}_{G}\Delta\mathbf{q}_{\text{lat}}$ and the disturbance vector $\mathbf{z} = [\kappa_G,\ \dot{\kappa}_G]^{\mathrm{T}}$, gives the equations of motion with respect to the planned path $\mathcal{P}$

$$\mathbf{M}\,{}_{G}\Delta\ddot{\mathbf{q}}_{\text{lat}} + \mathbf{D}\,\left(U_x(t)\right)\,{}_{G}\Delta\dot{\mathbf{q}}_{\text{lat}} + \mathbf{K}\,{}_{G}\Delta\mathbf{q}_{\text{lat}} = \mathbf{B}\mathbf{u} + \mathbf{E}\,(U_x(t))\,\mathbf{z} \tag{4.42}$$

with the damping matrix $\mathbf{D}$, see Equation (2.39), and the stiffness matrix $\mathbf{K}$, being

$$\mathbf{D} = \begin{bmatrix} \dfrac{C_\alpha^R + C_\alpha^F}{U_x} & -\dfrac{C_\alpha^R b - C_\alpha^F a}{U_x} \\ -\dfrac{C_\alpha^R b - C_\alpha^F a}{U_x} & \dfrac{C_\alpha^R b^2 + C_\alpha^F a^2}{U_x} \end{bmatrix} \text{ and } \mathbf{K} = \begin{bmatrix} 0 & -\left(C_\alpha^R + m\,\dot{U}_x + C_\alpha^F\right) \\ 0 & C_\alpha^R b - C_\alpha^F a \end{bmatrix} \tag{4.43}$$

and the control matrix $\mathbf{B}$ and the disturbance matrix $\mathbf{E}$, being

$$\mathbf{B} = \begin{bmatrix} C_\alpha^F & 0 \\ C_\alpha^F a & 1 \end{bmatrix} \quad \text{and} \quad \mathbf{E} = \begin{bmatrix} C_\alpha^R\, b - m{U_x}^2 - C_\alpha^F\, a & 0 \\ C_\alpha^F\, a^2 - C_\alpha^R\, b^2 + \dot{U}_x I_z & -I_z U_x \end{bmatrix} . \tag{4.44}$$

Notice that a known distribution of differential braking at front and rear axle is assumed, see Equation (4.12), and therefore $\mathbf{B}$ is quadratic. The control inputs are $\mathbf{u} = [\delta\ M_{\Delta F_x}^{F/R}]^{\mathrm{T}}$.

4.6 Stability Analysis and Controller Design

The general idea of a potential field controller guiding a vehicle along a planned path $\mathcal{P}$ based on the lateral and angular deviation was lined out. Subsequently, guidance kinematics and guidance dynamics were formulated in order to provide the equations of motion of the linear single-track model with respect to $\mathcal{P}$. Now, stability issues of the system are addressed and in this connection a design example of a potential field controller is discussed. The stability analysis is based on Lyapunov's direct method, which is briefly recalled first.

4.6.1 Lyapunov's Direct Method

Lyapunov's direct method is related to the fact that the energy of a dissipative mechanical system with no external force input decreases along any trajectory. The basic idea is to show that a scalar energy-like function L exists, which is positive definite and decreases in a monotone way with time. As L depends on the states of the system, the existence of a function L indicates that the states will saddle down to an equilibrium $\mathbf{x}$. The procedure of showing stability in the sense of Lyapunov for linear as well as for nonlinear systems employs the following results, see VINCENT AND GRANTHAM (1997, [119], p. 217):

Lyapunov's Stability Theorem: *The equilibrium solution at* $\mathbf{x} = \mathbf{0}$ *to a dynamical system* $\dot{\mathbf{x}} = \mathbf{f}(\mathbf{x})$ *is stable if a* C^1 *function* $L(\mathbf{x})$ *can be found satisfying the following conditions in some open region* X *containing the origin as an interior point:*

$$
\begin{array}{ll}
(i) & L(\mathbf{0}) = 0, \\
(ii) & L(\mathbf{x}) > 0 \quad \textit{for all nonzero} \quad \mathbf{x} \in X \quad \textit{and} \\
(iii) & \dot{L}(\mathbf{x}) \leq 0 \quad \textit{for all} \quad \mathbf{x} \in X.
\end{array}
$$

The equilibrium solution $\mathbf{x} = \mathbf{0}$ *is globally asymptotically stable if a function* L *can be found such that (i)-(iii) hold, and*

$$
\begin{array}{ll}
(iv) & \dot{L}(\mathbf{x}) < 0 \quad \textit{for all nonzero} \quad \mathbf{x} \in X \\
 & \textit{and in addition} \\
(v) & L(\mathbf{x}) \to \infty \quad \textit{as} \quad \|\mathbf{x}\| \to \infty, \quad \textit{regardless of direction.}
\end{array}
$$

Condition (v) is referred to as "growth" condition by VINCENT AND GRANTHAM (1997, [119], p. 217) or as radial unboundness by SLOTINE AND LI (1991, [105], p. 65).

A main advantage of Lyapunov's direct method in stability analysis is that it does not require to integrate the equations of motion. Besides that the procedure can be applied to higher dimensional nonlinear systems. However, the main challenge lies in finding a Lyapunov function for the considered system; some techniques for constructing Lyapunov functions are discussed by VINCENT AND GRANTHAM (1997, [119], pp. 221). A natural choice used in Section 4.6.2 is to consider the sum of kinetic and potential energy of the system as candidate Lyapunov function. Then, it has to be shown that the candidate function is a Lyapunov function and therefore satisfies Lyapunov's stability theorem. In the following Lyapunov's direct method is applied to the linear equations of motion of the

single-track model with respect to the planned path $\mathcal{P}$. Lyapunov candidate functions for linear systems are often formulated as quadratic forms

$$L = \mathbf{x}^{\mathrm{T}}\mathbf{P}\mathbf{x}. \tag{4.45}$$

In that context the definiteness of matrices such as $\mathbf{P}$ becomes important in order to check if the candidate function is a Lyapunov function. Here, *Sylvester's theorem* is helpful VINCENT AND GRANTHAM (1997, [119], p. 213):

Sylvester's Theorem: *A symmetric matrix, $\mathbf{P} = \mathbf{P}^{\mathrm{T}}$, and its corresponding quadratic form in Equation (4.45) are positive definite if and only if the determinants of the principle minors are all positive:*

$$|p_{11}| > 0, \quad \begin{vmatrix} p_{11} & p_{12} \\ p_{21} & p_{22} \end{vmatrix} > 0, \quad \dots, \quad \begin{vmatrix} p_{11} & \cdots & p_{1n} \\ \vdots & \ddots & \vdots \\ p_{n1} & \cdots & p_{nn} \end{vmatrix}. \tag{4.46}$$

Noteworthy, the assumption that $\mathbf{P}$ is symmetric is not restrictive as Equation (4.45) can be written equivalently in terms of a symmetric matrix. Considering the symmetric matrix $\mathbf{P}_{\mathrm{sym}} = \frac{1}{2}\left[\mathbf{P} + \mathbf{P}^{\mathrm{T}}\right] = \mathbf{P}_{\mathrm{sym}}^{\mathrm{T}}$ and on the other hand the skew symmetric matrix $\mathbf{P}_{\mathrm{skew}} = \frac{1}{2}\left[\mathbf{P} - \mathbf{P}^{\mathrm{T}}\right] = -\mathbf{P}_{\mathrm{skew}}^{\mathrm{T}}$, Equation (4.45) can be rewritten as

$$L = \mathbf{x}^{\mathrm{T}}\left[\mathbf{P}_{\mathrm{sym}} + \mathbf{P}_{\mathrm{skew}}\right]\mathbf{x}. \tag{4.47}$$

Since $\mathbf{x}^{\mathrm{T}}\,\mathbf{P}_{\mathrm{skew}}\,\mathbf{x} \equiv 0$, it follows

$$L = \mathbf{x}^{\mathrm{T}}\,\mathbf{P}\,\mathbf{x} = \mathbf{x}^{\mathrm{T}}\,\mathbf{P}_{\mathrm{sym}}\,\mathbf{x}. \tag{4.48}$$

4.6.2 Stability Analysis

An important prerequisite to apply Lyapunov's direct method is to ensure that no energy is transferred into the system by external disturbances. Otherwise the existence of Lyapunov functions cannot be guaranteed. Hence, the control input in Equation (4.42) is split into two parts, $\mathbf{u} = \mathbf{u}^{\mathrm{guid}} + \mathbf{u}^{\mathrm{dr}}$. The first part $\mathbf{u}^{\mathrm{guid}}$ is the map of the generalized virtual guidance force ${}_{V}\mathbf{Q}_{\mathrm{lat}}^{\mathrm{guid}}$, see Equation (4.4), regulating the path tracking error ${}_{G}\Delta\mathbf{q}_{\mathrm{lat}}(t)$, which is given in Equation (4.23). The second part $\mathbf{u}^{\mathrm{dr}}$ is then used to reject external disturbances $\mathbf{z} = \left[\kappa_G,\ \dot{\kappa}_G\right]^{\mathrm{T}}$. For linear time-variant systems as the equations of motion with respect to the planned path $\mathcal{P}$, recall Equation (4.42)

$$\mathbf{M}_G\Delta\ddot{\mathbf{q}}_{\mathrm{lat}} + \mathbf{D}\left(U_x(t)\right)_G\Delta\dot{\mathbf{q}}_{\mathrm{lat}} + \mathbf{K}_G\Delta\mathbf{q}_{\mathrm{lat}} = \mathbf{B}\mathbf{u} + \mathbf{E}\left(U_x(t)\right)\mathbf{z}\ , \tag{4.49}$$

the disturbance rejection, see FÖLLINGER (1994, [36], p. 518), is given by

$$\mathbf{B}\mathbf{u}^{\mathrm{dr}} + \mathbf{E}\big(U_x(t)\big)\,\mathbf{z} = \mathbf{0} \qquad \Rightarrow \qquad \mathbf{u}^{\mathrm{dr}} = -\mathbf{B}^{-1}\mathbf{E}\big(U_x(t)\big)\,\mathbf{z}\ . \tag{4.50}$$

The resulting control structure is depicted in Figure 4.6.

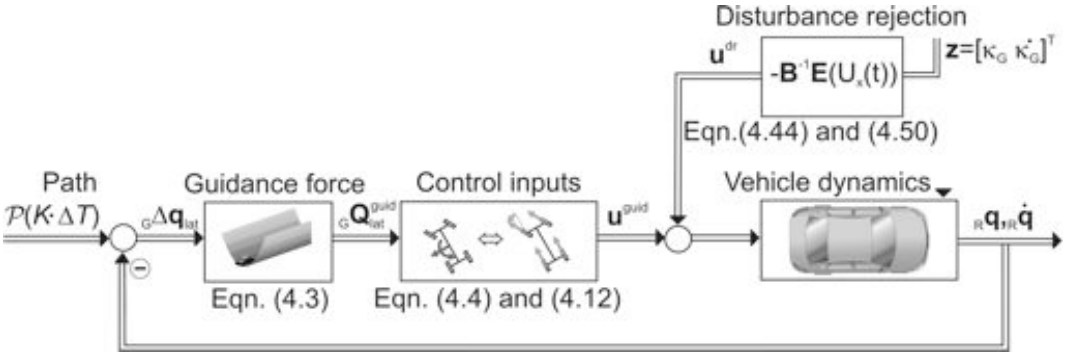

Figure 4.6: Control loop with potential field control and disturbance rejection

Thus, disturbances due to curvature κ_G and curvature rate $\dot{\kappa}_G$ are eliminated from the system. The potential field guidance controller only has to compensate for the remaining disturbances, as for example due to side wind or bank. Recalling the generalized virtual guidance force and the linear map on the control inputs

$$ {}_G\mathbf{Q}_{\text{lat}}^{\text{guid}} = -\mathbf{K}^{\text{guid}}\, {}_G\Delta\mathbf{q}_{\text{lat}} \quad \text{with} \quad \mathbf{K}^{\text{guid}} = k^{\text{guid}} \begin{bmatrix} k_{11}^{\text{guid}} & k_{12}^{\text{guid}} \\ k_{21}^{\text{guid}} & k_{22}^{\text{guid}} \end{bmatrix} \quad \text{and} \quad \mathbf{B}\mathbf{u}^{\text{guid}} \equiv {}_G\mathbf{Q}_{\text{lat}}^{\text{guid}} \tag{4.51} $$

from Equation (4.3) and Equation (4.12), the equations of motion of the closed-loop-system become

$$ \mathbf{M}\, {}_G\Delta\ddot{\mathbf{q}}_{\text{lat}} + \mathbf{D}\big(U_x(t)\big)\, \Delta\dot{\mathbf{q}}_{\text{lat}} + \big[\mathbf{K} + \mathbf{K}^{\text{guid}}\big]\, \Delta\mathbf{q}_{\text{lat}} = \mathbf{0} \qquad \text{with} \qquad U_x(t) > 0\,. \tag{4.52} $$

Requiring the longitudinal speed of the vehicle $U_x(t)$, controlled by the driver, to vary slowly and thus neglecting terms incorporating the longitudinal acceleration $\dot{U}_x$ in the equations of motion (4.52), the stiffness and the disturbance matrix become

$$ \mathbf{K} = \begin{bmatrix} 0 & -(C_\alpha^R + C_\alpha^F) \\ 0 & C_\alpha^R b - C_\alpha^F a \end{bmatrix} \quad \text{and} \quad \mathbf{E} = \begin{bmatrix} C_\alpha^R b - m\,U_x^{\,2} - C_\alpha^F a & 0 \\ -C_\alpha^R b^2 + C_\alpha^F a^2 & -I_z\,U_x \end{bmatrix} \tag{4.53} $$

and the following propositions hold.

Proposition 4.1. *For any generalized virtual guidance force* ${}_G\mathbf{Q}_{\text{lat}}^{\text{guid}} = -\mathbf{K}^{\text{guid}}\,{}_G\Delta\mathbf{q}_{\text{lat}}$ *with the components of* $\mathbf{K}^{\text{guid}}$ *satisfying the following conditions*

(*i*) *stiffness scaling factor* $k^{\text{guid}} > 0$,

(*ii*) *lateral stiffness* $k_{11}^{\text{guid}} > 0$,

(*iii*) *lateral-heading coupling stiffness* $k_{12}^{\text{guid}} \in \mathbb{R}$ *chosen arbitrarily* ,

(*iv*) *lateral-heading coupling stiffness* $k_{21}^{\text{guid}} = k_{12}^{\text{guid}} - \dfrac{C_\alpha^F + C_\alpha^R}{k^{\text{guid}}}$ *and*

(*v*) *heading stiffness*

$$k_{22}^{\text{guid}} > \frac{1}{k^{\text{guid}}}\Big[\big(C_\alpha^F\, a - C_\alpha^R\, b\big) + \frac{1}{k^{\text{guid}} k_{11}^{\text{guid}}}\big(C_\alpha^F + C_\alpha^R - k^{\text{guid}} k_{12}^{\text{guid}}\big)^2\Big] ,$$

and with

$$T({}_G\Delta\dot{\mathbf{q}}_{\text{lat}}) := \frac{1}{2}\,{}_G\Delta\dot{\mathbf{q}}_{\text{lat}}^{\text{T}}\mathbf{M}_G\Delta\dot{\mathbf{q}}_{\text{lat}} \tag{4.54}$$

being the kinetic energy of the lateral motion and with

$$V({}_G\Delta\mathbf{q}_{\text{lat}}) := \frac{1}{2}\,{}_G\Delta\mathbf{q}_{\text{lat}}^{\text{T}}\big[\mathbf{K} + \mathbf{K}^{\text{guid}}\big]\,{}_G\Delta\mathbf{q}_{\text{lat}} \tag{4.55}$$

being a potential energy-like function, the function

$$L({}_G\Delta\dot{\mathbf{q}}_{\text{lat}}, {}_G\Delta\mathbf{q}_{\text{lat}}) = T({}_G\Delta\dot{\mathbf{q}}_{\text{lat}}) + V({}_G\Delta\mathbf{q}_{\text{lat}}) \tag{4.56}$$

is a Lyapunov-Function to the linear-time-variant dynamical system in Equation (4.52) with the equilibrium point ${}_G\Delta\mathbf{q}_{\text{lat0}} = [0,0]^{\text{T}}, {}_G\Delta\dot{\mathbf{q}}_{\text{lat0}} = [0,0]^{\text{T}} \quad \forall t \geq t_0$.

Proof. To be a Lyapunov-Function the following conditions must hold, see Section 4.6.1, see also SATTEL AND BRANDT (2007, [95]):

1.) L is positive definite:
The kinetic energy T, given in Equation (4.54), is positive definite. Thus, the components of the controller stiffness matrix $\mathbf{K}^{\text{guid}}$ have to be chosen in order to guarantee that the potential energy-like function V, see Equation (4.55), and therefore the closed loop stiffness matrix $\big(\mathbf{K} + \mathbf{K}^{\text{guid}}\big)$ is positive definite. In order to do so, it is assumed that the closed loop stiffness matrix is symmetric, $\big(\mathbf{K} + \mathbf{K}^{\text{guid}}\big) = \big(\mathbf{K} + \mathbf{K}^{\text{guid}}\big)^{\text{T}}$, which is equivalent to condition (iv) in Proposition 4.1. Then, *Sylvester's theorem* (4.46) guarantees $\big(\mathbf{K} + \mathbf{K}^{\text{guid}}\big)$ to be positive definite for $k^{\text{guid}} > 0$, $k_{11}^{\text{guid}} > 0$, and $\det\big(\mathbf{K} + \mathbf{K}^{\text{guid}}\big) > 0$, which is satisfied by conditions (i), (ii), and (v) in Proposition 4.1.

2.) $\dot{L}$ is negative definite:
The time derivative of L gives $\dot{L} = {}_G\Delta\dot{\mathbf{q}}_{\text{lat}}^{\text{T}}\mathbf{M}_G\Delta\ddot{\mathbf{q}}_{\text{lat}} + {}_G\Delta\dot{\mathbf{q}}_{\text{lat}}^{\text{T}}(\mathbf{K} + \mathbf{K}^{\text{guid}})_G\Delta\mathbf{q}_{\text{lat}}$. Substituting $\mathbf{M}_G\Delta\ddot{\mathbf{q}}_{\text{lat}}$ by Equation (4.52) yields $\dot{L} = -{}_G\Delta\dot{\mathbf{q}}_{\text{lat}}^{\text{T}}\mathbf{D}(U_x)_G\Delta\dot{\mathbf{q}}_{\text{lat}}$. Since $\mathbf{D}(U_x)$ is positive definite, see Equation (2.39), it follows that $\dot{L} < 0$ holds. □

Proposition 4.2. *The equilibrium point* ${}_G\Delta\mathbf{q}_{\text{lat0}} = [0,0]^{\text{T}}, {}_G\Delta\dot{\mathbf{q}}_{\text{lat0}} = [0,0]^{\text{T}} \quad \forall t \geq t_0$ *of Equation (4.52) is Lyapunov-stable.*

Proof. With Proposition 4.1 a Lyapunov-Function L, see Equation (4.56), is given for the linear-time-variant system in Equation (4.52). Then, it follows from Lyapunov's stability theorem, see Section 4.6.1, that the equilibrium point is stable. □

It was shown for the linear-time-variant single-track model that the general potential field controller design given in Section 4.1 yields closed loop dynamics that are stable in the sense of Lyapunov if the guidance stiffness matrix $\mathbf{K}^{\text{guid}}$ satisfies the conditions given in Proposition 4.1. These conditions can be used for controller design. An example implementation is given later in Section 4.6.5.

4.6.3 Steady State Tracking Error

In the last section stability in the sense of Lyapunov with respect to the planned path $\mathcal{P}$ was shown for the linear single-track model guided by a general potential field controller in combination with a disturbance compensation. Now, the remaining steady state tracking error of this control concept is addressed. The equations of motion of the closed loop system were

$$\mathbf{M}\,{}_G\Delta\ddot{\mathbf{q}}_{\text{lat}} + \mathbf{D}\big(U_x(t)\big)\,{}_G\Delta\dot{\mathbf{q}}_{\text{lat}} + \left[\mathbf{K} + \mathbf{K}^{\text{guid}}\right]{}_G\Delta\mathbf{q}_{\text{lat}} = \mathbf{B}\mathbf{u}^{\text{dr}} + \mathbf{E}\left(U_x(t)\right)\mathbf{z}\,. \tag{4.57}$$

In steady state the time derivatives of the lateral tracking error vanish, ${}_G\Delta\dot{\mathbf{q}}_{\text{lat}} = \mathbf{0}$ and ${}_G\Delta\ddot{\mathbf{q}}_{\text{lat}} = \mathbf{0}$. Hence, solving the equation of motion of the closed loop system in Equation (4.57) for the lateral steady state tracking error gives

$${}_G\Delta\mathbf{q}_{\text{lat}} = \left[\mathbf{K} + \mathbf{K}^{\text{guid}}\right]^{-1}\left[\mathbf{B}\mathbf{u}^{\text{dr}} + \mathbf{E}\left(U_x(t)\right)\mathbf{z}\right]\,. \tag{4.58}$$

As the disturbance compensation was defined as

$$\mathbf{u}^{\text{dr}} = -\mathbf{B}^{-1}\mathbf{E}\big(U_x(t)\big)\,\mathbf{z}\,, \tag{4.59}$$

see Equation (4.50), the steady state tracking error with respect to $\mathcal{P}$ is identical zero

$${}_G\Delta\mathbf{q}_{\text{lat}} = \mathbf{0}\,. \tag{4.60}$$

Summarizing, the potential field control concept has no steady state tracking error if the disturbances due to curvature κ_G and curvature rate $\dot{\kappa}_G$ of the planned path are rejected.

4.6.4 A Bound on the Tracking Error - Collision Avoidance

By use of Lyapunov's direct method it was shown that the closed loop system under guidance of the potential field controller is stable at all speeds U_x and has no steady state tracking error if disturbances due to the planned trajectory $\mathcal{P}$ are compensated. However, the Lyapunov function L, given in Equation (4.56), is extremely powerful as it can be

used to bound the tracking error depending on the initial configuration. This fact was already noticed by ROSSETTER (2003, [93], p. 71) in context with lane-keeping. According to Lyapunov's stability theorem the energy-like Lyapunov function

$$L({}_G\Delta\dot{\mathbf{q}}_{\text{lat}},\, {}_G\Delta\mathbf{q}_{\text{lat}}) = T({}_G\Delta\dot{\mathbf{q}}_{\text{lat}}) + V({}_G\Delta\mathbf{q}_{\text{lat}}) \tag{4.61}$$

cannot increase over time as $\dot{L} \leq 0$ holds by definition. Thus, the maximal possible deviations from the planned path $\mathcal{P}$, representing the configuration level of the elastic band, can occur when the entire initial energy is transferred into the potential energy-like term

$$V \leq L({}_G\Delta\dot{\mathbf{q}}_{\text{lat}}(t),\, {}_G\Delta\mathbf{q}_{\text{lat}}(t)) \leq L({}_G\Delta\dot{\mathbf{q}}_{\text{lat}}(t_0),\, {}_G\Delta\mathbf{q}_{\text{lat}}(t_0))\ . \tag{4.62}$$

Recall that in each adaptation step from elastic band K to elastic band $K+1$ the trajectory does, in general, not start from the current position of the vehicle in order to avoid discontinuities in the control inputs, see Figure 4.7 and Equation (3.40).

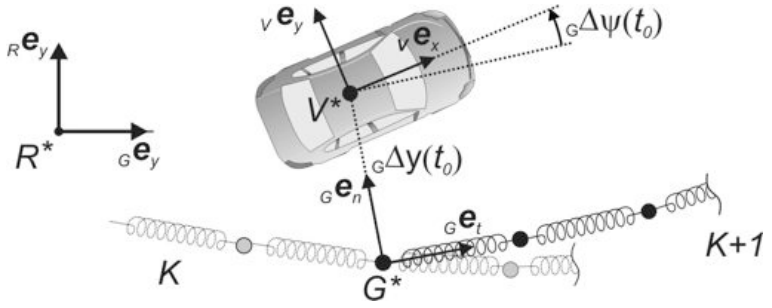

Figure 4.7: Initial deviation from elastic band

To determine the maximal possible lateral deviation ${}_G\Delta y_{\max}$ from the elastic band with respect to the given initial configuration

$$V = \frac{1}{2}\,{}_G\Delta\mathbf{q}_{\text{lat}}^{\text{T}}(t)\left[\mathbf{K} + \mathbf{K}^{\text{guid}}\right]{}_G\Delta\mathbf{q}_{\text{lat}}(t) = L({}_G\Delta\dot{\mathbf{q}}_{\text{lat}}(t_0),\, {}_G\Delta\mathbf{q}_{\text{lat}}(t_0)) \tag{4.63}$$

has to be satisfied. In two dimensions, ${}_G\Delta\mathbf{q}_{\text{lat}} = [{}_G\Delta y,\, {}_G\Delta\psi]^{\text{T}}$, constant contours for the positive definite quadratic form V are ellipses as sketched in Figure 4.8.

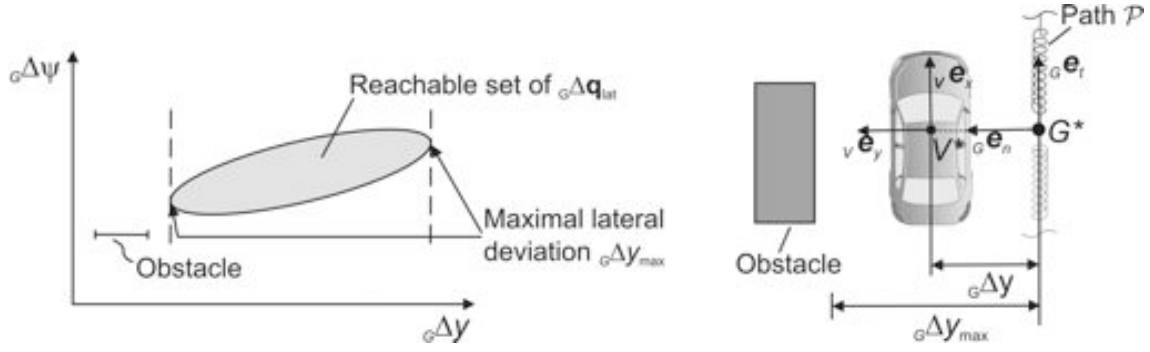

Figure 4.8: Qualitative presentation of the bound for the lateral deviation ${}_G\Delta\mathbf{q}_{\text{lat}}$

With the total initial energy being transferred into the potential energy-like term V, the necessary condition for finding the maximal possible lateral deviation ${}_G\Delta y_{\max}$ is

$$\frac{\partial V}{\partial {}_G\Delta\psi} = \tilde{k}_{12}\,{}_G\Delta y + \tilde{k}_{22}\,{}_G\Delta\psi = 0\ , \tag{4.64}$$

where $\widetilde{\mathbf{K}} := \mathbf{K} + \mathbf{K}^{\text{guid}}$ denotes the closed loop stiffness matrix being composed of the stiffness matrix of the equations of motion $\mathbf{K}$ and the stiffness matrix of the potential field controller $\mathbf{K}^{\text{guid}}$. Thus, the maximal possible lateral deviation ${}_G\Delta y_{\max}$ occurs for

$${}_G\Delta\psi = -\frac{\tilde{k}_{12}}{\tilde{k}_{22}}\,{}_G\Delta y\ . \tag{4.65}$$

Substituting Equation (4.65) into the potential V, see Equation (4.63), yields

$${}_G\Delta y^2_{\max} = \frac{2\,L({}_G\Delta\dot{\mathbf{q}}_{\text{lat}}(t_0),\ {}_G\Delta\mathbf{q}_{\text{lat}}(t_0))}{\tilde{k}_{11} - \tilde{k}_{12}/\tilde{k}_{22}}\ . \tag{4.66}$$

For a given closed loop stiffness matrix $\widetilde{\mathbf{K}}$, Equation (4.66) gives the maximal possible lateral deviation ${}_G\Delta y_{\max}$ to the planned path $\mathcal{P}$ depending on the initial configuration. However, the result can also be used to ensure collision avoidance! With ${}_Gd_{\min}$ describing the closest position of an obstacle with respect to the elastic band $\mathcal{P}$, see Figure 4.8,

$$\tilde{k}_{11} - \frac{\tilde{k}_{12}}{\tilde{k}_{22}} = \frac{2\,L({}_G\Delta\dot{\mathbf{q}}_{\text{lat}}(t_0),\ {}_G\Delta\mathbf{q}_{\text{lat}}(t_0))}{{}_Gd^2_{\min}} \tag{4.67}$$

gives a condition for the components of $\widetilde{\mathbf{K}}$ guaranteeing collision avoidance between the host-vehicle following the elastic band and the closest obstacle. This result is in particular useful as it does not include longitudinal dynamics. The kinetic energy of the longitudinal motion, at least for highway scenarios, is much higher than the kinetic energy of the lateral motion. Therefore, including longitudinal dynamics in the Lyapunov function would lead to more conservative results. However, it has to be emphasized that the preceding analysis only covers linear vehicle dynamics. Furthermore, it was assumed that disturbances are fully rejected.

4.6.5 Sample Controller Design

From the general potential field control concept introduced in the last sections, different implementations can be derived by choosing the parameters of $\mathbf{K}^{\text{guid}}$ according to Proposition 4.1. One possible implementation is illustrated in Figure 4.9. The spring with stiffness k_{lat} symbolizes the potential ${}_GV^{\text{guid}}({}_G\Delta\mathbf{q}_{\text{lat}}) = \frac{1}{2}\,{}_G\Delta\mathbf{q}^{\text{T}}_{\text{lat}}\,\mathbf{K}^{\text{guid}}\,{}_G\Delta\mathbf{q}_{\text{lat}}$ in the lateral deviation, evaluated at the look ahead point LA. In order to scale the lateral guidance force ${}_GF^{\text{guid}}_y$ with respect to the guidance moment ${}_GM^{\text{guid}}_z$, the guidance force is applied at the point LG with $l_{LG} = \lambda \cdot l_{LA}$. This particular controller was proposed by ROSSETTER (2003, [93]).

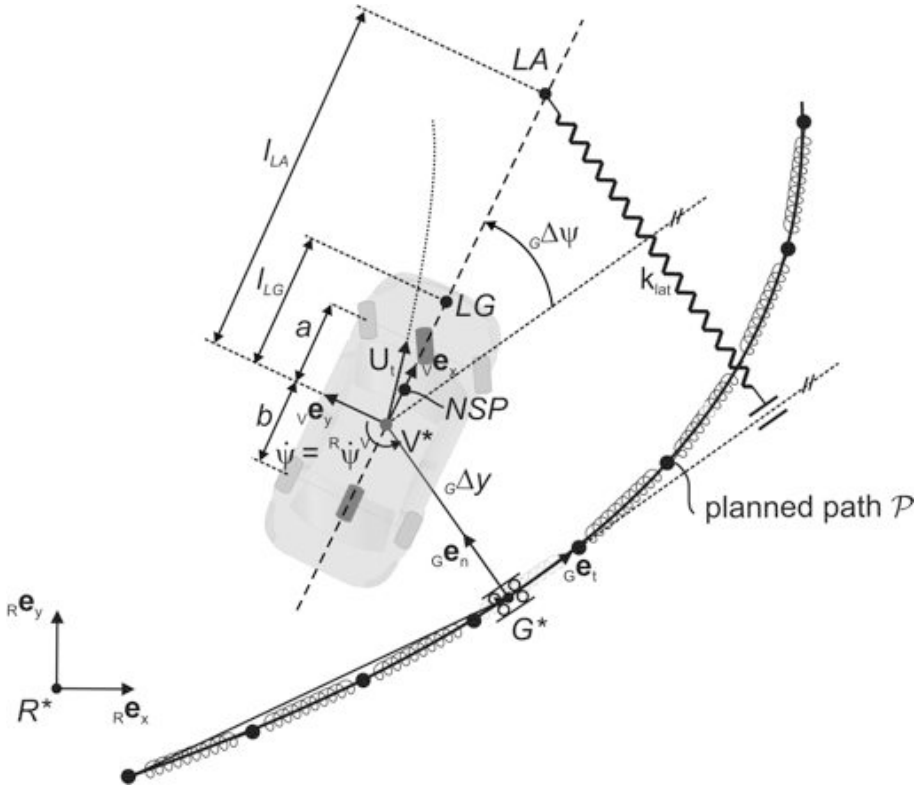

Figure 4.9: Sample potential field controller

The generalized guidance force reads

$$
\begin{aligned}
{}_G\mathbf{Q}_{\text{lat}}^{\text{guid}} \equiv \begin{bmatrix} {}_GF_y^{\text{guid}} \\ {}_GM_z^{\text{guid}} \end{bmatrix} &= -\underbrace{\begin{bmatrix} k_{\text{lat}} & k_{\text{lat}}\, l_{\text{LA}} \\ \lambda\, k_{\text{lat}}\, l_{\text{LA}} & \lambda\, k_{\text{lat}}\, l_{\text{LA}}^2 \end{bmatrix}}_{\mathbf{K}^{\text{guid}}} \begin{bmatrix} {}_G\Delta y \\ {}_G\Delta\psi \end{bmatrix} \\
&= -\begin{bmatrix} k_{\text{lat}}\big({}_G\Delta y + l_{\text{LA}}\,{}_G\Delta\psi\big) \\ \lambda\, k_{\text{lat}}\big({}_G\Delta y + l_{\text{LA}}\,{}_G\Delta\psi\big)\, l_{\text{LA}} \end{bmatrix},
\end{aligned}
\tag{4.68}
$$

where the expression $\big({}_G\Delta y + l_{\text{LA}}\,{}_G\Delta\psi\big)$ corresponds, for small angles $\sin {}_G\Delta\psi \approx {}_G\Delta\psi$, to the length of the spring depicted in Figure 4.9. The guidance moment ${}_GM_z^{\text{guid}}$ is scaled by shifting the point of attack LG of the lateral guidance force.

Applying the conditions in Proposition 4.1 or the underlying requirements $k_{11}^{\text{guid}} > 0$, $\det\big(\mathbf{K} + \mathbf{K}^{\text{guid}}\big) > 0$, and $\big(\mathbf{K} + \mathbf{K}^{\text{guid}}\big) = \big(\mathbf{K} + \mathbf{K}^{\text{guid}}\big)^{\text{T}}$ directly, it can be shown, that the equilibrium point is stable for

$$k_{\text{lat}} > 0 \tag{4.69}$$

$$l_{\text{LG}} > \frac{C_\alpha^F\, a - C_\alpha^R\, b}{C_\alpha^R + C_\alpha^F} =: l_{\text{NSP}} \tag{4.70}$$

$$l_{\text{LA}} = l_{\text{LG}} + \frac{C_\alpha^F + C_\alpha^R}{k_{\text{lat}}}\,. \tag{4.71}$$

The point $l_{\mathrm{NSP}} = \frac{C_\alpha^F a - C_\alpha^R b}{C_\alpha^R + C_\alpha^F}$ in Equation (4.70) has physical significance in being the neutral steer point NSP. The neutral steer point is that location on the centerline of a vehicle where an external force produces no steady state yaw velocity. This concept is often used to discuss sidewind sensitivity of a vehicle, see ZOMOTOR (1991, [128], p. 131), and has a natural interpretation when considering virtual forces and stability. For stability, the virtual force must be applied in front of the neutral steer point of the vehicle. This ensures that the vehicle will rotate in the same direction as the virtual control force points.

The equivalence condition in Equation (4.12) to map the generalized guidance force ${}_G\mathbf{Q}_{\mathrm{lat}}^{\mathrm{guid}}$, see Equation (4.68), on the control inputs reads

$$
\begin{aligned}
{}_V\mathbf{Q}_{\mathrm{lat}}^{\mathrm{guid}} = \mathbf{C}^{V,G}\,{}_G\mathbf{Q}_{\mathrm{lat}}^{\mathrm{guid}} &= -\begin{bmatrix} k_{\mathrm{lat}}\big({}_G\Delta y + l_{\mathrm{LA}}\,{}_G\Delta\psi\big)\cos{}_G\Delta\psi \\ \lambda\, k_{\mathrm{lat}}\big({}_G\Delta y + l_{\mathrm{LA}}\,{}_G\Delta\psi\big)\, l_{\mathrm{LA}}\cos{}_G\Delta\psi \end{bmatrix} \\
&\equiv \begin{bmatrix} C_\alpha^F\delta \\ aC_\alpha^F\delta + M_{\Delta F_x}^F + M_{\Delta F_x}^R \end{bmatrix}.
\end{aligned}
\tag{4.72}
$$

According to the h-metaphor, FLEMISCH ET. AL. (2003, [35]), the intended maneuver should be coordinated with the driver by use of haptic control elements that the driver can access and interpret, in this particular case the steering wheel. However, the map of the potential field guidance law in Equation (4.72) includes steering as well as differential braking, which can hardly be coordinated with the driver. For this reason $M_{\Delta F_x}^F = M_{\Delta F_x}^R = 0$ is chosen. Another beneficial side effect of avoiding differential braking on the guidance level is that conflicts with systems on the stability level, see DONGES (1982, [28]), such as ESP that use differential braking cannot occur. Consequently, the guidance control concept can be combined in a very modular way with systems that act on the stability level. The map on the control inputs, Equation (4.72), results in

$$
{}_V\mathbf{Q}_{\mathrm{lat}}^{\mathrm{guid}} = -\begin{bmatrix} k_{\mathrm{lat}}\big({}_G\Delta y + l_{\mathrm{LA}}\,{}_G\Delta\psi\big)\cos{}_G\Delta\psi \\ \lambda\, l_{\mathrm{LA}} k_{\mathrm{lat}}\big({}_G\Delta y + l_{\mathrm{LA}}\,{}_G\Delta\psi\big)\cos{}_G\Delta\psi \end{bmatrix} \equiv \begin{bmatrix} C_\alpha^F\delta \\ aC_\alpha^F\delta \end{bmatrix}. \tag{4.73}
$$

To fulfill both conditions in Equation (4.73), it is required that the lateral guidance force is applied on the front axle, $\lambda\, l_{\mathrm{LA}} = l_{\mathrm{LG}} = a$. Summarizing, the parameters of this sample controller according to equations (4.69)-(4.71) and Equation (4.73) become

$$
k_{\mathrm{lat}} > 0\,, \quad l_{\mathrm{LG}} = a > l_{\mathrm{NSP}} \quad \text{and} \quad l_{\mathrm{LA}} = l_{\mathrm{LG}} + \frac{C_\alpha^F + C_\alpha^R}{k_{\mathrm{lat}}}\,. \tag{4.74}
$$

The controller stiffness k_{lat} can for example be chosen according to Equation (4.67).

4.6.6 Feedforward Control

In Section 4.6.2 disturbances due to the curvature κ_G and due to the curvature rate $\dot{\kappa}_G$ of the planned path $\mathcal{P}$ were completely rejected by Equation (4.50). However, some remarks should be made:

- As already stated for the potential field guidance controller, the intended maneuver should be coordinated with the driver in accordance to the h-metaphor. Therefore, also the disturbance compensation should only use those control inputs that can be accessed by the driver, in this particular case the steering wheel. However, the disturbance rejection given in Equation (4.50) uses steering as well as differential braking.
- The access of differential braking by the disturbance rejection in Equation (4.50) as part of the guidance control scheme can lead to confusion with systems on the stability level such as ESP that also access differential braking.
- It cannot be guaranteed that the yaw moment implied by the steering angle δ and by differential braking $M_{\Delta F_x}^{F/R}$ have the same orientation.
- The potential field controller acts on the configuration level and does not require a very costly interpolation of the nodes of the elastic band (for a fairly high number of nodes even a linear interpolation is sufficient). However, the discussed disturbance rejection requires smoothness for curvature and curvature rate. To be continuous in the curvature rate $\dot{\kappa}_G$, a spline interpolation would require interpolation polynomials of order 7 or higher is necessary. Besides the high computational effort, higher order polynomials tend to oscillate between the nodes of the elastic band.

To address these issues, a feedforward control only incorporating the curvature κ_G, but not the curvature rate $\dot{\kappa}_G$, of the planned path $\mathcal{P}$ can be applied. Furthermore, using only the steering angle δ as control input, the driver can directly interpret the intended maneuver of the feedforward controller. By recalling the Ackermann steering angle δ_A from Equation (2.54) and the self steering gradient SG, refer to Equation (2.60), a possible feedforward control reads

$$\delta^{\text{ff}} = \delta_A + SG \cdot {}_G^R a_n^{CG} = (a+b) \cdot \kappa_G + \frac{m\,(C_\alpha^R\, b - C_\alpha^F\, a)}{C_\alpha^F\, C_\alpha^R\, (a+b)} \cdot U_x^2 \kappa_G \,. \tag{4.75}$$

The feedforward steering angle only depends on the curvature κ_G of the planned path $\mathcal{P}$. For low speeds U_x the Ackermann angle dominates, while for understeering vehicles the part incorporating the self steering gradient SG increases with the speed of the vehicle. The control scheme including potential field guidance and feedforward control is visualized in Figure 4.10.

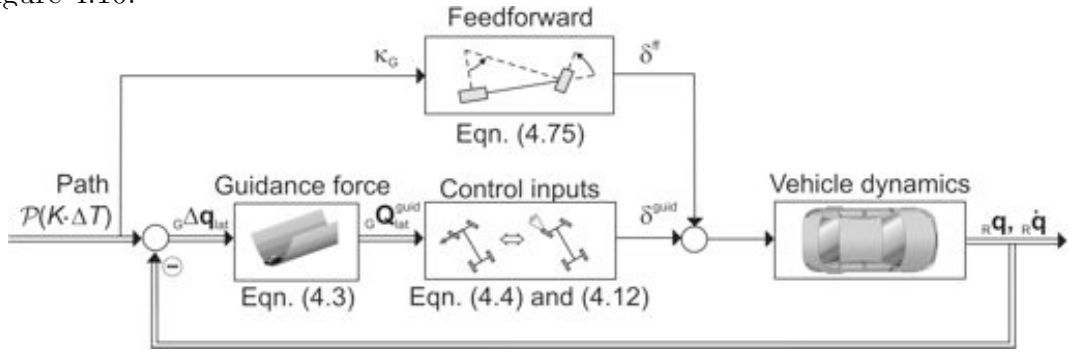

Figure 4.10: Control loop including potential field guidance and feedforward control

4.7 Simulations

The potential field guidance controller described in Section 4.6.5 in combination with disturbance rejection, see Equation (4.50), and with feedforward control, see Equation (4.75), is now illustrated for a double lane change scenario. The course given by splines of seventh order is followed at a longitudinal speed of $U_x = 30\,\mathrm{m/s}$. The intended course and the corresponding curvature κ_G and curvature rate $\dot{\kappa}_G$ are shown in Figure 4.11.

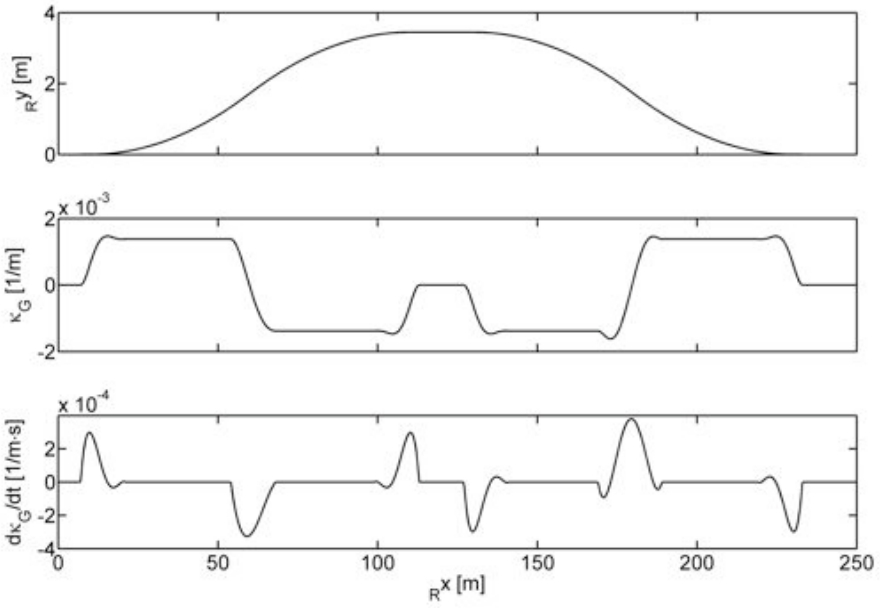

Figure 4.11: Double lane change maneuver with curvature κ_G and curvature rate $\dot{\kappa}_G$

The parameters of the nonlinear single-track model with differential braking used in the simulation are summarized in Table 4.1.

Table 4.1: Vehicle parameters

Parameter	**Symbol**	**Value**
Mass	m	1700 kg
Yaw moment of inertia	I_z	2500 kgm^2
Front axle distance to CG	a	1 m
Rear axle distance to CG	b	1.25 m
Track width	d	1.54 m
Cornering stiffness front tires	C_α^F	63000 N/rad
Cornering stiffness rear tires	C_α^R	63000 N/rad
Longitudinal stiffness front tires	C_x^F	160000 N
Longitudinal stiffness rear tires	C_x^R	160000 N
Effective roll radius	R_0	0.3 m
Wheel moment of inertia	I_{wheel}	0.9 kgm^2
Adhesion coefficient	μ_0	0.87

The potential field guidance controller is parametrized by the values given in Table 4.2, while the parameters of the feedforward controller as well as of the disturbance rejection follow from the vehicle model in Table 4.1.

Table 4.2: Controller parameters

Parameter	**Symbol**	**Value**
Look ahead distance	l_{LA}	35 m
Attack point of lateral guidance force	l_{LG} $(= a)$	1 m
Controller stiffness	k_{lat}	4500 N/m

Figure 4.12 shows the intended and the driven course for the vehicle guided by the potential field controller in combination with the feedforward law in Equation (4.75) based on Ackermann steering and the self steering gradient. The resulting steering angle, $\delta = \delta^{\mathrm{guid}} + \delta^{\mathrm{ff}}$, as well as the control inputs from the potential field controller δ^{guid} and from the feedforward controller δ^{ff} are depicted in the second part of the figure. In steady state, at constant curvatures κ_G, compare to Figure 4.11, the vehicle is guided by the feedforward controller. In transient phases from one constant curvature κ_G to another the resulting steering angle is dominated by the potential field controller regulating deviations from the intended course. The lateral deviation ${}_G\Delta y$ as well as the angular deviation are fairly low with maximal values of about 0.2 m and 0.5°, respectively.

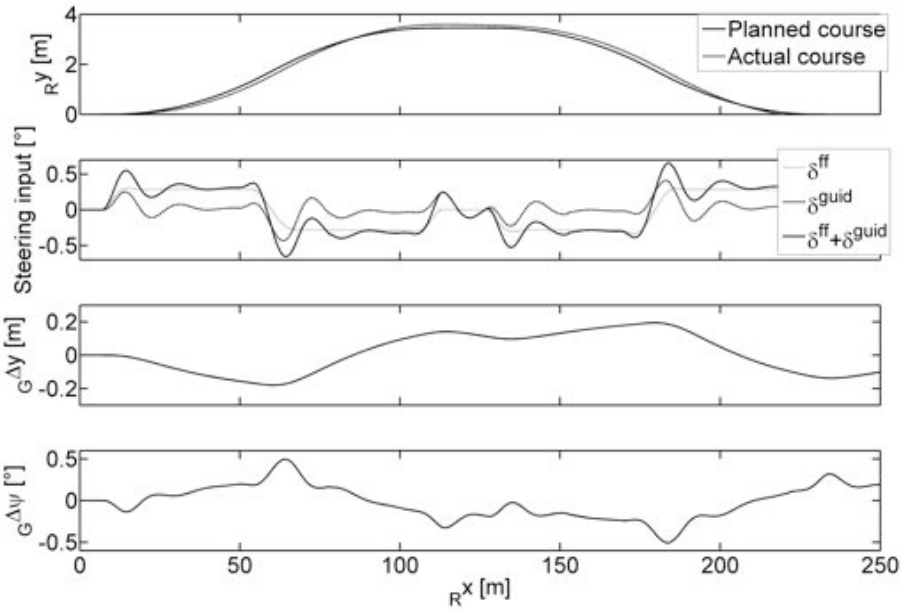

Figure 4.12: Double lane change at 30 m/s with potential field control δ^{guid} in combination with feedforward control δ^{ff} according to Equation (4.75)

The lateral acceleration ${}_V a_y$ and the side slip angle β exhibited by the vehicle are given in Figure 4.13. The low level of the lateral acceleration, compare to Section 2.7, indicates that the vehicle dynamics are in the linear range.

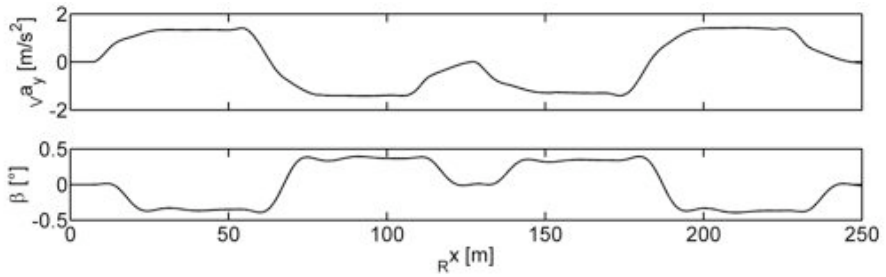

Figure 4.13: Lateral acceleration and side slip angle

Figure 4.14 shows the same maneuver driven by the potential field controller in combination with the disturbance rejection according to Equation (4.50). The disturbance rejection accesses the steering angle as well as differential braking. For simplicity, a fixed distribution applying differential braking solely at the rear axle is assumed. In contrast to the combination of potential field control and feedforward control, the steering angle of the potential field controller δ^{guid} and the disturbance rejection δ^{dr} counteract each other. Besides that, also the differential braking ΔF_x^R and the steering angle provided by the disturbance rejection δ^{dr} cause yaw moments in opposite directions.

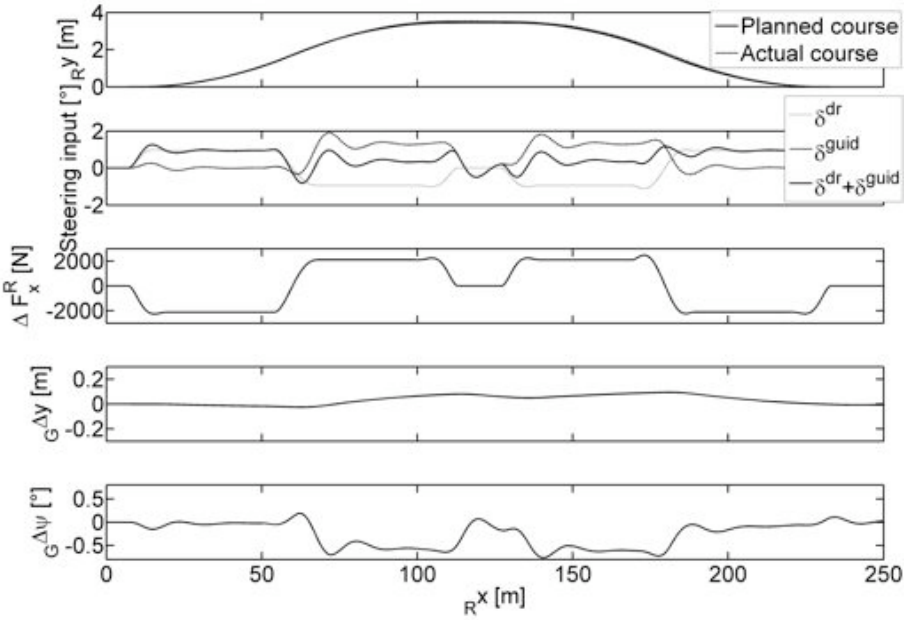

Figure 4.14: Double lane change at 30 m/s with potential field control δ^{guid} in combination with disturbance rejection δ^{dr}

The lateral and the angular deviation are in the same range as for the potential field controller in combination with feedforward control. But the amount of the control inputs is higher. As the resulting steering angle was limited to about 0.5° for the guidance concept consisting of potential field control and feedforward, the resulting steering angle of potential field guidance in combination with the disturbance rejection is about twice as much. Additionally, high differential braking forces of about 2 kN have to be generated. With increasing speed these effects become even more severe.

4.8 Comment on Human Vehicle Guidance

In general, human drivers handle the task of vehicle guidance on two layers: *anticipating* (open-loop) and *compensating* (closed-loop control), see for example MITSCHKE AND WALLENTOWITZ (2004, [74], p. 649). On the anticipation layer the curvature of the road is estimated by means of visual information and the according steering angle is chosen. On the compensation layer lateral deviations from the track are regulated. On roads with low curvature, good vision conditions and in absence of obstacles the anticipating control is dominant. Compared to the control scheme proposed in the last sections, the feedforward controller acts on the anticipation layer, while the potential field controller acts on the compensation layer. However, one difference between the potential field control concept with feedforward compared to human drivers is that drivers usually choose a reference point in some look-ahead distance. This concept could be adopted for guidance control by evaluating the path tracking error in a look-ahead distance. Then, the driven path would additionally be smoothed by the controller. However, large deviations at the look-ahead point, caused by high curvatures of the planned path, can cause local deviations of the vehicle from the planned path in the vicinity of obstacles. This problem becomes particular severe if obstacles are within the look-ahead distance, e.g. in passing maneuvers. Then, the guidance controller could cause collisions as illustrated in Figure 4.15.

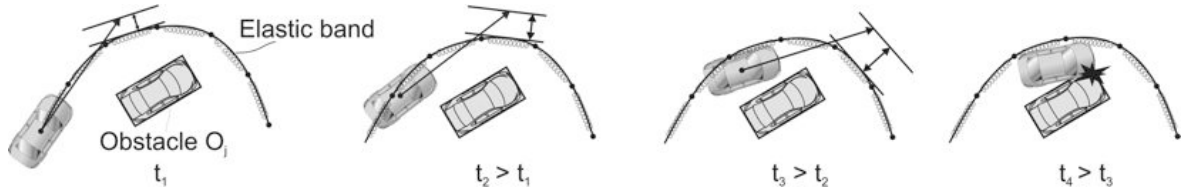

Figure 4.15: Over-steering of the planned path by a guidance controller with look-ahead

The situation depicted in Figure 4.15 could occur if the elastic band guides the host-vehicle around an obstacle and demands, after passing it, to return to the previously occupied lane: at time t_1, the controller predicts a deviation to the left at the look-ahead point, which is caused by the curvature κ_G of the elastic band. Therefore, the controller demands to steer the vehicle to the right, as indicated at time t_2. However, due to the curvature κ_G of the planned path the deviation at the look-ahead point becomes larger. This results in further corrections by the controller. The controller oversteers the planned path due to the look-ahead, which finally leads to a collision at time t_4.

The reference point for the control scheme proposed in the last section was that point on the planned path $\mathcal{P}$ being closest to the actual position of the vehicle, see Section 4.3. For situations as the one sketched in Figure 4.15 this strategy is similar to drivers reducing their look-ahead distance for maneuvers with high intended curvatures. However, in lane-keeping situations, in the absence of obstacles, the proposed control scheme differs from the strategies usually followed by drivers. To resemble the behavior of human drivers, the proposed control scheme could be applied in presence of obstacles, while in lane-keeping situations without obstacles the look-ahead point could be shifted forward. This would be analog to drivers balancing between anticipating and compensating control strategies.

Chapter 5

Shared Vehicle Guidance between Driver and Assistance System

Potential field motion planning and vehicle guidance control provide the basis for driver assistance on the guidance level. In order to guide a vehicle cooperatively with the driver, the guiding strategies of driver and assistance system have to be coordinated via a **H**uman **M**achine **I**nterface (HMI). In the following, the vehicle guidance control loop including driver, assistance system, human machine interface, and a first driving simulator exploration of the potential field based assistance system are presented.

5.1 Vehicle Guidance Control Loop

Driver and assistance system should work cooperatively. Therein, the driver should always be able to override the automation as for example recommended by Griffiths and Gillespie (2004, [44]). In particular, the driver should permanently be kept in the control loop as demanded by the h-metaphor of Flemisch et al. (2003, [35]). Focusing on acceptance, the approach of continuous haptic interaction is further supported by studies showing that systems without feedback to the driver, automatically engaging in vehicle guidance, are not accepted as reported by Wolf, Zöllner and Bubb (2005, [124]).

Figure 5.1 shows how potential field motion planning, lateral guidance control, and driver are embedded in the overall control structure. Therein, the driver remains completely responsible for the longitudinal vehicle dynamics, whereas driver and assistance system cooperate in the lateral vehicle guidance. Throttle and brake pedal forces $\mathbf{F}^{\mathrm{P/D}}$ of the driver are the inputs to the powertrain. The resulting driving and braking torques $\mathbf{M}_{\mathrm{d/b}}$ are control inputs for the longitudinal guidance, which is solely controlled by the driver. The assistance system displays guidance information to the driver via an additional steering wheel torque $M^{\mathrm{SW/A}}$. Hence, the resulting steering angle δ^{SW}, set cooperatively by the driver and the assistance system, corresponds to the equilibrium of torques at the steering wheel. As depicted in Figure 5.1, these torques consist of torques due to vehicle dynamics $M^{\mathrm{SW/V}}$, see for example Equation (2.15), the assistance torque $M^{\mathrm{SW/A}}$, and the torque exerted by the driver $M^{\mathrm{SW/D}}$. The motion planning module adapts to the driver's commands based on the vehicle's states and acceleration $[{}_R\mathbf{q},\ {}_V\mathbf{v},\ {}_V\mathbf{a}]$ as well as on the steering angle δ, as explained in Chapter 3. New trajectories are generated after planning

intervals of $\Delta T < 100\,\text{ms}$. By this means environmental changes can also be incorporated into the motion planning.

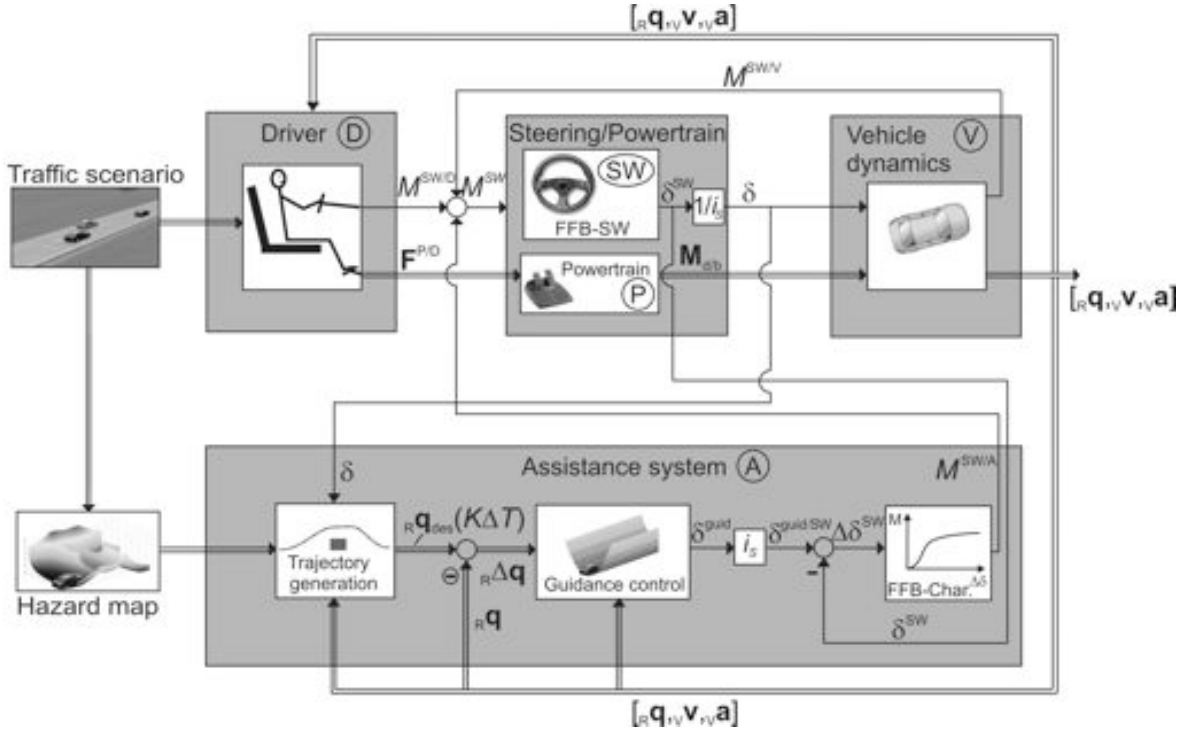

Figure 5.1: Control loop of potential field driver assistance for shared vehicle guidance

The guidance controller regulates position and heading deviation between the desired vehicle configuration, given by ${}_R\mathbf{q}_{\text{des}}$, and the actual vehicle configuration ${}_R\mathbf{q}$. Even without additional driver commands, the potential field controller would be able to guide the vehicle along the predicted trajectory by means of the proposed steering angle δ^{guid}. However, in order to keep the driver in the loop, δ^{guid} is not directly applied to the wheels. In fact, the proposed steering angle δ^{guid}, multiplied by the steering ratio i_S, is compared to the steering angle δ^{SW}, which is currently set at the steering wheel. In order to close the control loop, the difference $\Delta\delta^{\text{SW}}$ between the proposed and the set steering angle is used for haptic rendering. In doing so, the feedback characteristic acts as an impedance, providing the assistance torque $M^{\text{SW/A}}$ displayed to the driver. GRIFFITHS AND GILLESPIE (2004, [44]) define that impedance by using proportional control for a small handwheel that could be turned by one hand. In that case, the force feedback could be considered as a virtual torsion spring between the proposed and the actual steering angle. Noteworthy is, that simulator studies with alternative approaches were also conducted, see for example PENKA (2001, [84]) or POHL AND EKMARK (2003, [85]). In these contributions the feedback to the driver directly depends on the lateral deviation of the vehicle to the desired trajectory. However, approaches without guidance controller seem hardly applicable to evasion maneuvers. For this reason, here too an approach based on a virtual spring is chosen. Though, the stiffness of the virtual torsional spring is adapted as explained in Section 5.2.3. Most notably, the resulting assistance torque $M^{\text{SW/A}}$ can always be overcome by the driver.

5.2 Driving Simulator Exploration

The proposed control structure for shared vehicle guidance was studied in a driving simulator exploration. First, the haptic human machine interface used is presented, followed by the driving simulator setup and first lane-keeping and collision avoidance experiments.

5.2.1 Haptic Human Machine Interface

In the simulator exploration, the haptic human machine interface was realized by a force feedback steering wheel. To determine the requirements on the steering wheel, a brief introduction on human haptics is given first. Therein, the origin of the term haptic, which is broadly used to describe the mechanical interaction of human beings with their environment, goes back to the Greek word *hapteshai*, meaning "to touch". Furthermore, Gillespie (2005, [42]) categorizes haptic interfaces by the terms *tactile* and *kinesthetic* as depicted in Figure 5.2. The adjective tactile describes perceptions primarily served by sensors located in the skin, so-called *cutaneous mechanoceptors*, while the term kinesthetic refers to perceptions served by sensors in muscles and joints, called *muscle spindles* and *Golgi organs*, respectively. In general, manipulation involves tactile as well as kinesthetic perceptions. Nevertheless, haptic interfaces might be classified by their primary function. Thus, ignoring tactile perceptions such as sensing the surface, a force feedback steering wheel could be characterized as kinesthetic interface. Furthermore, a force feedback steering wheel is *grounded*, which refers to the fact that it is rigidly attached to its environment.

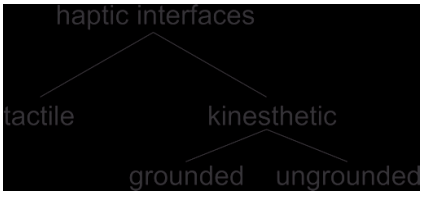

Figure 5.2: Taxonomy of haptic terms, Gillespie (2005, [42])

Besides the high demand on the visual channel, already mentioned in Section 1.1.3, the processing speed of haptic stimuli is another benefit of haptic human machine interaction. The haptic channel is the only one using the spinal cord for low level control, while acoustic and visual information is interpreted by the brain. For this reason, haptic stimuli can be processed within about 50 ms. The processing of visual or acoustic information takes about 200 ms and thus four times longer, see for example Penka (2001, [84], p. 4).

However, in order to define the requirements on the force feedback steering wheel, further information about human haptic performance is necessary. The amplitude of positional detection thresholds for example depends on the rate of change of positional clues. Therein, very slow motions generally provide subliminal stimuli that are not perceived consciously. Though, the resolution of positional clues rises with the frequency. According to Penka (2001, [84], p. 6) amplitudes of 10^{-1} mm can be perceived at 10 Hz, while a frequency of 200 Hz allows a resolution up to 10^{-4} mm.

Here, the force feedback steering wheel displays assistance torques generated by a DC-motor. Therefore, a torque resolution beyond the human detection thresholds is desirable in order to study arbitrary force feedback characteristics. PENKA (2001, [84], p. 7) cites a study, which gives torque detection thresholds in the range of 0.0036 Nm to 0.0054 Nm at a base torque of 0.5 Nm and a range of 0.0072 Nm to 0.009 Nm at a base torque of 1 Nm. These quantities were gained for active side sticks. For steering wheels BUSCHARDT (2003, [15]) reports a "just noticeable difference" in the range of 0.4 Nm to 0.5 Nm and torques of more than 0.8 Nm that are reliably detected by the driver. Further information on detection thresholds can for example be found in DOSHER, LEE AND HANNAFORD (2001, [29]).

Besides the ability to display small haptic effects in the range of the human detection threshold, it should be possible to display haptic information up to a hard stop. Also the ability to display high torque amplitudes is desired. For this reason the high performance "Active Steering Wheel System" developed by STIRLING DYNAMICS (2005, [115]) was chosen for the simulator experiments. In a range up to 8 Nm, a DC-motor is precisely controlled by a feedback controller based on a torque sensor. Beyond the range of 8 Nm the DC-motor generates torques up to 38 Nm in open loop mode. Characteristic technical data of the "Active Steering Wheel System" are collected in Table 5.1.

Table 5.1: Technical data of the "Active Steering Wheel System", (2005, [115])

Performance		
Max. Torque		38Nm at 12DC and 25°C
Torque Response		38Nm at 300°/s
		20Nm at 600°/s
Maximum Velocity		1000°/s
Input Signals		
Open Loop Torque Demand	Range	±35Nm
	Accuracy	-
Closed Loop Torque Demand	Range	±8Nm
	Accuracy	±0.001Nm
Output Signals		
Column Angle	Range	±1600°
	Accuracy	±0.1°
Column Rate	Range	±5rps
	Accuracy	±0.001rps
Column Torque	Range	±8Nm
	Accuracy	±0.001Nm

5.2.2 Driving Simulator Setup

The hardware and software architecture of the fixed-based driving simulator is summarized in Figure 5.3. The visualization is established by three Epson EMP-9100® projectors, which are rigidly mounted at the ceiling and project the traffic scenario on three 2.05 m × 2.62 m screens. The test subjects control the driving speed by means of Logitech MOMO® throttle and brake pedals, while for lateral guidance a force feedback steering wheel is used as described in the last section. The pedals are directly connected to the server by the **U**niversal **S**erial **B**us (USB), while the force feedback steering wheel signals are converted from the **C**ontroller **A**rea **N**etwork (CAN) to USB first. The simulation is distributed on three dual processor PCs at 3.2 GHz clock rate and 2 GB main memory each. One computer acts as server, the two clients are connected to the server via ethernet using the **U**ser **D**ata **P**rotocol (UDP).

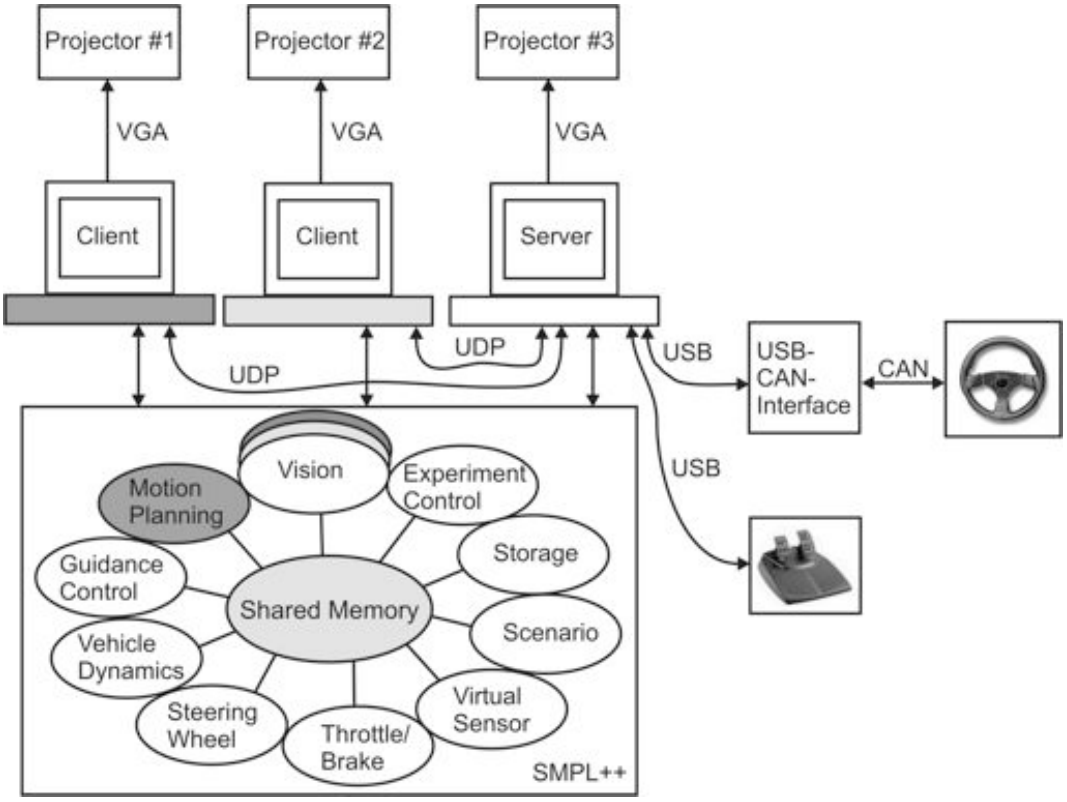

Figure 5.3: Simulator hardware and software architecture

The software architecture is based on the **S**traightforward **M**odular **P**rototyping **L**ibrary (*SMPL++*)[1], which is a C++ library that can be used conveniently for rapid prototyping of driver assistance systems. Due to the modular design new modules can very easily be integrated into the framework. Therein, the different modules communicate via a `Shared Memory` as depicted in Figure 5.3. The `Shared Memory` provides a common data basis with read and write access for the different modules.

[1]SMPL++ was provided by courtesy of the group headed by Dr. F. Flemisch at the German Aerospace Center (DLR)

In order to realize an equal processing load, the modules can be distributed on the available computers. Furthermore, the execution of the modules can be ranked by a priority flag. Figure 5.3 shows a possible distribution of the single modules on the three machines. The computationally intensive `Motion Planning` and one of the three `Vision` modules share for example an entire machine as indicated by the shading in Figure 5.3.

For the exploration the modules depicted in Figure 5.3 were included. Therein, `Motion Planning` based on methods described in Chapter 3, `Guidance Control` in a version with look-ahead, see Section 4.8, and `Vehicle Dynamics` play the same role as in Figure 5.1. The modules `Steering Wheel` and `Throttle/Brake` control the interfaces to the driver. While the `Throttle/Brake` module only reads the driver's inputs, the `Steering Wheel` module also contains the force feedback characteristic and computes the assistance torque $M^{\mathrm{SW/A}}$ displayed to the driver. The `Scenario` module contains the course of the road as well as information about possible obstacles. Further on, the `Virtual Sensor` emulates a sensor concept providing information about the course of the road and the obstacles. This information is used by the `Motion Planning` and `Guidance Control` modules. The three channel visualization is generated by the three `Vision` modules. The `Experiment Control` allows the instructor to control the exploration, e.g. different assistant torque characteristics or scenarios can be chosen. Simulation data are saved for analysis purposes by the `Storage` module.

Figure 5.4 a) shows a photo of the fixed-based driving simulator. In the foreground a test subject in front of the force feedback steering wheel, in the background the experiment control station with the instructor can be seen. Figure 5.4 b) shows the scenery presented to the test subjects.

(a) Test subject and experiment control (b) Scenery displayed to the test subjects

Figure 5.4: Driving simulator

5.2.3 Lane-Keeping and Collision Avoidance Experiments

In the following, the exploration of the potential field based driver assistance system in the fixed-based driving simulator is described. In particular, the haptic communication between the test subjects and the assistance system was studied. In previous simulator studies by Penka (2001, [84]), Buld and Krüger (2002, [13]), and Pohl and Ekmark (2003, [85]) the assistance torque depended directly on the lateral deviation from the lane. One outcome of these studies is that soft assistance torques in a limited range of tolerable deviation lead to the best results. However, the results vary significantly from subject to subject.

Noteworthy, Bender and Landau (2006, [6]) observed in experiments that many drivers do not react at all in critical situations. Hence, they propose that the assistance system should overrule the driver in those situations. However, according to the previous discussions, see Chapter 1, the driver should remain in the vehicle guidance control loop and always be able to override maneuvers proposed by the assistance system. Nevertheless, within the scope of the h-metaphor the degree of assistance should be adapted to the situation. In critical (tight rein) situations the driver should indicate by means of sufficiently high steering torques that he is aware of the situation.

Here, the assistance torque $M^{\mathrm{SW/A}}$ is generated based on the difference $\Delta\delta^{\mathrm{SW}}$ between the steering angle proposed by the assistance system and the actual set steering angle at the steering wheel. A similar design for lane-keeping was studied by Steele and Gillespie (2002, [109]) and Griffiths and Gillespie (2004, [44] and 2005, [45]). This design can be considered as a virtual torsional spring providing a torque $M^{\mathrm{SW/A}}$ depending on the steering angle deviation $\Delta\delta^{\mathrm{SW}}$.

Force Feedback Characteristic

In the exploration, a combination of a continuous base torque depending on the deviation $\Delta\delta^{\mathrm{SW}}$ from the proposed steering angle (virtual spring) and a vibration, initiated after a certain deviation threshold was studied. The intention of the base torque is to communicate the proposed steering strategy to the driver, while the vibration aims at ensuring the drivers attention when a maneuver is performed that does not match with the trajectories planned by the assistance system. The base torque has a linear characteristic without a threshold but with saturation. The vibration can be shaped in different ways: saw tooth and rectangular signal shapes can for example provide additional directional information. However, in pretests it turned out that these signal shapes are often misinterpreted as disturbances such as side wind. Hence, the directional information is rather counterproductive. Therefore, in the experiment sinusoidal vibrations were chosen, which are often similar to the mental model that drivers create for chattermarks. In doing so, two different types of sinusoidal vibration were used. In absence of obstacles a sinusoidal (lane-keeping) vibration with an amplitude of 2 Nm at a frequency of 40 Hz was generated beyond a threshold of $\left|\Delta\delta^{\mathrm{SW}}\right| \geq 15°$. If the virtual environmental sensors detected obstacles, a more aggressive (collision avoidance) vibration was applied in order to ensure the driver's attention: beyond a threshold of $\left|\Delta\delta^{\mathrm{SW}}\right| \geq 15°$ a vibration with an amplitude of 5 Nm at a frequency of 20 Hz was chosen. This design led to a limited range of deviations

of $\Delta\delta^{\mathrm{SW}}$ where the test subjects only experienced the continuous base torque as assistance torque.

For evaluation purposes of the proposed force feedback design and to gather information for further improvements of the force feedback characteristic, two different variants were studied. In order to be able to interpret different results in the exploration, the number of different parameters between both variants was limited. For this reason, only the continuous base torques were altered for ***s**oft **A**ssistance* (sA) and for ***h**ard **A**ssistance* (hA). For soft assistance a slope of 1 Nm/rad and for hard assistance a slope of 8 Nm/rad was used. In both variants the base torque saturated at ±5 Nm. The parameters of the assistance torque settings are summarized in Table 5.2; Figure 5.5 shows the resulting combinations of soft and hard assistance torques $M^{\mathrm{SW/A}}$ with lane-keeping and collision avoidance vibration plotted against the steering angle deviation $\Delta\delta^{\mathrm{SW}}$ and against the time t. Besides that, also test drives where ***n**o **A**ssistance* torque (nA) was applied were performed.

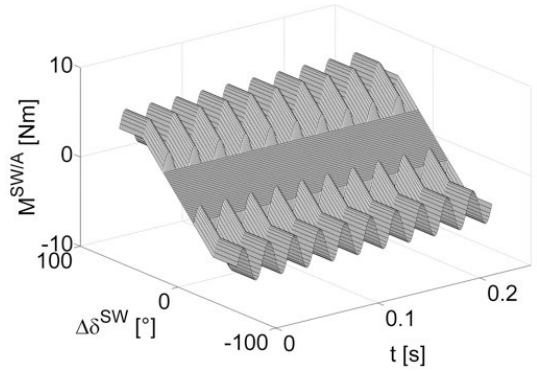

(a) Hard assistance (hA) with lane-keeping vibration

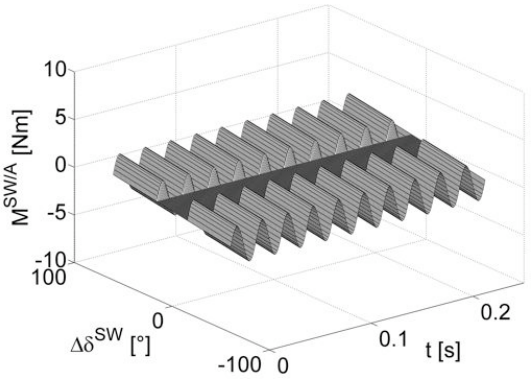

(b) Soft assistance (sA) with lane-keeping vibration

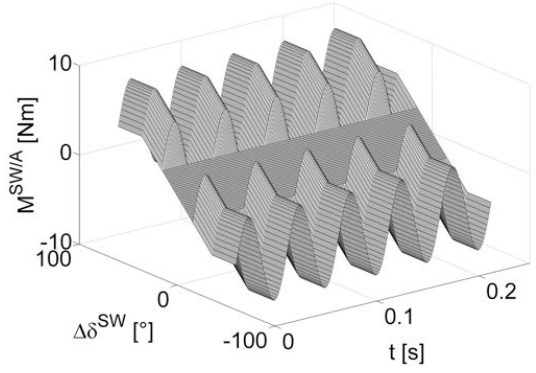

(c) Hard assistance (hA) with collision avoidance vibration

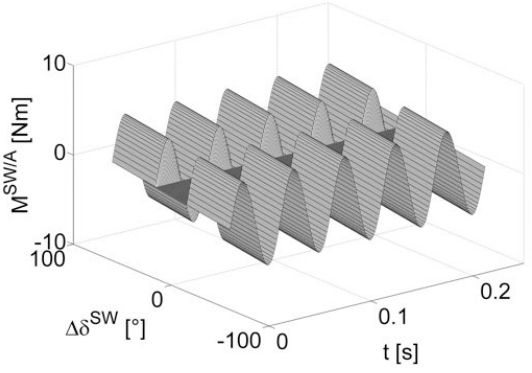

(d) Soft assistance (sA) with collision avoidance vibration

Figure 5.5: Soft and hard assistance torque combined with lane-keeping and collision avoidance vibration

Table 5.2: Parameters of assistance torques

	Base torque		Vibration		
Assistance	Slope	Saturation	Situation	Amplitude	Frequency
hard (hA):	8 Nm/rad	±5 Nm	lane-keeping:	2 Nm	40 Hz
soft (sA):	1 Nm/rad	±5 Nm	lane-keeping:	2 Nm	40 Hz
hard (hA):	8 Nm/rad	±5 Nm	collision avoidance:	5 Nm	20 Hz
soft (sA):	1 Nm/rad	±5 Nm	collision avoidance:	5 Nm	20 Hz

Test Group

The experiment was conducted with a heterogeneous group of sixteen test subjects as depicted in Table 5.3. The test group was split half into female and male test subjects as well as into experienced and unexperienced drivers, half of the test subjects were older than 35.

Table 5.3: Test subjects

Subject-No.	Age	Gender	Driving experience in km
1	26	male	260,000
2	40	male	550,000
3	27	male	150,000
4	39	male	750,000
5	27	female	60,000
6	23	female	50,000
7	36	female	2,000
8	31	female	75,000
9	56	female	216,000
10	28	female	35,000
11	26	female	2,000
12	42	male	1,200,000
13	23	male	25,000
14	49	male	500,000
15	64	male	1,500,000
16	56	female	750,000

Driving and Secondary Task

In this exploration the main focus lay on the lateral vehicle guidance. For this reason, the test subjects were asked to drive at a constant speed of 100 km/h. In order to avoid that the subjects get used to the virtual test track, two different tracks with a different order of left and right turns with radii between 800 m and 1000 m were used. Each of the test tracks depicted in Figure 5.6 had a length of approximately 6 km and therefore a driving time of 4 minutes.

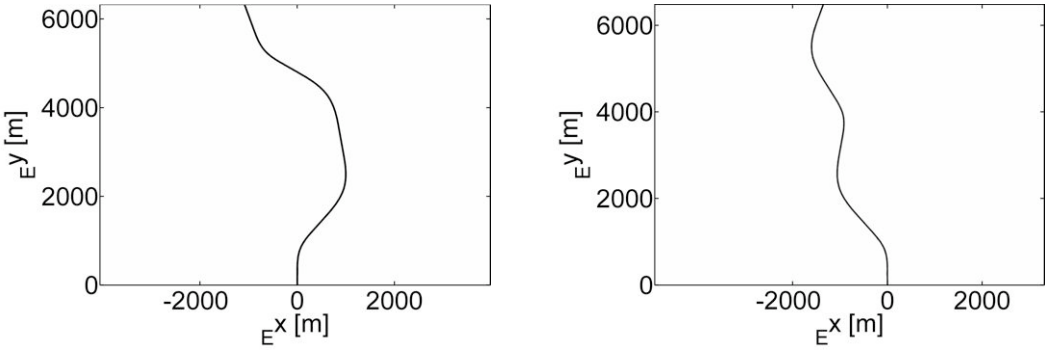

(a) Test track 1 (t1) (b) Test track 2 (t2)

Figure 5.6: Virtual test tracks used in exploration

In each test drive four 2 m x 2 m static obstacles suddenly appeared in front of the virtual test vehicle, see for example Figure 5.4 b). The lateral position of the obstacles as well as the distances in front of the vehicle varied. The obstacles appeared in distances between 80 m and 104 m ahead of the vehicle such that evasion maneuvers at a speed of 100 km/h are always feasible.

To analyze the assistance system under different conditions, the test subjects were asked to handle a secondary task in some of the test drives. In doing so, situations where drivers are inattentive or distracted could be simulated and the effect of the assistance system in these situations could be studied. The secondary task was presented on a display besides the steering wheel. Figure 5.7 shows a test subject in two different experimental configurations. In Figure 5.7 a) the subject is solely driving in the simulator and ***n**o **S**econdary task* (nS) has to be handled. In Figure 5.7 b) the subject is driving ***w**ith **S**econdary task* (wS). The experimental setup was configured in a way that the test subjects could not focus on the driving and on the secondary task at the same time.

(a) Subject solely driving (b) Subject driving and handling secondary task

Figure 5.7: Driving with and without secondary task

In the secondary task, the test subjects got an array of "T"s as shown in Figure 5.8. Within this array one different letter (E, F, H, I, L) appeared at a random position. The test subjects had to identify this letter and to press the corresponding key on the keyboard. For each configuration the test subjects had 10 s time to identify the different letter before the screen cleared and proceeded to the next configuration.

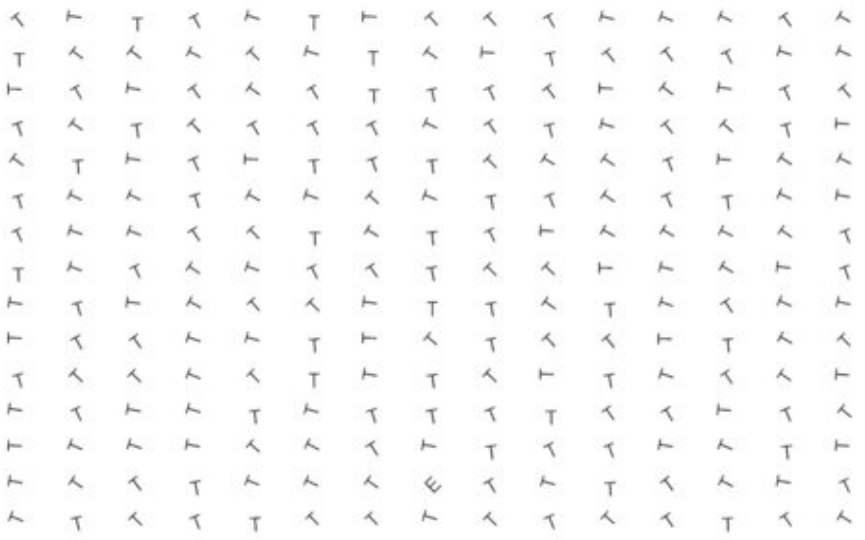

Figure 5.8: Secondary task

Experimental Design

The combination of the different force feedback characteristics (nA, sA, hA), with or without secondary task (wS, nS), with a particular test track (t1, t2) generates the test settings as collected in Table 5.4. Noteworthy, the parameters of motion planning and vehicle guidance control are kept constant in all test settings.

Table 5.4: Test settings

Test setting			**Label**
no assistance (nA)	/ no secondary task (nS)	/ test track 1 (t1)	nA/nS/t1
no assistance (nA)	/ with secondary task (wS)	/ test track 1 (t1)	nA/wS/t1
hard assistance (hA)	/ no secondary task (nS)	/ test track 1 (t1)	hA/nS/t1
hard assistance (hA)	/ with secondary task (wS)	/ test track 2 (t2)	hA/wS/t2
soft assistance (sA)	/ no secondary task (nS)	/ test track 2 (t2)	sA/nS/t2
soft assistance (sA)	/ with secondary task (wS)	/ test track 2 (t2)	sA/wS/t2

Before the experiment started, the test subjects had the opportunity to get used to the driving simulator on a training test track, which differs from track 1 and track 2 used in the exploration. This training period was divided into three sessions: first the subjects drove without assistance and secondary task in order to get familiar with the simulator environment. Second, they practiced the secondary task and finally, they drove and handled the secondary task in parallel. Noteworthy, in the training phase no obstacles appeared. There was no particular time limit for the training. The training phase ended, when the subjects felt confident in the driving as well as in the secondary task. Before the main exploration started the performance of the test subjects in the secondary task without driving was measured as baseline.

In order to avoid influences of the order in which the different test settings were presented to the subjects, the different test conditions were combined into four different sequences as collected in Table 5.5. Thereby, test settings with equal assistant variants (nA, hA, sA) are kept consecutively in each sequence. The test subjects were randomly assigned to one of the four sequences. Drive I and drive II were in all cases without assistance torques.

Table 5.5: Test sequences

	Sequence 1	**Sequence 2**	**Sequence 3**	**Sequence 4**
Drive I:	nA/nS/t1	nA/nS/t1	nA/nS/t1	nA/nS/t1
Drive II:	nA/wS/t1	nA/wS/t1	nA/wS/t1	nA/wS/t1
Drive III:	sA/nS/t2	hA/nS/t1	hA/wS/t2	sA/wS/t2
Drive IV:	sA/wS/t2	hA/wS/t2	hA/nS/t1	sA/nS/t2
Drive V:	hA/nS/t1	sA/nS/t2	sA/wS/t2	hA/wS/t2
Drive VI:	hA/wS/t2	sA/wS/t2	sA/nS/t2	hA/nS/t1

Before the test drives began, the subjects were reminded that the primary task consists in driving at a speed of 100 km/h and in remaining at the right lane. However, potential obstacles had to be evaded. Besides that, the subjects should perform in the secondary task as good as possible.

The simulation data of each test drive were stored for subsequent analysis. Besides these objective data, the subjects had to fill out a detailed questionnaire after each test drive. In this questionnaire topics ranging from acceptance of driver assistance systems in general down to acceptance of the presented system in particular situations such as lane-keeping or collision avoidance were covered. Besides that, the test subjects were asked for suggestions how to improve the presented assistance system. The answers are collected in the appendix.

5.2.4 Results and Discussion

One of the most significant results of the exploration is the mean lateral deviation from the planned trajectories. Figure 5.9 depicts mean values and standard deviations for all sixteen subjects. Hereby, the first two bars give the results for drive I and drive II without assistance, with and without secondary task, respectively. The third and forth bar indicate the mean lateral deviation with hard assistance (hA), again with and without secondary task (wS/nS). Finally, the same quantities are given for soft assistance (sA). It can be seen that the lateral deviations from the planned path, e.g. the center of the lane if no obstacles are present, grow if the subjects are distracted by a secondary task. This observation is independent whether the test drives are conducted with assistance or not and what kind of assistance is used. Most interesting, it can be noted that the assistance torques in general contribute in a way that the deviations can be reduced. Here, the hard assistance performed better in minimizing the deviations.

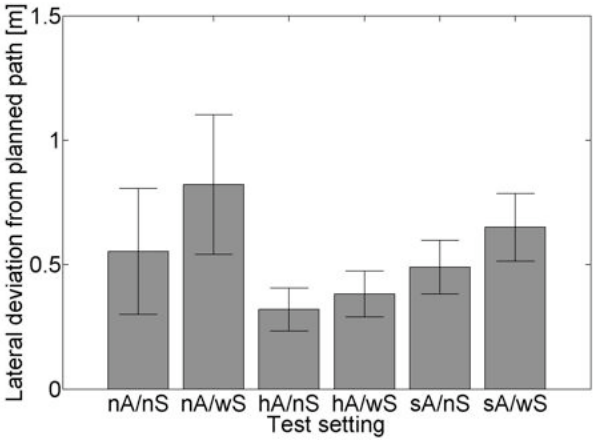

Figure 5.9: Mean lateral deviation from the planned path for different degrees of assistance

In Figure 5.10 the mean lateral deviation of all test subjects is dissolved for pure lane-keeping situations and for collision avoidance situations. Here, collision avoidance situations refer to situations where obstacles were detected including the evasion maneuver and the return to the right lane. In this case the above observations still hold, but it becomes obvious that the intentions of test subjects and potential field guidance system were less coordinated for collision avoidance than for lane-keeping. This result aligns with observations during the exploration. In general, the test subjects intended to change the lane earlier than the assistance system when they were aware of an obstacle ahead. On the other hand, the assistance system proposed to return to the right lane more quickly than intended by the test subjects. Here it might be interesting to adapt the parameters of the vehicle guidance controller to the situation as indicated in Section 4.8.

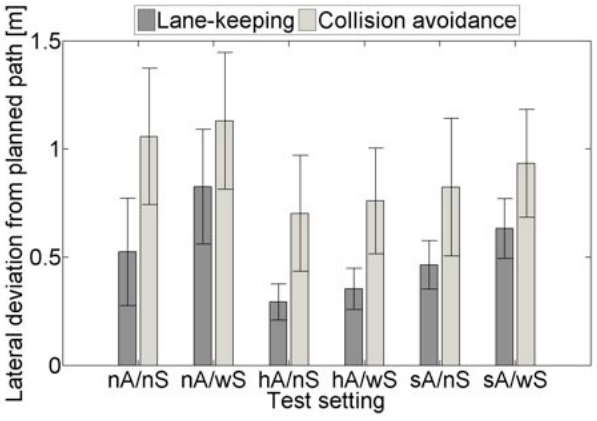

Figure 5.10: Lateral deviation from planned path depending on the degree of assistance, dissolved for lane-keeping and collision avoidance

However, another interesting result is the number of collisions with obstacles in the different test settings given in Table 5.6. In each test drive four obstacles appeared. As the test settings in Table 5.4 were presented to each of the sixteen subjects, 64 collisions were in principal possible in each test setting. The number of actual collisions shows that

the test subjects in general managed to avoid collisions if they were not distracted by the secondary task. The only exception was one test subject who collided twice with soft assistance. With secondary task and without assistance 19 collisions were detected. This number was dramatically reduced in the test settings with the assistance system. Here, the hard assistance configuration with 4 collisions performed best.

Table 5.6: Total number of collisions of all test subjects

	with secondary task (wS)	**no secondary task (nS)**
no assistance (nA)	19/64	0/64
soft assistance (sA)	6/64	2/64
hard assistance (hA)	4/64	0/64

These objective data promise that shared vehicle guidance with an assistance system based on the proposed potential field framework can contribute to a better driving performance. In particular, in situations where drivers are distracted and not aware of potential hazards, the system might help to avoid accidents. However, the discussed objective quantities contain no information how far the assistance system is accepted by the test subjects. These aspects are covered by the questionnaire that the test subjects answered after each test drive. For the complete set of questions and the collected answers of the test subjects refer to the appendix.

In general, the acceptance of the system for lane-keeping as well as for collision avoidance was satisfying. The cooperation with the assistance system was more harmonic in lane-keeping situations, which was also reflected in the test subject's comments. In order to get an information basis how to adapt the level of assistance, the test subjects were asked for their opinion concerning the strength of the assistance torque. As Figure 5.11 shows, the test subjects rated the hard assistance as too hard, and the soft assistance as too soft. This tendency is more pronounced in collision avoidance, where lane-change maneuvers are demanded, than in lane-keeping situations. Most of the test subjects felt patronized by the hard assistance variant up to comments like "I was driven". On the other hand, the test subjects formulated problems in interpreting the intention of the assistance system if the assistance torque was too low.

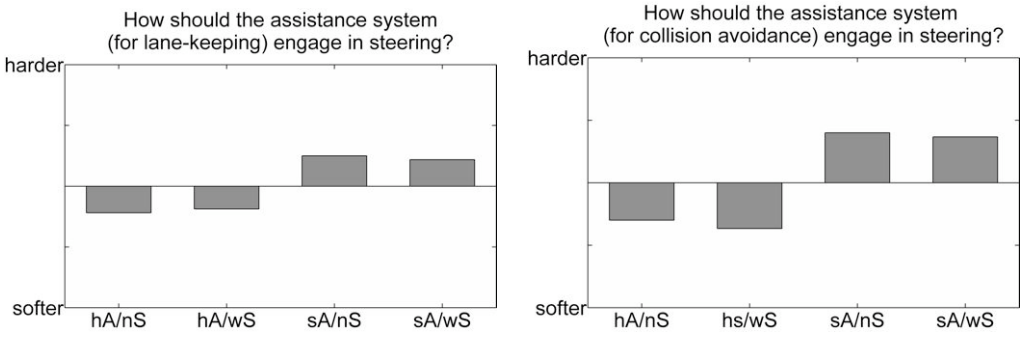

(a) Lane-keeping (b) Collision avoidance

Figure 5.11: Mean ratings of the assistance torque by the test subjects

To estimate the driving demand, the questionnaire as well as the performance of the test subjects in the secondary task can be analyzed, see for example BUSCHARDT (2003, [15], pp. 240). However, most of the test subjects showed a higher performance in the secondary task with rising duration of the experiment, which might indicate learning effects. Therefore, only the subjective rating of the influence of the assistance system on the driving demand is considered, see Figure 5.12. The test subjects in general agreed that the driving demand was reduced by the assistance system. This effect was more pronounced for hard assistance.

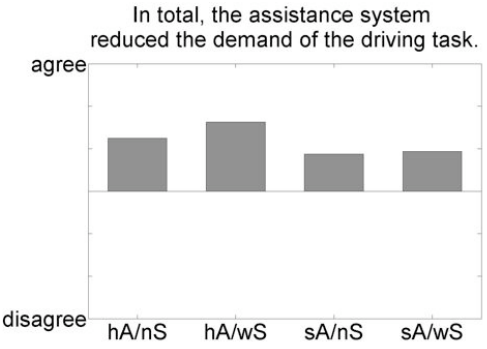

Figure 5.12: Influence of the assistance system on the driving demand

Summarizing, the results of the exploration are promising in terms of reducing the number of collisions and providing a good lane-keeping performance as well as in the reduction of driving demand experienced by the test subjects. However, in further studies the force feedback characteristics should be adapted. In doing so, the hard and the soft variant, studied in this exploration, might serve as upper and lower bound. In between the characteristics might individually be customized. Also a combination of the haptic interaction with visual or acoustic warnings, particular in critical situations, see for example FRICKE, DE FLIPPIS AND THÜRING (2006, [38]), should be considered. Another point is to tune the parameters of the motion planning and the guidance controller such that the proposed maneuvers are closer to the driver's intention. Besides that, another important step is the experimental validation of the proposed system in real traffic situations.

Chapter 6

Conclusion

6.1 Summary

Modern driver assistance systems gradually engage in vehicle guidance. First examples on the market are lane departure warning and lane-keeping systems. Nevertheless, more advanced systems including the capability of evasion maneuvers are still subject to intensive research. One key issue that has to be addressed is the motion planning that enables advanced driver assistance systems to function at the guidance level. However, most research projects in vehicle motion planning only consider autonomous driving or emergency scenarios where the driver is overruled completely by the safety system.

In this thesis, methods for cooperative vehicle guidance of driver and assistance system were contributed. In particular, a unified framework of motion planning and tracking control was provided. This unified framework for shared vehicle guidance is established by the potential field methods given in Chapter 3 and 4. In doing so, the concept of searching for equilibrium configurations of an elastic band in a hazard map, which encodes the environmental information, was introduced and shown to provide collision-free solutions. Therein, the elastic band, originally introduced in robotics, acts like a virtual antenna of an insect sensing trajectories of low hazards in the environment. Necessary numeric procedures were outlined to compute the equilibrium configurations. For automotive applications the motions of other traffic participants are anticipated by means of extrapolation methods. Hence, the proposed potential field motion planning is predictive spatially as well as temporally. This in turn is not only beneficial to the motion planning itself, but it also resembles the predictive motion planning of human drivers and facilitates the coordination between driver and assistance system.

Information about the planned trajectory, in particular the curvature, which can be considered as a disturbance, can be incorporated into the tracking algorithms. In order to do so, the potential field guidance controller, combined with disturbance rejection or feedforward control, was shown to provide closed-loop dynamics that are stable in the sense of Lyapunov. Besides that, the given Lyapunov function provides bounds for the tracking error depending on the initial conditions and on the parameters of the controller. Therefore, the maximal deviation from the planned trajectory can be predicted and the gains of the controller can be chosen to guarantee collision-free vehicle guidance.

The steering angle, proposed by the guidance system, is communicated to the driver via a force feedback steering wheel. In parallel, the driver's steering intension is used to shape the planned trajectories. The interactive guidance concept was experimentally tested in a fixed-based driving simulator with a test group of sixteen subjects. Therein, different configurations of the assistance torques, reflecting loose rein and tight rein of the h-metaphor, were analyzed. Distracting the subjects with a secondary task, it turned out that the performance of the test subjects in tracking the planned trajectories in test drives using the guidance system was higher than in test drives without. Besides that, the number of collisions with obstacles decreased in test drives with the driver assistance system.

Summarizing this thesis provided a unified potential field framework for shared vehicle guidance of driver and assistance system. The underlying potential field methods cover motion planning as well as trajectory tracking. The concept can be applied to complex traffic scenarios and is not, contrary to other methods, limited in the number of obstacles that can be handled. Lane-keeping and collision avoidance assistance are sample applications of this guidance concept.

6.2 Future Work

This thesis establishes a basis from which different directions for further theoretical and experimental research can be taken. Some examples are: The elastic band, sensing the hazard map for trajectories of low hazard levels, substantially contributes to the predictive character of the motion planning concept. Therein, internal potentials distribute local deformations over the entire elastic band in order to avoid locally high curvatures. Here, a further interesting approach could be the extension of the elastic band approach by introducing additional bending stiffnesses. Of particular interest is also the further incorporation of vehicle dynamics in the motion planning procedure. The stiffness parameters of the elastic band could for example be adapted according to the drivability of a trajectory. Nevertheless, it should be reminded that evaluating drivability in the end relies on the adhesion factor between tires and ground, which is hard to determine.

The potential field controller can be parameterized in order to keep the tracking error smaller than the distances to passed obstacles and therefore avoid collisions. An interesting point for further research is the automatic adaptation of the guidance controller with respect to the hazard map, which demands further stability analysis.

However, substantial next steps are also the incorporation of longitudinal vehicle guidance into the potential field concept and test drives to verify the results gained in the driving simulator. Further research is also demanded in the field of haptic interaction between driver and assistance system.

Appendix: Exploration Questionnaire

In the following, a translated extract of the questionnaire used in the exploration, see Chapter 5, is presented; the exploration was originally conducted in German. Instructions given to the test subjects and demographic data are omitted here for brevity. After each test drive, the subjects were asked to express their degree of accordance to the statements given in each question by marking a small box. In the following, the boxes are replaced by numbers that indicate how many of the test subjects chose a particular degree of accordance. First, that part of the questionnaire is presented, which was used after the initial test drives without assistance system. In Drive I the subjects could completely focus on the driving task, while in Drive II they were additionally stressed by a secondary task.

Extract of the questionnaire

Drive I

The vehicle always behaved as expected.

"I abs. disagree."	0	0	0	2	7	7	"I abs. agree."

It was easy to avoid obstacles.

"I abs. disagree."	0	0	1	0	5	10	"I abs. agree."

It was easy to keep the lane.

"I abs. disagree."	0	1	0	1	9	5	"I abs. agree."

Drive II

The vehicle always behaved as expected.

"I abs. disagree."	0	2	3	2	3	6	"I abs. agree."

It was easy to avoid obstacles.

"I abs. disagree."	1	0	1	9	3	2	"I abs. agree."

It was easy to keep the lane.

"I abs. disagree."	2	3	2	6	3	0	"I abs. agree."

How intensively were you stressed by the secondary task?

not at all	0	1	1	2	6	6	very intensively

The following questions were posed after each test drive with driver assistance (Drives III-IV). The tuple of four numbers denotes the total number of votes given by the test subjects in the corresponding test drive; the answers are arranged in the following order:

1. hard assistance / no secondary task (hA/nS)
2. hard assistance / with secondary task (hA/wS)
3. soft assistance / no secondary task (sA/nS)
4. soft assistance / with secondary task (sA/wS).

Drives III-VI

Please answer the following questions with respect to collision avoidance assistance.

In presence of obstacles the driver assistance system perceptibly engaged in vehicle guidance.

yes	15|14|10|8	no	1|1|6|7

How should the assistance system engage in the steering?

earlier	0|1|0|1	2|2|3|3	10|12|7|10	3|0|3|1	0|0|1|0	later
softer	1|2|0|0	7|7|0|0	7|6|6|6	0|0|4|7	0|0|4|2	harder

How should warnings, by means of vibration at the steering wheel, be realized?

earlier	0|1|1|1	3|3|4|5	12|11|8|8	0|0|1|1	0|0|0|0	later
softer	0|3|0|0	7|3|2|1	7|9|8|8	1|0|2|3	0|0|1|3	harder

How should it be possible to overrule the assistance system?

easier	0|0|0|0	8|10|5|2	7|5|5|10	0|0|4|3	0|0|0|0	harder

Please answer the following questions with respect to lane-keeping assistance.

In absence of obstacles the driver assistance system perceptibly engaged in vehicle guidance.

yes	11|13|10|13	no	2|0|5|2

How should the assistance system engage in the steering?

earlier	0|0|1|1	0|2|2|0	12|14|10|13	3|0|2|2	1|0|0|0	later
softer	1|0|0|0	5|6|1|0	10|10|7|11	0|0|5|3	0|0|2|2	harder

How should warnings, by means of vibration at the steering wheel, be realized?

earlier	0|0|1|1	1|1|1|1	12|14|12|13	3|1|1|1	0|0|0|0	later
softer	0|0|0|0	4|4|1|0	10|11|8|10	2|1|5|4	0|0|1|2	harder

How should it be possible to overrule the assistance system?

easier	1|1|0|0	8|6|3|3	7|9|8|11	0|0|4|2	0|0|0|0	harder

Please rate how far you agree to the following statements.

The vehicle always behaved as expected.
"I abs. disagree." 0|0|0|0 1|0|2|0 1|5|2|5 4|5|1|3 5|1|6|4 5|5|5|4 "I abs. agree."

It was easy to avoid obstacles.
"I abs. disagree." 0|0|0|0 0|2|0|1 0|4|0|3 3|2|5|3 6|4|5|8 7|4|6|1 "I abs. agree."

It was easy to keep the lane.
"I abs. disagree." 0|0|0|0 0|0|0|1 0|1|0|7 1|6|1|1 7|4|9|6 8|5|6|1 "I abs. agree."

I always knew what the assistance system intended to do or me to do.
"I abs. disagree." 0|0|1|2 3|3|4|6 1|5|3|2 4|1|4|4 5|4|2|2 3|3|2|0 "I abs. agree."

I felt overruled by the assistance system.
"I abs. disagree." 4|2|7|8 5|3|3|4 2|5|2|2 2|4|4|2 1|2|0|0 2|0|0|0 "I abs. agree."

I always recognized when the assistance system engaged in vehicle guidance.
"I abs. disagree." 0|0|0|0 0|0|3|1 0|0|0|2 0|0|2|1 6|8|7|10 10|8|4|2 "I abs. agree."

The system assisted me in lane-keeping.
"I abs. disagree." 0|0|2|1 0|0|1|0 1|0|2|2 2|2|2|3 6|9|7|6 7|5|2|4 "I abs. agree."

The system assisted me in collision avoidance.
"I abs. disagree." 0|0|2|0 0|1|2|2 1|1|1|3 2|1|0|3 7|7|7|5 6|6|4|3 "I abs. agree."

I always had trust in the assistance system.
"I abs. disagree." 0|0|1|1 1|3|4|3 5|2|2|5 5|4|4|3 2|4|3|3 3|3|2|1 "I abs. agree."

I was annoyed by the assistance system.
"I abs. disagree." 7|4|6|6 2|4|4|6 3|6|1|3 3|2|3|1 1|0|2|0 0|0|0|0 "I abs. agree."

The assistance system took at least one wrong decision.
"I abs. disagree." 7|5|7|7 4|1|5|4 2|4|2|0 2|1|0|3 1|1|1|2 0|4|1|0 "I abs. agree."

In total, the assistance system relieved the driving task to me.
"I abs. disagree." 0|0|1|1 1|0|1|0 3|3|2|2 4|3|4|7 3|4|7|5 5|6|1|1 "I abs. agree."

The assistance system additionally stressed me.
"I abs. disagree." 6|5|5|4 6|5|4|5 1|3|5|3 3|2|2|3 0|1|0|0 0|0|0|1 "I abs. agree."

In addition, the assistance system should give visual warnings.
"I abs. disagree." 5|5|5|6 5|3|5|3 2|1|0|0 0|2|2|2 2|3|4|4 2|2|0|1 "I abs. agree."

In addition, the assistance system should give acoustic warnings.
"I abs. disagree." 3|4|3|3 6|4|4|4 0|2|1|0 4|1|3|5 0|3|2|0 3|2|3|4 "I abs. agree."

How intensively were you stressed by the secondary task?
not at all -|0|-|0 -|1|-|2 -|0| -|0 -|4|-|2 -|8|-|7 -|3|-|5 very intensively

Please answer the following questions about your opinion about lane-keeping and collision avoidance assistance in general.

I think lane-keeping and collision avoidance are, in general, valuable.
"I abs. disagree." 0|0|0|0 0|0|0|0 1|0|0|0 1|1|4|1 7|9|5|9 7|6|7|6 "I abs. agree."

I think lane-keeping and collision avoidance, in general, might increase traffic safety.
"I abs. disagree." 0|0|0|0 0|0|0|0 1|0|0|0 1|1|3|2 6|10|5|6 8|5|8|8 "I abs. agree."

I think lane-keeping and collision avoidance might, in general, increase driving comfort.
"I abs. disagree." 0|1|0|0 0|0|1|0 2|0|0|1 2|1|5|4 4|9|4|4 8|5|6|7 "I abs. agree."

Bibliography

[1] *Automotive Handbook*. 6th edition. Plochingen : Robert Bosch GmbH, 2004

[2] *Unfallgeschehen im Straßenverkehr 2005*. Statistisches Bundesamt, July 2006

[3] *Richtlinie für die Anlage von Straßen (RAS), Teil L: Linienführung*. Forschungsgesellschaft für Straßen- und Verkehrswesen, berichtigter Nachdruck 1999

[4] Ameling, C.: *Steigerung der aktiven Sicherheit von Kraftfahrzeugen durch ein Kollisionsvermeidungssystem*. Hamburg, Helmut-Schmidt University, Dissertation, 2002

[5] Bajcinca, N.: *Robust Control Methods with Applications to Steer-by-Wire-Systems*, Technical University Berlin, Dissertation, January 2006

[6] Bender, E. ; Landau, K.: Fahrerverhalten bei automatischen Brems- und Lenkeingriffen eines Fahrerassistenzsystems zur Unfallvermeidung. In: *VDI-Berichte Nr. 1931, Steuerung und Regelung von Kraftfahrzeugen und Verbrennungsmotoren AUTOREG 2006*. Düsseldorf, Germany : VDI, March 2006, p. 219–228

[7] Bielaczek, C.: Die Auswirkung der aktiven Fahrerbeeinflussung auf die Fahrsicherheit. In: *Automobiltechnische Zeitschrift (ATZ)* 101 (1999), No. 9, p. 714 – 725

[8] Brandt, T. ; Sattel, T. ; Wallaschek, J.: Ein Ansatz zur automatischen Kollisionsvermeidung. In: *VDI Berichte Nr. 1864, VDI/VW Gemeinschaftstagung Integrierte Sicherheit und Fahrerassistenzsysteme*. Wolfsburg, Germany, October 2004, p. 125–143

[9] Brandt, T. ; Sattel, T. ; Wallaschek, J.: Zur integrierten Längs- und Querführung von Kraftfahrzeugen in Notsituationen. In: *VDI-Berichte Nr. 1892, Mechatronik 2005 - Innovative Produktentwicklung*. Wiesloch, June 2005, p. 779–808

[10] Brandt, T. ; Sattel, T. ; Wallaschek, J.: On Automatic Collision Avoidance Systems. In: *SAE 2005 Transactions Journal of Passenger Cars: Electronic and Electrical Systems* (2006), February, p. 431–440

[11] Bronstein, I.N. ; Semendjaev, K.A.: *Taschenbuch der Mathematik*. 3rd edition. Verlag Harri Deutsch, 1997

[12] BRÜDIGAM, C.: *Intelligente Fahrmanöver sehender autonomer Fahrzeuge in autobahnähnlicher Umgebung*, University of the Federal Armed Forces, Munich, Dissertation, 1994

[13] BULD, S. ; KRÜGER, H.-P.: Wirkungen von Assistenz und Automation auf Fahrerzustand und Fahrsicherheit - Projekt EMPHASIS (Effort-Management and Performance Handling in sicherheitsrelevanten Situationen) / Interdisziplinäres Zentrum für Verkehrswissenschaften (IZVW), Universität Würzburg. 2002. – technical report

[14] BULIRSCH, R. ; VÖGEL, M. ; VON STRYK, O. ; CHUCHOLOWSKI, C. ; WOLTER, T.-M.: *An Optimal Control Approach To Real-Time Vehicle Guidance* In : MATHEMATICS Key Technology for the Future. Springer, 2003, p. 84–102

[15] BUSCHARDT, B.: *Synthetische Lenkmomente*, Technical University of Berlin, Fortschritt-Berichte VDI, Reihe 22 No. 12, Dissertation, 2003

[16] CHANG, D. ; MARSDEN, J. E.: *Gyroscopic Forces and Collision Avoidance with Convex Obstacles*. In : New Trends in Nonlinear Dynamics and Control and their Applications, Springer, New York, October 2003, p. 145–160

[17] CHANG, D.E. ; SHADDEN, S.C. ; MARSDEN, J.E. ; OLFATI-SABER, R.: Collision Avoidance For Multiple Agent Systems. In: *Proceedings of the 42nd IEEE Conference on Decision and Control*. Maui, Hawai USA, December 2003, p. 539–543

[18] CHOSET, H. ; LYNCH, K. ; HUTCHINSON, S. ; KANTOR, G. ; BURGARD, W. ; KAVRAKI, L. ; THRUN, S.: *Principles of Robot Motion*. MIT Press, June 2005

[19] CONNOLLY, C. I. ; GRUPEN, R. A.: The Applications of Harmonic Functions to Robotics. In: *Journal of Robotic Systems* 10 (1993), No. 7, p. 931–946

[20] CONSANO, L. ; MURDOCCO, V.: Haptical Lane Assistant for Heavy Trucks. In: *Nutzfahrzeuge*. Böblingen : VDI, Oktober 2005, p. 231 – 241

[21] CONSOLINI, L. ; PIAZZI, A. ; TOSQUES, M.: Motion Planning for Steering Car-Like Vehicles. In: *ECC 2001, Proceedings of the European Control Conference*, 2001, p. 1834–1839

[22] CREMEAN, L. B. ; MURRAY, R.M.: Model-Based Estimation of Off-Highway Road Geometry using Single-Axis LADAR and Inertial Sensing. In: *Proceedings of 2006 Intelligent Transportation Systems Conference*, 2006

[23] DARMS, M. ; WINNER, H.: Umfelderfassung für ein Fahrerassistenzsystem zur Unfallvermeidung. In: *VDI-Berichte Nr. 1931, Steuerung und Regelung von Kraftfahrzeugen und Verbrennungsmotoren AUTOREG 2006*. Düsseldorf, Germany, March 2006, p. 207–217

[24] DICKMANNS, E. D.: Vision for ground vehicles: history and prospects. In: *International Journal of Vehicle Autonomous Systems* 1 (2002), p. 1–44

[25] DICKMANNS, E. D. ; MYSLIWETZ, B. D.: Recursive 3-D road and relative ego-state recognition. In: *IEEE Transactions on Pattern Analysis and Machine Intelligence* 14 (1992), February, No. 2, p. 199–213

[26] DICKMANNS, E. D. ; MYSLIWETZ, B. D. ; CHRISTIANS, T.: An Integrated Spatio-Temporal Approach to Automatic Visual Guidance of Autonomous Vehicles. In: *IEEE Transactions on Systems, Man and Cybernetics* 20 (1990), November / December, No. 6, p. 1273–1284

[27] DJOUANI, K. ; HAMAM, Y.: Optimal Constrained Multi-Criteria Trajectory Planning For Ship Maneuvering and Control. In: *Proceedings of the 2nd IEEE Conference on Control Applications, Vancouver, B.C.*, 1993, p. 525–530

[28] DONGES, E.: Aspekte der aktiven Sicherheit bei der Führung von Personenkraftwagen. In: *Automobil - Industrie* (1982), No. 2, p. 183 – 190

[29] DOSHER, J. ; LEE, G. ; HANNAFORD, B.: How low can you go? Detection thresholds for small haptic effects. In: *Touch in Virtual Environments. Proceedings USC Workshop on Haptic Interfaces*, Prentice Hall, February 2001

[30] DUGOFF, H. ; FANCHER, P. S. ; SEGEL, L.: Tire Perfomance Characteristics Affecting Vehicle Characteristics to Steering and Braking Control Inputs. / Highway Safety Research Institute, University of Michigan. Ann Arbor, 1969. – technical report

[31] EHMANNS, D.: *Modellierung des taktischen Fahrerverhaltens bei Spurwechselvorgängen*, RWTH Aachen, Dissertation, January 2003

[32] FENG, K. ; TAN, H. ; TOMIZUKA, M.: Design of Vehicle Lateral Guidance System for Driver Assistance. In: *Proceedings of the 2000 American Control Conference*, 2000

[33] FIORINI, P. ; SHILLER, Z.: Motion Planning in Dynamic Environments Using Velocity Obstacles. In: *The International Journal of Robotics Research* 17 (1998), July, No. 7, p. 760–772

[34] FLEMISCH, F.: Wie könnte es über Assistenzsysteme hinausgehen? Die H-Metapher als Richtschnur für Fahrzeugautomation- und interaktion. In: *VDI-Berichte Nr. 1864, Integrierte Sicherheit und Fahrerassistenzsysteme.* Düsseldorf, 2004, p. 561–585

[35] FLEMISCH, F. ; ADAMS, C. ; CONWAY, S. ; GOODRICH, K. ; PALMER, M. ; SCHUTTE, P.: The H-Metaphor as a Guideline for Vehicle Automation and Interaction, NASA, TM-2003-212672, December 2003

[36] FÖLLINGER, O.: *Regelungstechnik - Einführung in die Methoden und ihre Anwendung.* 8th edition. Heidelberg, Germany : Huethig Buch Verlag GmbH, 1994

[37] Freund, E. ; Mayr, R.: Nonlinear Path Control in Automated Vehicle Guidance. In: *IEEE Transactions on Robotics and Automation* 13 (1997), February, No. 1, p. 49–60

[38] Fricke, N. ; De Filippis, M. ; Thüring, M.: Zur Gestaltung der Semantik von Warnmeldungen. In: *VDI-Berichte Nr. 1960, Intergrierte Sicherheit und Fahrerassistanzsysteme*, VDI-Gesellschaft, October 2006, p. 133–148

[39] Frik, S.: *Untersuchungen zur erforderlichen Modellkomplexität bei der Fahrdynamiksimulation*. Düsseldorf, University of Duisburg, Dissertation, February 1994

[40] Gehrig, S. K. ; Stein, F. J.: Elastic Bands to Enhance Vehicle Following. In: *Proceedings of 2001 IEEE Intelligent Transportation Systems, Oakland, CA, USA*, 2001, p. 597–602

[41] Gerdes, J. C. ; Rossetter, E. J. ; Saur, U.: Combining Lanekeeping and Vehicle Following with Hazard Maps. In: *Vehicle System Dynamics* 36 (2001), November, No. 4-5, p. 391–411

[42] Gillespie, R. B.: *Robotics and Automation Handbook - Haptic Interface to Virtual Environments*. CRC Press, 2005, p. 23.1–23.23

[43] Goodrich, M. A. ; Boer, E. R.: Designing Human-Centered Automation: Tradeoffs in Collision Avoidance System Design. In: *IEEE Transactions of Intelligent Transportation Systems* 1 (2000), March, No. 1, p. 40–54

[44] Griffiths, P. ; Gillespie, R.B.: Shared Control Between Human and Machine: Haptic Display of Automation During Manual Control of Vehicle Heading. In: *Proceedings of the 12th International Symposium on Haptic Interface for Virtual Environment and Teleoperator Systems (HAPTICS'04)*, IEEE Computer Society, March 2004, p. 358–366

[45] Griffiths, P. ; Gillespie, R.B.: Sharing Control Between Human and Automation Using Haptic Interface: Primary and Secondary Task Performance Benefits. In: *Human Factors* (2005), No. 47, p. 574–590

[46] Guldner, J. ; Tan, H.-S. ; Patwardhan, S.: Analysis of Automatic Steering Control for Highway Vehicles with Look-Down Lateral Reference Systems. In: *Vehicle System Dynamics* 26 (1996), p. 243–269

[47] Hattori, A. ; Hosaka, A. ; Taniguchi, M. ; Nakano, E.: Driving Control System for an Autonomous Vehicle Using Multiple Observed Point Information. In: *Proceedings of the Intelligent Vehicles 92 Symposium*. Detroit, USA, June/July 1992, p. 207–212

[48] Hennessey, M.P. ; Shankwitz, C. ; Donath, M.: Sensor Based "Virtual Bumpers" for Collision Avoidance: Configuration Issues. In: *SPIE Photonics 95 Conference, Collision Avoidance and Automated Traffic Management Sensors* 2592 (1995), October, p. 48–59

[49] HILGERT, J. ; HIRSCH, K. ; BERTRAM, T. ; HILLER, M.: Emergency Path Planning for Autonomous Vehicles Using Elastic Band Theory. In: *IEEE/ASME International Conference on Advanced Intelligent Mechatronics AIM 2003, Kobe, Japan*, 2003

[50] HOLLE, M.: Aktivlenkung - Untersuchung zum Lenkgefühl. In: *13. Achener Kolloquium Fahrzeug- und Motorentechnik*. Aachen : RWTH Aachen, 2004, p. 1455–1478

[51] HUANG, P.: *Regelkonzepte zur Fahrzeugführung unter Einbeziehung der Bedienelementeigenschaften*, Technical University of Munich, Dissertation, March 2004

[52] KAGEYAMA, I. ; NOZAKI, Y.: Control Algorithm for Autonomous Vehicle with Risk Level. In: *Proceedings of the Second World Congress on Intelligent Transport Systems 95 Yokohama*, 1995, p. 1284–1288

[53] KALTENBACH, J. ; WERRIES, H. ; GAZYAKAN, Ü. ; KNÖDLER, H.: Entwicklungsprozess für ein mechatronisches System am Beispiel Steer-by-Wire. In: *Mechatronik - Mechanisch/Elektrische Antriebstechnik, VDI-Berichte 1533*. Düsseldorf : VDI, 2000, p. 385 – 401

[54] KÄMPCHEN, N. ; FÜRSTENBERG, K. ; DIETMAYER, K.: Ein Sensorfusionsystem für automotive Sicherheits- und Komfortapplikationen. In: *Aktive Sicherheit durch Fahrerassistenz*, 2004

[55] KÄMPCHEN, N. ; WEISS, K. ; SCHÄFER, M. ; DIETMAYER, K.: IMM Object Tracking for High Dynamic Driving Maneuvers. In: *Intelligent Vehicles Symposium*, IEEE, 2004

[56] KARNOPP, D.: *Vehicle Stability*. New York : Marcel Dekker, Inc., 2004

[57] KHATIB, O.: Real-time Obstacle Avoidance for Manipulation and Mobile Robots. In: *International Journal of Robotics Research* 5 (1986), No. 1, p. 90–98

[58] KIENCKE, U. ; NIELSEN, L.: *Automotive Control Systems*. 2nd edition. Springer-Verlag GmbH, 2005

[59] KIM, Y. J. ; KIM, J. H. ; KWON, D. S.: Evolutionary Programming-Based Univector Field Navigation Method for Fast Mobile Robots. In: *IEEE Transactions on Systems, Man, and Cybernetics - Part B: Cybernetics* 31 (2001), June, No. 3, p. 450–458

[60] KINDEL, R. ; HSU, D. ; LATOMBE, J.-C. ; ROCK, S.: Kinodynamic Motion Planning Amidst Moving Obstacles. In: *Proceedings of the 2000 IEEE International Conference on Robotics and Automation*. San Francisco, CA, April 2000, p. 537–543

[61] KOEPELE, B. ; STARKEY, J. M.: Closed-Loop Vehicle and Driver Models for High-Speed Trajectory Following. In: *Transportation Systems - 1990 ASME WAM, Dallas, TX*, 1990, p. 59–68

[62] KOMAINDA, A. ; HILLER, M.: Control of Heavy Load Manipulators in Varying Environments. In: *Automation and Robotics in Construction* 16 (1999), p. 301–306

[63] König, L. ; Kretschmer, M. ; Neubeck, J. ; Wiedemann, J.: Nichtlineare Lenkregelung zur automatischen Spurführung im querdynamischen Grenzbereich. In: *Steuerung und Regelung von Fahrzeugen und Motoren - AUTOREG*. Wiesloch, Germany, March 2006

[64] Kovács, S. ; Kóczy, L.T.: Application of an Approximate Fuzzy Logic Controller in an AGV Steering System, Path Tracking and Collision Avoidance Strategy. In: *Tatra Mountains Mathematical Publications* 16 (1999), p. 325–338

[65] Krogh, B. H.: A Generalized Potential Field Approach To Obstacle Avoidance Control. In: *Proceedings Of International Robotics Research Conference*. Bethlehem, Pennsylvania, August 1984

[66] Lachner, R.: *Echtzeitsynthese optimaler Strategien für Differentialspiele schneller Dynamik mit Anwendungen bei der Kollisionsvermeidung*, Technical University Clausthal, Germany, Dissertation, 1997

[67] Lages, U.: Collision Avoidance System for Fixed Obstacle - Fuzzy Controller Network for Robot Driving of an Autonomous Vehicle. In: *Proceedings of IEEE Intelligent Transportation Systems Conference*. Oakland, CA, USA, August 2001, p. 489–491

[68] Lammen, B.: *Automatische Kollisionsvermeidung für Kraftfahrzeuge*, University of Dortmund, Dissertation, 1993

[69] Latombe, J. C.: *Robot Motion Planning*. Kluwer, 1991

[70] Laws, S. ; Gadda, C. ; Kohn, S. ; Yih, P. ; Gerdes, J.C. ; Milroy, J.C.: Steer-By-Wire Suspension and Steering Design for Controllability and Observability. In: *Proceedings of 16th IFAC World Congress*. Prague, Czech Republic : Elsevier, July 2005

[71] Li, Q. ; Zheng, N. ; Cheng, H.: Springrobot: A Prototype Autonomous Vehicle and its Algorithmns for Lane Detection. In: *IEEE Transactions on Intelligent Transportation Systems* 5 (2004), December, No. 4, p. 300–308

[72] Lübke, A.: Car-to-Car Communication - Technologische Herausforderungen. In: *Proceedings of ITG Fachtagung*, 2004

[73] Mildner, F.: *Untersuchungen zur Erkennung und Vermeidung von Unfällen für Kraftfahrzeuge*, Helmut-Schmidt University, Hamburg, Germany, Dissertation, 2004

[74] Mitschke, M. ; Wallentowitz, H.: *Dynamik der Kraftfahrzeuge*. 4th edition. Berlin Heidelberg : Springer, 2004

[75] Monemerlo, M. ; Thrun, S. ; Dahlkamp, H. ; Stavens, D. ; Strohband, S.: Winning the DARPA Grand Challenge with an AI Robot. In: *The 21th National Conference on Artificial Intelligence and the 18th Innovative Applications of Artificial Intelligence Conference, AAAI*. Massachusetts, USA, July 2006

[76] MURRAY, R. ; LI, Z. ; SASTRY, S.: *A Mathematical Introduction to Robotic Manipulation*. CRC, March 1994

[77] NAAB, K. ; REICHART, G.: Driver Assistance Systems for Lateral and Longitudinal Vehicle Guidance - Heading Control and Active Cruise Support. In: *International Symposium on Advanced Vehicle Control (AVEC)*. Japan, October 1994, p. 449–454

[78] NEUSSER, S. ; NIJHUIS, J. ; SPAANENBURG, L.: Developments in Autonomous Vehicle Navigation. In: *Proceedings of CompEuro '92, Computer Systems and Software Engineering*, 1992, p. 453–458

[79] NIEHAUS, A. ; STENGEL, R. F.: An Expert System for Automated Highway Driving. In: *Proceedings of the 1990 American Control Conference,* Vol. 1, 1990, p. 274–280

[80] ORTEGA, J.M. ; RHEINBOLDT, W.C.: *Iterative Solution of Nonlinear Equations in Several Variables*. New York : Academic Press, 1970

[81] PACEJKA, H. B.: *Tyre and Vehicle Dynamics*. Butterworth-Heinemann Ltd., 2002

[82] PARK, J. ; NIKRAVESH, P.E.: A Look-Ahead Driver Model for Autonomous Cruising on Highways. In: *SAE Technical Paper Series 961686*, 1996

[83] PENG, H. ; TOMIZUKA, M.: Vehicle Lateral Control for Highway Automation. In: *Proceedings of the American Control Conference, San Diego, USA*, 1990, p. 788–794

[84] PENKA, A.: *Vergleichende Untersuchung zu Fahrerassistenzsystemen mit unterschiedlichen aktiven Bedienelementen*. München, Technische Universität München, Dissertation, 2001

[85] POHL, J. ; EKMARK, J.: Development of a Haptic Intervention System for Unintended Lane Departure. In: *SAE Transactions* 112 (2003), p. 243 – 247

[86] POPP, K. ; SCHIEHLEN, W.: *Fahrzeugdynamik*. Stuttgart : B.G. Teubner, 1993

[87] QUINLAN, S. ; KHATIB, O.: Elastic Bands: Connecting Path Planning and Control. In: *IEEE International Conference on Robotics and Automation, Atlanta, USA*, 1993, p. 802–807

[88] REICHARDT, D.: *Kontinuierliche Verhaltenssteuerung eines autonomen Fahrzeugs in dynamischer Umgebung*, Technical University of Kaiserslautern, Germany, Dissertation, 1996

[89] REICHART, G.: Driver Assistance, Collision Avoidance and Automated Driving. In: *Proceedings Micro.Tec 2000, Hannover*, 2000, p. 263–269

[90] RICHARDS, A. ; HOW, J. P.: Aircraft Trajectory Planning with Collision Avoidance using Mixed Integer Linear Programming. In: *Proceedings of the American Control Conference Anchorage*, 2002, p. 1936–1941

[91] RIEKERT, P. ; SCHUNCK, T.E.: Zur Fahrmechanik des gummibereiften Kraftfahrzeugs. In: *Ingenieur Archiv* Vol. 11, 1940, p. 210–224

[92] Rill, G.: *Simulation von Kraftfahrzeugen*. Braunschweig / Wiesbaden : Vieweg Verlag, 1994

[93] Rossetter, E.J.: *A Potential Field Framework for Active Vehicle Lanekeeping Assistance*, Stanford University, Department of Mechanical Engineering, Dissertation, 2003

[94] Ryu, J.: *State and Parameter Estimation for Vehicle Dynamics Control using GPS*, Stanford University, Dissertation, December 2004

[95] Sattel, T. ; Brandt, T.: A note on vehicle guidance control using a mechanical analogy (GAMM Annual Meeting Berlin 2006). In: *PAMM* Vol. 6, No. 1. Weinheim WILEY-VCH Verlag GmbH & Co. KGaA, January 2007, p. 841–842

[96] Sattel, T. ; Brandt, T.: Ein Beitrag zur interaktiven Querführungsassistenz von Kraftfahrzeugen. In: *VDI Berichte 1960, VDI/VW Gemeinschaftstagung Integrierte Sicherheit und Fahrerassistenzsysteme*. Wolfsburg, Germany, October 2006, p. 207–222

[97] Schattenberg, K.: *Fahrzeugführung und gleichzeitige Nutzung von Fahrerassistenz- und Fahrerinformationssystemen*, RWTH Aachen, Dissertation, October 2002

[98] Schiller, B. ; Morellas, V. ; Donath, M.: Collision Avoidance for Highway Vehicles using the Virtual Bumper Controller. In: *Proceedings of the 1998 Intelligent Vehicles Conference*, 1998, p. 149–155

[99] Schraut, M.: *Umgebungserfassung auf Basis lernender digitaler Karten zur vorausschauenden Konditionierung von Fahrerassistenzsystemen*, Technical University of Munich, Dissertation, May 2000

[100] Schuster, M. ; Grupp, M. ; Richter, T. ; Pischinger, M.: Die Aktivlenkung des neuen BMW 3er. In: *Automobiltechnische Zeitschrift (ATZ) - Sonderausgabe Der neue BMW 3er*, 2005

[101] Schweigert, W. and Veltmann, H. and Grather, G. and Schütze, R. and Brendler, R. and Corsten, P.: Das Fahrwerk des neuen Passat. In: *Automobiltechnische Zeitschrift (ATZ) - Sonderausgabe Der neue Passat* Vol. 107, 2005, p. 84–98

[102] Segel, l.: Theoretical Prediction and Experimental Substantiation of the Responses of the Automobile to Steering Control. In: *Proceedings IMechE Automobile Division* Vol. 7, 1956-57, p. 310–330

[103] Siegwart, R. ; Nourbakhsh, I.: *Introduction to Autonomous Mobile Robots*. Cambridge, Massachusetts : The MIT Press, 2004

[104] Simon, A.: *Führung eines autonomen Straßenfahrzeugs mit redundanten Sensorsystemen*, Technical University of Braunschweig, Dissertation, 2003

[105] SLOTINE, J. J. E. ; LI, W.: *Applied Nonlinear Control*. Englewood Cliffs, New Jersey : Prentice Hall, 1991

[106] SOENITZ, I.: *Querregelung eines autonomen Straßenfahrzeugs*, Technical University of Braunschweig, Germany, Dissertation, 2001

[107] SPARBERT, J. ; KUMPEL, J. ; HOFER, E.: Methoden zur Navigation eines mobilen Roboters in typischen Büroumgebungen. In: *at - Automatisierungstechnik* (2001), No. 49, p. 151–159

[108] STÄHLIN, U. ; SCHORN, M. ; ISERMANN, R.: Notausweichen für ein Fahrerassistenzsystem zur Unfallvermeidung. In: *VDI-Berichte Nr. 1931: Steuerung und Regelung von Kraftfahrzeugen und Verbrennungsmotoren AUTOREG 2006*. Düsseldorf, Germany : VDI Verlag, March 2006, p. 197–206

[109] STEELE, M. ; GILLESPIE, R. B.: Shared Control between Human and Machine: Using Haptic Steering Wheel to aid in Land Vehicle Guidance. In: *proceedings of Human Factors and Ergonomics Society 45th Annual Meeting*. Minneapolis, USA, October 2002

[110] STILLER, C. ; SIMON, A. ; WEISSER, H.: A Driving Robot for Autonomous Vehicles on Extreme Courses. In: *Proceedings of the 1st Conference on Telematics Applications in Automation and Robotics*. Ravensburg-Weingarten, July 2001, p. 361–367

[111] SULLIVAN, J. ; WAYDO, S. ; CAMPBELL, M.: Using Stream Functions for Complex Behavior and Path Generation. In: *Guidance, Navigation and Control Conference*. Austin, USA : American Institute of Aeronautics and Astronautics (AIAA), 2003

[112] SUZUKI, K. ; JANSSON, H.: An Analysis of Driver's Steering Behaviour during Auditory or Haptic Warnings for the Designing of Lane Departure Warning System. In: *JSAE Review* 24 (2003), p. 65 – 70

[113] THURNER, T.: X-By-Wire: Safety Related Fault Tolerant Systems in Vehicles. In: *Document No. X-by-Wire-DB-6/6-25, X-by-Wire Consortium*. Stuttgart, 1998

[114] TOMLIN, C. ; MITCHELL, I. ; GHOSH, R.: Safety Verification of Conflict Resolution Maneuvers. In: *IEEE Transactions on Intelligent Transportation Systems* 2 (2001), June, No. 2, p. 110–120

[115] TRW Conekt and Stirling Dynamics: *Active Stirling Wheel System Part No. 020 User Guide*. Issue 1. April 2005

[116] TSOULARIS, A. ; KAMBHAMPATI, C.: On-Line Planning for Collision Avoidance on the Nominal Path. In: *Journal of Intelligent Robotic Systems* (1998), No. 21, p. 327–371

[117] VAHIDI, A. ; ESKANDARIAN, A.: Research Advances in Intelligent Collision Avoidance and Adaptive Cruise Control. In: *IEEE Transactions on Intelligent Transportation Systems* 4 (2003), September, No. 3, p. 143–153

[118] VASQUEZ, A. D. ; LARGE, F. ; FRAICHARD, Th. ; LAUGIER, C.: High-Speed Autonomous Navigation with Motion Prediction for Unknown Moving Obstacles. In: *Proceedings of the IEEE-RSJ International Conference on Intelligent Robots and Systems*. Sendai (JP), October 2004, p. 82–87

[119] VINCENT, T. L. ; GRANTHAM, W. J.: *Nonlinear and Optimal Control Systems*. New York : John Wiley & Sons, 1997

[120] VINCENT, T.L.: Collision Avoidance at Sea. In: *International Symposium on Differential Games and Applications* (1977), p. 205–221

[121] VUKOTICH, A. ; KIRCHNER, A.: Sensorfusion für Fahrerassistenzsysteme. In: *VDI Berichte 1646, Elektronik im Kraftfahrzeug*. Baden-Baden : VDI-Verlag, 2001, p. 857–875

[122] WINNER, H. ; ISERMANN, R. ; HANSELKA, H. ; SCHÜRR, A.: Wann kommt By-Wire auch für Bremse und Lenkung? In: *VDI Berichte 1828 Steuerung und Regelung von Fahrzeugen und Motoren AUTOREG 2004*. Wiesloch : VDI-Verlag, 2004

[123] WINNER, H. ; WITTE, S. ; UHLER, W. ; LICHTENBERG, B.: Adaptive Cruise Control, System Aspects and Development Trends. In: *SP 1143* SAE, 1996

[124] WOLF, H. ; ZÖLLNER, R. ; BUBB, H.: Ergonomische Aspekte der Mensch-Maschine-Interaktion bei gleichzeitig agierenden Fahrerassistenzsystemen. In: *Zeitschrift für Verkehrssicherheit* 51 (2005), No. 3, p. 119 – 124

[125] WÜRTENBERGER, M.: *Modellgestützte Verfahren zur Überwachung des Fahrzustandes eines PKW*, Technical University of Darmstadt, Dissertation, 1997

[126] ZANTEN, A. van: Evolution of Electronic Control Systems for Improving the Vehicle Dynamic Behaviour. In: *AVEC*, 2002

[127] ZEILINGER, S.: *Aktive haptische Bedienelemente zur Interaktion mit Fahrerinformationssystemen*. Munich, Germany, University of Armed Forces, Dissertation, March 2005

[128] ZOMOTOR, A.: *Fahrwerktechnik: Fahrverhalten* 2nd edition. Würzburg, Germany : Vogel Verlag und Druck KG, 1991

[129] ZWIERZEWICZ, Z.: Algorithms for the Ship Trajectory Planning and its Tracking in the Collision Avoidance Process. In: *Control Applications in Marine Systems 2001 (CAMS 2001)*, 2001

Related Publications

1. Brandt, T. ; Sattel, T. ; Wallaschek, J.: Ein Ansatz zur automatischen Kollisionsvermeidung. In: *VDI Berichte Nr. 1864, VDI/VW Gemeinschaftstagung Integrierte Sicherheit und Fahrerassistenzsysteme*. Wolfsburg, October 2004, p. 125-143

2. Brandt, T. ; Sattel, T. ; Wallaschek, J.: Ein Ansatz zur automatischen Kollisionsvermeidung. In: *Jahrbuch 2005 Fahrzeug- und Verkehrstechnik, VDI-Verlag Düsseldorf* (2005), January, p. 257-278 (selected reprint of 1.)

3. Brandt, T. ; Sattel, T. ; Wallaschek, J.: On Automatic Collision Avoidance Systems. In: *SAE World Congress 2005, SP-1920 Intelligent Vehicle Initiative (VI) Technology 2005-Advanced Controls and Navigation Systems*. Detroit, April 2005

4. Brandt, T. ; Sattel, T. ; Wallaschek, J.: Zur integrierten Längs- und Querführung von Kraftfahrzeugen in Notsituationen. In: *VDI Berichte Nr. 1892, Mechatronik 2005 - Innovative Produktentwicklung*. No. 2, Wiesloch, June 2005, p. 779-808

5. Brandt, T. ; Sattel, T.: Path Planning for Automotive Collision Avoidance based on Elastic Bands. In: *Proceedings of 16th IFAC World Congress*. : Elesevier, ISBN: 0-08-045108-X, Prague, Czech Republic, July 2005

6. Brandt, T. ; Sattel, T. ; Wallaschek, J.: On Automatic Collision Avoidance Systems. In: *SAE 2005 Transactions Journal of Passenger Cars: Electronic and Electrical Systems* (2006), February, p. 431-440 (selected reprint of 3.)

7. Brandt, T. ; Sattel, T. ; Wallaschek, J.: Towards vehicle trajectory planning for collision avoidance based on elastic bands. In: *International Journal of Vehicle Autonomous Systems* 5 (2007), No. 1/2, p. 28-46

8. Hanisch, S. ; Nölle, R. ; Brandt, T. ; Sattel, T.: On the Computation of Equilibrium Configurations of Elastically Coupled Nodes in Potential Fields. In: *WSEAS Transactions on Systems* 4 (2005), January, No. 1, p. 68-73

9. Löper, C. ; Hesse, T. ; Brandt, T. ; Sattel, T.: Developing Driver Assistance Systems using CarSim as a Reference Model. In: *Proceedings of 1st European CarSim User Conference*. Braunschweig, September 2005

10. LÖPER, C. ; SCHOMERUS, J. ; BRANDT, T. ; FLEMISCH, F. ; SATTEL, T.: Bahnplanung, Bahnführung und haptische Interaktion für ein Fahrerassistenzsystem zur Querführung. In: *VDI Berichte Nr. 1960, VDI/VW Gemeinschaftstagung Integrierte Sicherheit und Fahrerassistenzsysteme.* Wolfsburg, October 2006, p. 189-205

11. SATTEL, T. ; BRANDT, T.: Ground Vehicle Guidance along Collision-Free Trajectories using Elastic Bands. In: *IFAC 24th American Control Conference (ACC)*, IEEE Catalog No. 05CH37668C (American Automatic Control Council and IFAC), Portland Oregon, USA, June 2005, p. 4991-4996

12. SATTEL, T. ; BRANDT, T.: Ein Beitrag zur interaktiven Querführungsassistenz von Kraftfahrzeugen. In: *VDI Berichte Nr. 1960, VDI/VW Gemeinschaftstagung Integrierte Sicherheit und Fahrerassistenzsysteme.* Wolfsburg, October 2006, p. 207-222

13. SATTEL, T. ; BRANDT, T.: A note on vehicle guidance control using a mechanical analogy. (GAMM Annual Meeting Berlin 2006) In: *PAMM (6), No. 1*, WILEY-VCH Verlag GmbH & Co. KGaA, Weinheim, January 2007, p. 841-842